Technische Universität München
TUM School of Natural Sciences

Photo- and Electrocatalytic CO_2 Reduction with Mono- and Binuclear Transition Metal Mabiq Complexes

Kerstin Rickmeyer

Vollständiger Abdruck der von der TUM School of Natural Sciences der Technischen Universität München zur Erlangung einer

Doktorin der Naturwissenschaften (Dr. rer. nat.)

genehmigten Dissertation.

Vorsitz:	Prof. Dr. Klaus Köhler
Prüfende der Dissertation:	
	1. Prof. Dr. Corinna Hess
	2. Prof. Dr. Hubert A. Gasteiger

Die Dissertation wurde am 23.01.2025 bei der Technischen Universität München eingereicht und durch die TUM School of Natural Sciences am 30.06.2025 angenommen.

This thesis describes the work carried out in the field of Bioinorganic Chemistry at the Technical University Munich between July 2019 and March 2024. The project described herein was supervised by Prof. Dr. Corinna R. Hess.

Acknowledgements

First of all, I wish to thank my supervisor Prof. Dr. Corinna R. Hess for giving me the opportunity to conduct my thesis in her group. I have learned a lot over these past years and am deeply thankful for the support and guidance I have experienced in my time as a PhD student.

I would like to thank all of the other Hess group members, Raffa, Andi, Ceren, Lukas, Zek, Philippe, Matthias and our newbies Sayonika and Nataliia for the great atmosphere in the lab, the support and helpful ideas and all the good vibes that definitely boosts our chemistry. Many thanks to especially Lukas, my tea time partner and our caretaker of the lab, you kept it running. I learned so much from you and I was always astonished how you never ran out of ideas and hypothesis. But also Philippe and Matthias, thank you for your critical thinking, for many fruitful discussions and proof-reading.

Also thanks to my students, Johannes, Ivan and Roman for your enthusiasm and contribution to the Mabiq project.

Furthermore, I wish to thank our secretary Lucia, you did a great job in supporting us with all the bureaucratic stuff and were always a really good person to talk to when stepping by your office. Rest in peace, you passed too early and left quite a hole.

I also want to thank Jürgen Kudermann from the central analytic department for his never ending support with the instruments in particular the gas-chromatograph, where he spent a decent amount of time to get it running and training everyone in using it properly.

In this regard also thanks to our collaborators in Erlangen, Martin Keilwerth and Dr. Jörg Sutter from Prof. Karsten Meyer's chair, for the Mößbauer measurements and Prof. Inke Siewert and her student Lukas Paul for helpful discussions on electrocatalysis.

Lastly, I would like to express my deepest gratitude to my family and friends. I couldn't have done it without your great support. Thank you for having my back. Many thanks Cari, you are my best friend, we understand each other without a word and I know you are there when I need you. A special thanks goes to Martin, for enduring me during stressful times, always providing me with tasty food and most of all for your love. You are the best!

List of Abbreviations

BIH	1,3-dimethyl-2-phenylbenzimidazoline
BNAH	1-benzyl-1,4-dihydronicotinamide
bpy	bipyridine
CPE	controlled potential electrolysis
cpo	cyclopentadienone
CT	charge-transfer
CV	cyclic voltammetry
cyclam	1,4,8,11-tetraazacylcotetradecane
DFT	density functional theory
DIPEA	N,N-diisopropylethylamine
DMF	dimethylformamide
$\mathbf{E^0_{CO_2}}$	thermodynamic potential for reduction of CO_2
EEC	two electron transfer step, followed by a chemical step
$\mathbf{E_{onset}}$	onset potential
$\mathbf{E^*_{ox}}$	excited state oxidation potential
$\mathbf{E_{red}}$	reduction potential
$\mathbf{E^*_{red}}$	excited state reduction potential
ET	electron transfer
Fc	ferrocene
FE	faradaic efficiency
GC	gas-chromatography
HAE	heavy atom effect
HER	H_2 evolution reaction
IC	internal conversion
IR	infrared
ISC	intersystem crossing
LIFDI-MS	liquid injection field desorption ionization mass spectrometry
LUMO	lowest unoccupied molecular orbital
Mabiq	[2-4:6- 8-bis(3,3,4,4-tetra-methyldihydropyrrolo)-10-15-(2,2'-biquinazolino)-[15]-1,3,5,8,10,14-hexaene-1,3,-7,9,11,14-N_6]
MeCN	acetonitrile
MLCT	metal to ligand

	charge-transfer
MO	molecular orbital
NAD	nicotinamide adenine dinucleotide
NHC	N-heterocyclic carbene
NHE	normal hydrogen electrode
[Ni,Fe]-CODH	[Ni,Fe]-carbon monoxide dehydrogenase
NMR	nuclear magnetic resonance
PDI	pyridine(diimine)
phen	1,10-phenanthroline
PhOH	phenol
PS	photosensitizer
PyMe	*N*-methylpyridinium
qpy	quaterpyridine
Quin	quinuclidine
Φ	quantum yield
SC-XRD	single crystal X-Ray diffractometry
SEA	sacrificial electron acceptor
SED	sacrificial electron donor
SHE	standard hydrogen electrode
SOC	spin-orbit coupling
TADF	thermally activated delayed fluoresence
TEA	triethylamine
TEOA	triethanolamine
TOF	turnover frequency
TON	turnover number
TPP	tetraphenylporphyrin
tpy	terpyridine
UV-Vis	ultraviolett-visible

Publication List

- Rickmeyer K., Huber M., Hess C. R. ”Influence of a neighbouring Cu centre on electro- and photocatalytic CO_2 reduction by Fe-Mabiq” *Chem. Commun.*, **2024**, *60*, 819–822.

- Rickmeyer K., Niederegger L., Keilwerth M., Hess C. R. ”Multifaceted Role of the Noninnocent Mabiq Ligand in Promoting Selective Reduction of CO_2 to CO” *ACS Catal.*, **2022**, *12*, 3046–3057.

Conference Contributions

- Rickmeyer K., Wang Z., Niederegger L., Rauh F., Stutzmann M., Hess C. R. ”Electrocatalytic CO_2 reduction with transition metal complexes of the non-innocent Mabiq ligand” 3rd e-conversion conference **2022**, Venice, Italy; Poster

- Rickmeyer K., Niederegger L., Keilwerth M., Hess C. R. ”Electrocatalytic CO_2 reduction with transition metal complexes of the non-innocent Mabiq ligand” 16th European Biological Inorganic Chemistry Conference **2022**, Grenoble, France; Poster

- Rickmeyer K., Tok G. C., Gasteiger H. A., Hess C. R. ”Electrocatalytic small molecule activation by macrocylclic Co- and Fe-Mabiq Complexes” Anglo-German Inorganic Chemistry Conference **2021**; Poster

- Rickmeyer K., Niederegger L., Hess C. R. ”Electrocatalytic CO_2 reduction by Fe-Mabiq” 2nd e-conversion conference **2021**, Munich, Germany; Poster

- Rickmeyer K., Lauenstein R., Hess C. R. ”Photochemical Properties of Transition Metal Mabiq Complexes” 15th National Coordination Chemistry Conference **2020**, Freiburg, Germany; Poster

- Rickmeyer K., Lauenstein R., Tok G. C., Gasteiger H. A., Hess C. R. ”Photo- and Electrocataylsis by Transition Metal Mabiq Complexes” 1st e-conversion conference **2019**, Venice, Italy; Poster

Contents

Introduction

For many decades researchers have put immense efforts into the development of suitable catalysts for the reduction of the deleterious greenhouse gas CO_2.[1] With over 100 Mt of CO_2 produced per day we are at an all time high of CO_2 emission due to combustion of fossil fuels for power generation which still make up about 80 % of the worldwide energy source and their use in e.g. petrochemical and construction industry.[2,3] Over the past years renewable energies such as wind power or solar technologies have become more and more present. However, chemical industry still requires carbon based raw materials.[2] Therefore, one strategy is to use CO_2 as C_1 building block for these materials ideally employing renewable energies.[1,3–5] This is not an easy task—underscored by the long time period during which researchers are still investigating systems for efficient CO_2 reduction—as CO_2 is thermodynamically very stable. Reduction of CO_2 by one electron leads to a geometry distortion from a linear to a bent molecule.[1,2] This high reorganisation energy is reflected by the very negative potential required for a direct, i.e. uncoupled outersphere reduction of CO_2 by one electron (Table 1). Coupling the reduction of CO_2 with protons facilitates the electron transfer (ET). Reduction of CO_2 is now feasible at less negative potentials, however, production of H_2 becomes an unwanted side-reaction lowering the yield for carbon-containing products.[6] Reduction products beyond the two electrons i.e. toward the C_1 reaction products formaldehyde, methanol, methane or even $C_{n>1}$ products still remains challenging.[8] Thus, the most commonly observed products from CO_2 reduction are the two electron reduction products CO and HCO_2^-. Since proton reduction as well as CO and HCO_2^- formation takes place at very similar potentials (Table 1), the development of efficient and selective catalysts for CO_2 reduction is crucial. CO_2 reduction can be carried out by both homogeneous and heterogeneous catalysts and both fields are still under extensive investigation. Herein the focus will be on homogeneously catalyzed CO_2 reduction. Molecular catalysts provide several benefits as they are well-defined which allows researchers to identify key catalytic intermediates and/or functional groups that are important in the reaction mechanism using combinations of various spectroscopic, electrochemical and theoretical methods.[1,4,9,10] Moreover, further modification based on those findings can be carried out considerably easy, leading to the development of more efficient catalysts.

Table 1: Overview of reduction potentials of CO_2 and H^+. All potentials are given vs. normal hydrogen electrode (NHE) at pH 7.[7]

$CO_2 + e^-$	$\longrightarrow$	$CO_2^{\bullet-}$	$E^{\circ\prime} = -1.93$ V
$2\,H^+ + 2\,e^-$	$\longrightarrow$	H_2	$E^{\circ\prime} = -0.41$ V
$CO_2 + 2\,H^+ + 2\,e^-$	$\longrightarrow$	$CO + H_2O$	$E^{\circ\prime} = -0.53$ V
$CO_2 + H^+ + 2\,e^-$	$\longrightarrow$	HCO_2^-	$E^{\circ\prime} = -0.39$ V

Electrocatalytic CO_2 reduction

The first attempts toward CO_2 reduction using transition metal complexes were carried out electrocatalytically already in the 1970s.[11–13] Over the years many examples for molecular CO_2 reduction catalysts have been reported. Most commonly, complexes employing late transition metals were studied. Only a few examples with early transition metals, e.g. Cr, that can act as CO_2 reduction catalysts have been investigated thus far.[14] While early studies relied on precious metals such as Re,[15] Ru[16] or Pd,[17] researchers have now turned their interest toward earth-abundant metals.[1,18] For one, for economic reasons, as the latter are considerably cheaper due to their higher abundance and second for environmental reasons.[19–21] Various complexes with first row late transition metals such as Mn,[7,22,23] Fe,[24–28] Co,[27,29–31] Ni,[32,33] Cu[34,35] and even Zn[36] are reported to act as CO_2 reduction catalysts. Among those, Fe-complexes were frequently investigated due to the high abundance of Fe in the earth's crust[21] and its versatile coordination chemistry and redox properties.[10]

Benchmarking electrocatalysis

In order to make various systems and set-ups comparable it is crucial to define a number of goodness factors that can be used to evaluate the performance of the investigated catalytic system. Beside the common parameters like durability, stability, selectivity, turnover number (TON) and turnover frequency (TOF) which are commonly used to compare catalysts, there are a few more parameters specific for electrocatalysis. First, the faradaic efficiency (FE) which is defined according to equation 1 with the number of moles of product formed ($n_{product}$ in [mol]), the number of electrons involved (z = 2 for CO_2 reduction to CO or HCOOH), the Faraday constant (F = 96485 C·mol^{-1}) and the total charge passed during electrolysis (Q_{passed} in [C]). In an optimal case the FE is 100 % indicating that no charge is lost via unwanted side reactions or catalyst decomposition.[1]

$$FE = \frac{n_{product}}{z \cdot F \cdot Q_{passed}} \tag{1}$$

In order to achieve reasonable reaction rates higher potentials—more negative potentials for reductions and more positive ones for oxidations—than the required thermodynamic potential are applied in electrocatalysis. This so-called overpotential requirement (η) is defined as the difference between the standard electrode potential (E^{00}) and the potential that is required to drive the reaction at a specific rate (E_{cat}) (equation 2).[37]

$$\eta = E^{00} - E_{cat} \tag{2}$$

Unsurprisingly, the aim is to design a catalytic system that operates with the lowest possible overpotential requirement while still leading to reasonable TOFs. Catalytic Tafel plots correlate

the log(TOF) with the respective overpotential requirement which allows for a good comparison between different catalysts as well as the determination of optimal catalytic conditions.[37]

Overpotential determination

For determination of the overpotential requirement (equation 2) it is crucial to know the standard electrode potential for the reaction. Many electrocatalytic CO_2 reduction reactions were and still are carried out in organic solvents. However, experimental data in nonaqueous solvents remained scarce.[38–40] In the past decade various researchers contributed to this field, reporting a series of standard electrode potentials for the reduction of CO_2 to CO in dimethylformamide (DMF) and acetonitrile (MeCN), determined both computationally and experimentally.[26,38–42] For a correct estimation of the standard electrode potential also the amount and type of acid present has to be considered. Azcarate et al. presented the following approach for the determination of E^{00} in DMF and MeCN as solvent and depending on the acid involved in the reaction (equations 3 and 4).[42]

$$E^{00}_{CO_2/CO,DMF,HA} = -0.307 - \frac{RTln(10)}{F} pK_{a(HA,DMF)} \qquad \text{in } [V_{SHE}] \tag{3}$$

$$E^{00}_{CO_2/CO,MeCN,HA} = 0.287 - \frac{RTln(10)}{F} pK_{a(HA,MeCN)} \qquad \text{in } [V_{SHE}] \tag{4}$$

For the determination of E^{00} the pK_a of the strongest acid present needs to be considered. Even though the authors used phenol as the proton source in their experiments they postulate that it is not the strongest acid present.[26,42] MeCN is difficult to render entirely water-free. It is thus reasonable to assume that even “dry” MeCN still contains a tiny amount of water. Moreover, water is a side product in the reduction of CO_2 to CO. In the presence of water, CO_2 is the strongest acid present with a pK_a = 7.37 in DMF or pK_a = 17.03 in MeCN, respectively. This leads to a standard electrode potential of $E^{00}_{CO_2/CO,DMF,HA} = -0.74\ V_{SHE} = -1.46\ V_{Fc}$ and $E^{00}_{CO_2/CO,MeCN,HA} = -0.72\ V_{SHE} = -1.41\ V_{Fc}$.[a]

For some acids the pK_a of the acid is higher than anticipated due to an effect called homoconjugation.[43] Homoconjugation describes a phenomenon in which hydrogen bonding between the acid and the conjugate base stabilizes the latter, as it increases their acidity at high concentrations. This phenomenon is known since the 1950s but was long not taken into account even though it affects most of the acids used in MeCN. Neglection of this effect may thus lead to a missleading estimation of catalyst performances with respect to the overpotential requirement. Artero and co-workers presented a parameter which denotes when homoconjugation of an acid needs to be taken into consideration (equation 5) depending on the association constant K_c and the concentration of the acid c_{HA}. If $\kappa > 1$ the effect of homoconjugation cannot be

[a] The conversion factors reported by Elgrishi et al. were used for the conversion from V vs. SHE [V_{SHE}] to V vs. $Fc^{+/0}$ [V_{Fc}].[18]

neglected.

$$\kappa = K_c c_{HA} \tag{5}$$

The standard electrode potential can be then estimated using the method and equations reported by Matsubara.[41] For this approach more parameters need to be considered and in most publications the authors thus refer to the method from Savéant and co-workers. Generally both routes should yield similar potentials within the margin of error.[44]

Mechanism for CO_2 reduction

Before looking at different strategies and catalyst design for CO_2 reduction it is important to understand the steps involved in the CO_2 reduction reaction. CO_2 is an amphoteric molecule with a lewis acidic carbon and lewis basic oxygen atoms. For activation of CO_2 three coordination modes can be envisioned as depicted in Figure 1, via the carbon in an η^1 fashion, in an end-on coordination via one of the terminal oxygens or in an η^2 side-on mode. As CO_2 is a better electron acceptor than donor the η^1-C coordination is the most commonly observed in CO_2 reduction where often electron-rich metals are involved which allow for a strong charge-transfer (CT) between the metal center and the antibonding σ^* and π^* orbitals of CO_2. The η^1-O end-on coordination is rare and preferred with electron-poor metals.[1]

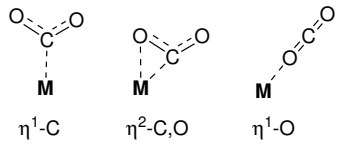

Figure 1: Three common coordination modes of CO_2 to a single metal center.[1]

Considering the most commonly observed active species in CO_2 reduction, metal centers with low oxidation states ($M^{I/0}$), a d^8 configuration and in a square pyramidal ligand field play an integral role.[45–48] As depicted in the qualitative molecular orbital (MO) diagram in Figure 2 the d_{z^2} as well as the d_{xz} and d_{yz} have the appropriate geometry to overlap with the antibonding σ^* and π^* orbitals of CO_2. Upon coordination to a sufficiently electron-rich metal center, the antibonding, lowest unoccupied molecular orbital (LUMO) of CO_2 will be occupied. This interaction leads to the aforementioned geometry change from a linear to a bent molecule (*vide supra*), as also shown in Figure 1. Both coordination modes that are preferred with electron-rich metals yield a bent CO_2 whereas the η^1-O coordination mode observed with electron-poor metals exhibits a linear CO_2.

Generally, two main CO_2 reduction mechanisms are discussed. The reduced metal center can either operate via the *CO_2-activation-first* pathway where it activates CO_2 in the first step (Scheme 1a) or via the *protonation-first* pathway where the first step involves the formation of a

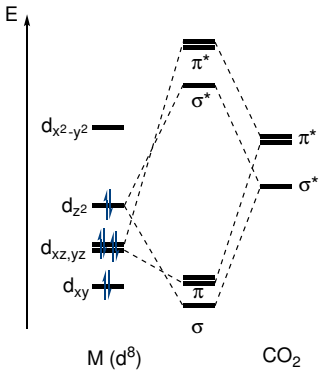

Figure 2: Qualitative MO diagram for interaction between a metal d^8 center and CO_2.[1,45,47]

metal-hydride (Scheme 1b).[1,6,45,47] CO is solely obtained via the *CO_2-activation-first* pathway

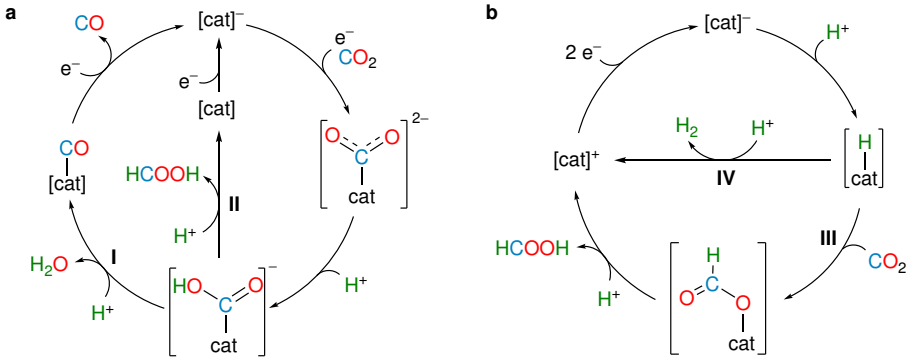

Scheme 1: Plausible routes for *CO_2-activation-first* (a) and *protonation-first* (b) pathway in the $2\,e^-/2\,H^+$ reduction of CO_2.

(Scheme 1a path **I**). The next step after CO_2 activation is most commonly protonation of the activated CO_2. Then protonation by a second H^+ at the oxygen followed by release of water leads to a metal carbonyl species. In many reports reduction of that metal carbonyl is required to yield CO and regenerate the active catalytic species. It should be noted though that sometimes the order of reduction and protonation can slightly vary between different systems. If the second protonation in the *CO_2-activation-first* pathway occurs at the carbon rather than the oxygen (Scheme 1a path **II**), formate can be obtained instead.[1,45,47] Another possible route toward formate is via the *protonation-first* pathway by insertion of CO_2 into a metal-hydride bond (Scheme 1b path **III**). However, the metal-hydride could also react with yet another proton (Scheme 1b path **IV**) leading to the formation of H_2 instead. This unwanted side reaction lowers the overall carbon-containing yield as it siphons electrons away from CO_2 reduction.[1,6]

Toward selective and effective CO_2 reduction catalysts

Over the past years many strategies were reported to enhance the efficiency and selectivity of CO_2 reduction catalysts. In order to increase the selectivity, e.g. suppression of the H_2 evo-

lution reaction (HER)—an unwanted side-reaction due to the presence of protons in the reaction mixture—is sought after. The usage of redox-active ligands, installation of e^--withdrawing groups as well as the presence of a second metal or cationic charges in proximity to the active center were tested toward this goal. Moreover, for economic reasons it is desirable to perform the reaction at the lowest overpotential requirement possible while still achieving reasonable TOFs. The TOF may be increased by removing CO from the reaction mixture as this might poison the catalyst. Lower overpotential requirements were obtained following multiple attempts reaching from extension of the ligand π-conjugation over modifications of the first coordination sphere, incorporation of e^--withdrawing groups or proton relays to having a second metal or positive charges in proximity to the active center. All noted effects are listed in Figure 3 and discussed in more detail in the sections below.

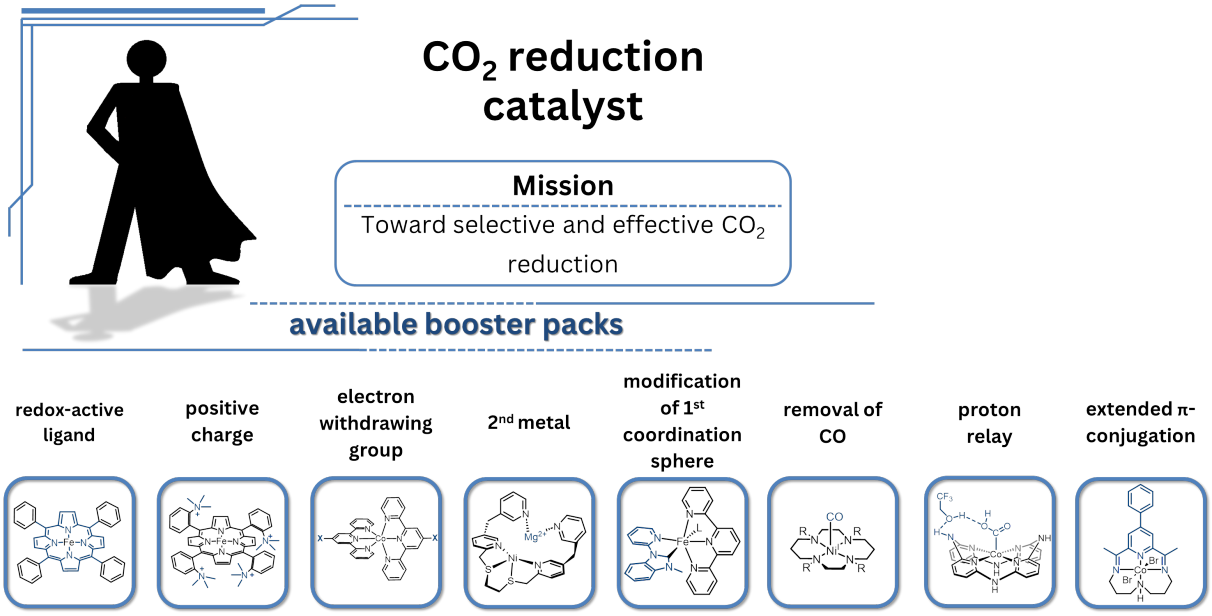

Figure 3: Overview of select strategies that were used to enhance the performance of homogeneous CO_2 reduction catalysts.

Strategies to suppress H_2 evolution

In light of the CO_2 reduction mechanisms presented in Scheme 1, the most straight forward attempt to circumvent the HER would be to avoid the formation of the metal-hydride, i.e. favoring the *CO_2-reduction-first* over the *protonation-first* pathway. Relevant for the affinity of a metal center toward formation of a metal-hydride is the pKa of the metal-hydride. The pKa correlates linearly with the reduction potential of the metal center.[6] The more reducing the metal center, the stronger is its Brønsted basicity. Thus, the more likely becomes the formation of a metal-hydride. However, electron-rich systems are required for CO_2 activation.

In the study by Su et al. the authors reported an exemplary approach that demonstrates how

the affinity of the active species can be shifted from a *protonation-first* to a *CO_2-activation-first* pathway. Three similar Ni-catalysts were investigated. While the first one (**Ni-I**) was coordinated by a broken macrocycle, the second one (**Ni-II**) employed a flexible macrocycle and the third (**Ni-III**) was coordinated by a rigid macrocycle (Figure 4). When studying CO_2 reduction with

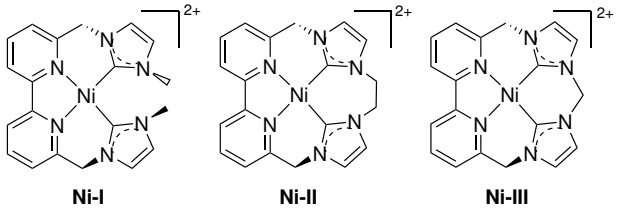

Figure 4: Ni-catalysts studied by Su et al. for CO_2 reduction.[49]

these catalysts, they observed that **Ni-I** gave H_2 as the main product with 93% selectivity. **Ni-II** yielded an equal composition of H_2 and CO (CO: 53%, H_2: 46%) while **Ni-III** on the other hand mainly produced CO with 87% selectivity. A plausible explanation for this behavior was obtained from density functional theory (DFT) calculations on the electronic structure of the doubly reduced species. When inspecting the electron density of the two-electron reduced species, which is the active species in this CO_2 reduction reaction, they found that while the first electron is stored on the bipyridine site of the ligand in all three cases the location of the second electron varies within the series. Due to the broken macrocycle, two electron reduction of **Ni-I** led to $[Ni^{I}(L^{\bullet-})]$, i.e. reduction of the Ni^{II} to Ni^{I} took place upon addition of the second electron. Investigation of the two-electron reduced **Ni-III** showed that both electrons are stored on the ligand so in contrast to **Ni-I** no metal-centered reduction took place. Hence the formation of a metal-hydride becomes less likely for **Ni-III**. **Ni-II** shows a mixture of both cases which is also in line with the experimental findings. In conclusion, one strategy to avoid HER is the use of redox-active ligands that are capable of storing necessary electrons for CO_2 reduction.
This approach can be found in multiple systems reported for CO_2 reduction and in fact they often lead to CO as the sole product without significant H_2 formation.[4,44,50–54] Some exemplary systems are shown in Figure 5.

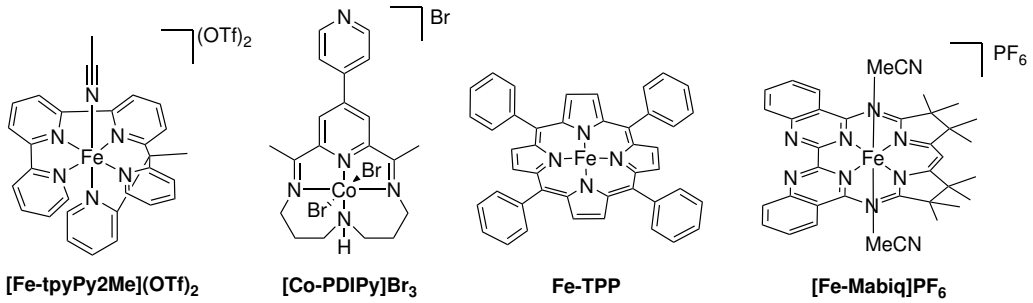

Figure 5: Some exemplary systems used for CO_2 reduction employing redox-active ligands capable of storing electrons.[26,44,50,51]

Another strategy to inhibit the HER was presented by Elgrishi et al. for a Co complex bearing

two modified terpyridine (tpy) ligands (Figure 6, left).[31] Tuning of the ancillary ligand field by

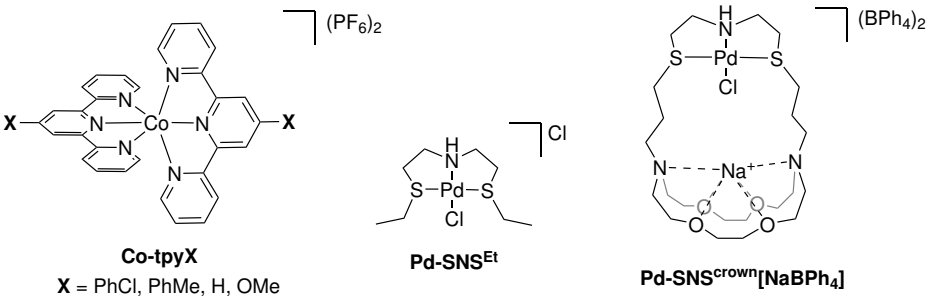

Figure 6: Strategies to inhibit HER by ligand modifications[31] and proximal cations.[55]

incorporation of electron-withdrawing or -donating groups allowed the authors to disfavor or favor HER. With more electron-rich ancillary ligand fields, higher proton reduction rates were obtained. Studying the same series for CO_2 reduction showed that the trend is reversed, i.e. higher yields for CO formation were obtained for the complex with lower proton reduction rates. Based on their studies the rate for CO_2 reduction is not as drastically affected by the ligand modification as the proton reduction rate. Therefor, installing electron-withdrawing groups on the ligand can help in "turning-off" the HER.

Modifications of the ligand can also be used to install a second metal binding site. In a recent work from the group of J. Yang, a crown ether was installed in proximity to the active site to bind cations such as Na^+ or Ba^{2+} (Figure 6, right).[55] Electrochemical investigations showed that the modified complex with the proximal cation (**Pd−SNS^{crown}[NaBPh$_4$]**) exhibits a significantly higher overpotential for the HER compared to its unmodified parent complex (**Pd−SNS^{Et}**). While **Pd−SNS^{Et}** gave H_2 as the only product in the presence of CO_2, CO_2 reduction to CO was observed for **Pd−SNS^{crown}[NaBPh$_4$]** albeit with low yields. The authors postulate that the HER is inhibited due to electrostatic interactions with the cationic charges from the proximal cation. As CO_2 is neutral, it is not negatively affected. In contrast, the cationic charge in proximity to the active center might be additionally beneficial for CO_2 reduction. The anionic intermediate could be stabilized via coulombic interaction which leads to lower overpotential requirements.

Ligand modifications for more effective CO_2 reduction

Incorporation of cationic charges does not only help in inhibiting the HER but can further be harnessed to stabilize the activated CO_2 at the metal center via coulombic interactions. This strategy led to the development of one of the most efficient CO_2 reduction electrocatalysts to date, exhibiting an overpotential requirement of only 220 mV.[24] Azcarate et al. synthesized a modified tetraphenylporphyrin (TPP) with trimethylammonium residues in ortho position (**Fe-oTMA**, Figure 7). Another modified TPP with the trimethylammonium residues in para positions (**Fe-pTMA**) was prepared as well and also exhibited enhancement in CO_2 reduction compared

to the unmodified TPP, but shows worse performance than **Fe-oTMA**. Within **Fe-oTMA** the residues are ideally positioned around the active center to stabilize the activated CO_2, which results in the low overpotential requirement as well as the highest TOF within the series.

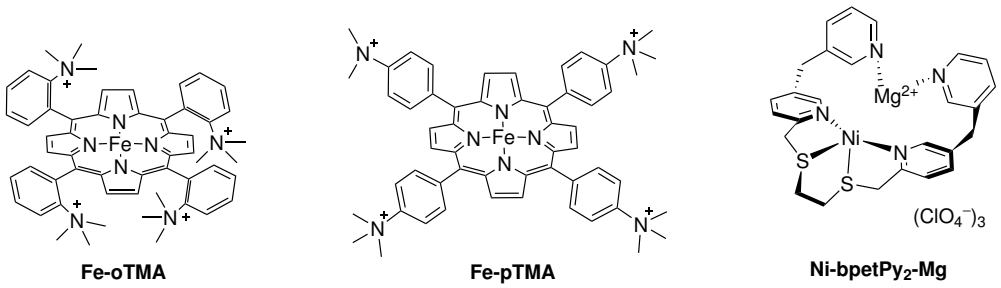

Figure 7: Cationic charges in proximity of the active center lead to enhancement in CO_2 reduction (**Fe-oTMA**, **Fe-pTMA**)[24] and modified Ni-catalyst (**Ni-bpetPy$_2$**) to trap Mg^{2+} in proximity to the active center.[56]

However, the system from Azcarate et al. is not the only example where incorporation of cationic charges lead to an enhancement in CO_2 reduction. Another example is a modified Co-PDI complex (PDI = pyridine(diimine)) by McCrory and co-workers (Figure 8).[51] In their study the authors investigated the effect of various ligand modifications, starting with extension of the conjugation within the ligand (**[Co−PDIPh]Br$_3$**), followed by addition of electron-withdrawing groups (**[Co−PDIPy]Br$_3$**) up to implementation of cationic charge within the ligand scaffold (**[Co−PDIPyMeI]Br$_3$**). Introduction of the phenyl residue in **[Co-PDIPh]Br$_3$** led to a moderate positive shift in potential for each couple compared to those of the unmodified parent complex **[Co−PDI]Br$_3$**. The authors postulate that this shift is attributed solely to the extended π-conjugation as the e^--withdrawing effect of the phenyl group is negligible. This extended conjugation does not affect the onset potential (E_{onset}) but led to a slightly higher catalytic current for **[Co-PDIPh]Br$_3$** compared to **[Co-PDI]Br$_3$**. The pyridyl group, however, exhibits a significant e^--withdrawing effect. Replacing the phenyl residue with pyridyl led to an additional positive shift for all redox potentials for **[Co−PDIPy]Br$_3$** compared to **[Co−PDIPh]Br$_3$** due to the added e^--withdrawing effect. The E_{onset} under CO_2 atmosphere is now shifted to more positive potentials. The addition of the cationic *N*-methylpyridinium (PyMe) group in **[Co−PDIPyMeI]Br$_3$** also led to a positive shift of the $Co^{III/II}$ and $Co^{II/I}$ couples, indicating that this group further facilitates reduction of the complex. Due to the additional positive charge on the ligand scaffold, **[Co−PDIPyMeI]Br$_3$** exhibits an even higher catalytic current alongside a more positive E_{onset} than **[Co−PDIPy]Br$_3$**. In the presence of both CO_2 and the proton source H_2O an increased catalytic activity is observed for all complexes with the same qualitative trend within the series with respect to increase in activity and positive shift of E_{onset} as in the absence of H_2O. It should be noted though that for **[Co−PDIPyMeI]Br$_3$** also a change in the catalytically active species from the quadruply reduced to the triply reduced species is observed with addition of the proton source. This effect is explained by the change of the thermodynamic potential for reduction of CO_2 ($E^0_{CO_2}$) with increasing amount of H_2O. At higher [H_2O] the $E^0_{CO_2}$ becomes positive enough

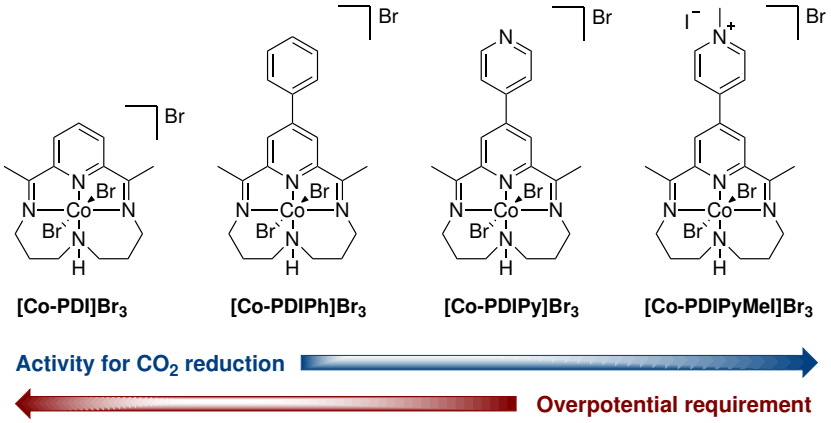

Figure 8: Consecutive ligand modifications to enhance CO_2 reduction.[51]

that the triply reduced species of **[Co−PDIPyMeI]Br$_3$** has sufficient reducing power to drive the reaction. Overall, their work nicely combined the findings from previous reports in one system showing how each modification lead to an increase in activity for CO_2 reduction alongside a lower overpotential requirement.

Stabilization of the activated CO_2 can be further achieved via H-bonding. Already in 1993 Fujita et al. reported a Co-macrocycle (**Co-dieneN$_4$**, Figure 9, left) bearing two N−H groups which aid in stabilizing the activated CO_2. The resulting CO_2 complex (**Co-dieneN$_4$-CO$_2$**, Figure 9, left) could be characterized by UV-Vis absorption, IR and NMR spectroscopy. H-bond donors in proximity to the active center may have yet another effect. In a modified TPP with hydroxyl groups in ortho positions (**Fe-TDHPP**, Figure 9, middle) Costentin et al. showed that the phenol residues enhance CO_2 reduction by stabilization of the activated CO_2 via hydrogen bonding interaction and further act as proton relays.[26,58] Analysis of the electrochemical data revealed that the rate-determining step in the reaction is an electron transfer from the iron center concerted with proton transfer and C−O bond cleavage.[61] The necessary proton originates from one of the pre-positioned phenolic groups which gets thus reprotonated by added phenol in solution.[58]

It is also possible that a pendant proton relay is formed *in situ* when working with non-innocent ligands that can undergo (de)protonation during the reaction mechanism. In the system reported by Beller and co-workers (**Fe-cpOH**, Figure 9, middle) the hydroxyl group plays a double

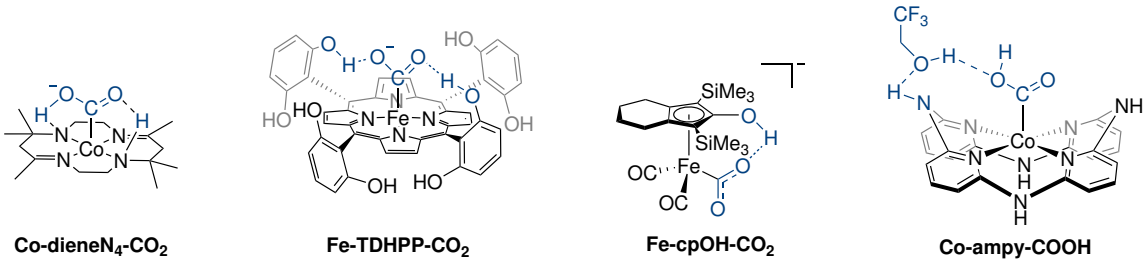

Figure 9: H-bonding to stabilize the bound CO_2 and as proton relay to enhance protonation.[57–60]

role by stabilizing the bound CO_2 as well as donating the second proton for the dehydration step facilitating the C−O bond cleavage.[59] Direct protonation of the activated CO_2 via the pendant proton relay was also believed to take place in the system studied by the group of Marinescu. Therein a Co complex coordinated by a macrocycle with pendant N−H groups (**Co-ampy**, Figure 9, right) was found to be more effective than its methylated analogue.[29] However, further mechanistic investigations showed that the pendant N−H groups establish a hydrogen bonding network which traps the acid needed for protonation of the activated CO_2 in proximity to the active center thereby facilitating the protonation step leading to high TOFs.[60] In conclusion, H-bonding can enhance CO_2 reduction in multiple ways by either stabilizing the bound CO_2 leading to lower overpotential requirements and/or by facilitating the protonation step, directly or via establishment of a H-bonding network, which results in higher TOFs as the protonation and release of H_2O is often the rate-determining step in the reaction.

Already in the early days of CO_2 reduction, Savéant and co-workers discovered that addition of Lewis acids such as Mg^{2+} into the reaction solution enhances CO_2 reduction.[62] This approach was taken to a next level in the work of Hong et al. where they installed two pyridine arms on their ligand.[56] These arms are capable to trap a Mg^{2+} ion in proximity to the active Ni-center (**Ni-bpetPy$_2$-Mg**, Figure 7). The Mg^{2+} then interacts with the activated CO_2 via ion-pairing with the negatively charged oxygen atoms. It further aids in breaking one of the C−O bonds by a push-pull mechanism. This is a very commonly observed motif in nature with prominent examples such as the [Ni,Fe]-carbon monoxide dehydrogenase ([Ni,Fe]-CODH) where the neighboring Fe^{II} acts as the Lewis acid that pulls while the active Ni center pushes electron density onto the activated CO_2.[46]

Depending on the type of the second metal different effects may be envisioned. If the metal is redox-inert like the Mg^{2+} or Na^+ mentioned earlier, the effect should be limited to electrostatics. In the case of redox-active metal centers the two centers can be electronically coupled, i.e. the electrons would be delocalized between the two centers.[63] Also dual catalysis may be possible with two active metal centers,[64] where CO_2 would be activated at one metal center while the second metal center catalyses the incorporation of the activated CO_2 or one of its reduction products, e.g. CO, into an organic compound yielding more valuable reaction products.[65]
In the most recent study from McCrory and co-workers the authors investigated the effect of a second metal with their system.[63] They found that the heterobimetallic dimer **[Co-PDI-PDI-Zn]Br$_5$** outperformed its homobimetallic analogue (Figure 10), indicating that the larger electrostatic effect due to the proximal redox-inert Zn^{2+} outweighs the effect of electron delocalization between the two linked redox-active Co sites. The same trend was also observed by Liu et al. when they compared a homobimetallic **CoCo-bpbp** with the analogous heterobimetallic **CoZn-bpbp** system (Figure 10).[66] The superior behavior of **CoZn-bpbp** over **CoCo-bpbp** is attributed to a lower energy barrier for CO_2 binding which was identified as the rate-determining step in their reaction. These studies provide another examples how and that incorporation of redox-inert metal sites can enhance the catalytic activity for CO_2 reduction. In accordance with

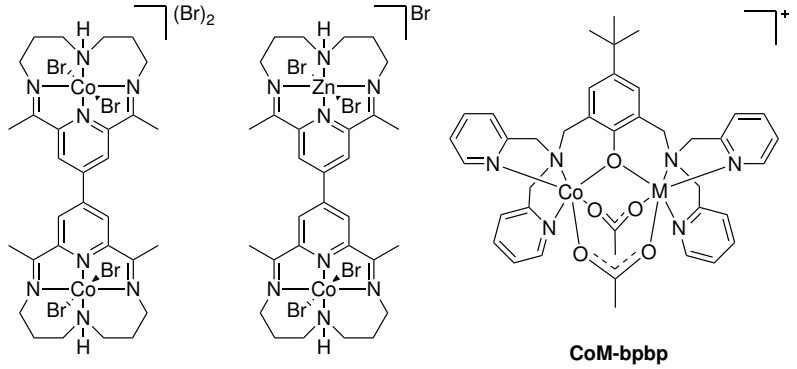

[Co-PDI-PDI-Co]Br$_6$ **[Co-PDI-PDI-Zn]Br$_5$**

Figure 10: Bimetallic systems highlighting the effect of a redox-inert vs. a redox-active second metal.[63,66]

their previous findings with the monometallic **[Co−PDIX]Br$_3$** system, McCrory and co-workers postulate that the electrostatic effect leads to an increased stabilization of the activated CO_2 bound to the metal center.[51,63] For once, the positively charged metal has a strong electron-withdrawing effect, increasing the stability of the ligand radicals which ultimately leads to a better stabilization of the CO_2 adduct. The positively charged metal in proximity to the active center may also stabilize the negatively charged CO_2^- ligand directly via Coulombic interactions similarly to the positively charged groups in **Fe-oTMA** by Azcarate et al. (*vide supra*).[24,63]

All these approaches listed above worked with modifications of the second coordination sphere by positioning functional groups or a second metal in proximity to the active metal center maintaining its first coordination sphere. However, especially when studying non-heme metal complexes it is also worthwhile to investigate effects of the first-coordination sphere. For instance, Fe complexes employing the tpy ligand and modifications thereof were already reported to be suitable CO_2 reduction catalysts.[50,52] Considering a six-coordinate Fe center, the tridentate tpy ligand leaves three free coordination sites. After finding a dramatic acceleration for Ru-complexes employing a tpy ligand with a strongly σ-donating N-heterocyclic carbene (NHC) ligand trans to the active site,[67,68] Gonell et al. also investigated the Fe-analogue (**Fe-MbimPy-tpy**, Figure 11) for CO_2 reduction.[69] The system selectively gave CO as the only product with

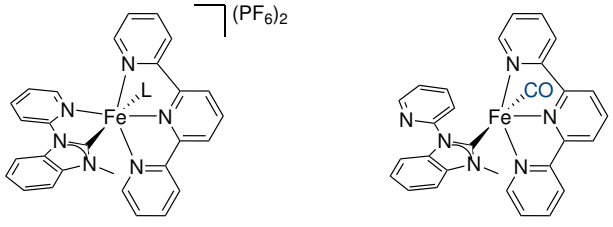

Fe-MbimPy-tpy **Fe^0-MbimPy-tpy-CO**

Figure 11: Fe-complex for CO_2 reduction employing a redox-active and a strong σ-donating redox-innocent NHC-ligand trans to the active site (L = MeCN) and reduced metal-carbonyl intermediate.[69]

an exceptional low overpotential requirement of $\eta = 240$ mV but only a FE of 33% (not taking any CO bound by the complex into account). The authors further investigated the mechanism for CO_2 reduction by **Fe-MbimPy-tpy** and found that first, similar to other CO_2 reduction systems, the complex is reduced by two electrons before CO_2 activation. This two electron reduction occurs at the same potential in an EEC mechanism, i.e. two electron transfer step, followed by a chemical step, involving loss of acetonitrile as the chemical step.[69] The doubly reduced complex is then attacked by the nucleophilic CO_2. Protonation and loss of H_2O results in a metal-carbonyl complex. DFT calculations indicated that the Fe^{II}-carbonyl complex is easier to reduce than **Fe-MbimPy-tpy**. Due to the lability of the pyridine residue of the redox-inert NHC ligand two electron reduction leads to a stable 18 e^- metal-carbonyl complex. The stability of this metal-carbonyl hampers activity of the complex and CO release and binding of CO_2 determines the TOF of the system. The authors therefore went to continuous flow CO_2 to directly remove the formed CO from the reaction mixture and thus were able to boost the FE to 95% with an overpotential requirement of $\eta = 150$ mV which is lower by even 70 mV than the one for the most efficient Fe-porphyrin (**Fe-oTMA**, Figure 7 left).[24] In conclusion, introducing the NHC ligand in their system led to an improvement in overpotential requirement but brought another difficulty as the resulting carbonyl complex (**[Fe^0−MbimPy−tpy−CO]**, Figure 11, right) turned out to be rather stable. However, these bottle-necks can be identified via mechanistic investigations and tackled accordingly.

Releasing CO from the complex

As CO is a good ligand itself, the problem of CO release from the complex is not seldom encountered. In many cases reduction of the metal-carbonyl complex by one electron, as described in the mechanism in Scheme 1, is sufficient, e.g. for Fe-porphyrin complexes.[61] In other cases the problem is circumvented by shifting the thermodynamic equilibrium by removing CO from the reaction mixture or by addition of CO scavengers to avoid catalyst deactivation. Especially Ni-complexes often suffer from so-called CO-poisoning, meaning that CO can not be released from the complex leading to a deactivation of the catalyst. Kubiak and co-workers studied electrocatalytic CO_2 reduction with **Ni-cyclam** (Figure 12, left) and observed that the rate-limiting step during catalysis is the loss of CO from the deactivated carbonyl species (**Ni^I-cyclam-CO**, Figure 12, right).[32] Addition of a CO scavenger (**Ni-TMC**, Figure 12, left) led to increased catalytic rates as the deactivation of **Ni^I-cyclam** is inhibited.

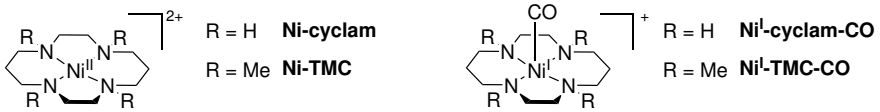

Figure 12: Ni-cyclam studied by Kubiak and co-workers, the used CO scavenger **Ni-TMC** and the respective Ni^I-CO complexes.[32]

In the study from Gonell et al. (*vide supra*), CO was removed from the reaction mixture by working under continuous CO_2 flow conditions leading to an enhanced FE alongside a low overpotential requirement.[69] This method is rarely reported so far but provides an interesting opportunity to achieve high efficiencies at low overpotential requirements without the use of other additives.

Switching reactivity between CO and HCOOH

In the above sections it was shown how altering the first or second coordination sphere can enhance CO_2 reduction in multiple ways. However, only recently Dey and co-workers reported a modified porphyrin (Figure 13) with which they were able to switch the reactivity from CO to selective HCOOH production.[70] Until then Fe-porphyrins were known to efficiently and selectively give CO as the only product of CO_2 reduction.[26,58,62,70] The synthesized iron chlorin, which is a

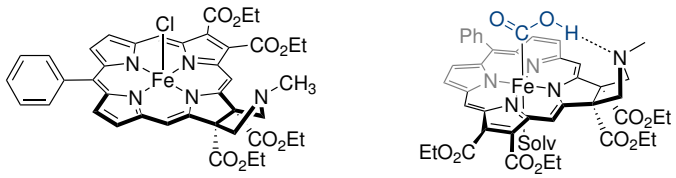

Fe-TEsC-Cl **Fe-TEsC-COOH**

Figure 13: Fe-chlorin (**Fe-TEsC-Cl**) capable of selective reduction of CO_2 to HCOOH and $Fe^{III}-COOH$ intermediate.[70]

saturated porphyrin analogue, is further equipped with four electron-withdrawing groups and a pendant amine. While all other porphyrin systems need to be reduced to the formal 'Fe^0' state to be able to activate CO_2,[24,26,42,58,61,70–73] **Fe-TEsC-Cl** can bind CO_2 already in its Fe^I state leading to a low overpotential requirement for CO_2 reduction, however, only in the presence of a proton source, e.g. H_2O.[70] DFT calculations as well as cyclic voltammetry (CV) studies showed that in the absence of H_2O, CO_2 does not bind to the Fe^I state of **Fe-TEsC-Cl**. The calculations indicate that CO_2 binding only occurs when the pendant amine is protonated leading to the $Fe^{III}-COOH$ intermediate. The reactivity could thus be shifted entirely from CO to HCOOH production by implementing a pendant amine in proximity to the active center, opening a new mechanistic route for Fe-porphyrins via second sphere interactions. Thus far, for porphyrins, a similar effect was only observed for an Fe-TPP with an additional tertiary amine as auxiliary ligand.[74] Therein the reactivity could also be shifted toward HCOOH formation albeit with a lower overall FE of only 70% while **Fe-TEsC-Cl** yielded 97%. Among the series of tertiary amines tested, the FE depended on amine basicity and ligand strength. The strongest catalytic enhancement was found for quinuclidine (Quin) ($pK_a = 10.2$[b]), followed by triethylamine (TEA) ($pK_a = 9.2$[b]) and Hünig's base[c] ($pK_a = 8.8$[b]). While Quin and NEt_3 gave similar FE, Hünig's base

[b] pK_a of conjugate acid in DMF
[c] N,N-diisopropylethylamine (DIPEA)

performed poorly which can be explained given its amine basicity and its steric bulkiness, which hampers coordination resulting in a poor ligand strength. Thus, amine binding to the metal center is crucial in this reaction mechanism. Their combined results suggested that amine binding to the metal center concomitant with or after activation of CO_2 increases CO_2 susceptibility toward protonation at the central C-atom rather than the oxygen, further assisting with formate dissociation by activating the Fe−C bond via a trans ligand effect.[74] These two examples of modifications of the first and second coordination sphere already highlight nicely key factors that guide reactivity toward either CO or formate production. In both cases the reaction occurs via the *CO_2-activation-first* pathway. The evolution of H_2 could thus be avoided. To yield formate instead of CO protonation needs to occur at the carbon rather than the oxygen (scheme 1). This is directed by the pK_a of the carbon and oxygen which is dependent on the bonding interaction of the [M−COOH] intermediate.[45] A strong M−C σ bond will deplete electron density from the carbon atom, rendering the oxygen more basic, thus facilitating oxygen protonation resulting in the breaking of the C−O bond and release of CO and H_2O. On the other hand, if the M−C σ bond is weak, the carbon center becomes more prone to protonation which allows for the release of HCOOH.

Another way to direct the strength of the M−C bond is by choice of the metal. Robert and co-workers found that complexes employing a pentadentate N5 ligand (**PDIdeeda**, Figure 14) were capable of CO_2 reduction. They selectively gave either CO or HCOOH depending on

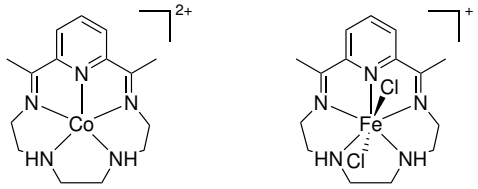

Co-PDIdeeda **Fe-PDIdeeda-Cl**

Figure 14: Co and Fe complex with pentadentate N5 ligand capable of selective CO_2 reduction leading to either CO or HCOOH depending on the metal center.[27]

the choice of metal.[27] While the Co complex yielded CO as the only product, when switching the metal center to Fe, HCOOH was obtained instead in high selectivity. No H_2 was observed for the Fe complex and mechanistic investigations showed that both complexes operate via the *CO_2-activation-first* pathway. The Co center was found to be a better π-donor than Fe. Donation into the π^*-orbital of CO_2 lead to a weaker C−O bond, facilitating C−O bond breaking favoring the release of CO and H_2O. In the case of **Fe-PDIdeeda** the Fe center is a poor π donor which allows for an isomerization of the η^1-C bound $[Fe{-}COOH]^+$ intermediate into the η^1-O $[Fe{-}OCHO]^+$ species. Subsequent protonation then yields HCOOH as the only product.

In addition to the aforementioned Fe, Co and Ni complexes, also various Mn complexes have been studied for CO_2 reduction. In most of the reported cases CO was obtained as the main or

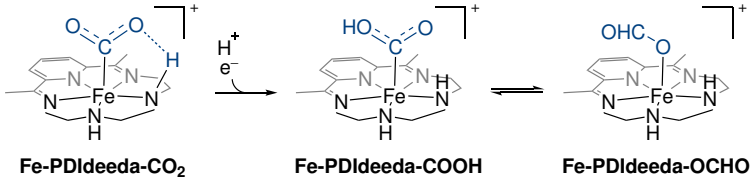

Figure 15: Isomerization between the η^1-C and η^1-O coordination in **Fe-PDIdeeda** leading to the release of HCOOH after subsequent protonation instead of CO.[27]

even only product.[1] Recently, Jurss and co-workers investigated a modified Mn-bpy with aniline groups in the second coordination sphere for CO_2 reduction under both electro- and photocatalytic conditions.[23] Apart from the beneficial effects of having H-bond donors in proximity to the active center (see section) they also found that when performing photocatalytic CO_2 reduction at low catalyst concentrations the reactivity was shifted from CO to HCOOH production. A plausible explanation for this behavior lies in the general mechanism for CO_2 reduction by the family of Mn-bpy complexes. The formation of CO often involves a dimeric $Mn^0{-}Mn^0$ species while formate is presumably obtained via a monomeric Mn-hydride species (*protonation-first-pathway*, Scheme 1b).[1,23] The fact that H_2 was also found as a minor product beside HCO_2H in the photocatalytic CO_2 reduction at low catalyst concentration supports this hypothesis.

Photocatalytic CO_2 reduction

Even if the energy for electrocatalytic CO_2 reduction stems from renewable energy sources such as solar panels, wind, tidal or hydroelectric power plants, the issue remains that the energy needs to be stored as electrical energy first before it can be harnessed for catalysis.[75] The conversion into electrical energy as well as the storage and use in catalysis to finally store it in chemical bonds comes with energy losses at each step. However, nature has already achieved use of the most abundant energy source, sunlight, to store energy in chemical bonds millions of years ago. Inspired by nature, in the past decades researchers turned their interest toward photocatalysis where they ideally use visible or sunlight directly as an energy source.[75] This is underscored by the number of publications in the field of photocatalysis exceeding 10,000 in 2023 (Figure 16).

A typical photocatalytic system consists of three components. The catalyst that catalyses the desired reaction, a photosensitizer (PS) which is required to harness the photon energy and a sacrificial electron donor (SED) or sacrificial electron acceptor (SEA). For reduction reactions a SED is required while SEA are essential in oxidation reactions. As the conversion of CO_2 into valuable fuels and chemicals is a reductive process, a SED is required in the photocatalytic CO_2 reduction. For all of these components to work together their potentials need to match. When the mixture is irradiated with light of an appropriate wavelength the PS gets excited. These

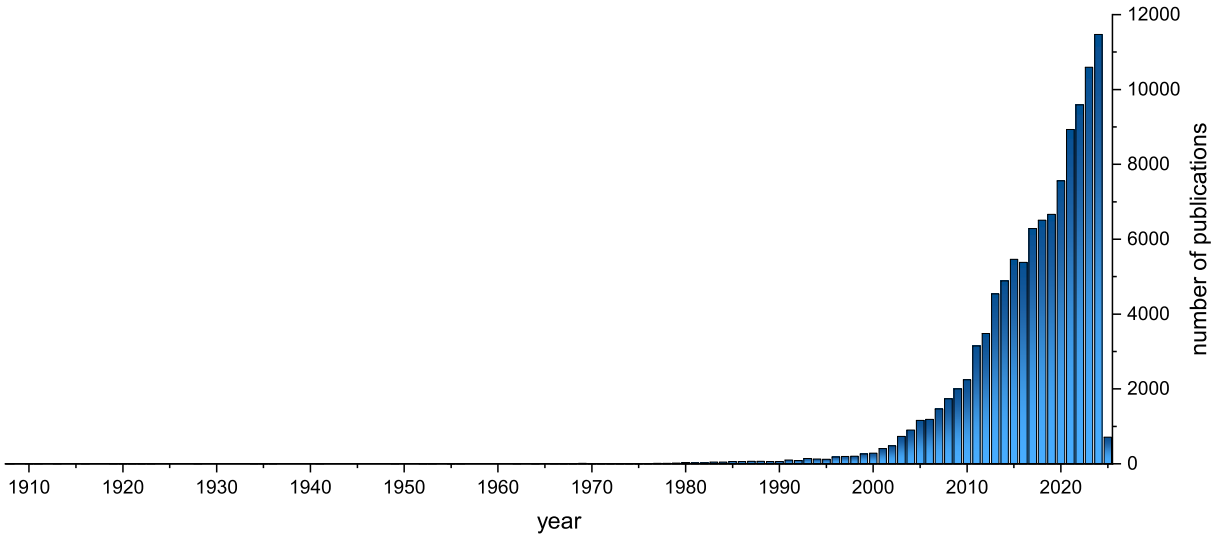

Figure 16: Number of publications on photocatalysis since 1908 according to SciFinder websearch on 03.01.2025 with the keyword “photocatalysis”.

excited states are short-lived; the lifetime strongly depends on the type of PS. For the reaction to proceed, the excited state of the PS needs to be quenched. This can go via either a reductive or an oxidative quenching pathway.[76] In CO_2 reduction, or any other photocatalytic reduction reaction, the SED would react with the excited PS via the reductive quenching pathway leading to the reduced PS and the oxidized SED (Figure 17 left). In this case the SED needs to have

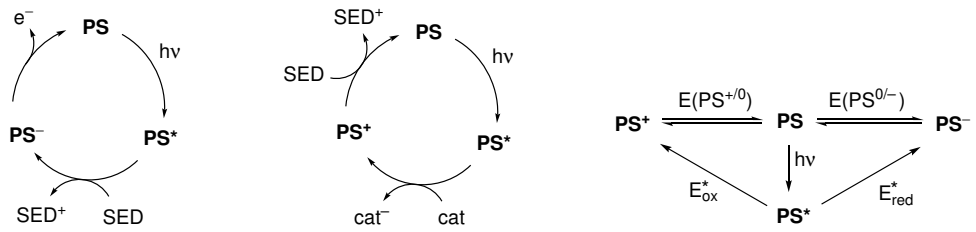

Figure 17: Reductive (left) and oxidative (middle) quenchig pathway for PS. Right: Overview of oxidation, reduction, excitation and quenching routes for PS with the respective descriptors.

a more negative potential than the excited state reduction potential (E^*_{red}) of the PS. In addition the potential of the reduced PS ($E(PS^{0/-})$) needs to be lower than the potential required to drive the reaction (E_{cat}). Alternatively, the excited state could be quenched oxidatively directly by the catalyst (Figure 17 middle, cat = catalyst). In this case the SED is required to reduce the oxidized PS back to its original state. Then, E_{cat} has to be more positive than the excited state oxidation potential (E^*_{ox}) of PS and the reduction potential (E_{red}) of the SED needs to be strong enough to reduce PS^+ back to PS.

Sacrificial electron donors for photocatalytic CO_2 reduction

While there is a vast number of SEDs, a few have been used commonly in photocatalytic CO_2 reduction in organic media. These are the tertiary amines TEA and its analogue triethanolamine (TEOA) and 1,3-dimethyl-2-phenylbenzimidazoline (BIH) (Figure 18). In earlier reports the

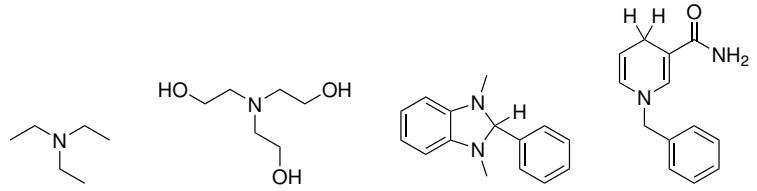

Figure 18: Common SEDs for photocatalytic CO_2 reduction with their potentials given vs. the $Fc^{+/0}$ couple [V_{Fc}].[76] Conversion to V_{Fc} was carried out using the conversion factors provided by Elgrishi et al..[18]

nicotinamide adenine dinucleotide (NAD) analogue 1-benzyl-1,4-dihydronicotinamide (BNAH) was used as well as SED but researchers turned their interest to BIH, which shares some common features with BNAH, for stability reasons.[76] Both BIH and BNAH are formal hydride donors. The monooxidized form of BIH and BNAH is very acidic and easily donates a proton to an appropriate base in the mixture (Figures 19-20). The resulting neutral radical $BI^{\bullet}$ or

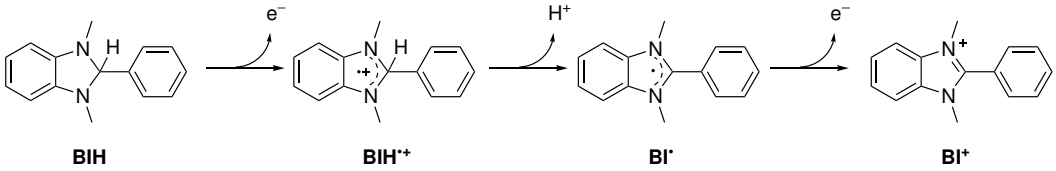

Figure 19: One-electron oxidation of BIH and following steps leading to the stable BI^{+} after overall donating a hydride.[76]

$BNA^{\bullet}$, respectively, is strongly reducing and capable of donating yet another electron in a dark process. However, the neutral $BNA^{\bullet}$ could also simply dimerize instead of donating that second electron. Thus, if the kinetics for the dimerization are more favorable than the formation of the pyridinium species BNA^{+}, BNAH remains only a one electron donor.[76] The high acidity of the monooxidized BIH and BNAH is the reason why an additional base such as TEA or TEOA is sometimes added in photocatalytic reactions employing those SEDs to rapidly accept the proton. In those reports these bases are hence often stated as the “proton source” in the reaction mixture.[23,76–96] Though, it should be noted that since TEA or TEOA could also function as SED themselves their presence in the reaction mixture might complicate the mechanism.[97,98] At least, their contribution in photocatalysis should be studied and, if found to be relevant, stated.

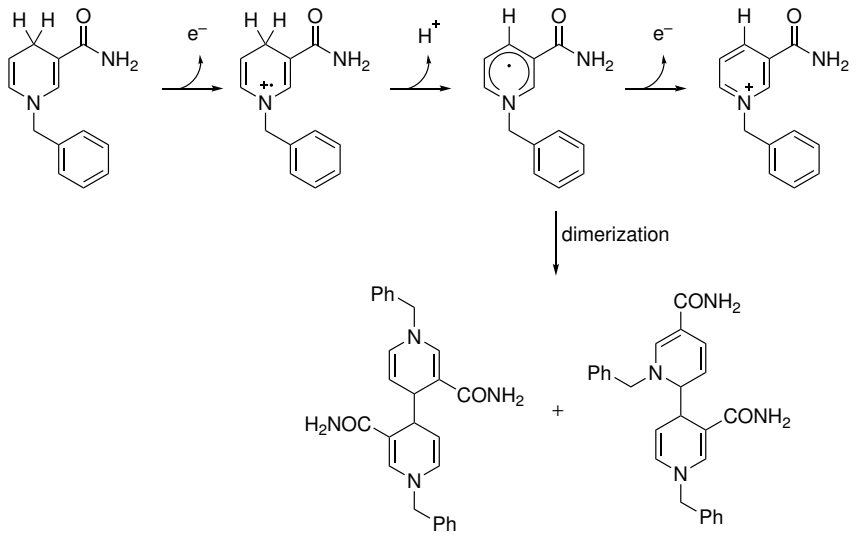

Figure 20: One-electron oxidation of BNAH and following steps leading to either dimerization or BNA^+ after overall donating a hydride.[76]

Photosensitizer in photocatalytic CO_2 reduction

The choice of a suitable PS is crucial for any photocatalytic reaction. An ideal PS should harvest light in the visible spectrum, exhibit long lived excited triplet states to enable adequate electron transfer to the catalyst (oxidative quenching, Figure 17 middle) or from the SED (reductive quenching, Figure 17 left) and high robustness during the photoreaction.[99,100] Moreover, especially for CO_2 reduction which often operates at lower potentials compared to e.g. HER, strong reducing power i.e. low excited state oxidation potentials or reduction potentials are required. After absorption of a photon of adequate energy, excitation in a metal-based PS can occur in three different ways. Transitions are possible either from an occupied ligand-based orbital into an unoccupied ligand orbital ($\pi \rightarrow \pi^*$ transition) or between metal-centered d-orbitals (d-d transition). The third option is a metal to ligand charge-transfer (MLCT) where the metal center acts as a reductant donating an electron to the ligand which operates as an oxidant.[101] The nature of the transition depends on the type of PS. After relaxation to the lowest spin-allowed singlet state via internal conversion (IC), intersystem crossing (ISC) occurs which allows the population of the photocatalytically acitve triplet states (Figure 21). This spin-forbidden ISC requires a strong driving force from efficient spin-orbit coupling (SOC) between the singlet and triplet wavefunctions.[102] SOC can be enhanced by the presence of a heavy atom, the so-called heavy atom effect (HAE).[103] Depending on the location of the heavy atom, two types of the HAE are distinguished. If the heavy atom is chemically affixed to the respective molecule, one speaks of an internal HAE. However, an enhancement may even be observed for unsubstituted aromatic hydrocarbons if they are embedded in alkyl halide matrices or solutions. To distinguish this effect from the internal HAE, it is called external HAE.[103]

Ru- or Ir-based complexes are commonly employed as PS as they exhibit strong SOC, long-

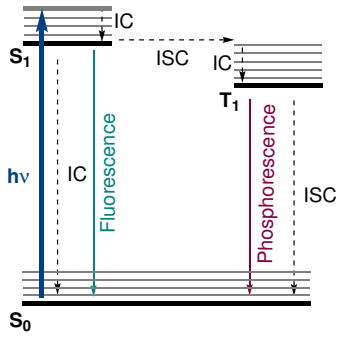

Figure 21: Simplified Jablonski diagram showing the population of the photocatalytically active triplet state (T_1) after excitation ($h\nu$), ISC and IC as well as radiative (plain arrows) and non-radiative (dashed arrows) quenching of the excited singlet (S_1) or triplet states.[101,102,104–106]

lived triplet excited states and low reduction potentials.[107] Until today most of the PS used in photocatalytic CO_2 reductions are still Ru- or Ir-based (Figure 22).[108] However, the aim is to per-

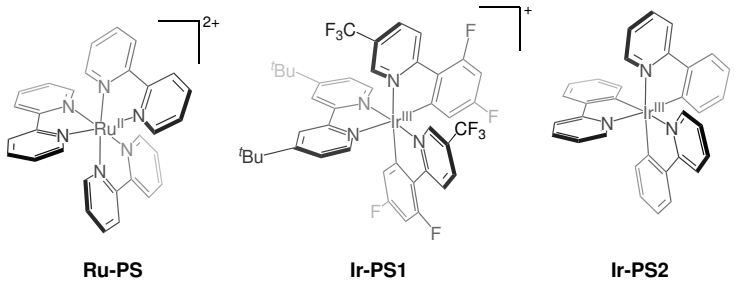

Figure 22: Common precious metal based PS in photocatalytic CO_2 reduction.

form catalysis using earth-abundant complexes (*vide supra*).[109] Hence, it would be contradictory to continue using those precious metal PS. One strategy is the use of earth-abundant metal complexes as PS. Among those Cu^I complexes have been vastly studied as Cu^I posseses a closed-shell d^{10} ground state configuration. Therefore, these complexes don't show fast nonradiative deactivation of the excited state via low-lying metal-centered states as observed for other first row transition metal complexes with a d^1–d^9 electron configuration.[105,107,110] Cu^I PS are either homo- or heteroleptic Cu-diimine complexes as well as mixed diimine/diphosphine Cu^I complexes.[105,110] For application in photocatalytic CO_2 reduction, mixed diimine/diphosphine complexes have drawn increasing attention due to their stronger emission abilities and longer lived excited states compared to the homoleptic systems.[108,111] The first report of an entirely earth-abundant catalytic system for photocatalytic CO_2 reduction was from the Ishitani group in 2016 where they successfully reduced CO_2 to CO photocatalytically using a Cu^I PS together with an Fe complex as catalyst (Figure 23a)).[112] In the following years more contributions from other groups such as the Beller group[90] who already studied Cu^I PS in HER[113] or the Bizzarri group[83,114,115] were reported. In all studies both catalyst and PS solely employed earth-abundant metals (Figure 23). Quenching studies revealed that the excited state of the PSs is quenched by the SED BIH, whereas the catalysts didn't quench the excited state. All systems

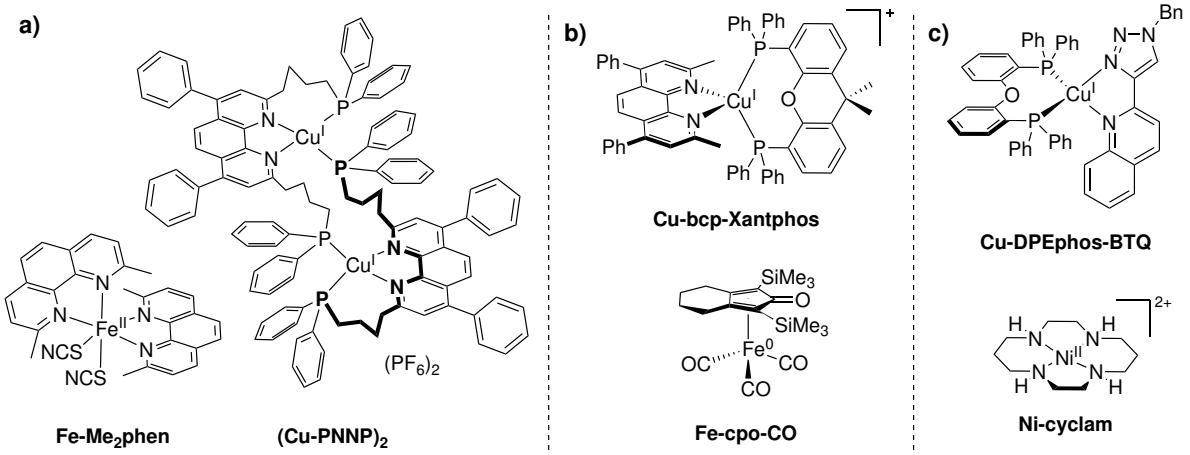

Figure 23: a) Binuclear Cu^{I} PS and Fe complex used by Takeda et al. in earth-abundant photocatalytic CO_2 reduction;[112] b) Mixed diimine/diphosphine Cu^{I} PS (**Cu-bcp-Xantphos**) with an Fe cyclopentadienone (cpo) catalyst studied by Beller and co-workers[90] and c) earth-abundant system for photocatalytic CO_2 reduction from the Bizzarri group.[83]

therefore follow the reductive quenching pathway (Figure 17 left).[83,90,112]

Zn^{II} also exhibits a d^{10} ground state configuration. In contrast to the aforementioned Cu^{I} complexes, whose photoinduced electron transfer processes arise from MLCT exited states, the isoelectronic Zn^{II} complexes show generally ligand-based ones due to their higher oxidation state energy relative to Cu^{I}.[108,116] The examples employing Zn^{II} complexes as PS in photocatalytic CO_2 reduction are thus far limited to Zn-porphyrins often in combination with a Re-based catalyst.[108] An entirely earth-abundant system was reported by Bian and co-workers in 2016, where they used [Zn(TPP)] as a PS for photocatalytic CO_2 reduction with a Mn-phen complex as catalyst.[117]

Recently, Wang et al. reported a series of homoleptic Al^{III} PS for CO_2 reduction alongside an earth-abundant Fe quaterpyridine (qpy) catalyst (Figure 24).[95] Within this series, the fully-methylated **Al-PS4** performed best, even outperforming the benchmarking **Ru-PS** and **Cu-bcp-Xantphos** as PS in terms of durability under similar conditions. Under optimized conditions a quantum yield (Φ) of 2.8 % was obtained for **Al-PS4** which is already almost half of the Φ

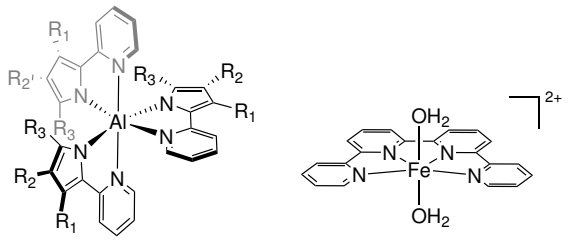

Figure 24: Entirely earth-abundant system for photocatalytic CO_2 reduction employing homoleptic Al^{III}-PS and Fe^{II}-qpy catalyst.[95]

observed for the benchmarking **Ru-PS** (6.1 %). Quenching studies revealed that within their system the reductive quenching pathway takes place.[95]
Overall, a variety of earth-abundant metal complexes have already been reported for photocatalytic CO_2 reduction, however, there is still quite some room for improvement. Compared to their precious metal containing working horses such as **Ru-PS**, **Ir-PS1** or **Ir-PS2** (Figure 22), they often suffer from durability issues, lower overall quantum efficiency or require more complex synthesis protocols.[108] Though, systems like the one reported by Wang et al.[95] already present a good alternative.

Another approach toward entirely earth-abundant systems for photocatalytic CO_2 reduction is the use of organic dyes instead of metal complexes as PS. Compared to metal-based PS fewer examples where organic dyes were used as PS can be found in the literature. In part this might be attributable to the fact that organic dyes usually show only weak SOC, hence less population of the lowest triplet state.[102–104] Nonetheless, a number of organic dyes have already been reported for photocatalytic CO_2 reduction (Figure 25), which often exhibit E_{red} and E^*_{ox} in the same range as the metal complexes used as PS (Figures 26, 27).[104] However, in early

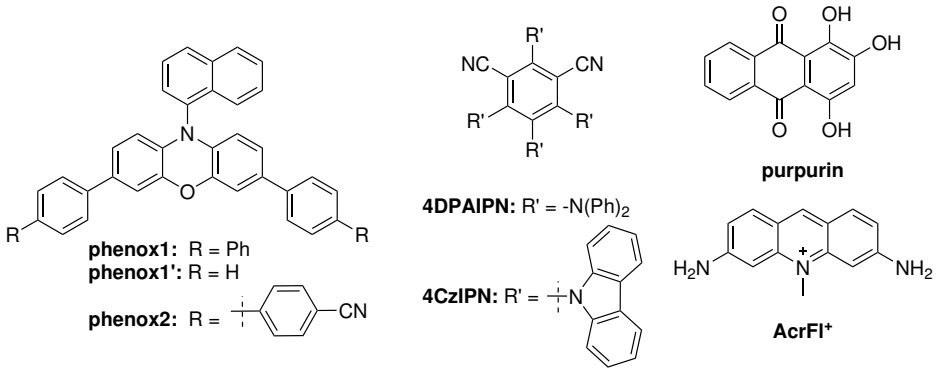

Figure 25: Select organic dyes for photocatalytic CO_2 reduction.[79,84,118–122]

reports employing organic dyes, they often performed worse compared to the benchmarking precious metal PS such as **Ru-PS** or **Ir-PS2**.[104] Replacing **Ru-PS** with purpurin using either Co- or Fe-qpy (Figures 28 right (Co) and 24 right (Fe)) as catalyst still selectively gave CO as the only product, but with up to half of the TON compared to the experiments with **Ru-PS**.[84] As their E_{red} are very close (Figure 26) this finding may be attributable to the weaker SOC of purpurin compared to **Ru-PS** (*vide supra*).
To elucidate whether quenching of the excited state of the PS occurs via the oxidative or reductive quenching pathway, the authors performed the respective quenching studies. Under catalytic conditions the reductive quenching pathway takes place where the excited state of the PS gets quenched by the SED BIH to yield the reduced PS. That then has enough reducing power to reduce the catalyst to the formal 'M^0(qpy)' (M = Fe, Co). It should be noted though that the authors also found some CO production in the absence of the SED BIH where the PS can thus be only quenched oxdiatively by the catalyst. However, under catalytic conditions the PS predominantly undergoes reductive quenching by BIH as the concentration of BIH and its

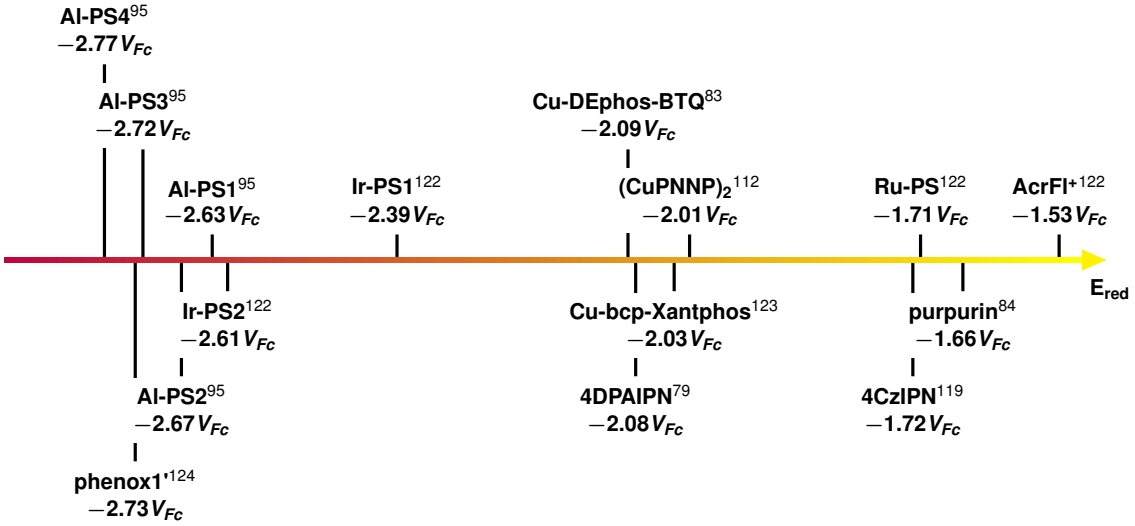

Figure 26: Overview of reduction potentials in V_{Fc} of PS presented herein. Potentials were converted, if necessary, using the conversion factors reported by Elgrishi et al..[18]

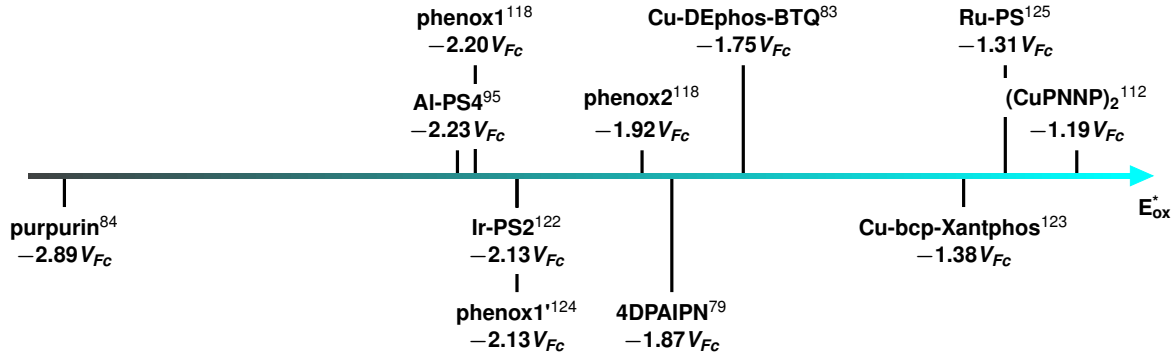

Figure 27: Overview of excited state oxidation potentials given in V_{Fc} of select PS. Potentials were converted, if necessary, using the conversion factors reported by Elgrishi et al..[18]

quenching rate of the PS is substantially higher compared to the catalyst.[84]
Among other examples, the reductive quenching pathway is also observed in the studies carried out by De La Torre et al. using **AcrFl+** as PS and **[Fe-tpyPy2Me](OTf)$_2$** as catalyst[122] or by Bassan et al. who studied thermally activated delayed fluoresence (TADF) dyes (**4DAIPN** and its derivatives) alongside a Mn catalyst for CO_2 reduction.[79] For catalysis to occur the reduction potential (E_{red}) of the reduced PS has to be strong enough to form the active species of the catalyst (*vide supra*, Figure 17). Therefore the respective potentials of all components need to match within the photocatalytic system. This also means that a PS which did not perform well with one catalyst might yet be optimal for another. For example, the E_{red} of **4CzIPN** which was not strong enough for the Mn complex used by Bassan et al. was sufficient enough for the study carrried out in the group of Chao. Therein, photocatalytic CO_2 reduction was performed with a series of TADF dyes and Fe-tpy complexes.[119,120] Generally the reductive quenching pathway is most commonly observed in literature.[79,84,119,120,122]

One of the few examples where the PS underwent oxidative quenching by the catalyst was

with phenoxazine dyes (**phenox1** and derivatives) and **Fe-pTMA** as catalyst.[118,121] Using **Fe-pTMA** as catalyst and **phenox1** as PS, Rao et al. even observed CO_2 reduction beyond the two electrons to CH_4.[118] They identified the formation of CO as one of the key intermediates as CH_4 production was also possible from a CO saturated solution. Moreover, in these studies the organic PS, **phenox1** in the study by Rao et al. and **phenox2** in the work from Kientz et al., even outperformed the benchmarking precious metal based PS **Ir-PS2** which exhibits a similar E^*_{ox} (Figure 27).[118,121] Kientz et al. found that in their system the regeneration of the PS by reduction by the SED is involved in the rate determining step of the reaction even though it is generally thought that the catalyst activation step dictates the performance of a photocatalytic system.[121]

Overall, researchers have investigated a vast number of PS for application in photocatalytic CO_2 reduction. Their compiled data may help in designing an economic system, where ideally all aspects from availability and synthetic difficulty of the respective components as well as their performance is taken into consideration.

Self-sensitized photocatalytic CO_2 reduction

Some systems have also been reported that operate in a self-sensitized manner, i.e. in the absence of an added PS. Even though this field is still dominated by precious metal-based complexes—for similar reasons as to why they have also been used as PS—a few earth-abundant metal complexes can perform CO_2 reduction without an additional PS. Supramolecular compounds like the $Ru^{II}-Re^{I}$ or multinuclear Ru complexes investigated by Ishitani and co-workers[86,93,126–129] where a PS is attached to a catalyst to facilitate the electron transfer between PS and catalyst (Figure 28 left), will not be discussed herein among the self-sensitized systems. One might argue that according to the upper definition they should, however in these systems photosensitization and catalysis occur at distinct sites.[86] One of the first systems that

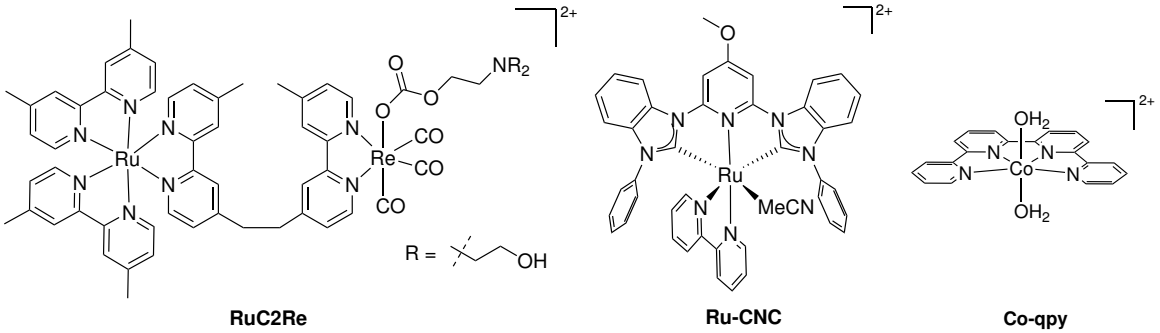

Figure 28: Left: Exemplary supramolecular system for photocatalytic CO_2 reduction with the Ru-PS tethered to the Re catalyst,[86] Middle: Ru-based photocatalyst reported by Papish and co-workers as one of the best performing photocatalysts for CO_2 reduction,[130] Right: Earth-abundant Co-qpy complex employed in self-sensitized CO_2 reduction.[84]

was reported to photocatalytically reduce CO_2 to CO in the absence of a PS employing only earth-abundant metals was a **Co-qpy** (Figure 28 right) complex albeit with only low TOF of $2.45\,h^{-1}$.[84] A similarly low TON was found for the self-sensitized photocatalytic CO_2 reduction by **Fe-pTMA** (Figure 7 middle) which performed excellently in electrocatalysis or in photocatalysis with an appropriate PS.[131] Only recently Chang and co-workers showed that their **[Fe-tpyPy2Me](OTf)$_2$** (Figure 5, left) could also operate in the absence of PS yielding TOFs of $56–75\,h^{-1}$.[122] Considering that one of the best catalysts for self-sensitized photocatalytic CO_2 reduction, **Ru-CNC** (Figure 28 middle) investigated by Papish and co-workers, achieved a TON of $250\,h^{-1}$,[130] these results are encouraging.

Benchmarking photocatalysis

Comparing photocatalytic systems is more complicated than for electrocatalytic ones as the system itself is more complex. For once, due to the higher amount of components since a SED and PS are needed instead of an electrode. Moreover, a vast number of different set-ups for photocatalytic CO_2 reduction are currently used. Apart from varying total volumes, reactor shapes, the type of lightsource as well as its distance to the reactor may differ.[132] In order to make all of these systems comparable a goodness factor is needed similar to the FE in electrocatalysis. In photocatalysis this is the Φ of the reaction. It is defined as the amount of product formed per number of photons absorbed which is the product of the photon flux and the reaction time (equation 6).[132]

$$\Phi = \frac{N_{product}}{N_{photons}} = \frac{n_{product} \cdot N_A}{photon\,flux \cdot t} \tag{6}$$

It should be noted that if the photon flux is given or determined in [$Einstein \cdot s^{-1}$] rather than [s^{-1}] the moles of product formed ($n_{product}$ instead of $N_{product}$) need to be used. Experimentally the photon flux can be determined by chemical actinometry.[133,134]

In addition to the photon flux also the energy of the respective photons, i.e. the wavelength is important. It is difficult to compare systems with respect to their efficiency when different wavelengths are used. With the goal of performing artificial photosynthesis the system should ideally use sunlight.[75] All systems reported to date already operate with visible, mostly blue ($\lambda \approx 450\,nm$), light while sunlight has a maximum at circa 550 nm.[100] The type of wavelength that can be used for the reaction is determined by the choice of PS (*vide supra*).

Scope of this work

Small molecule chemistry (e.g. CO_2 reduction, H_2 evolution...) plays a central role in efforts to store renewable energy in chemical bonds. In this regard, CO_2 represents an abundant and inexpensive source for C_1 building blocks (vide supra). Molecular catalysts play an integral role in small molecule activation. The use of well-defined molecular catalysts provides unique access to detailed mechanistic and spectroscopic studies. Hence, our understanding of the underlying processes can be increased, which consequently leads to the development of more stable and efficient catalysts.[135] Moreover, the use of non-innocent ligands, i.e. ligands that also participate in the reaction by e.g. storing electrons in their scaffold is a promising approach toward more selective and effective CO_2 reduction (*vide supra*). The ability to store electrons provides access to lower oxidation states which are required for small molecule activation such as CO_2 reduction (*vide supra*).[54] In the past decades the focus has also shifted to the use of earth-abundant metals to render the reaction more cost-efficient and environmentally friendly.[19,20]

The Mabiq ligand[d] (Figure 29 left) developed by the Hess group belongs to this group of non-innocent ligands. Late transition metal complexes, M-Mabiq (M = Fe,[136] Co,[137] Ni,[138] Cu,[139]

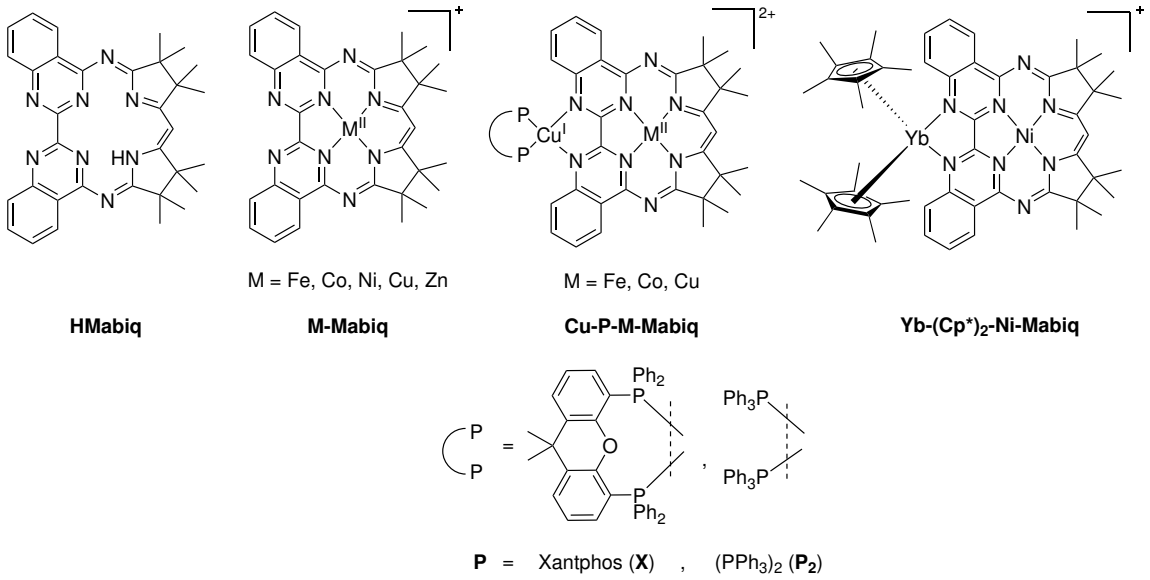

Figure 29: Left to Right: Structure of the free HMabiq ligand, M^{II}-Mabiq complexes, bimetallic Cu-M-Mabiq complexes (P = phosphine ligand, e.g. Xantphos or triphenylphosphine) and **Yb-(Cp*)$_2$-Ni-Mabiq** studied by the Hess group.

Zn[140]), have already been successfully synthesized and characterized. Intriguingly, all complexes in this series are photoactive, i.e. can be reduced to the formal 'M^{I}-Mabiq' by irradiation at λ = 455 nm in the presence of a SED such as TEA or BIH.[138–141] Both the Ni- and the Co-Mabiq complexes have thus been successfully employed as photocatalysts in light-driven

[d] [2-4:6-8-bis(3,3,4,4-tetramethyldihydropyrrolo)-10-15-(2,2'-biquinazolino)-[15]-1,3,5,8,10,14-hexaene-1,3,7,9,-11,14-N_6] (Mabiq)

organic transformation such as cyclization of a bromoalkyl-substituted indole (Ni-Mabiq)[138] or markovnikov-selective C- and N-alkylation of indoles and indazoles (Co-Mabiq),[142] respectively. Co-Mabiq was also investigated for small molecule activation, in particular for electrocatalytic HER.[143] Mechanistic investigations carried out by Tok et al. using a combination of spectroscopic, electrochemical and computational methods showed that the Co-Mabiq acts as a "hydride-sink" during HER storing at least two electrons and one proton.[143,144] These properties might be beneficial for CO_2 reduction (*vide supra*).

Based on these previous studies, the aim of this project was to investigate the use of M-Mabiq (M = Fe^{II}, Co^{II}) as electrocataysts for CO_2 reduction. The Fe-Mabiq was chosen to compare its performance to Co-Mabiq. Many Fe-complexes have been used in CO_2 reduction due to their high abundance and low cost.[10] Moreover, the choice of the metal center can affect the performance of the catalyst (*vide supra*).[27]

The Mabiq ligand offers a unique second binding site. Previously, bimetallic M_2-Mabiq complexes with Cu at the outer binding site were successfully synthesized and fully characterized by Stark et al. in the Hess group.[139] Recently, Boyce et al. even reported heterobimetallic Mabiq complexes emplyoing a lanthanide at the outer binding site.[145] In light of the beneficial influence that a second metal bears e.g. in enzymes such as the [Ni,Fe]-CODH, the heterobimetallic M_o,M_i-Mabiq (M_o = Cu^I, M_i = Fe^{II}) with the bidentate xantphos ligand occupying the two free coordination sites at the Cu^I (Figure 29) was synthesized, characterized and first also studied for electrocatalytic CO_2 reduction.

Since photocatalysis is a growing research field, efforts were also undertaken to perform CO_2 reduction photocatalytically. Sometimes different mechanism are observed when switching from electro- to photocatalysis[91,146,147] and former stability issues might be mitigated.[122] Photocatalysis with both the monometallic Fe-Mabiq as well as the heterobimetallic Cu-P-Fe-Mabiq was carried out in the presence of a PS (**Ru-PS**) whose reduction potential should be sufficient to form the active species in the reaction based on the electrocatalysis results. As the M-Mabiq complexes can be photoreduced in the presence of a suitable SED (*vide supra*), photocatalytic CO_2 reduction in the absence of PS was investigated as well for both the mono- and bimetallic complex.

Summary

Toward the goal of an earth-abundant metal complex for electro- and photocatalytic CO_2 reduction, this work was focused on the use of mono- and heterobimetallic metal Mabiq complexes. This involved the synthesis and characterization of a novel Cu,Fe-Mabiq complex, which has a Cu-Xantphos unit at the outer binding site,[141] as well as the two electron reduced Fe-Mabiq, the formal 'Fe^0-Mabiq' (Figure 30).[44] The complexes were characterized using different spectroscopic methods and electronic measurements such as nuclear magnetic resonance (NMR), infrared (IR), ultraviolett-visible (UV-Vis) spectroscopy, single crystal X-Ray diffractometry (SC-XRD) and CV. DFT calculations support the findings from Evans' NMR in combination with Mößbauer spectroscopy which revealed a ligand biradical with one electron located on the biketiminate and one on the bipyrimidine site of the Mabiq ligand and an intermediate spin Fe^{II} metal center for the formal 'Fe^0-Mabiq'. A ligand biradical was also observed for the previously synthesized formal 'Co^0-Mabiq'.[148]

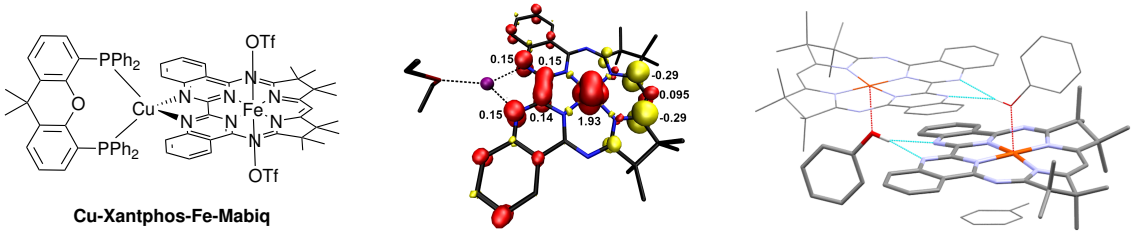

Figure 30: Structure of the new heterobimetallic Cu-Xantphos-Fe-Mabiq, spin-density plot of the formal 'Fe^0-Mabiq' and hydrogen bonding network established by the protonated intermediate formed during CO_2 reduction.

Both the Co^{II}- and Fe^{II}-Mabiq were investigated as electrocatalysts in CO_2 reduction.[44] CV experiments showed that both complexes can reduce CO_2 in the presence of added phenol (PhOH) with the Fe-Mabiq exhibiting a lower overpotential requirement than Co-Mabiq. Similar to the previous HER studies with Co-Mabiq a redox event preceding catalysis was present for both the Fe- and Co-complex. Experiments with varying amount of PhOH further showed that in the case of Fe-Mabiq this redox event corresponds to an addition of one electron and two equivalents of PhOH to the formal 'Fe^I-Mabiq'. A protonated intermediate, where a proton was added to the Mabiq ligand, played a role in the mechanism for HER by Co-Mabiq.[144] Hence, a similar situation seemed reasonable for the reduction of CO_2. To further investigate the mechanism and this protonated intermediate the formal 'Fe^0-Mabiq' was treated with PhOH. Upon addition of two equivalents of PhOH the same absorption spectrum as the one observed during catalysis was obtained. Fortunately, crystals suitable for SC-XRD could be grown and measured indicating a proton attached to the diketiminate site of the Mabiq ligand. This pendant proton aids in establishing a hydrogen-bonding network (Figure 30 right) bringing the PhOH in proximity to the active center and thereby facilitating protonation. The role of the pendant proton could either be direct protonation of the activated CO_2 (intramolecular pathway) or indirect by bringing the proton donor PhOH close to the active center (intermolecular pathway). From the

current mechanistic data it is not evident whether the protonation of the activated CO_2 occurs in an intra- or intermolecular fashion. More detailed investigations such as operando spectroscopy studies at e.g. low temperature or modeling of the possible mechanistic pathways using DFT calculations need to be carried out for further mechanistic information. These findings were part of the study *Multifaceted Role of the Noninnocent Mabiq Ligand in Promoting Selective Reduction of CO_2 to CO*—shown in the following section—and are described therein in more detail.

Furthermore, the heterobimetallic Cu-Xantphos-Fe-Mabiq was investigated for electrocatalytic CO_2 reduction.[141] In the presence of PhOH Cu-Xantphos-Fe-Mabiq is also capable of CO_2 reduction. Interestingly, no proton-dependent precatalytic wave was observed for the bimetallic complex in the electrochemical studies. Thus, the presence of the second metal prevents protonation of the ligand leading to a different mechanism for the bimetallic complex. However, the bimetallic complex was not stable under the electrocatalytic conditions which prevented further mechanistic investigations.

The interest was hence turned toward photocatalytic CO_2 reduction. In photocatalysis, stability issues that occured in electrocatalysis might be mitigated[122] and in some cases different mechanisms have been observed.[91,146,147] First, the photocatalytic reduction of CO_2 was carried out in the presence of BIH as SED and **Ru-PS** as PS. Both catalysts yielded CO as the only product but with the bimetallic performing better, achieving a higher TOF. Photocatalytic CO_2 reduction in the absence of PS was tested as well. In contrast to Fe-Mabiq which only performs in the presence of added PS, good yields were obtained with the bimetallic system. The TOF of $92 \pm 30\,h^{-1}$ is even slightly higher than the one obtained by Chang and co-workers under similar conditions (*vide supra*)[122] and only one third of the TOF obtained by one of the best self-sensitized photocatalysts for CO_2 reduction (**Ru-CNC**, Figure 28, TOF = $250\,h^{-1}$).[130] The work described in these latter two paragraphs was reported in the second study *Influence of a neighbouring Cu centre on electro- and photocatalytic CO_2 reduction by Fe-Mabiq* which is shown in the following sections.

Multifaceted Role of the Noninnocent Mabiq Ligand in Promoting Selective Reduction of CO_2 to CO

Title:	"Multifaceted Role of the Noninnocent Mabiq Ligand in Promoting Selective Reduction of CO_2 to CO"
Status:	Research Article, published online 21. February 2022
Journal:	*ACS Catalysis* **2022**, *12*, 3046–3057
Publisher:	American Chemical Society
DOI:	10.1021/acscatal.1c04636
Authors:	Kerstin Rickmeyer, Lukas Niederegger, Martin Keilwerth, Corinna R. Hess

Content: Encouraged by the results on electrocatalytic HER with Co-Mabiq from Tok et al.,[143,144] both the Co- and Fe-Mabiq were investigated as electrocatalysts for CO_2 reduction. Upon switching of the metal center, marked differences were observed as the Fe complex exhibits a lower overpotential requirement and superior FE compared to its Co-containing analogue. CO_2 was selectively reduced to CO by Fe-Mabiq with an overpotential requirement of only 500 mV and FE of 96 ± 11 %. The mechanism of CO_2 reduction by the Fe complex was studied in more detail. For that purpose the two-electron reduced $Na(OEt_2)$[Fe(Mabiq)] was synthesized and fully characterized. This formal 'Fe^0-Mabiq' exhibits a unique S = 1 spin state with an intermediate spin Fe^{II} center coupled to a ligand biradical. Early electrocatalytic investigations as well as reactivity studies with the formal 'Fe^0-Mabiq'pointed toward the involvement of a protonated precatalytic intermediate ($\mathbf{I_{PhOH}}$). $\mathbf{I_{PhOH}}$ was successfully synthesized and the molecular structure indicates that the Mabiq ligand underwent protonation at the diketiminate site. It further shows the ability of the Mabiq ligand to estabilish a hydrogen bonding network. This study therefore provides a great example how a non-innocent ligand could act in a dual role, as electron reservoir and also as a proton storage site. This, in combination with the metal center leads to a lower overpotential requirement and facilitates selective CO_2 reduction.

K. Rickmeyer planned and executed all experiments and wrote the manuscript. L. Niederegger conducted all SC-XRD measurements and managed the processing of the respective data. M. Keilwerth performed the Mößbauer measurements and analyzed the respective data. All work was conducted under the supervision of C. R. Hess.

ACS Catalysis

pubs.acs.org/acscatalysis

Research Article

Multifaceted Role of the Noninnocent Mabiq Ligand in Promoting Selective Reduction of CO_2 to CO

Kerstin Rickmeyer, Lukas Niederegger, Martin Keilwerth, and Corinna R. Hess*

Cite This: *ACS Catal.* 2022, 12, 3046−3057

Read Online

ACCESS | Metrics & More | Article Recommendations | Supporting Information

ABSTRACT: We have investigated the ability of Co− and Fe−Mabiq complexes (Mabiq = 2−4:6−8-bis(3,3,4,4-tetramethyldihydropyrrolo)-10-15-(2,2′-biquinazolino)-[15]-1,3,5,8,10,14-hexaene1,3,7,9,11,14-N_6) to act as electrocatalysts for CO_2 reduction. We observed marked differences in activity when switching the metal center, as the Fe complex outperforms its Co-containing analogue, both in terms of overpotential (η) and faradaic efficiency (FE). $[Fe(Mabiq)_2(MeCN)_2]PF_6$ ($[\mathbf{2}]^+$) selectively reduces CO_2 to CO with an overpotential requirement of 500 mV. We have synthesized and fully characterized the two-electron reduced $Na(OEt_2)[Fe(Mabiq)]$ ($[\mathbf{2}]^-$), which consists of an intermediate spin Fe^{II} center coupled to a ligand biradical and exhibits a unique S = 1 spin state. Both electrochemical and reactivity studies with $[\mathbf{2}]^-$ point toward a protonated precatalytic intermediate ($\mathbf{I_{PhOH}}$). The molecular structure of $\mathbf{I_{PhOH}}$ indicates the diketiminate carbon as the site of protonation and the ability of the Mabiq ligand to engage in hydrogen bonding interactions. The noninnocent Mabiq ligand, therefore, acts not only as an electron reservoir but also as a proton storage site. Our ligand system uniquely combines two beneficial features, a redox-active unit and a proton donor site, that in combination with the metal ion reduces overpotentials and facilitates selective CO_2 conversion.

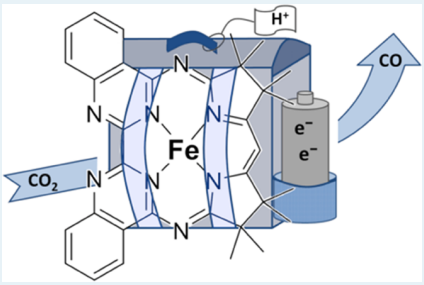

KEYWORDS: *molecular catalysts, electrocatalysis, CO_2 reduction, redox-active ligands*

INTRODUCTION

The electrocatalytic conversion of CO_2 into valuable fuels or chemical feedstocks (e.g., CO, formate, methanol) offers a promising strategy to offset the negative impact of this greenhouse gas.[1] As detailed in several recent review articles, the proton and electron transfer processes associated with CO_2 reduction present several challenges, and although many complexes can facilitate these steps, nearly all catalysts still suffer shortcomings with respect to catalytic rates, overpotentials, and/or selectivity of the overall reaction.[1a,2] Most electrocatalysts have targeted the two-electron reduction of CO_2 to CO or formate. Whereas formate production is believed to involve the insertion of CO_2 into a metal hydride bond (protonation-first pathway), CO production requires the initial binding of CO_2 to the metal center (CO_2-activation-first pathway).[1a,3] H_2 evolution is commonly a competing side reaction.[3a] The ability to direct the reaction toward CO or formate production and to suppress H_2 evolution requires discriminating catalysts.

Molecular electrocatalysts offer distinct advantages for optimizing catalyst properties; catalytic performance is affected by the choice of metal, whereby earth-abundant metals are currently at focus and can be fine-tuned through changes to the ligand environment.[1a,2a,d,4] The potential in harnessing the extended ligand environment of molecular compounds for reaction optimization, i.e., the second coordination sphere, is increasingly being recognized.[2a,4a,5]

For example, the effect of incorporated proton donor sites is manifold (Scheme 1). Positively charged trimethylanilinium groups, as included in the periphery of porphyrin ligands, can stabilize M−CO_2 intermediates through Coulombic interactions.[8] Proton donor groups in proximity to the active metal center, such as amine and phenol functionalities, also stabilize reactive intermediates, and moreover, facilitate proton transfer to the metal-bound CO_2.[5b,6,7,10] These proton relays can either engage in direct proton transfer or operate *via* hydrogen bonding networks and lead to an increase in the local acid concentration near the active site, effects deduced from electrochemical, spectroscopic, or computational studies. Consequently, systems with protonated ligand sites exhibit accelerated reaction rates, lower overpotentials, and/or selective CO formation.

The influence of redox-active ligands on the activity and selectivity of CO_2 reduction catalysts has also been assessed in a number of systems.[11] CO_2 activation at a metal center generally involves binding of the molecule to an electron-rich M^I or M^0 metal center.[3b,12] However, these low metal

Received: October 8, 2021
Revised: February 3, 2022
Published: February 21, 2022

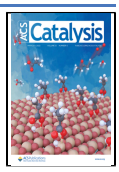

Scheme 1. Exemplary Systems in Which CO_2 Reduction is Assisted by the Ligand Environment[a]

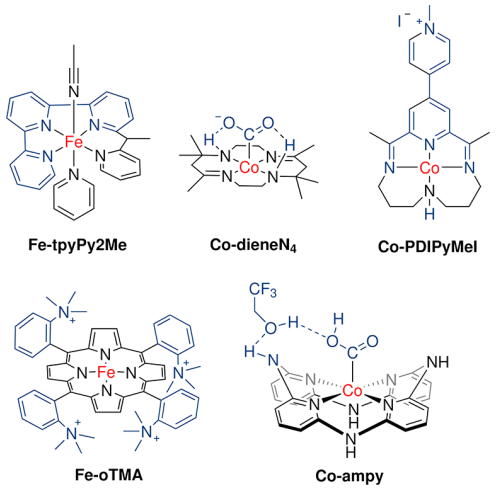

[a]The ligands can facilitate direct proton transfer (Co-dieneN$_4$),[6] support H-bonding networks (Co-ampy),[7] stabilize intermediates through Coulombic interactions (Fe-oTMA),[8] and store electrons in redox-active units (Fe−tpyPy2Me).[9] In rare cases, a combination of functionalities to support these varied interactions is present in the ligand system (Co-PDIPyMeI).[4b]

oxidation states frequently are not attained in complexes with redox-active ligands, where ligand-centered reduction is instead favored.[11,13] The electron storage capacity of such ligands can again influence catalysis in a number of ways, e.g., by lowering the metal nucleophilicity, the required overpotentials, and reorganization energies.[4b,9,11,14] These varied effects often disfavor H_2 formation and favor CO production but can also lead to diminished catalyst activity. We note that, among CO_2 reduction catalysts, proton and electron storage generally occur at separate functionalities——i.e., redox-active units, such as porphyrins, pyridyl diimines, and terpyridines in these systems, do not also house protons. This contrasts with H_2 evolution, where ligand-assisted and -centered pathways involve concurrent ligand reduction and protonation.[15]

Over the last years, we have been studying earth-abundant transition metal complexes containing the redox-active macrocyclic biquinazoline (Mabiq) ligand, also with the aim of understanding the influence of ligand noninnocence on catalysis.[13b,16] We recently showed that the cobaltous compound, [Co(Mabiq)(THF)]PF_6 ([**1**]$^+$), acts as an electrocatalyst for H_2 evolution and that the Mabiq ligand acquires electrons and protons during this process.[16a,b] We herein present our studies on CO_2 reduction by [**1**]$^+$ and its Fe analogue [Fe(Mabiq)$(MeCN)_2$]PF_6 ([**2**]$^+$, Scheme 2). The metal center has a significant effect on the electrocatalytic performance, whereby the latter outperforms the Co complex. We have successfully isolated and characterized the doubly reduced Na(OEt_2)[Fe(Mabiq)] ([**2**]$^-$, Scheme 2), the form preceding protonation and CO_2 binding steps, which has a unique $S = 1$ ground state induced by the interaction between the ferrous center and the ligand biradical. Furthermore, we demonstrate that protonation of [**2**]$^-$ generates a precatalytic intermediate in the CO_2 reduction mechanism. We have successfully obtained the molecular structure of this unique intermediate, which confirms that protonation occurs at the Mabiq ligand and provides rare structural evidence for the

Scheme 2. Fe Complex [2]$^+$ and Its One- ([2]^0) and Two-Electron Reduced ([2]$^-$) Forms Used in This Work

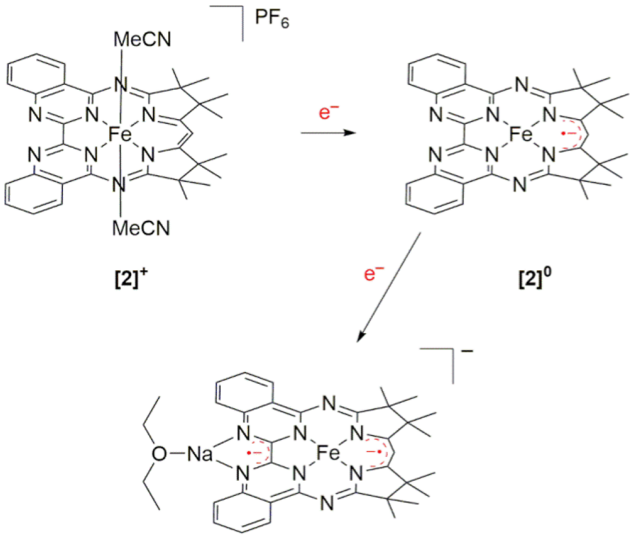

ability of redox-active ligands to support proton transfer as well as hydrogen bonding networks. These studies highlight the role of synergistic metal−ligand interactions, and in particular, the multifaceted influence of the redox-active ligand on CO_2 reduction.

RESULTS AND DISCUSSION

Electrocatalytic Studies. *Cyclic Voltammetry (CV).* Electrochemical studies with [**1**]$^+$ and [**2**]$^+$ evidence catalytic CO_2 reduction by both compounds and highlight differences in their electrochemical properties, both in the presence and the absence of substrates. The cyclic voltammograms (CVs) of [**1**]$^+$ and [**2**]$^+$ in the absence of CO_2 and the proton source were previously reported, but we briefly summarize key comparative redox features.[13b,16c] The Co-containing [**1**]$^+$ exhibits three reversible redox couples at 0.3, −0.8, and −1.8 V_{Fc} (V_{Fc} = potential vs $Fc^{+/0}$; Figure 1 left, blue trace, and Figure S1), the first of which corresponds to the $Co^{III/II}$ couple ([**1**]$^{2+/+}$). The two ensuing reductions correspond to successive ligand-centered reductions and are well separated, with the Mabiq/Mabiq$^{\bullet-}$ couple ([**1**]$^{+/0}$) 1 V more positive than the Mabiq$^{\bullet-}$/Mabiq^{2-} ([**1**]$^{0/-}$) couple. Both [**1**]^0 and [**1**]$^-$ were isolated and characterized in previous studies, confirming the reduction of the Mabiq ligand in the reduced forms of the Co complex.[13b,17] CV measurements of [Zn(Mabiq)(OTf)] further support the ligand-centered nature of these reductions (Figure S2; $E_{1/2}$, Mabiq/Mabiq$^{\bullet-}$ = −1.308 V_{Fc}; $E_{1/2}$, Mabiq$^{\bullet-}$/Mabiq^{2-} = −1.643 V_{Fc}). For the purpose of this study, we scanned to more negative potentials in the CV and observed additional reductive events below −2.2 V_{Fc}. The CV of the Fe analogue [**2**]$^+$ is similar (Figure 1 right, blue trace, and Figure S1), but the switch from Co to Fe has a significant effect on the ligand-centered reduction processes. Whereas the first reduction ([**2**]$^{+/0}$; [**2**]^0 = [Fe^{II}(Mabiq$^{\bullet}$)], as previously characterized)[16c] takes place at significantly lower potentials (−1.2 V_{Fc}), the second redox event ([**2**]$^{0/-}$) is instead shifted positively by 250 mV to −1.55 V_{Fc} compared to the analogous processes of [**1**]$^+$. Thus, the initial reduction of

https://doi.org/10.1021/acscatal.1c04636
ACS Catal. 2022, 12, 3046−3057

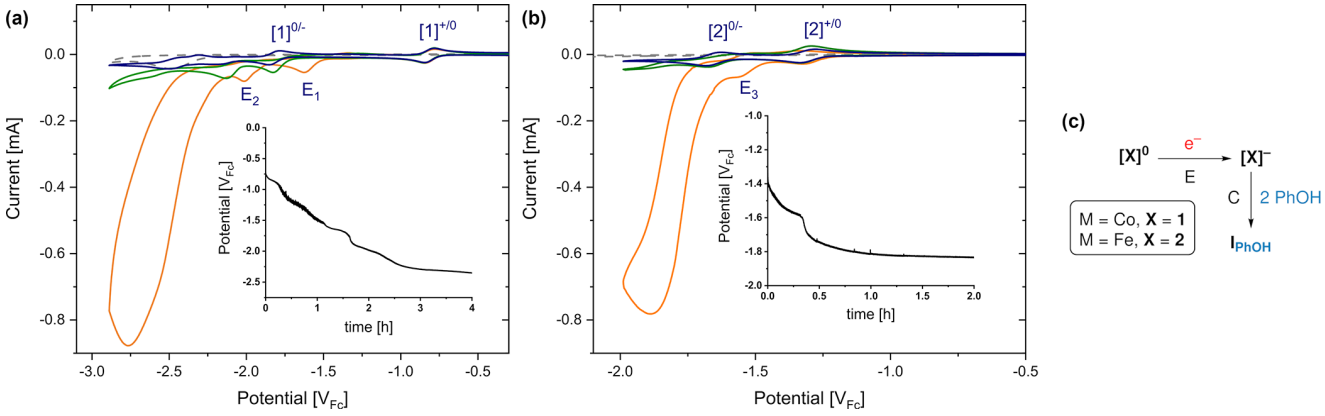

Figure 1. CV of 1 mM $[\mathbf{1}]^+$ (a) and $[\mathbf{2}]^+$ (b), respectively, under Ar (blue), CO_2 (green), and CO_2 plus 85 mM PhOH (orange); glassy carbon electrode, 0.1 M $[N(n\text{-}Bu)_4]PF_6$, MeCN, 100 mV s^{-1}. The dashed gray traces depict the control CVs of a solution of 85 mM PhOH under a CO_2 atmosphere at the glassy carbon disk. The insets show the controlled current electrolysis (CCE) data for solutions of 0.5 mM $[\mathbf{1}]^+$ or $[\mathbf{2}]^+$, with 85 equiv of PhOH under a CO_2 atmosphere, with an applied current of −322 μA. (c) Proposed EC process at the E_1 or E_3 couples of $[\mathbf{1}]^+$ or $[\mathbf{2}]^+$, respectively.

the Mabiq ligand is less favorable for the iron complex, yet the complex readily acquires a subsequent electron.

To assess the ability of $[\mathbf{1}]^+$ and $[\mathbf{2}]^+$ to act as electrocatalysts for CO_2 reduction, CV measurements were carried out under a CO_2 atmosphere both in the absence and the presence of a suitable proton source (Figure 1). For the proton source, we used PhOH, which is a weak acid (pK_a = 29.14 in MeCN)[18] widely used for the conversion of CO_2 to CO.[10a,19] The addition of CO_2, in the absence of PhOH, neither has an effect on the $M^{III/II}$ couples nor on the first reductive events of either $[\mathbf{1}]^+$ or $[\mathbf{2}]^+$. The third redox couple ($[\mathbf{X}]^{0/-}$; **X** = **1** or **2**), however, becomes irreversible upon CO_2 exposure, and is followed by a single, irreversible wave at $E_{p,c}$ = −2.13 V_{Fc}, denoting that CO_2 interacts with these reduced forms. No significant increase in cathodic current, attributable to the rapid formation of oxalate[1a,20] or the disproportionation of CO_2 leading to CO and CO_3^{2-},[1a,2c,19c,21] is observed at any potential for either complex. Thus, we next examined the behavior of the complexes with added phenol.

The CVs in the presence of both PhOH and CO_2 are indicative of catalytic CO_2 reduction by the complexes (Figure 1, orange traces). However, the onset for catalysis differs significantly between the two catalysts. The CV of $[\mathbf{1}]^+$ exhibits a current increase beyond the $[\mathbf{1}]^{-/2-}$ couple, at ca. −2.1 V_{Fc}. Both the $[\mathbf{1}]^{+/0}$ and $[\mathbf{1}]^{0/-}$ couples are shifted to significantly more positive potentials vs their position in the absence of the proton source. Indeed, these same potential shifts are observed in the CV of $[\mathbf{1}]^+$ in the presence of PhOH only (i.e., without CO_2, Figure S3), suggesting that these electron transfer steps now coincide with proton addition to the complex. The behavior of the first "precatalytic" redox events (E_1, Figure 1a) with varying [PhOH] confirms the PhOH dependence (Figures 1c and S4−S5). The apparent redox potential of the $[\mathbf{X}]^{0/-}$ couple in the presence of phenol is related to $E^0([X]^{0/-})$ via eq 1[22]

$$E^0_{app} = E^0([X]^{0/-}) + \frac{RT}{F}\ln(1 + K[\mathrm{PhOH}]^n) \quad (1)$$

where K is the apparent binding constant and n is the number of phenol molecules involved in the EC step. The best fit of this equation as a function of varied $[\mathrm{PhOH}]^n$ (10−85 mM) gives n = 2 (see Supporting Information, SI for further details, and Figures S8−S11). Thus, the data demonstrate that the precatalytic E_1 event corresponds to an EC process involving two equivalents of the proton source.

Similar behavior was observed previously for hydrogen evolution by $[\mathbf{1}]^+$ using the stronger acids, *para*-cyanoanillinium (pK_a = 7 in MeCN)[18] and *para*-bromoanilinium (pK_a = 9.43 in MeCN),[18] as proton sources.[16a,b] In that case, a set of precatalytic events near the original $[\mathbf{1}]^{+/0}$ couple preceded H_2 evolution and involved protonation of the one-electron reduced Mabiq ligand. Protonation of the ligand by PhOH is therefore also likely. However, in this case, the weaker acid only interacts with the two-electron reduced $[\mathbf{1}]^-$, similar to what was previously observed using *para*-anisidium (pK_a = 11.86 in MeCN).[16b] Catalytic H_2 evolution by $[\mathbf{1}]^+$/PhOH occurs subsequently at −2.23 V_{Fc} (Figure S3), close to the potential of CO_2 conversion by the cobalt complex. Based on the CV data, both H_2 evolution and CO_2 reduction appear to require the addition of at least four electrons to $[\mathbf{1}]^+$.

In contrast to the cobalt complex, reduction of CO_2 by Fe−Mabiq already takes place near the $[\mathbf{2}]^{0/-}$ couple, with an onset potential of −1.6 V_{Fc} (Figure 1b). Catalysis thus occurs near the formal "Fe^0" state, in analogy to the structurally related Fe porphyrins. However, CO_2 reduction by Fe−Mabiq requires a ∼400 mV lower overpotential compared to the well-studied FeTPP (for Fe-tetraphenylporphyrin (FeTPP), E_{onset} = −1.35 V_{NHE} in DMF was reported,[23] resulting in −2.07 V_{Fc} after conversion to the $Fc^{+/0}$ couple[24]). The maximum catalytic current for CO_2 reduction by $[\mathbf{2}]^+$ was observed using 85 equiv of PhOH. Higher concentrations of the proton source led to a decrease in the catalytic current, which may reflect an inhibitory process (Figure S12). Notably, H_2 evolution by $[\mathbf{2}]^+$/PhOH occurs at more negative potentials than CO_2 reduction (E_{onset} = −1.78 V_{Fc}, Figure S3).

The $[\mathbf{2}]^{0/-}$ couple is again shifted to more positive potentials in the presence of PhOH, both in the absence and the presence of CO_2 (couple defined as E_3; Figures 1 and S3). Analysis of the [PhOH] dependence of the E_3 couple again shows that formation of the intermediate, $\mathbf{I_{PhOH}}$ (Figure 1c), coincides with the addition of 2 equiv of the proton source (Figures S10 and S11). In contrast, the weaker acid, trifluoroethanol (TFE; pK_a(TFE) = 23.5 in dimethylsulfoxide (DMSO)[25] vs pK_a(PhOH) = 18.0 in DMSO[26]), has no effect on the $[\mathbf{2}]^{0/-}$

https://doi.org/10.1021/acscatal.1c04636
ACS Catal. 2022, 12, 3046−3057

Table 1. Results from Headspace Analysis after CPE Experiments with $[1]^+$ or $[2]^+$[a]

		CO		H_2	
catalyst	E_{CPE} [V_{Fc}]	TON	FE [%]	TON	FE [%]
$[1]^+$[b]	−2.34	2 ± 0.1	60 ± 6[e]	nd	nd
$[2]^+$[b]	−1.84	10 ± 1	96 ± 11[e]	nd	nd
No[c]	−2.34		1 ± 0.5		3 ± 4
$[1]^+$ no CO_2[d]	−2.34	0.1 ± 0.03	0.5 ± 0.1	14 ± 3	65 ± 14
$[2]^+$ no CO_2[d]	−1.84	(6 ± 4) × 10^{-3}	0.11 ± 0.07	2.2 ± 0.3	40 ± 5

[a]General conditions: 43 mM PhOH in 0.1 M $[N(n\text{-}Bu)_4]PF_6$ in MeCN; CPE was performed for 1 h (2 h for the control experiments) to ensure sufficient turnovers; gaseous products were analyzed with a combination of a flame-ionization detector with a methanizer (FID-M) and a thermal conductivity detector (TCD); see SI for further details. nd = below detection limit of TCD. [b]500 μM catalyst, 0.28 M CO_2,[19a] and electrolysis for 1 h. [c]CO_2 (0.28 M),[19a] electrolysis for 2 h. [d]500 μM catalyst, electrolysis for 2 h. [e]Considering the initial electrons required to generate the active species, FEs of 47 ± 4 and 93 ± 9% are obtained; further correcting for background current, FEs of 60 ± 6 and 96 ± 11% are derived for $[1]^+$ and $[2]^+$, respectively. See SI for details.

couple, and a proton-dependent shift is only observed at the subsequent $[2]^{-/2-}$ couple (Figure S13). The pK_a of $\mathbf{I_{PhOH}}$, therefore, is estimated to lie between 18 and 23.5 on the DMSO pK_a scale. To rule out that the shift is not simply due to PhOH coordination, the CV behavior of $[2]^+$ was examined upon titration of the methylated analogue, anisol (PhOMe). In this case, an anodic shift of the $[2]^{0/-}$ couple was not observed (Figure S14). The data, therefore, suggest that the PhOH-dependent shift of the redox couple stems from a proton-coupled process.

As previously noted, protonation sites in proximity to the metal CO_2-binding site have a favorable effect on CO_2 reduction. In the case of the Fe−Mabiq complex, the bridging imines, diketiminate carbon, and bipyrimidine unit all offer possible protonation sites, based on previous findings concerning H_2 evolution by the Co−Mabiq complex.[13b,16b] Regardless of the site involved, protonation of the ligand clearly leads to more favorable reduction of the $[X]^0$ species and may facilitate the ensuing CO_2 activation steps as per the effects observed in porphyrin and aminopyridine systems.[5b,7,10a,b,e]

Overall, the CV data already demonstrate that although both metal−Mabiq reductions ($[X]^{+/0}$ and $[X]^{0/-}$) are ligand-centered (*vide infra*), the metal ion has an indisputable impact on the redox properties and catalytic behavior. $[2]^+$ clearly outperforms its Co analogue in the electrochemical CO_2 reduction, with a ∼600 mV lower overpotential requirement than $[1]^+$. Catalysis by the Fe complex already takes place near the $[2]^{0/-}$ couple, preceded by the formation of $\mathbf{I_{PhOH}}$. This precatalytic intermediate results from the addition of two equivalents of PhOH to $[2]^-$; specifically, $\mathbf{I_{PhOH}}$ corresponds to a protonated form of the latter species. As found in other systems,[9,27] metal−ligand cooperativity plays a significant role in the electrocatalytic behavior of the metal−Mabiq complexes.

Controlled Potential Electrolysis (CPE) Studies for Direct Product Measurements. Controlled potential electrolysis (CPE) experiments were next carried out to assess catalyst performance and to quantify CO_2 reduction products and competing H_2 formation. The applied potentials (E_{CPE}) were derived from controlled current electrolysis (CCE; Figure 1 insets) experiments under catalytic conditions and correspond roughly to the half-peak potential[28] of the catalytic peak in the CV. The respective potentials for $[1]^+$ and $[2]^+$ are −2.34 or −1.84 V_{Fc} (Tables 1, S2, S3 and Figure S15). For the conversion of applied potentials into overpotentials (η), we referred to the method and value of $E^0_{CO_2/CO,MeCN}$ = −1.34 V_{Fc} reported by Saveant.[19a] Comparable values of $E^0_{CO_2/CO}$ = −1.36 ± 0.05 V_{Fc} ($[1]^+$) and −1.28 ± 0.05 V_{Fc} ($[2]^+$) are derived when further considering homoconjugation of the acid (see SI for a detailed discussion of the overpotential calculations).[29] The required overpotentials for $[1]^+$ and $[2]^+$ were thus determined to be 1 and 0.5 V, respectively (Table 1).

$[1]^+$ performed poorly in the bulk electrolysis experiments, giving low faradaic efficiencies (FE, 60 ± 6%, considering the initial electrons required to generate the active species and correcting for the background current; see SI for details) and turnover numbers (TONs), and with a high overpotential requirement (1 V, Table 1). In contrast, the Fe-containing $[2]^+$ showed good performance in the reduction of CO_2 to CO, with no detectable formation of H_2, an excellent FE of 96 ± 11%, and a good overpotential requirement (η = 500 mV). Isotope labeling studies with $^{13}CO_2$ in deuterated MeCN confirmed that neither formate nor other soluble products, e.g., oxalate or methanol, were generated by either $[1]^+$ or $[2]^+$ in the reaction.

Several control experiments were carried out to confirm the catalytic activity of the complexes. Bulk electrolysis in the absence of the catalyst showed only negligible amounts of CO and hydrogen. Hydrogen was produced by both catalysts in the absence of CO_2, once more highlighting the ability of both compounds to act as catalysts for this competing reaction. However, the amount of H_2 generated by $[2]^+$ was minimal, as expected at −1.84 V_{Fc} based on the CV of $[2]^+$/PhOH (Figure S3). Only trace amounts of CO were detected in these control experiments carried out in the absence of CO_2. Thus, the significant amount of CO obtained in the reduction of CO_2 by $[1]^+$ or $[2]^+$ with both PhOH and CO_2 clearly originates from carbon dioxide, rather than from organic degradation products. Interestingly, hydrogen evolution by both complexes appears to be suppressed in the presence of CO_2. No detectable H_2 is generated (detection limit ∼ 0.3%) by either complex, even though H_2 evolution and CO_2 reduction by $[1]^+$ occurred at similar potentials to CO_2 reduction. In accord with the fact that CO is obtained as the sole reduction product after catalysis, this implies that in the presence of CO_2, the so-called CO_2-activation-first pathway[1a,3a] is preferred over the formation of a metal hydride.[3a] This is likely due to the fact that the reductive processes of the Mabiq complex are ligand-centered. Thus, the ability of the redox-active ligand to acquire electrons and protons seems to be advantageous for CO_2 chemistry.

For the Fe complex, we additionally monitored the species generated during 1 h bulk electrolysis at −1.84 V_{Fc} by absorption spectroscopy ($[2]^+$ with 85 equiv of PhOH in a

https://doi.org/10.1021/acscatal.1c04636
ACS Catal. 2022, 12, 3046−3057

CO_2-saturated MeCN/$[N(n\text{-}Bu)_4]PF_6$ solution; Figure S16). During this time, $[\mathbf{2}]^+$ rapidly converts to a species that features a strong absorbance at 609 nm and a series of bands of lower intensity between 700 and 1000 nm. The same spectrum was obtained when bulk electrolysis was performed at −1.65 V_{Fc}, just beyond the precatalytic E_3 couple (Figure S17). Thus, the species generated in the bulk electrolysis are assigned to the precatalytic species, $\mathbf{I_{PhOH}}$. The findings nicely support the notion that $\mathbf{I_{PhOH}}$ is formed in the EC step at E_3 (Figure 1c) prior to catalysis, and is likewise regenerated following turnover (Figures S16 and 17). We note that a decrease of the $\mathbf{I_{PhOH}}$ absorption bands is observed after 1 h of an applied potential of −1.84 V_{Fc} (Figure S16). Together with the observed stagnation in CO production and the loss of current after 1 h, the data suggest that the long-term stability of the catalyst is an issue (Figures S15 and S16) to be addressed in future studies with this system. The low solubility of $\mathbf{I_{PhOH}}$ in MeCN (*vide infra*) is likely a significant contributing factor to the lower performance of $[\mathbf{2}]^+$ over time. A rinse test of the glassy carbon plates conducted after the bulk electrolysis indicated that no catalyst material was deposited on the electrode surface (Figure S18). Polishing of the electrode in the middle of the bulk electrolysis experiment did not lead to recovery of activity (Table S4). Thus, the decrease in activity over longer time periods does not seem to stem from electrode modification.

In summary, Fe complex $[\mathbf{2}]^+$ represents a very good CO_2 reduction catalyst with excellent product selectivity and low overpotential, especially in comparison to the similar FeTPP complex. We consequently focused further studies on the Fe−Mabiq complex to examine the nature of intermediates, gain further insight into the CO_2 reduction mechanism, and assess the contributions of the redox-active ligand.

Synthesis and the Electronic Structure of [2]$^-$. The electrochemical studies demonstrate that CO_2 reduction by the Fe−Mabiq complex occurs subsequent to the formation of $[\mathbf{2}]^-$. CO_2 appears to be able to coordinate to this *formal* Fe^0 form, and this species also is readily protonated by PhOH. Thus, we set out to generate and characterize the doubly reduced complex to examine its electronic structure and reactivity. As previously noted, the electronic structure of low valent species involved in CO_2 activation influences their selectivity and activity. The formally Fe^0, $[Fe(TPP)]^{2-}$, species was recently shown to be an intermediate spin Fe^{II} center, antiferromagnetically coupled to a porphyrin-based biradical, with an overall $S = 0$ spin state.[14a,30] The doubly reduced form of the Fe−terpyridine-based catalyst, $[Fe(tpyPy2Me)]^0$, has an analogous electronic structure: a singlet ground state resulting from the antiferromagnetic coupling between the $S = 1$ ferrous center and the $S = 1$ ligand biradical.[9] In both cases, the two-electron-reduced forms were identified as the putative catalytically active species; electron storage by the redox-active ligand conferred advantages for catalysis. Assignment of the electronic structure of the doubly reduced $[\mathbf{2}]^-$ is thus important for understanding electrocatalytic CO_2 reduction by Fe−Mabiq.

The electronic structure of the cobalt-containing homologue, $[\mathbf{1}]^-$, was previously investigated, and also found to contain a doubly reduced ligand biradical.[13b] This compound, described as $[Co^{II}(Mabiq^{\bullet\bullet})]^-$ has an overall doublet ground state ($S_{Co} = 1/2$; $S_L = 1$). The precursor to $[\mathbf{2}]^-$, the *formal* Fe^I−Mabiq complex $[\mathbf{2}]^0$, contains an intermediate spin Fe^{II} center and a one-electron-reduced ligand, as established in our previous work.[16c] The ferrous center is antiferromagnetically coupled to the Mabiq-based radical ($[Fe^{II}(Mabiq^{\bullet})]$; $S_{Fe} = 1$, $S_L = 1/2$, $S_T = 1/2$) localized on the diketiminate unit. Further reduction of $[\mathbf{2}]^0$ to generate $[\mathbf{2}]^-$ could, in principle, be metal- or ligand-centered, with possible triplet $S = 1$ (e.g., $S_{Fe} = 3/2$, $S_L = 1/2$; or $S_{Fe} = 1$, $S_L = 0$), or singlet $S = 0$ ($S_{Fe} = 1$, $S_L = 1$) ground states. By analogy to the Co complex, one might expect a ligand-centered reduction. Yet, the CVs of the two complexes already show markedly different potentials for the reductive processes.

The dark purple $[\mathbf{2}]^-$ was synthesized upon treatment of $[\mathbf{2}]^0$ with Na in tetrahydrofuran (THF), and single crystals of the complex were successfully obtained. The molecular structure of $[\mathbf{2}]^-$ (Figures 2 and S20) is comparable to that

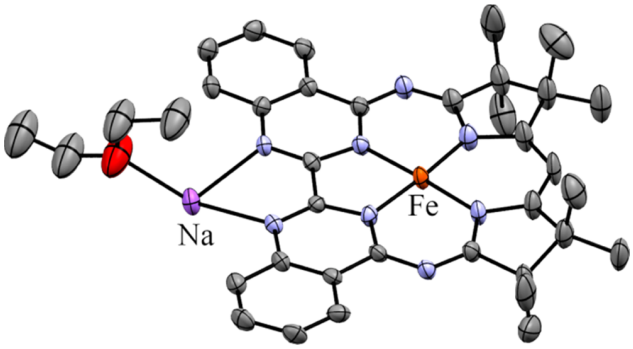

Figure 2. Molecular structure of $[\mathbf{2}]^-$ (50% probability ellipsoids); hydrogen atoms are omitted for clarity. $[\mathbf{2}]^-$ is a dimer in the solid state (Figure S20), whereas only the monomeric unit is depicted here.

of the doubly reduced cobalt complex ($[\mathbf{1}]^-$)[13b] and provides some initial insight into the metal and ligand oxidation states. The Fe complex likewise exists as a dimer of {$Na(OEt_2)$[Fe(Mabiq)]} units in the solid state; the two bipyrimidine (bpm) units are within π-stacking distance (3.47 Å) and the outer diimine-bound sodium ion further promotes association of the macrocycles (Figure S20). The dimer dissociates in solution, as demonstrated by Evans' measurements, which yielded μ_{eff} = 2.75 μ_B consistent with an $S = 1$ spin state for the monomeric $[\mathbf{2}]^-$. The dimeric solid state $[\mathbf{1}]^-$ likewise was monomeric in solution.[13b] The C−C bond of the bipyrimidine unit is longer than in $[\mathbf{1}]^-$, such that bipyrimidine reduction is not unequivocally evidenced. The trend in the diketiminate C−C and C−N bonds (Table S6) across the series of Fe−Mabiq complexes ($[\mathbf{2}]^+$, $[\mathbf{2}]^0$, $[\mathbf{2}]^-$) is consistent with increasing electron density on the diketiminate unit. The Fe−N bond lengths among the three complexes (Fe−N_{avg} ($[\mathbf{2}]^+$) = 1.925(9) Å > Fe−N_{avg} ($[\mathbf{2}]^0$) = 1.902(4) Å > Fe−N_{avg} ($[\mathbf{2}]^-$) = 1.891(2) Å) suggest that the metal center remains divalent in all cases.[16c]

The Mößbauer spectrum of $[\mathbf{2}]^-$ (solid sample, Figure 3a) confirms the metal oxidation state. The isomer shift and quadrupole splitting (δ = 0.29 mm s^{-1}; $|\Delta E_Q|$ = 2.06 mm s^{-1}) are within the range of values of ferrous centers, including intermediate spin complexes.[14a,16c,31] The values are also in agreement with the parameters derived from density functional theory (DFT) calculations (B3LYP) on $[\mathbf{2}]^-$ (δ_{calcd} = 0.43 mm s^{-1}, $|\Delta E_{Q,calcd}|$ = 2.11 mm s^{-1}), within the established uncertainty range for the isomer shift of ∼0.1 mm s^{-1}.[32] Since the iron center of $[\mathbf{2}]^-$ remains divalent and intermediate spin, the Mabiq ligand must indeed be doubly reduced.

https://doi.org/10.1021/acscatal.1c04636
ACS Catal. 2022, 12, 3046−3057

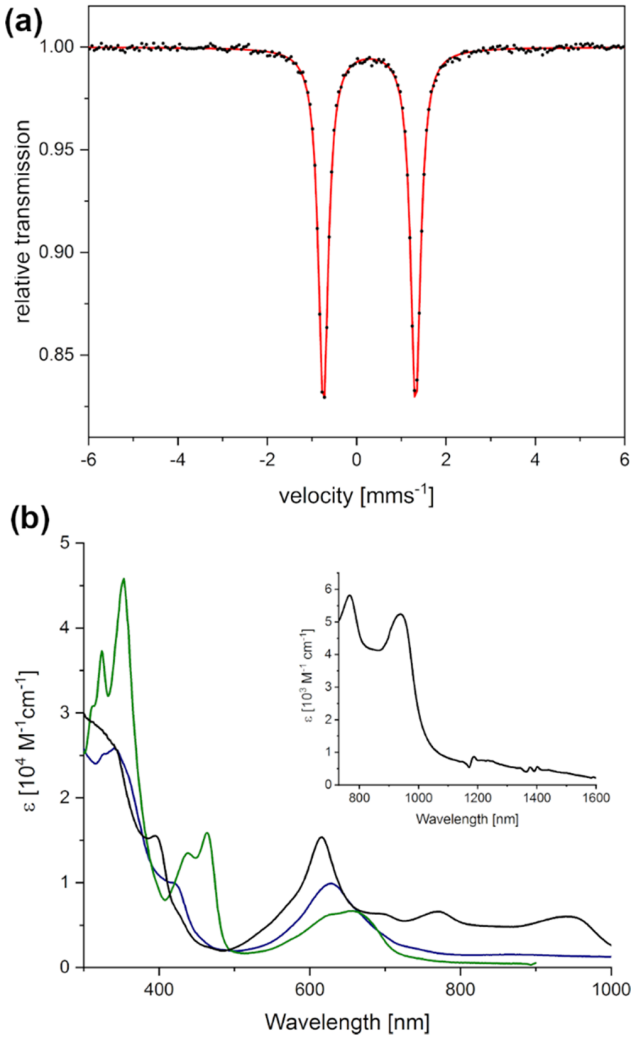

Figure 3. (a) Mößbauer spectrum of [**2**]$^-$ recorded at 80 K (black dots); the red line shows the simulation of the target compound with δ = 0.29 mm s^{-1}, $|\Delta E_Q|$ = 2.06 mm s^{-1}. (b) Comparison of the UV−vis absorption spectra of Fe−Mabiq compounds [**2**]$^+$ (green) in MeCN and [**2**]^0 (blue) and [**2**]$^-$ (black) in THF, respectively. The inset shows the NIR spectrum of [**2**]$^-$.

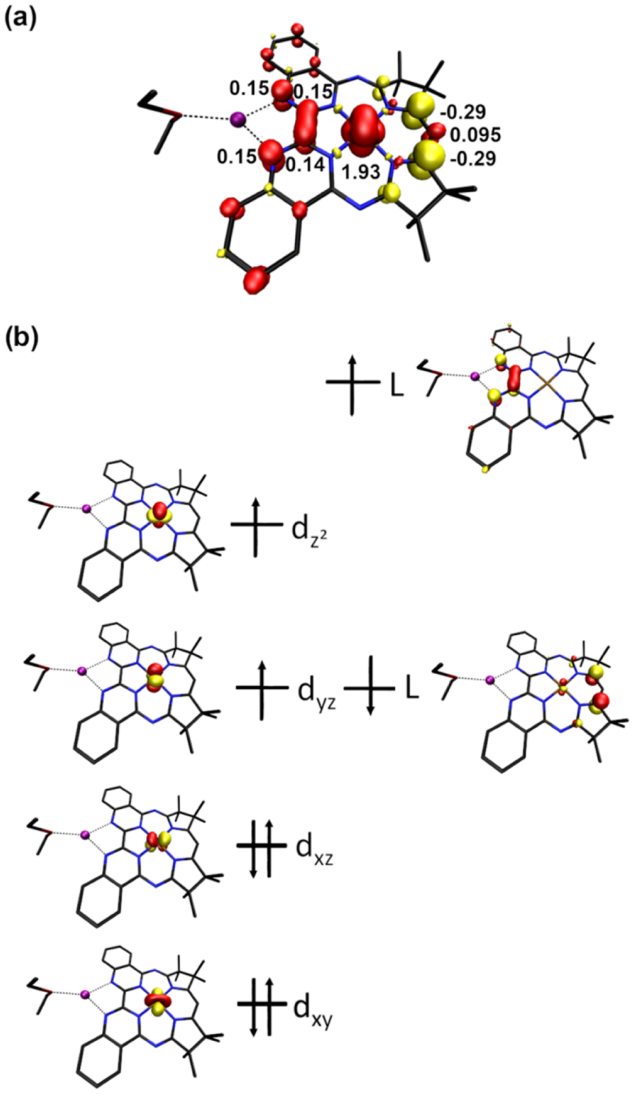

Figure 4. DFT-derived spin density map based on Loewdin spin population analysis (a) and qualitative MO diagram (b) derived from BS(3,1) DFT calculations of [**2**]$^-$.

Considering also the overall S = 1 spin state determined by the Evans' measurement (Figure S21), the electronic structure is thus best described by the [(Fe↑↑)(Mabiq↑↓)] formulation, where the overall spin state of the ligand is S_L = 0. The absorption spectrum of [**2**]$^-$ (Figure 3b) bears resemblance to that of [**2**]^0,[16c] suggesting common electronic structure features. However, the former species exhibits a series of more pronounced features in the vis−NIR region between 700 and 1000 nm (λ_{max} = 697 nm, ε = 6.3 × 10^3 M^{-1} cm^{-1}; 768 nm, ε = 6.6 × 10^3 M^{-1} cm^{-1}; and 940 nm, ε = 6.0 × 10^3 M^{-1} cm^{-1}). The strong absorption band at λ_{max} = 616 nm (ε = 1.5 × 10^4 M^{-1} cm^{-1}) is slightly blue-shifted compared to the analogous band of [**2**]^0 (λ_{max} = 628 nm).

The [Fe^{II}(Mabiq^{2-})] formulation of [**2**]$^-$ deduced from the spectroscopic data was further confirmed by density functional theory (DFT) calculations. The computational results provide an explanation for the overall S = 1 ground state of the complex and evidence reduction of the bipyrimidine site. The DFT-derived spin density map (Figure 4a) shows two unpaired α spins on the Fe center, an unpaired spin of opposite sign on the diketiminate unit of the ligand, with yet another unpaired α spin on the bipyrimidine. The iron center features a $d_{xy}^2 d_{xz}^2 d_{yz}^1 d_{z^2}^1$ configuration (Figure 4b), where the electron situated in the d_{yz} orbital is antiferromagnetically coupled to the diketiminate-localized singly occupied molecular orbital (SOMO). The lack of an overlap between the Fe d_{z^2} and the bipyrimidine orbitals leads to α-spin occupancy of both and an overall triplet ground state.

Interestingly, although the aforementioned [Fe(TPP)]$^{2-}$ and [Fe(tpyPy2Me)]^0 have similar electron configurations (intermediate spin Fe^{II} ion, a ligand biradical), these compounds possess diamagnetic ground states.[9,14a] The unique triplet ground state of [**2**]$^-$ may contribute to observed differences in the electrocatalytic behavior of the compounds. The electronic structures of the Fe-containing [**2**]$^-$ and its Co analogue [**1**]$^-$ are also worth comparing.[13b] Both complexes contain M^{II} centers, and the electron density on the Mabiq ligand is similarly localized, with antiferromagnetic coupling between the d_{yz}-based and diketiminate-localized radicals. However, the doubly occupied Co d_{z^2} orbital of [**1**]$^-$ was

https://doi.org/10.1021/acscatal.1c04636
ACS Catal. 2022, 12, 3046−3057

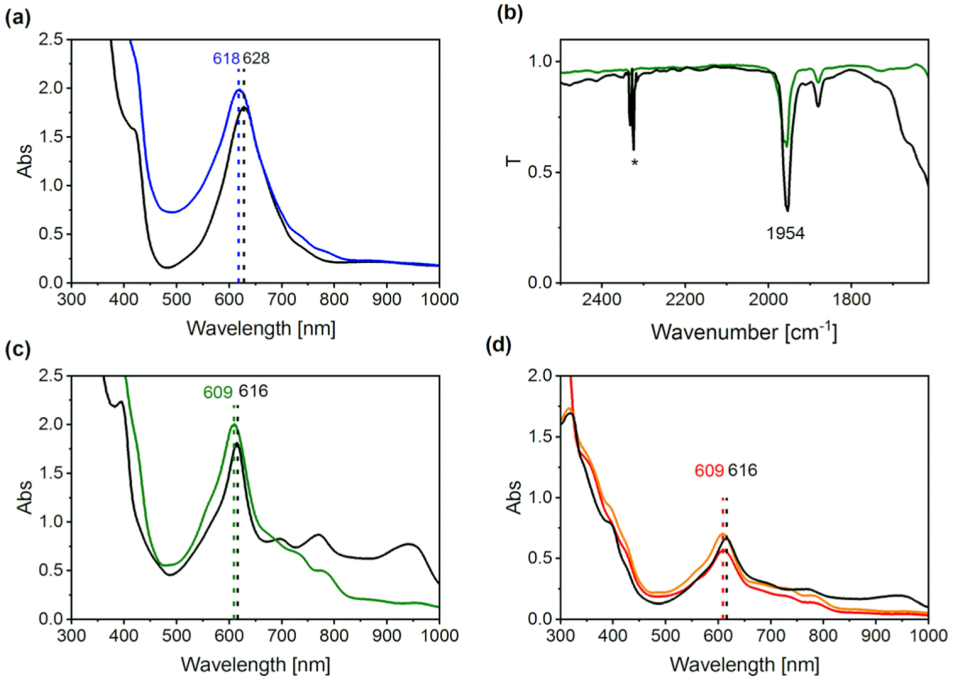

Figure 5. (a) Absorption spectra of (black) $[\mathbf{2}]^0$ (180 μM) and (blue) $[\mathbf{2}]^-$ (130 μM) purged with CO_2. (b) IR spectra of (black) $[\mathbf{2}]^-$ (12 mM) purged with CO_2; the same CO stretch is observed in the IR of a solution of $[\mathbf{2}]^0$ (6 mM) purged with CO (green). The bands marked with an asterisk can be assigned to CO_2 in solution.[19c,37] (c) Absorption spectra of (black) $[\mathbf{2}]^-$ (120 μM) and (green) $[\mathbf{2}]^-$ (130 μM) plus 85 equiv of PhOH. (d) Absorption spectra of (black) $[\mathbf{2}]^-$ (40 μM), (orange) $[\mathbf{2}]^-$ (50 μM) plus 85 equiv of PhOH purged with CO_2, (red) 200 μL aliquot (diluted in 2 mL of THF) of a bulk electrolysis sample of $[\mathbf{2}]^+$ (500 μM) with 85 equiv of PhOH, under a CO_2 atmosphere, after 1 h of applied potential at −1.85 V_{Fc} (glassy carbon plates; 0.1 M $[N(n\text{-}Bu)_4]PF_6$; MeCN). All spectra shown are of samples in THF.

found to lie energetically below the d_{xz} and d_{yz} orbitals, based on DFT calculations. These factors may account for the need for further reduction of the Co−Mabiq complex prior to CO_2 activation and differences in the activity of the complexes.

Reactivity of $[\mathbf{2}]^-$ toward CO_2. With the reduced species $[\mathbf{2}]^-$ at hand, we set out to investigate its reactivity toward CO_2. Although this species first acquires protons and must be further reduced for catalytic activity, the CV in the absence of protons already points to an interaction between $[\mathbf{2}]^-$ and CO_2. An η^1−C Fe−CO_2 adduct is a common intermediate in CO_2 reduction by iron complexes[12] and generally favored by charge transfer from the d_{z^2} orbital of an electron-rich metal center (e.g., Fe^I or Fe^0) to the π^* orbital of CO_2.[1a,3,33] $[\mathbf{2}]^-$ has a high-lying, singly occupied d_{z^2} orbital (Figure 4b) that could interact with the small molecule, initially yielding such a M−η^1−CO_2 complex. However, transient Fe^I−$CO_2^{\bullet-}$ species are rarely observed and either react further with protons or, under aprotic conditions, with Lewis acids (e.g., another CO_2 molecule) to yield Fe−carbonyl species.[12,34]

The spectroscopic data corresponding to the product of the reaction between $[\mathbf{2}]^-$ with CO_2 indeed denote the formation of an Fe−carbonyl complex. The addition of CO_2 to a solution of $[\mathbf{2}]^-$ leads to an immediate change in its absorption spectrum, with loss of the characteristic NIR bands. The final product spectrum resembles that of $[\mathbf{2}]^0$ (Figure 5a), suggesting that $[\mathbf{2}]^-$ is oxidized upon reaction with CO_2. The IR of the $[\mathbf{2}]^-/CO_2$ solution features a new band at 1954 cm^{-1} (Figure 5b), typical of a metal−carbonyl species.[6,19c,22,28,34a,35] In the absence of protons, the carbonyl complex likely results from the reaction of the transient Fe−Mabiq−CO_2 adduct with another CO_2 molecule (or with another molecule of $[\mathbf{2}\text{-}CO_2^{\bullet-}]^-$) to yield $[\mathbf{2}\text{-}CO]^+$ (Scheme 3). However, $[\mathbf{2}\text{-}CO]^+$ represents a doubly oxidized product, whose spectrum might thus be expected to rather resemble

Scheme 3. Possible Mechanism toward a Carbonyl Complex after Addition of CO_2 to $[\mathbf{2}]^-$

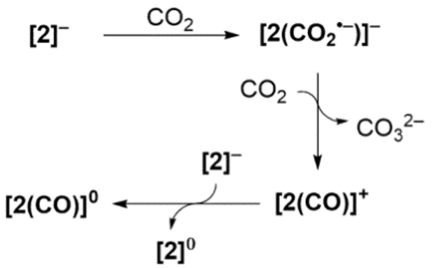

that of $[\mathbf{2}]^+$. The absorption spectrum of $[\mathbf{2}]^-/CO_2$ (Figure 5a) instead is indicative of a one-electron oxidized Fe−Mabiq species. Therefore, we propose a comproportionation reaction between $[\mathbf{2}\text{-}CO]^+$ and unreacted $[\mathbf{2}]^-$ in solution to account for $[\mathbf{2}\text{-}CO]$ as the final product (Scheme 3). Comproportionation reactions between formal "Co^0" and Co^{2+} species were observed in our prior studies concerning H_2 evolution by the Co−Mabiq complexes.[16b] The presence of the second carbon dioxide-derived product, carbonate, could not be confirmed directly by IR spectroscopy due to the overlap of the intrinsic bands of $[\mathbf{2}]^0$ in the IR region where the carbonate C−O stretches are observed ($\bar{\nu} \approx 1440$ cm^{-1}).[36] However, the production of carbonate was confirmed via an indirect assay, in which acetic acid was added to the dried $[\mathbf{2}]^-/CO_2$ reaction product, and the resultant CO_2 was measured by GC (for further information, refer to SI, Figure S22). The subsequent

https://doi.org/10.1021/acscatal.1c04636
ACS Catal. 2022, 12, 3046−3057

addition of PhOH (85 equiv) to the $[2]^-/CO_2$ solution yields no further change in the absorption spectrum (Figure S23), as expected, given the formation of the Fe−Mabiq carbonyl species. The reactivity of $[2]^0$ and $[2]^+$ toward CO also was investigated and further supports our assignment of [**2-CO**] as the $[2]^-/CO_2$ reaction product (see SI for details, Figures S24−S29).

Overall, despite the fact that $[2]^-$ does not contain a true Fe^0 center, the complex appears capable of coordinating and reducing CO_2, the necessary electrons are derived from the ligand. Nevertheless, from the electrochemical data, it is evident that a proton-coupled process precedes CO_2 activation by the complex; proton addition is more favorable than CO_2 binding and may confer advantages for the subsequent catalysis.

Protonated Precatalytic Intermediate, I_{PhOH}. We next examined the direct reaction of $[2]^-$ with protons, in an attempt to synthesize and characterize the protonated Fe−Mabiq complex, I_{PhOH}, generated prior to catalysis (*vide supra*). The reaction of $[2]^-$ with PhOH leads to precipitation of Na^+PhO^-, and liquid injection field desorption ionization mass spectrometry (LIFDI-MS) of the product solution shows a peak of m/z = 621.21 corresponding to $[Na(FeMabiq)H]^+$ (Figure S30), denoting the acquisition of at least one proton by the complex. The product is soluble in toluene and THF but only slightly soluble in MeCN. Evans' NMR measurement shows that the complex retains an S = 1 spin state (Figure S31).

The reaction of $[2]^-$ with PhOH also was monitored by absorption spectroscopy, whereupon the addition of alcohol, a blue shift of the band at 616 to 609 nm is observed, concomitant with the loss of the feature at 940 nm (Figures 5c and S32). The product spectrum is distinct from either $[2]^-$ or $[2]^0$, yet shares several features with the spectrum of $[2]^-$. The spectrum of the $[2]^-$/PhOH reaction product also is identical to that obtained in the previously discussed bulk electrolysis experiments carried out at −1.65 and −1.84 V_{Fc} (Figures 5d and S33). Therefore, the synthesized $[2]^-$/PhOH product can unequivocally be assigned to the precatalytic species I_{PhOH} generated in the EC step at E_3 (Figure 1c and Scheme 4). Indeed, the behavior of I_{PhOH} and $[2]^+$ under electrocatalytic conditions (85 equiv of PhOH in a CO_2 saturated MeCN/$N[(n\text{-}Bu)_4]PF_6$ solution) is virtually identical (Figure S34).

To assess the reversibility of proton addition to $[2]^-$, we subsequently added KO^{t}Bu to the $[2]^-$/PhOH sample ($pK_a(^t$BuOH) = 32.2 in DMSO[25] vs pK_a(PhOH) = 18.0 in DMSO[26]). Indeed, the original absorption spectrum of $[2]^-$ is fully restored by the addition of the base (Figure S35). The Fe−Mabiq complex, therefore, is not irreversibly modified during catalysis; rather, the added proton can be abstracted by a suitable base. When the $[2]^-$/PhOH solution was exposed to CO_2, no change in the absorption spectrum was observed (Figure S36). The lack of reactivity is fully consistent with the requirement for the addition of at least one more electron to this species, as deduced from the CV data, to enable CO_2 binding and activation.

Gratifyingly, we were able to obtain a molecular structure of I_{PhOH}, providing final verification of ligand protonation and that the intermediate corresponds to [Fe(MabiqH)PhOH]. The unit cell of I_{PhOH} is defined by two Fe−Mabiq molecules of opposing orientation, separated by a toluene molecule (Figure 6; see SI for further discussion of the molecular structure and assignment of the protonation site, and Figures

Scheme 4. Proposed Mechanism for CO_2 Reduction by $[2]^+$[a]

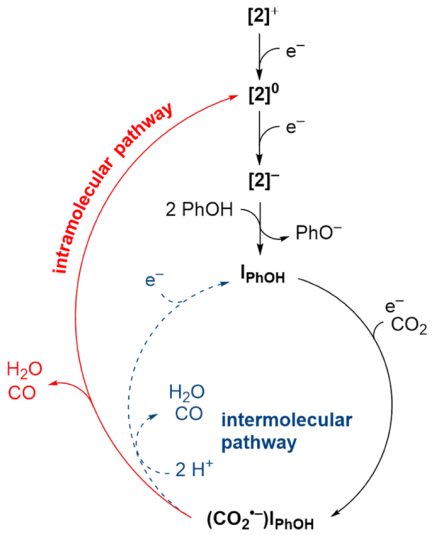

[a]The Protonation of the bound CO_2 can proceed either via an inter- (blue) or an intramolecular (red) pathway.

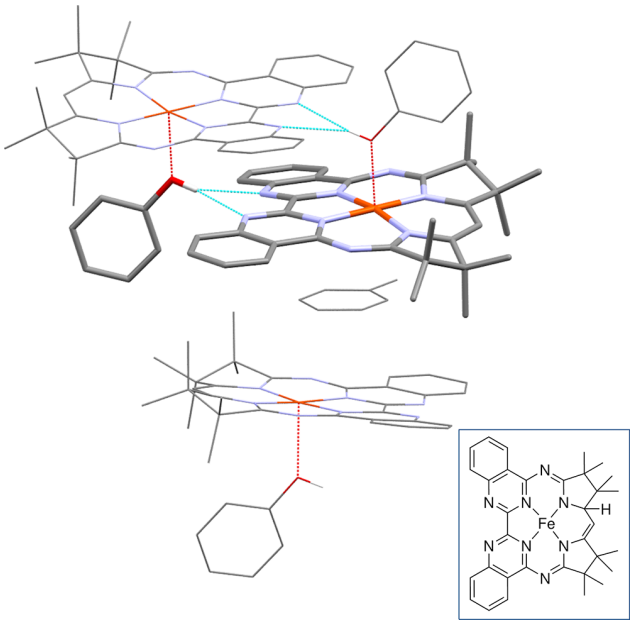

Figure 6. H-bonding interactions in I_{PhOH} in the solid state. Hydrogen atoms that are not involved in hydrogen bonding have been omitted for clarity. The suggested protonation site at the diketiminate unit is shown in the inset.

S37−S40). One PhOH molecule is associated with each Fe center with a long Fe−O_{avg} distance of 2.67 Å and thus likely dissociates in solution. PhOH also engages in hydrogen bonding with the outer bipyrimidine nitrogen atoms of a neighboring Fe−Mabiq molecule (N_{bpm}···H = 1.95−2.67 Å). Notably, the structure reveals that a proton has been taken up by the diketiminate unit (Figure 6 inset). Residual electron density peaks are localized at the diketiminate carbons (within 0.872−0.934 Å of the carbon atoms), with slight axial elongation of the anisotropic displacement parameters of the related carbons, designating these as the protonation sites. The diketiminate carbons also were possible protonation sites in

https://doi.org/10.1021/acscatal.1c04636
ACS Catal. 2022, 12, 3046−3057

the mechanism of H_2 evolution by the Co−Mabiq complexes based on computational and spectroscopic studies.[16b] The Fe−N distances of $\mathbf{I_{PhOH}}$ are only slightly longer than in $[\mathbf{2}]^-$ (1.91 and 1.89 Å, respectively), which along with its absorption spectrum rules out the oxidation of the Fe ion.

Several features of $\mathbf{I_{PhOH}}$ are especially relevant for CO_2 reduction by the Fe−Mabiq complex. The assigned diketiminate proton is ideally positioned for direct transfer to an Fe-bound CO_2 adduct generated upon further reduction of the complex. We estimate the OCO···H distance of such a species to be within ∼2.3 Å. The H-bonding interactions between the PhOH and the bipyrimidine nitrogen atoms are likely a consequence of the negative charge at the latter moiety; the phenolic proton effectively replaces the Na ion observed in this position in $[\mathbf{2}]^-$. This hydrogen bonding network may further aid CO_2 reduction by increasing the local acid concentration and by offering another pathway for proton transfer.

Mechanism of CO_2 Reduction by $[\mathbf{2}]^+$. Taking all of the abovementioned findings into consideration, we propose the following catalytic cycle for electrocatalytic CO_2 reduction by $[\mathbf{2}]^+$ (Scheme 4). The cationic starting compound, $[\mathbf{2}]^+$, must first be two-electron reduced to the anionic $[\mathbf{2}]^-$, which becomes protonated by PhOH to give the precatalytic species $\mathbf{I_{PhOH}}$. CO_2 binding coincides with the reduction of $\mathbf{I_{PhOH}}$ (in the absence of CO_2, reduction of this species occurs at significantly more negative potentials). CO is subsequently released from a putative $Fe-CO_2^{\bullet-}$ intermediate, following the final electron and proton transfer. The proposed pathways shown in Scheme 4 assume another CE mechanism to affect the CO release from $(\mathbf{CO_2^{\bullet-}})\mathbf{I_{PhOH}}$, in accord with the mechanisms proposed for Fe porphyrins,[12,23,38] though a concerted proton-coupled electron transfer (PCET) process is also entirely plausible.

Two pathways are feasible for the formation and release of CO from $(\mathbf{CO_2^{\bullet-}})\mathbf{I_{PhOH}}$, denoted by the inter- and intramolecular pathways in Scheme 4, which differ with respect to the origin of the protons. These protons can be delivered to the bound $CO_2^{\bullet-}$ from PhOH in a bimolecular fashion (intermolecular pathway, inner dashed arrows, Scheme 4). However, in light of the structure of $\mathbf{I_{PhOH}}$, as well as the ability to readily remove the proton with an added base, we favor the alternative pathway, in which the proton attached to the Mabiq backbone is directly transferred to the $CO_2^{\bullet-}$ species (intramolecular pathway, outer red arrow, Scheme 4), yielding the unmodified, neutral $[\mathbf{2}]^0$. The ensuing reduction would then regenerate the *formal* Fe^0 complex, $[\mathbf{2}]^-$, which in the presence of PhOH is reprotonated to again give $\mathbf{I_{PhOH}}$. Hydrogen bonding interactions in the bipyrimidine periphery may further assist CO release.

CONCLUSIONS

Overall, we have shown that $[\mathbf{2}]^+$ acts as a highly selective electrocatalyst for CO_2 reduction (>99% selectivity in favor of CO), operating at an overpotential requirement of 500 mV and exhibiting a FE of 96 ± 11%. Even though the first two reductions are ligand- and not metal-centered, a clear difference in the activity of the Fe and Co complexes is observed. Reactivity differences have been observed in other systems upon switching of the metal center from Co to Fe, with effects on product formation or overpotential dependent on the nature of the ligand scaffold.[22,27,39] In our system, the selectivity for CO is comparable for the two Mabiq complexes, but the Fe complex clearly is a superior catalyst in terms of overpotential and FE. This is, in part, due to the requirement for additional electrons to initiate catalysis by the Co complex. Therefore, ligand-centered reduction may be a contributing factor in lowering the overpotential, as determined for other systems. However, interactions between the redox-active ligand and the metal ion govern key electronic structure differences. This aspect is highlighted by the $[\mathbf{X}]^-$ forms of the metal−Mabiq compounds, with a high-lying d_{z^2} orbital only available for $[\mathbf{2}]^-$, which may also be relevant to the reactivity of the active species.

Our studies highlight further influences of the Mabiq ligand on catalysis by the Fe complex. The preference for ligand-centered reduction not only disfavors metal hydride formation but renders the reduced ligand susceptible to protonation. This contrasts with the FeTPP and Fe−tpyPy2Me complexes, which also have Fe^{II}−ligand biradical formulations in their two-electron reduced forms, as well as with other catalysts containing redox-active bipyridine- or PDI-based ligands.[9,10c,14,40] The Mabiq properties disfavor H_2 evolution by the Fe−Mabiq complex, which occurs at significantly more negative potentials than CO_2 reduction. Concurrently, the resultant protonation of the Mabiq ligand introduces a potential, and unconventional, proton relay site that can assist in the stabilization of and proton transfer to $M-CO_2$ adducts. The Mabiq ligand is thus a highly unique motif that is noninnocent with respect to both electron and proton storage, offering a ligand-assisted pathway for selective CO_2 to CO conversion.

ASSOCIATED CONTENT

Supporting Information

The Supporting Information is available free of charge at https://pubs.acs.org/doi/10.1021/acscatal.1c04636.

Additional data (CVs, calculation of proton dependence, overpotential determination, headspace analysis in CPE experiments, DFT calculations, crystallographic parameters, UV−vis, LIFDI, and IR spectra) (PDF)

Crystallographic data (CIF)

Crystallographic data (CIF)

Accession Codes

CCDC 2111145−2111146 contains the supplementary crystallographic data for this paper. These data can be obtained free of charge via www.ccdc.ac.uk/data_request/cif, or by emailing data_request@ccdc.cam.ac.uk, or by contacting The Cambridge Crystallographic Data Centre, 12 Union Road, Cambridge CB2 1EZ, U.K.; fax: +44 1223 336033.

AUTHOR INFORMATION

Corresponding Author

Corinna R. Hess − *Department of Chemistry and Catalysis Research Center (CRC), Technical University of Munich, 85748 Garching, Germany*; orcid.org/0000-0002-9607-9184; Email: corinna.hess@ch.tum.de

Authors

Kerstin Rickmeyer − *Department of Chemistry and Catalysis Research Center (CRC), Technical University of Munich, 85748 Garching, Germany*

Lukas Niederegger − *Department of Chemistry and Catalysis Research Center (CRC), Technical University of Munich, 85748 Garching, Germany*

Martin Keilwerth − *Department of Chemistry and Pharmacy, Inorganic Chemistry, Friedrich-Alexander-University Erlangen-Nürnberg (FAU), 91058 Erlangen, Germany;* orcid.org/0000-0002-8801-6888

Complete contact information is available at: https://pubs.acs.org/10.1021/acscatal.1c04636

Author Contributions

All authors have given approval to the final version of the manuscript.

Funding

Funding for this work was provided by the German Research Foundation (DFG) under Germany's Excellence Strategy—EXC 2089/1—390776260.

Notes

The authors declare no competing financial interest.

■ ACKNOWLEDGMENTS

The authors thank R. Lauenstein for contributing to synthesis and electrochemical studies. We are grateful to Prof. Karsten Meyer and Dr. Jörg Sutter for providing access to and assistance with the Mößbauer measurements (supported by the Friedrich−Alexander-University of Erlangen−Nürnberg). K.R. would like to thank Jürgen Kudermann from the TUM-CRC Analytic Department for his great support in setting up the GC. We also thank Dr. Alexander Pöthig, Prof. Inke Siewert, and Lucas A. Paul for helpful discussions.

■ ABBREVIATIONS

CCE, controlled current electrolysis; CPE, controlled potential electrolysis; CV, cyclic voltammetry; FeTPP, Fe−tetraphenylporphyrin; FID-M, flame-ionization detector with methanizer; IR, infrared; LIFDI-MS, liquid injection field desorption ionization mass spectrometry; PDI, pyridine diimine; TCD, thermal conductivity detector

■ REFERENCES

(1) (a) Francke, R.; Schille, B.; Roemelt, M. Homogeneously Catalyzed Electroreduction of Carbon Dioxide-Methods, Mechanisms, and Catalysts. *Chem. Rev.* **2018**, *118*, 4631−4701. (b) Nitopi, S.; Bertheussen, E.; Scott, S. B.; Liu, X.; Engstfeld, A. K.; Horch, S.; Seger, B.; Stephens, I. E. L.; Chan, K.; Hahn, C.; Nørskov, J. K.; Jaramillo, T. F.; Chorkendorff, I. Progress and Perspectives of Electrochemical CO_2 Reduction on Copper in Aqueous Electrolyte. *Chem. Rev.* **2019**, *119*, 7610−7672. (c) Appel, A. M.; Bercaw, J. E.; Bocarsly, A. B.; Dobbek, H.; DuBois, D. L.; Dupuis, M.; Ferry, J. G.; Fujita, E.; Hille, R.; Kenis, P. J. A.; Kerfeld, C. A.; Morris, R. H.; Peden, C. H. F.; Portis, A. R.; Ragsdale, S. W.; Rauchfuss, T. B.; Reek, J. N. H.; Seefeldt, L. C.; Thauer, R. K.; Waldrop, G. L. Frontiers, Opportunities, and Challenges in Biochemical and Chemical Catalysis of CO_2 Fixation. *Chem. Rev.* **2013**, *113*, 6621−6658. (d) Qiao, J.; Liu, Y.; Hong, F.; Zhang, J. A review of catalysts for the electroreduction of carbon dioxide to produce low-carbon fuels. *Chem. Soc. Rev.* **2014**, *43*, 631−675.

(2) (a) Franco, F.; Rettenmaier, C.; Jeon, H. S.; Roldan Cuenya, B. Transition metal-based catalysts for the electrochemical CO_2 reduction: from atoms and molecules to nanostructured materials. *Chem. Soc. Rev.* **2020**, *49*, 6884−6946. (b) Dalle, K. E.; Warnan, J.; Leung, J. J.; Reuillard, B.; Karmel, I. S.; Reisner, E. Electro- and Solar-Driven Fuel Synthesis with First Row Transition Metal Complexes. *Chem. Rev.* **2019**, *119*, 2752−2875. (c) Barrett, A. J. A.; Brunner, B. F. M.; Cheung, C. P. L.; Kubiak, D. C. P.; Lee, E. G. L.; Miller, F. C. J.; Waldie, G. K. M.; Zhanaidarova, H. A. Approaches to Controlling Homogeneous Electrochemical Reduction of Carbon Dioxide. In *Carbon Dioxide Electrochemistry: Homogeneous and Heterogeneous Catalysis*; The Royal Society of Chemistry, 2021; Chapter 1, pp 1−66. (d) Boutin, E.; Merakeb, L.; Ma, B.; Boudy, B.; Wang, M.; Bonin, J.; Anxolabéhère-Mallart, E.; Robert, M. Molecular catalysis of CO_2 reduction: recent advances and perspectives in electrochemical and light-driven processes with selected Fe, Ni and Co aza macrocyclic and polypyridine complexes. *Chem. Soc. Rev.* **2020**, *49*, 5772−5809.

(3) (a) Barlow, J. M.; Yang, J. Y. Thermodynamic Considerations for Optimizing Selective CO_2 Reduction by Molecular Catalysts. *ACS Cent. Sci.* **2019**, *5*, 580−588. (b) Jiang, C.; Nichols, A. W.; Machan, C. W. A look at periodic trends in d-block molecular electrocatalysts for CO_2 reduction. *Dalton Trans.* **2019**, *48*, 9454−9468.

(4) (a) Bullock, R. M.; Chen, J. G.; Gagliardi, L.; Chirik, P. J.; Farha, O. K.; Hendon, C. H.; Jones, C. W.; Keith, J. A.; Klosin, J.; Minteer, S. D.; Morris, R. H.; Radosevich, A. T.; Rauchfuss, T. B.; Strotman, N. A.; Vojvodic, A.; Ward, T. R.; Yang, J. Y.; Surendranath, Y. Using nature's blueprint to expand catalysis with Earth-abundant metals. *Science* **2020**, *369*, No. eabc3183. (b) Nie, W.; Tarnopol, D. E.; McCrory, C. C. L. Enhancing a Molecular Electrocatalyst's Activity for CO_2 Reduction by Simultaneously Modulating Three Substituent Effects. *J. Am. Chem. Soc.* **2021**, *143*, 3764−3778.

(5) (a) Wang, V. C. C. Beyond the Active Site: Mechanistic Investigations of the Role of the Secondary Coordination Sphere and Beyond in Multi-electron Electrocatalytic Reactions. *ACS Catal.* **2021**, *11*, 8292−8303. (b) Chabolla, S. A.; Yang, J. Y. For CO_2 Reduction, Hydrogen-Bond Donors Do the Trick. *ACS Cent. Sci.* **2018**, *4*, 315−317. (c) Amanullah, S.; Saha, P.; Nayek, A.; Ahmed, M. E.; Dey, A. Biochemical and artificial pathways for the reduction of carbon dioxide, nitrite and the competing proton reduction: effect of 2nd sphere interactions in catalysis. *Chem. Soc. Rev.* **2021**, *50*, 3755−3823.

(6) Fujita, E.; Creutz, C.; Sutin, N.; Brunschwig, B. S. Carbon dioxide activation by cobalt macrocycles: evidence of hydrogen bonding between bound CO_2 and the macrocycle in solution. *Inorg. Chem.* **1993**, *32*, 2657−2662.

(7) Chapovetsky, A.; Welborn, M.; Luna, J. M.; Haiges, R.; Miller, T. F., 3rd; Marinescu, S. C. Pendant Hydrogen-Bond Donors in Cobalt Catalysts Independently Enhance CO_2 Reduction. *ACS Cent. Sci.* **2018**, *4*, 397−404.

(8) (a) Azcarate, I.; Costentin, C.; Robert, M.; Savéant, J.-M. Through-Space Charge Interaction Substituent Effects in Molecular Catalysis Leading to the Design of the Most Efficient Catalyst of CO_2-to-CO Electrochemical Conversion. *J. Am. Chem. Soc.* **2016**, *138*, 16639−16644. (b) Martin, D. J.; Mayer, J. M. Oriented Electrostatic Effects on O_2 and CO_2 Reduction by a Polycationic Iron Porphyrin. *J. Am. Chem. Soc.* **2021**, *143*, 11423−11434.

(9) Derrick, J. S.; Loipersberger, M.; Chatterjee, R.; Iovan, D. A.; Smith, P. T.; Chakarawet, K.; Yano, J.; Long, J. R.; Head-Gordon, M.; Chang, C. J. Metal−Ligand Cooperativity via Exchange Coupling Promotes Iron- Catalyzed Electrochemical CO_2 Reduction at Low Overpotentials. *J. Am. Chem. Soc.* **2020**, *142*, 20489−20501.

(10) (a) Costentin, C.; Drouet, S.; Robert, M.; Saveant, J.-M. A Local Proton Source Enhances CO_2 Electroreduction to CO by a Molecular Fe Catalyst. *Science* **2012**, *338*, 90−94. (b) Costentin, C.; Passard, G.; Robert, M.; Savéant, J.-M. Pendant Acid−Base Groups in Molecular Catalysts: H-Bond Promoters or Proton Relays? Mechanisms of the Conversion of CO_2 to CO by Electrogenerated Iron(0)Porphyrins Bearing Prepositioned Phenol Functionalities. *J. Am. Chem. Soc.* **2014**, *136*, 11821−11829. (c) Lacy, D. C.; McCrory, C. C.; Peters, J. C. Studies of cobalt-mediated electrocatalytic CO_2 reduction using a redox-active ligand. *Inorg. Chem.* **2014**, *53*, 4980−4988. (d) Amanullah, S.; Saha, P.; Dey, A. Activating the Fe(I) State of Iron Porphyrinoid with Second-Sphere Proton Transfer Residues for Selective Reduction of CO_2 to HCOOH via Fe(III/II)−COOH Intermediate(s). *J. Am. Chem. Soc.* **2021**, *143*, 13579−13592. (e) Margarit, C. G.; Schnedermann, C.; Asimow, N. G.; Nocera, D. G. Carbon Dioxide Reduction by Iron Hangman Porphyrins. *Organometallics* **2019**, *38*, 1219−1223. (f) Roy, S. S.; Talukdar, K.; Jurss, J. W. Electro- and Photochemical Reduction of CO2 by Molecular Manganese Catalysts: Exploring the Positional Effect of

Second-Sphere Hydrogen-Bond Donors. *ChemSusChem* **2021**, *14*, 662−670.
(11) Queyriaux, N. Redox-Active Ligands in Electroassisted Catalytic H^+ and CO_2 Reductions: Benefits and Risks. *ACS Catal.* **2021**, *11*, 4024−4035.
(12) Bonetto, R.; Crisanti, F.; Sartorel, A. Carbon Dioxide Reduction Mediated by Iron Catalysts: Mechanism and Intermediates That Guide Selectivity. *ACS Omega* **2020**, *5*, 21309−21319.
(13) (a) Lyaskovskyy, V.; de Bruin, B. Redox Non-Innocent Ligands: Versatile New Tools to Control Catalytic Reactions. *ACS Catal.* **2012**, *2*, 270−279. (b) Kaspar, M.; Altmann, P. J.; Pothig, A.; Sproules, S.; Hess, C. R. A macrocyclic 'Co(0)' complex: the relevance of ligand non-innocence to reactivity. *Chem. Commun.* **2017**, *53*, 7282−7285. (c) Praneeth, V. K. K.; Ringenberg, M. R.; Ward, T. R. Redox-Active Ligands in Catalysis. *Angew. Chem., Int. Ed.* **2012**, *51*, 10228−10234. (d) Chirik, P. J.; Wieghardt, K. Radical Ligands Confer Nobility on Base-Metal Catalysts. *Science* **2010**, *327*, 794−795.
(14) (a) Römelt, C.; Song, J.; Tarrago, M.; Rees, J. A.; van Gastel, M.; Weyhermüller, T.; DeBeer, S.; Bill, E.; Neese, F.; Ye, S. Electronic Structure of a Formal Iron(0) Porphyrin Complex Relevant to CO_2 Reduction. *Inorg. Chem.* **2017**, *56*, 4745−4750. (b) Su, X.; McCardle, K. M.; Chen, L.; Panetier, J. A.; Jurss, J. W. Robust and Selective Cobalt Catalysts Bearing Redox-Active Bipyridyl-N-heterocyclic Carbene Frameworks for Electrochemical CO_2 Reduction in Aqueous Solutions. *ACS Catal.* **2019**, *9*, 7398−7408.
(15) Das, A.; Hessin, C.; Ren, Y.; Desage-El Murr, M. Biological concepts for catalysis and reactivity: empowering bioinspiration. *Chem. Soc. Rev.* **2020**, *49*, 8840−8867.
(16) (a) Tok, G. C.; Freiberg, A. T. S.; Gasteiger, H. A.; Hess, C. R. Electrocatalytik H_2 Evolution by the Co-Mabiq Complex Requires Tempering of the Redox-Active Ligand. *ChemCatChem* **2019**, *11*, 3973−3981. (b) Tok, G. C.; Reiter, S.; Freiberg, A. T. S.; Reinschlüssel, L.; Gasteiger, H. A.; de Vivie-Riedle, R.; Hess, C. R. H_2 Evolution from Electrocatalysts with Redox-Active Ligands: Mechanistic Insights from Theory and Experiment vis-à-vis Co-Mabiq. *Inorg. Chem.* **2021**, *60*, 13888−13902. (c) Banerjee, P.; Company, A.; Weyhermüller, T.; Bill, E.; Hess, C. R. Zn and Fe Complexes Containing a Redox Active Macrocyclic Biquinazoline Ligand. *Inorg. Chem.* **2009**, *48*, 2944−2955.
(17) Puttock, E. V.; Banerjee, P.; Kaspar, M.; Drennen, L.; Yufit, D. S.; Bill, E.; Sproules, S.; Hess, C. R. A Series of [Co(Mabiq)Cl2−n] (n = 0, 1, 2) Compounds and Evidence for the Elusive Bimetallic Form. *Inorg. Chem.* **2015**, *54*, 5864−5873.
(18) McCarthy, B. D.; Martin, D. J.; Rountree, E. S.; Ullman, A. C.; Dempsey, J. L. Electrochemical reduction of Bronsted acids by glassy carbon in acetonitrile-implications for electrocatalytic hydrogen evolution. *Inorg. Chem.* **2014**, *53*, 8350−8361.
(19) (a) Azcarate, I.; Costentin, C.; Robert, M.; Savéant, J.-M. Dissection of Electronic Substituent Effects in Multielectron−Multistep Molecular Catalysis. Electrochemical CO_2-to-CO Conversion Catalyzed by Iron Porphyrins. *J. Phys. Chem. C* **2016**, *120*, 28951−28960. (b) Ceballos, B. M.; Yang, J. Y. Directing the reactivity of metal hydrides for selective CO_2 reduction. *Proc. Natl. Acad. Sci. U.S.A.* **2018**, *115*, 12686−12691. (c) Bonetto, R.; Altieri, R.; Tagliapietra, M.; Barbon, A.; Bonchio, M.; Robert, M.; Sartorel, A. Electrochemical Conversion of CO_2 to CO by a Competent Fe^I Intermediate Bearing a Schiff Base Ligand. *ChemSusChem* **2020**, *13*, 4111−4120.
(20) Angamuthu, R.; Byers, P.; Lutz, M.; Spek, A. L.; Bouwman, E. Electrocatalytic CO_2 Conversion to Oxalate by a Copper Complex. *Science* **2010**, *327*, 313−315.
(21) (a) Isse, A. A.; Gennaro, A.; Vianello, E.; Floriani, C. Electrochemical reduction of carbon dioxide catalyzed by [Co^I(salophen)Li]. *J. Mol. Catal.* **1991**, *70*, 197−208. (b) Sullivan, B. P.; Bolinger, C. M.; Conrad, D.; Vining, W. J.; Meyer, T. J. One- and two-electron pathways in the electrocatalytic reduction of CO_2 by fac-Re(bpy)$(CO)_3$Cl (bpy = 2,2′-bipyridine). *J. Chem. Soc., Chem. Commun.* **1985**, *20*, 1414−1416.
(22) Cometto, C.; Chen, L.; Lo, P.-K.; Guo, Z.; Lau, K.-C.; Anxolabéhère-Mallart, E.; Fave, C.; Lau, T.-C.; Robert, M. Highly Selective Molecular Catalysts for the CO_2-to-CO Electrochemical Conversion at Very Low Overpotential. Contrasting Fe vs Co Quaterpyridine Complexes upon Mechanistic Studies. *ACS Catal.* **2018**, *8*, 3411−3417.
(23) Costentin, C.; Drouet, S.; Passard, G.; Robert, M.; Saveant, J. M. Proton-coupled electron transfer cleavage of heavy-atom bonds in electrocatalytic processes. Cleavage of a C-O bond in the catalyzed electrochemical reduction of CO_2. *J. Am. Chem. Soc.* **2013**, *135*, 9023−9031.
(24) Elgrishi, N.; Chambers, M. B.; Wang, X.; Fontecave, M. Molecular polypyridine-based metal complexes as catalysts for the reduction of CO_2. *Chem. Soc. Rev.* **2017**, *46*, 761−796.
(25) Olmstead, W. N.; Margolin, Z.; Bordwell, F. G. Acidities of water and simple alcohols in dimethyl sulfoxide solution. *J. Org. Chem.* **1980**, *45*, 3295−3299.
(26) Bordwell, F. G.; McCallum, R. J.; Olmstead, W. N. Acidities and hydrogen bonding of phenols in dimethyl sulfoxide. *J. Org. Chem.* **1984**, *49*, 1424−1427.
(27) Chen, L.; Guo, Z.; Wei, X. G.; Gallenkamp, C.; Bonin, J.; Anxolabehere-Mallart, E.; Lau, K. C.; Lau, T. C.; Robert, M. Molecular Catalysis of the Electrochemical and Photochemical Reduction of CO_2 with Earth-Abundant Metal Complexes. Selective Production of CO vs HCOOH by Switching of the Metal Center. *J. Am. Chem. Soc.* **2015**, *137*, 10918−10921.
(28) Fokin, I.; Denisiuk, A.; Wurtele, C.; Siewert, I. The Impact of a Proton Relay in Binuclear alpha-Diimine-Mn$(CO)_3$ Complexes on the CO_2 Reduction Catalysis. *Inorg. Chem.* **2019**, *58*, 10444−10453.
(29) (a) Matsubara, Y. Unified Benchmarking of Electrocatalysts in Noninnocent Second Coordination Spheres for CO_2 Reduction. *ACS Energy Lett.* **2019**, *4*, 1999−2004. (b) Fourmond, V.; Jacques, P.-A.; Fontecave, M.; Artero, V. H_2 Evolution and Molecular Electrocatalysts: Determination of Overpotentials and Effect of Homoconjugation. *Inorg. Chem.* **2010**, *49*, 10338−10347.
(30) Römelt, C.; Ye, S.; Bill, E.; Weyhermüller, T.; van Gastel, M.; Neese, F. Electronic Structure and Spin Multiplicity of Iron Tetraphenylporphyrins in Their Reduced States as Determined by a Combination of Resonance Raman Spectroscopy and Quantum Chemistry. *Inorg. Chem.* **2018**, *57*, 2141−2148.
(31) (a) Bachmann, J.; Nocera, D. G. Multielectron Redox Chemistry of Iron Porphyrinogens. *J. Am. Chem. Soc.* **2005**, *127*, 4730−4743. (b) Mashiko, T.; Reed, C. A.; Haller, K. J.; Scheidt, W. R. Nature of iron(I) and iron(0) tetraphenylporphyrin complexes. Synthesis and molecular structure of (dibenzo-18-crown-6)bis-(tetrahydrofuran)sodium (meso-tetraphenylporphinato)ferrate and bis[tris(tetrahydrofuran)sodium] (meso-tetraphenylporphinato)-ferrate. *Inorg. Chem.* **1984**, *23*, 3192−3196. (c) Collman, J. P.; Hoard, J. L.; Kim, N.; Lang, G.; Reed, C. A. Synthesis, stereochemistry, and structure-related properties of $\alpha,\beta,\gamma,\delta$-tetraphenylporphinatoiron(II). *J. Am. Chem. Soc.* **1975**, *97*, 2676−2681. (d) Lang, G.; Spartalian, K.; Reed, C. A.; Collman, J. P. Mössbauer effect study of the magnetic properties of S=1 ferrous tetraphenylporphyrin. *J. Chem. Phys.* **1978**, *69*, 5424−5427.
(32) Römelt, M.; Ye, S.; Neese, F. Calibration of Modern Density Functional Theory Methods for the Prediction of ^{57}Fe Mössbauer Isomer Shifts: Meta-GGA and Double-Hybrid Functionals. *Inorg. Chem.* **2009**, *48*, 784−785.
(33) Pandey, K. K. Reactivities of carbonyl sulfide (COS), carbon disulfide (CS_2) and carbon dioxide(CO_2)with transition metal complexes. *Coord. Chem. Rev.* **1995**, *140*, 37−114.
(34) (a) Fernández, S.; Franco, F.; Casadevall, C.; Martin-Diaconescu, V.; Luis, J. M.; Lloret-Fillol, J. A Unified Electro- and Photocatalytic CO_2 to CO Reduction Mechanism with Aminopyridine Cobalt Complexes. *J. Am. Chem. Soc.* **2020**, *142*, 120−133. (b) Schneider, J.; Jia, H.; Muckerman, J. T.; Fujita, E. Thermodynamics and kinetics of CO_2, CO, and H^+ binding to the metal centre of CO_2 reduction catalysts. *Chem. Soc. Rev.* **2012**, *41*, 2036−2051.

https://doi.org/10.1021/acscatal.1c04636
ACS Catal. 2022, 12, 3046−3057

(35) (a) Froehlich, J. D.; Kubiak, C. P. The Homogeneous Reduction of CO_2 by [Ni(cyclam)]$^+$: Increased Catalytic Rates with the Addition of a CO Scavenger. *J. Am. Chem. Soc.* **2015**, *137*, 3565−3573. (b) Cotton, F. A.; Kraihanzel, C. S. Vibrational Spectra and Bonding in Metal Carbonyls. I. Infrared Spectra of Phosphine-substituted Group VI Carbonyls in the CO Stretching Region. *J. Am. Chem. Soc.* **1962**, *84*, 4432−4438. (c) Iffland, L.; Khedkar, A.; Petuker, A.; Lieb, M.; Wittkamp, F.; van Gastel, M.; Roemelt, M.; Apfel, U.-P. Solvent-Controlled CO_2 Reduction by a Triphos−Iron Hydride Complex. *Organometallics* **2019**, *38*, 289−299.

(36) Dutcher, B.; Fan, M.; Leonard, B.; Dyar, M. D.; Tang, J.; Speicher, E. A.; Liu, P.; Zhang, Y. Use of Nanoporous FeOOH as a Catalytic Support for $NaHCO_3$ Decomposition Aimed at Reduction of Energy Requirement of Na_2CO_3/$NaHCO_3$ Based CO_2 Separation Technology. *J. Phys. Chem. C* **2011**, *115*, 15532−15544.

(37) Pun, S.-N.; Chung, W.-H.; Lam, K.-M.; Guo, P.; Chan, P.-H.; Wong, K.-Y.; Che, C.-M.; Chen, T.-Y.; Peng, S.-M. Iron(i) complexes of 2,9-bis(2-hydroxyphenyl)-1,10-phenanthroline (H2dophen) as electrocatalysts for carbon dioxide reduction. X-Ray crystal structures of $[Fe(dophen)Cl]_2{\cdot}2HCON(CH_3)_2$ and $[Fe(dophen)(N\text{-}MeIm)_2]$-$ClO_4$ (N-MeIm = 1-methylimidazole). *J. Chem. Soc., Dalton Trans.* **2002**, *291*, 575−583.

(38) Mondal, B.; Rana, A.; Sen, P.; Dey, A. Intermediates Involved in the $2e^-/2H^+$ Reduction of CO_2 to CO by Iron(0) Porphyrin. *J. Am. Chem. Soc.* **2015**, *137*, 11214−11217.

(39) Behar, D.; Dhanasekaran, T.; Neta, P.; Hosten, C. M.; Ejeh, D.; Hambright, P.; Fujita, E. Cobalt Porphyrin Catalyzed Reduction of CO_2. Radiation Chemical, Photochemical, and Electrochemical Studies. *J. Phys. Chem. A* **1998**, *102*, 2870−2877.

(40) Su, X.; McCardle, K. M.; Panetier, J. A.; Jurss, J. W. Electrocatalytic CO_2 reduction with nickel complexes supported by tunable bipyridyl-N-heterocyclic carbene donors: understanding redox-active macrocycles. *Chem. Commun.* **2018**, *54*, 3351−3354.

https://doi.org/10.1021/acscatal.1c04636
ACS Catal. 2022, 12, 3046−3057

Influence of a neighbouring Cu centre on electro- and photocatalytic CO_2 reduction by Fe-Mabiq

Title:	"Influence of a neighbouring Cu centre on electro- and photocatalytic CO_2 reduction by Fe-Mabiq"
Status:	Communication, published online 14. December 2023
	Correction, published online 29. April 2024
Journal:	*Chemical Communications* **2024**, *60*, 819–822
Publisher:	Royal Society of Chemistry
DOI:	10.1039/d3cc04777f and 10.1039/d4cc90124j
Authors:	Kerstin Rickmeyer, Matthias Huber, Corinna R. Hess

Content: This study shows the effect of occupation of the unique second binding site at the Mabiq ligand with a Cu^{I} center. A novel heterobimetallic Cu,Fe-Mabiq was synthesized and fully characterized. Its performance in electro- and photocatalytic CO_2 reduction was examined and compared to the monometallic Fe-Mabiq. The neighboring Cu-Xantphos unit lead to marked changes in the electrocatalytic mechanism as no protonated precatalytic intermediate is observed with the bimetallic complex. Occupation of the second binding site thus renders the complex less prone to protonation leading to a different mechanistic pathway. Both catalysts were further investigated in photocatalytic CO_2 reduction in the presence of BIH as SED and **Ru-PS** as PS. The bimetallic complex performs better exhibiting a higher TOF compared to its monometallic parent complex. Intriguingly, the Cu,Fe-Mabiq is also capable to photocatalytically reduce CO_2 in the absence of PS in a self-sensitized manner exhibiting one of the highest TOF for a complex employing solely earth-abundant metals. The interaction of both catalysts with the SED BIH was investigated as well, showing comparable Φ for both complexes. Mechanistic studies under the photocatalytic conditions confirm the initial findings from the electrocatalysis. While the protonated precatalytic intermediate ($\mathbf{I_{PhOH}}$) was also observed as an intermediate in photocatalysis with the monometallic Fe-Mabiq, no such intermediate was found with the bimetallic Cu,Fe-Mabiq. This study highlights how the occupation of the outer binding site of the Mabiq ligand with Cu-Xantphos alters the complex' redox-properties, prevents ligand protonation and leads to enhanced photocatalytic performance.

K. Rickmeyer planned and executed all experiments and wrote the manuscript. M. Huber performed all SC-XRD measurements, managed the processing of the respective data and assisted in analyzing the data from gas-chromatography (GC) measurements. All work was conducted under the supervision of C. R. Hess.

ChemComm

COMMUNICATION

Cite this: *Chem. Commun.*, 2024, **60**, 819

Received 26th September 2023,
Accepted 12th December 2023

DOI: 10.1039/d3cc04777f

rsc.li/chemcomm

Influence of a neighbouring Cu centre on electro- and photocatalytic CO_2 reduction by Fe-Mabiq†

Kerstin Rickmeyer,[ab] Matthias Huber[ab] and Corinna R. Hess *[ab]

Electrocatalytic and photocatalytic CO_2 reduction by a heterobimetallic Cu/Fe–Mabiq complex were examined and compared to the monometallic [Fe(Mabiq)]$^+$. The neighbouring Cu–Xantphos unit leads to marked changes in the electrocatalytic mechanism and enhanced photocatalytic performance.

The efficient and selective transformation of CO_2 into more valuable chemical fuels using renewable energy sources is an essential sustainability issue.[1] Numerous transition metal catalysts have been developed for electrocatalytic CO_2 reduction.[2–4] With sunlight the most abundant energy source, intense efforts have also been devoted to photo-driven CO_2 conversion,[1,5,6] which offers advantages for *e.g.* catalyst stability,[7] and alternate mechanistic pathways *vs.* those in electrocatalytic processes.[2,8]

With respect to the nature of molecular catalysts, [NiFe]–carbon monoxide dehydrogenase ([NiFe]CODH)[9–11] underscores the advantages conferred by synergistic effects between metal centres for selective CO_2 conversion.[9,12] Consequently, various CODH-inspired dinuclear catalysts have been developed,[4,6,11,13] in which cooperative effects lead to improved overpotential requirements, selectivity, turnover numbers (TONs) and turnover frequencies (TOFs).[6,9] In most of these synthetic systems—as for CODH—the second metal enhances CO_2 reduction through its role as a Lewis acid.[6,14] However, the neighbouring metal of binuclear complexes can affect small molecule chemistry in other ways, *e.g.* by tuning redox properties.[15] Multinuclear systems can also enable another bifunctional strategy for photocatalytic processes involving combination of a catalyst and photosensitizer within a single complex. This latter strategy – which has mainly been explored in supramolecular complexes[16]—can result in accelerated electron transfer and reaction rates, as well as improved catalyst durability.

In light of the above, we have now examined the electro- and photocatalytic activity of a bimetallic Cu/Fe–Mabiq complex ((Mabiq = 2–4 : 6–8-bis(3,3,4,4-tetramethyldihydropyrrolo)-10–15-(2,2′-biquinazolino)-[15]1,3,5,8,10,14-hexaene-1,3,7,9,11,14-N_6)), and compared its activity to that of our monometallic Fe–Mabiq compound. Our macrocyclic Fe–Mabiq complex [Fe(Mabiq)-$(MeCN)_2$]$^+$ (**1**, Chart 1) selectively reduces CO_2 to CO electrocatalytically with a good overpotential requirement of only 500 mV.[17] We showed that electron and proton uptake by the Mabiq ligand is a unique feature of our catalyst and contributes to selective CO formation. The Mabiq ligand offers a valuable platform to probe the influence of a neighbouring metal centre on catalysis due to the second metal binding site. We therefore synthesized the heterobimetallic [Cu(Xantphos)Fe(Mabiq)-$(OTf)_2$] (**2**, Chart 1), to assess the influence of the Cu site on electrocatalytic CO_2 reduction. Furthermore, we examined photocatalytic CO_2 reduction by both **1** (in this case, [Fe(Mabiq)-$(MeCN)_2$]OTf, containing triflate as the counter ion) and **2**, to probe how the compounds perform under such conditions. Slight differences are observed between the electro- and photocatalytic pathways, and pronounced differences between the mono- and bimetallic compounds. The Cu centre influences CO_2 reduction by the Fe centre in varied ways, not only through electrostatic effects.

The bimetallic **2** was prepared by adding a solution of the Cu-precursor [Cu(Xantphos)(OTf)] (**3**) to a solution of **1** in THF

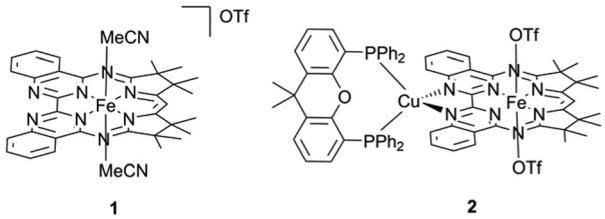

1 2

Chart 1 Overview of the complexes **1** and **2**.

[a] *Department of Chemistry and Catalysis Research Center (CRC), Technical University of Munich, Garching 85748, Germany*
[b] *Faculty of Chemistry and Pharmacy, University of Regensburg, Regensburg 93053, Germany. E-mail: corinna.hess@ur.de*

† Electronic supplementary information (ESI) available: Synthesis procedures, NMR, XRD, UV-Vis, GC and CV data. CCDC 2284733 and 2284734. For ESI and crystallographic data in CIF or other electronic format see DOI: https://doi.org/10.1039/d3cc04777f

and its successful formation was confirmed by NMR, (Fig. S1–S9, *vide infra*, ESI†). The molecular structure of **2** confirms the expected tetrahedral geometry at the Cu^{I} centre and shows a six-coordinate ferrous centre, with triflate bound in an axial position (Fig. S10 and Tables S1–S3, ESI†). The solution state NMR exhibits clear shifts of the Mabiq and Xantphos proton signals (Fig. S9, ESI†). The ^{31}P NMR signal is also slightly shifted down-field (Fig. S4 and S7, ESI†) in comparison to that of **3**. Although the mono- and the bimetallic complexes exhibit very similar UV-Vis spectra (Fig. S11, ESI†) in MeCN, their IR spectra are distinctive (Fig. S12, ESI†). Both the NMR and IR spectroscopy thus indicate that **2** remains intact in solution (see ESI† for details, Fig. S13).

Cyclic voltammetry (CV) reveals the effect of the Cu–Xantphos centre on the redox potentials of the Fe–Mabiq unit (Fig. 1a). The $Fe^{III/II}$ couple of **2** is only slightly shifted anodically by 20 mV, whereas more substantial shifts are observed for the reductive events. The first two reductions are each shifted anodically by 150 mV, while the final reductive event occurs at 400 mV more positive for **2** (Table S4, ESI†). As the first two reductions of our Mabiq complexes are ligand-centred,[17,18] coordination of the outer metal ion likely modulates the electron density on the ligand, and is consistent with the differences observed in the NMR spectra (*vide supra* and see Fig. S9, ESI†).

Since complex **1** can reduce CO_2 electrocatalytically, we investigated the analogous reactivity of **2** toward CO_2, likewise using PhOH as the proton source. A marked difference is observed in the activity of the bi- *vs.* the monometallic complex, particularly with respect to formation of a reactive intermediate. We had previously observed a proton-dependent shift of the second reductive event (the *formal* $Fe^{I/0}$ couple) of **1** upon addition of PhOH—both in the presence and absence of CO_2. We assigned this behaviour to the formation of an intermediate species, $\mathbf{I_{PhOH}}$, in which the Mabiq ligand becomes protonated at the diketiminate carbon.[17] However, a similar proton-dependent shift of the formal $Fe^{I/0}$ couple is not observed for **2** (Fig. 1b and Fig. S14, ESI†). Occupation of the second binding site by the Cu–Xantphos moiety renders the ligand less nucleophilic. CO_2 reduction by **2** must thus proceed *via* a different mechanism than we had proposed for **1**—one that does not involve $\mathbf{I_{PhOH}}$. Both complexes have a similar overpotential requirement since a three-electron input (starting from the Fe^{II} form) is also required for CO_2 activation by **2**. However, **1** achieves a significantly higher current density with a peak current of −0.34 mA, compared to **2**, which only reaches a peak current of −0.083 mA (Fig. 1c and d). The apparent lower activity may be partly due to the fact that the beneficial proton-shuttling pathways conferred by $\mathbf{I_{PhOH}}$ are not available to **2**.[17] However, during bulk electrolysis experiments with **2** (at $-1.84\ V_{Fc}$) we observed the formation of a Cu-mirror on the working electrode, which indicates instability of the bimetallic complex under the electrocatalytic conditions. Stability issues also would affect performance and precluded more detailed analysis of the electrocatalytic mechanism.

We hence turned toward the photocatalytic reduction of CO_2. Stability issues in electrocatalysis are often mitigated in photocatalysis,[7] and in some cases different mechanistic pathways operate.[2,8] $[Ru(bpy)_3](PF_6)_2$ (**Ru–PS**) was used as the photosensitizer (PS) and 1,3-dimethyl-2-phenyl-2,3-dihydro-1*H*-benzo[*d*]imidazole (BIH) served as the sacrificial electron donor (SED). The reduction potential of $\mathbf{Ru–PS^-}$ ($E(\mathbf{Ru–PS}^{0/-}) = -1.71\ V_{Fc}$)[7] should be sufficient to generate the three-electron reduced active species of either **1** or **2** required for CO_2 reduction in the presence of PhOH, based on our CV experiments (Fig. 1c and d).[17] Under our standard photocatalysis conditions (2 μM catalyst, 200 μM **Ru–PS**, 170 μM PhOH, 100 mM BIH, 1 h irradiation at 455 nm) both complexes produced CO as the only product in excellent yields, leading to TONs of up to 16×10^3 for **1** and 24×10^3 for **2** (Table S5, ESI† and Fig. 2a) and TOFs of 4.4 s^{-1} and 6.7 s^{-1}, respectively. The values are higher than those reported for the most effective modified Fe-porphyrin complexes (TOFs *ca.* 1 s^{-1})[19] and are on the order of magnitude as photocatalytic CO_2 reduction by [Fe(tpyPY2Me)] (typPY2Me: pentadentate polypyridyl ligand, TOF of 15 s^{-1}), which is among the most efficient molecular catalysts.[7] Thus, **1** and **2** are highly effective CO_2 reduction photocatalysts, with the bimetallic performing slightly better. The performance of **2** contrasts with the electrocatalytic activity, which was hampered by its low stability.

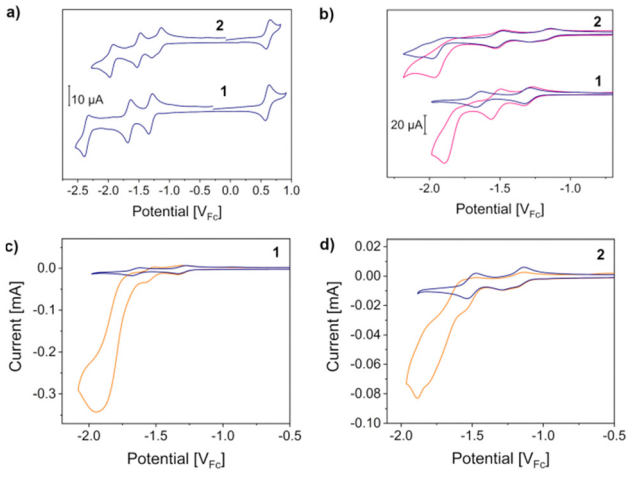

Fig. 1 (a) CV of a 0.5 mM solution of **1** (lower trace) and **2** (upper trace) under Ar; (b) CV of 0.5 mM solution of **1** (lower trace) and **2** (upper trace) before (blue) and after addition of 85 equiv. of PhOH (pink) under Ar; (c) CV of a 0.5 mM solution of **1** (blue) and in the presence of 85 equiv. PhOH and CO_2 (orange); (d) CV of a 0.5 mM solution of **2** (blue) and in the presence of 85 equiv. PhOH and CO_2 (orange). All in MeCN, 0.1 M $[(n\text{-}Bu)_4N]PF_6$, scan rate 100 mV s^{-1}.

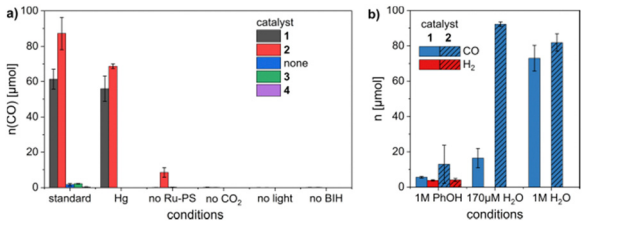

Fig. 2 (a) Amount of CO produced by **1** (black), **2** (red), **3** (green), **4** (purple) and in the absence of catalyst (blue); (b) amount of CO (blue) and H_2 (red) produced by **1** (solid columns) and **2** (dashed column), dependant on the proton source. Standard conditions (2 μM catalyst, 170 μM PhOH, 200 μM **Ru–PS**, 100 mM BIH, V_T = 2 mL purged with CO_2 for 2 min).

CO production by **1** and **2** was observed up to 3 h, after which the product formation stagnates (Fig. S15, ESI†). Replenishing experiments with fresh **Ru–PS**/BIH solution, added after 1 h of irradiation did not revive catalysis (Fig. S16, ESI†), while the addition of fresh catalyst yielded up to 49% of the amount of CO initially obtained after 1 h. The full activity was only restored by replenishing all components. Experiments with added Hg provided evidence that nanoparticles are not responsible for the reactivity (Fig. 2a and Table S5, ESI†). Controls in the absence of light, CO_2 or BIH showed negligible CO formation, such that all are essential for photocatalytic CO_2 reduction. The control experiments also confirmed CO_2 as the product source (Fig. S17, ESI†) and the absence of other reduction products (see ESI† for details, Fig. S18). Using the Cu-precursor **3** or [Zn(Mabiq)(OTf)] (**4**), negligible CO formation was observed (Fig. 2a and Table S5, ESI†). In these cases, **Ru–PS** most likely acted as the photocatalyst,[20] considering the amount produced in the absence of catalyst.

Interestingly, a marked difference in activity between the two complexes was observed in the absence of **Ru–PS**. Under these conditions, **2** produced a substantial amount of CO, with a TON of up to 3×10^3. This is, to our knowledge, one of the highest TONs reported for a self-sensitized system, particularly employing earth-abundant transition metals; and in stark contrast to the behaviour of **1**.[21] Thus, although the monometallic Fe–Mabiq complex is photoactive,[22] the formation of key intermediates in the CO_2 reduction pathway still require an added photosensitizer. The Mabiq coordinated Cu–Xantphos moiety in **2** may serve as the photosensitizer under the photocatalytic conditions; [Cu(Xantphos)(Biquinoline)]$^+$ complexes are known photosensitizers.[23] The result highlights the potential for the two metals in the bimetallic Mabiq complexes to operate in a cooperative or even bifunctional manner involving a catalyst/photosensitizer combination.

We also examined the dependence of the reaction on the catalyst concentration and proton source. Lower catalyst loading often leads to higher TONs since catalyst-catalyst deactivation pathways can compete with CO_2 reduction pathways at high concentrations, or not all of the catalyst in solution is active.[24,25] Reduced catalyst loading (0.5 μM) for **1** indeed yielded a slightly higher TON. In contrast, a drop in activity was observed at lower concentrations of **2** (Table S6 and Fig. S19, ESI†), possibly due to stability issues when the bimetallic compound is diluted.[24] As expected, lower TONs were observed with increased catalyst loading for both compounds (50 μM; Table S6 and Fig. S19, ESI†). With increased [PhOH] (1 M), we also observed a significant drop in activity and selectivity (Fig. S20, ESI†), along with H_2 production. This is in accord with the previously observed, [PhOH]-dependent electrocatalytic behaviour of **1**.[17]

A substantial amount of CO was produced in the absence of PhOH (Table S7 and Fig. S20, ESI†), presumably caused by trace water. This motivated our investigation of photocatalytic CO_2 reduction with H_2O as the proton source. Approximately 80 μmol CO were produced by both **1** and **2** using 1 M H_2O, similar to the amounts produced at low [PhOH] (170 μM PhOH; Table S7, ESI† and Fig. 2b). Based on our electrocatalytic studies, CO_2 reduction by our Fe–Mabiq complexes occurs at lower potentials in the presence of water *vs.* PhOH (Fig. S21 and 22, $E_{onset} = -2.02$ V_{Fc} (**1**), $E_{onset} = -1.75$ V_{Fc} (**2**) in the presence of H_2O; $E_{onset} = -1.6$ V_{Fc} for **1** and **2** in the presence of PhOH, ESI†). The Cu site in **2** shifts the catalytic onset potential 270 mV more positive than that of **1**. Nonetheless, **Ru–PS**$^-$ ($(E(\mathbf{Ru–PS}^{0/-}) = -1.71$ $V_{Fc})$) would not have enough reducing power to drive the reaction with water as a proton source for either catalyst. However, the highly acidic BIH$^{\bullet+}$—the species formed when BIH donates one electron—may lower the pH of the photocatalytic mixture[26] and thereby shift the onset potential required for CO_2 reduction in the presence of H_2O. Furthermore, BI$^\bullet$ which is obtained after deprotonation of BIH$^{\bullet+}$ would have a high enough reducing power ($E(BI^{+/\bullet}) = -2.055$ V_{Fc}) to drive the reaction at 1 M H_2O for both catalysts.

Surprisingly, a significant amount of CO (93 μmol) was also produced by **2** at low [H_2O] (170 μM), whereas **1** only generated 22 μmol CO (comparable to the amount in the absence of added proton source; Fig. 2b and Fig. S20 and Table S7, ESI†). The better performance of **2** *vs.* **1** may be partly attributed to the fact that at low [H_2O] BI$^\bullet$ is still a strong enough reductant for **2** but no longer for **1** ($E_{onset} = -2.2$ V_{Fc} (**1**); $E_{onset} = -1.8$ V_{Fc} (**2**); Fig. S23 and S24, ESI†). The clear differences in amounts of CO production at low H_2O concentrations, again highlight the beneficial influence of the Cu site on the reaction.

To gain initial insight into the photocatalytic process, we examined the interaction of our catalysts with the PS and with BIH. All metal–Mabiq complexes that we have generated to date are photoactive, and can be photoreduced in the presence of NEt_3.[22,27] BIH is also an effective SED for photoreduction, yielding comparable quantum yields (QYs) for **1** (8×10^{-5}) and **2** (6×10^{-5}, see ESI† for details, Fig. S25, 26 and Table S8). The QYs for the photoreduction in the presence of both BIH and **Ru–PS** (Fig. S27, 28 and Table S8, ESI†) were one order of magnitude higher (7×10^{-4} for **1** and 4×10^{-4} for **2**) than with BIH alone. Electron transfer from **Ru–PS**$^-$ to **1** or **2** thus also can take place. A doubly reduced metal–Mabiq species could not be observed. However, this *formal* Fe^0 species (*i.e.*, [Fe^{II}(Mabiq$^{\bullet\bullet}$)]$^-$) may be too short-lived under the photoreduction conditions. Finally, we also monitored the spectral evolution under photocatalytic conditions (50 μM catalyst, 85 equiv. PhOH, 200 μM **Ru–PS**, 500 equiv. BIH). The formation of the one-electron reduced species is initially observed for both complexes. Upon longer irradiation **1** exhibits the spectrum of our $\mathbf{I_{PhOH}}$, the electrocatalytic intermediate previously observed (Fig. S29, ESI†).[17] $\mathbf{I_{PhOH}}$ is therefore also implicated as an intermediate in photocatalysis by **1**. The formation of $\mathbf{I_{PhOH}}$ was not observed after continued irradiation of the solution containing **2** (Fig. S30, ESI†), as expected based on the electrochemical studies (Fig. 1b and Fig. S14, ESI†). The result confirms that the Cu centre alters the CO_2 reduction pathway.

Further studies are warranted to obtain a detailed mechanistic picture. However, based on our findings, we propose the following preliminary catalytic cycles (Scheme 1). Under photocatalytic conditions the first reduction (formal Fe$^{II/I}$) can occur either *via* reductive quenching of the excited state of **1** or **2** by BIH (Scheme 1 right path) or *via* electron transfer from **Ru–PS**$^-$ or BI$^\bullet$ to the complex (Scheme 1 left path). A subsequent electron transfer yields the formal Fe^0 species. $\mathbf{I_{PhOH}}$ is formed

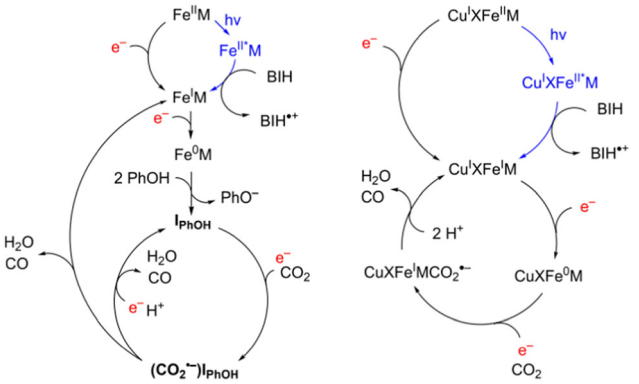

Scheme 1 Proposed mechanistic pathway for photocatalytic CO_2 reduction by **1** and **2** with PhOH as proton source; M = Mabiq and X = Xantphos. The oxidation states given are formal oxidation states. Both BI• ($E(BI^{+/\bullet}) = -2.055$ V_{Fc}) and **Ru–PS** ($E(\textbf{Ru–PS}^{0/-}) = -1.71$ V_{Fc}) can act as reductants where e^- is denoted.

by **1** in the presence of PhOH, with CO release occurring as previously described for electrocatalytic CO_2 reduction.[17] In contrast, CO_2 reduction by **2** does not involve $\mathbf{I_{PhOH}}$ (*vide supra*).

In conclusion, the performance of our new Cu/Fe–Mabiq complex in photocatalytic CO_2 reduction reveals that occupation of the outer Mabiq binding site with Cu–Xantphos leads to altered redox-properties and impedes Mabiq protonation. Although the Mabiq ligand of **2** may not provide a proton relay during CO_2 reduction, its photocatalytic activity is better than that of **1**. Intriguingly, the bimetallic compound can photocatalytically produce CO in a self-sensitized manner in admirable yields. Thus, the Cu site affects both electrostatic and photochemical properties. The studies are promising for further development of discrete bimetallic photocatalysts.

Funding was provided by the German Research Foundation (DFG, EXC 2089/1 – 390776260 and 426785626).

Conflicts of interest

There are no conflicts to declare.

Notes and references

1 H. B. Gray, *Nat. Chem.*, 2009, **1**, 7; S. Berardi, S. Drouet, L. Francàs, C. Gimbert-Suriñach, M. Guttentag, C. Richmond, T. Stoll and A. Llobet, *Chem. Soc. Rev.*, 2014, **43**, 7501–7519.
2 C. Steinlechner, A. F. Roesel, E. Oberem, A. Päpcke, N. Rockstroh, F. Gloaguen, S. Lochbrunner, R. Ludwig, A. Spannenberg, H. Junge, R. Francke and M. Beller, *ACS Catal.*, 2019, **9**, 2091–2100.
3 K. E. Dalle, J. Warnan, J. J. Leung, B. Reuillard, I. S. Karmel and E. Reisner, *Chem. Rev.*, 2019, **119**, 2752–2875; H. Takeda, C. Cometto, O. Ishitani and M. Robert, *ACS Catal.*, 2017, **7**, 70–88.
4 E. Boutin, L. Merakeb, B. Ma, B. Boudy, M. Wang, J. Bonin, E. Anxolabéhère-Mallart and M. Robert, *Chem. Soc. Rev.*, 2020, **49**, 5772–5809.
5 D. R. Whang and D. H. Apaydin, *ChemPhotoChem*, 2018, **2**, 148–160.
6 J.-W. Wang, D.-C. Zhong and T.-B. Lu, *Coord. Chem. Rev.*, 2018, **377**, 225–236.
7 P. De La Torre, J. S. Derrick, A. Snider, P. T. Smith, M. Loipersberger, M. Head-Gordon and C. J. Chang, *ACS Catal.*, 2022, **12**, 8484–8493.
8 S. Fernández, F. Franco, C. Casadevall, V. Martin-Diaconescu, J. M. Luis and J. Lloret-Fillol, *J. Am. Chem. Soc.*, 2020, **142**, 120–133; S. Grau, M. Schilling, D. Moonshiram, J. Benet-Buchholz, S. Luber, A. Llobet and C. Gimbert-Suriñach, *ChemSusChem*, 2020, **13**, 2745–2752.
9 H. Chen, L. Chen, G. Chen, M. Robert and T.-C. Lau, *Chem. Phys. Chem.*, 2021, **22**, 1835–1843.
10 T. Kojima, *ChemPhotoChem*, 2021, **5**, 512–520.
11 R. M. Bullock, J. G. Chen, L. Gagliardi, P. J. Chirik, O. K. Farha, C. H. Hendon, C. W. Jones, J. A. Keith, J. Klosin, S. D. Minteer, R. H. Morris, A. T. Radosevich, T. B. Rauchfuss, N. A. Strotman, A. Vojvodic, T. R. Ward, J. Y. Yang and Y. Surendranath, *Science*, 2020, **369**, eabc3183; H.-L. Wu, X.-B. Li, C.-H. Tung and L.-Z. Wu, *Chem. Commun.*, 2020, **56**, 15496–15512.
12 J.-H. Jeoung and H. Dobbek, *Science*, 2007, **318**, 1461–1464.
13 C. Su, Z. Chen, Q. Feng, F. Wei, A. Mo, H.-H. Huang, H. Hu, H. Zou, F. Liang and D. Liu, *Dalton Trans.*, 2023, **52**, 4548–4553.
14 D. Hong, T. Kawanishi, Y. Tsukakoshi, H. Kotani, T. Ishizuka and T. Kojima, *J. Am. Chem. Soc.*, 2019, **141**, 20309–20317; D. Liu, M. Zhang, H.-H. Huang, Q. Feng, C. Su, A. Mo, J.-W. Wang, Z. Qi, X. Zhang, L. Jiang and Z. Chen, *ACS Sustainable Chem. Eng.*, 2021, **9**, 9273–9281; T. Ouyang, H.-H. Huang, J.-W. Wang, D.-C. Zhong and T.-B. Lu, *Angew. Chem., Int. Ed.*, 2017, **56**, 738–743; E. A. Mohamed, Z. N. Zahran and Y. Naruta, *Chem. Commun.*, 2015, **51**, 16900–16903.
15 A. H. Reath, J. W. Ziller, C. Tsay, A. J. Ryan and J. Y. Yang, *Inorg. Chem.*, 2017, **56**, 3713–3718; C. Matlachowski and M. Schwalbe, *Dalton Trans.*, 2015, **44**, 6480–6489.
16 Y. Tamaki and O. Ishitani, *ACS Catal.*, 2017, **7**, 3394–3409; J.-W. Wang, Z. Li, Z.-M. Luo, Y. Huang, F. Ma, S. Kupfer and G. Ouyang, *Proc. Natl. Acad. Sci. U. S. A.*, 2023, **120**, e2221219120.
17 K. Rickmeyer, L. Niederegger, M. Keilwerth and C. R. Hess, *ACS Catal.*, 2022, **12**, 3046–3057.
18 P. Banerjee, A. Company, T. Weyhermüller, E. Bill and C. R. Hess, *Inorg. Chem.*, 2009, **48**, 2944–2955; M. Kaspar, P. J. Altmann, A. Pöthig, S. Sproules and C. R. Hess, *Chem. Commun.*, 2017, **53**, 7282–7285; E. V. Puttock, P. Banerjee, M. Kaspar, L. Drennen, D. S. Yufit, E. Bill, S. Sproules and C. R. Hess, *Inorg. Chem.*, 2015, **54**, 5864–5873.
19 E. Pugliese, P. Gotico, I. Wehrung, B. Boitrel, A. Quaranta, M.-H. Ha-Thi, T. Pino, M. Sircoglou, W. Leibl, Z. Halime and A. Aukauloo, *Angew. Chem., Int. Ed.*, 2022, **61**, e202117530.
20 E. Cuéllar, L. Pastor, G. García-Herbosa, J. Nganga, A. M. Angeles-Boza, A. Diez-Varga, T. Torroba, J. M. Martín-Alvarez, D. Miguel and F. Villafañe, *Inorg. Chem.*, 2021, **60**, 692–704.
21 K. Kamada, J. Jung, Y. Kametani, T. Wakabayashi, Y. Shiota, K. Yoshizawa, S. H. Bae, M. Muraki, M. Naruto, K. Sekizawa, S. Sato, T. Morikawa and S. Saito, *Chem. Commun.*, 2022, **58**, 9218–9221; H. Rao, J. Bonin and M. Robert, *Chem. Commun.*, 2017, **53**, 2830–2833; A. V. Müller, L. A. Faustino, K. T. de Oliveira, A. O. T. Patrocinio and A. S. Polo, *ACS Catal.*, 2023, **13**, 633–646.
22 R. Lauenstein, S. L. Mader, H. Derondeau, O. Z. Esezobor, M. Block, A. J. Römer, C. Jandl, E. Riedle, V. R. I. Kaila, J. Hauer, E. Thyrhaug and C. R. Hess, *Chem. Sci.*, 2021, **12**, 7521–7532.
23 B. J. McCullough, B. J. Neyhouse, B. R. Schrage, D. T. Reed, A. J. Osinski, C. J. Ziegler and T. A. White, *Inorg. Chem.*, 2018, **57**, 2865–2875.
24 N. P. Liyanage, W. Yang, S. Guertin, S. Sinha Roy, C. A. Carpenter, R. E. Adams, R. H. Schmehl, J. H. Delcamp and J. W. Jurss, *Chem. Commun.*, 2019, **55**, 993–996.
25 Z. Guo, S. Cheng, C. Cometto, E. Anxolabéhère-Mallart, S.-M. Ng, C.-C. Ko, G. Liu, L. Chen, M. Robert and T.-C. Lau, *J. Am. Chem. Soc.*, 2016, **138**, 9413–9416.
26 Y. Pellegrin and F. Odobel, *C. R. Chimie*, 2017, **20**, 283–295.
27 H. S. Stark, P. J. Altmann, S. Sproules and C. R. Hess, *Inorg. Chem.*, 2018, **57**, 6401–6409; O. Z. Esezobor, W. Zeng, L. Niederegger, M. Grübel and C. R. Hess, *J. Am. Chem. Soc.*, 2022, **144**, 2994–3004.

ChemComm

ROYAL SOCIETY OF CHEMISTRY

CORRECTION

Check for updates

Cite this: DOI: 10.1039/d4cc90124j

Correction: Influence of a neighbouring Cu centre on electro- and photocatalytic CO_2 reduction by Fe-Mabiq

Kerstin Rickmeyer,[ab] Matthias Huber[ab] and Corinna R. Hess *[ab]

DOI: 10.1039/d4cc90124j

rsc.li/chemcomm

Correction for 'Influence of a neighbouring Cu centre on electro- and photocatalytic CO_2 reduction by Fe-Mabiq' by Kerstin Rickmeyer *et al.*, *Chem. Commun.*, 2024, **60**, 819–822, https://doi.org/10.1039/D3CC04777F.

In determining the amount of CO produced by our Fe–Mabiq complexes, **1** and **2** ([Fe(Mabiq)(MeCN)$_2$]OTf and [Cu(Xantphos)Fe(Mabiq)(OTf)$_2$], respectively), an error was made in the calculations. The amount of CO produced by the reported catalysts, and therefore the TON_{CO} and TOF_{CO} values, are lower than originally reported in our manuscript. The corrected values and corresponding revised statements in the manuscript are as follows:

Under the reported standard photocatalysis conditions (2 μM catalyst, 200 μM **Ru-PS**, 170 μM PhOH, 100 mM BIH, 1 h irradiation at 455 nm) **1** and **2** produced CO as the only product in good yields, with TONs of 663 ± 61 for **1** and 942 ± 98 for **2** (the updated Fig. 2a is shown herein, and an amended Table S5 is provided in the update to the original ESI) and TOFs of 0.18 s^{-1} and 0.26 s^{-1}, respectively. The values are lower than the ones reported by Chang and co-workers for photocatalytic CO_2 reduction by [Fe(tpyPY2Me)] (tpyPY2Me: pentadentate polypyridyl ligand, TOF of 15 s^{-1}).[1] However, the values are still better than those reported for the most efficient Fe–porphyrin complexes under similar conditions (MeCN as solvent; TOF 0.013 s^{-1}).[2]

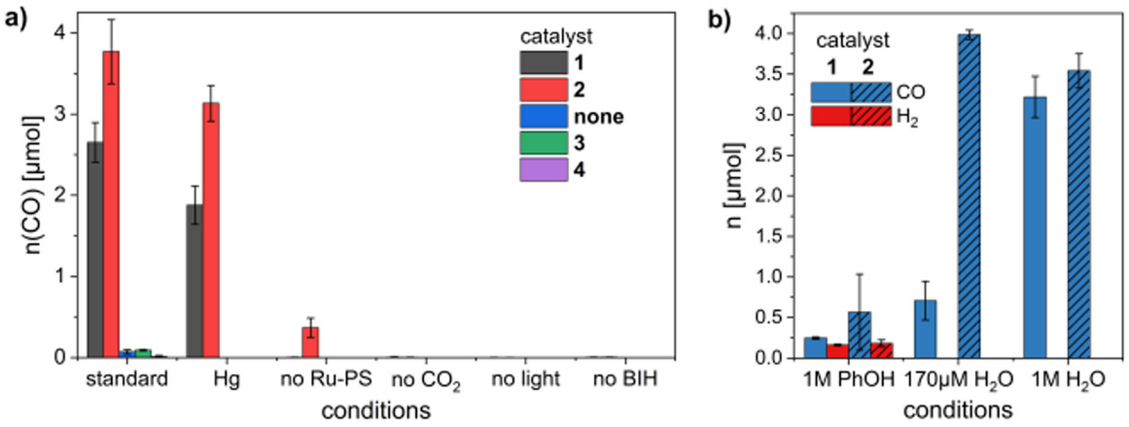

Fig. 2 (a) Amount of CO produced by **1** (black), **2** (red), **3** (green) and **4** (purple) and in the absence of catalyst (blue); (b) amount of CO (blue) and H_2 (red) produced by **1** (solid columns) and **2** (dashed columns), dependent on the proton source. Standard conditions (2 μM catalyst, 170 μM PhOH, 200 μM **Ru-PS**, 100 mM BIH, V_T = 2 mL purged with CO_2 for 2 min).

The CO produced by **2** in the absence of the $[Ru(bpy)_3]^{2+}$ photosensitizer (**Ru-PS**) corresponds to a TON of 92 ± 30, which is one of the highest TONs reported for a self-sensitized system employing earth-abundant transition metals.[1,3,4]

[a] *Department of Chemistry and Catalysis Research Center (CRC), Technical University of Munich, Garching 85748, Germany*
[b] *Faculty of Chemistry and Pharmacy, University of Regensburg, Regensburg 93053, Germany. E-mail: corinna.hess@ur.de*

In the investigation of photocatalytic CO_2 reduction using H_2O as the proton source, approximately 3 μmol CO were produced by both **1** and **2** using 1 M H_2O, similar to the amounts produced at low [PhOH] (170 μM PhOH; updated Fig. 2b and Table S7 in the updated ESI). The amount of CO produced by **2** at low [H_2O] (170 μM) is 3.99 μmol, whereas **1** generated 0.7 μmol CO (updated Fig. 2b, and Fig. S20 and Table S7 in the update to the ESI).

An updated Fig. 2 depicting the results described above is shown herein. Corrected CO values under all the various conditions investigated for **1** and **2** and for control studies can be found in the update to the ESI.

We note that the relative trends reported in our original manuscript all remain the same and that the overall conclusions of this work are not affected. In particular, as originally described, the Cu site of our new Cu/Fe–Mabiq complex leads to altered redox-properties, impedes Mabiq protonation and enhances photocatalytic performance. The bimetallic compound can also photocatalytically produce CO in a self-sensitized manner in good yields.

The Royal Society of Chemistry apologises for these errors and any consequent inconvenience to authors and readers.

References

1 P. De La Torre, J. S. Derrick, A. Snider, P. T. Smith, M. Loipersberger, M. Head-Gordon and C. J. Chang, *ACS Catal.*, 2022, **12**, 8484–8493.
2 E. Pugliese, P. Gotico, I. Wehrung, B. Boitrel, A. Quaranta, M.-H. Ha-Thi, T. Pino, M. Sircoglou, W. Leibl, Z. Halime and A. Aukauloo, *Angew. Chem., Int. Ed.*, 2022, **61**, e202117530.
3 Z. Guo, S. Cheng, C. Cometto, E. Anxolabéhère-Mallart, S.-M. Ng, C.-C. Ko, G. Liu, L. Chen, M. Robert and T.-C. Lau, *J. Am. Chem. Soc.*, 2016, **138**, 9413–9416.
4 H. Rao, J. Bonin and M. Robert, *Chem. Commun.*, 2017, **53**, 2830–2833.

Conclusion and Outlook

In the first study both the Co- and Fe-Mabiq complex were tested for their ability to act as electrocatalysts for CO_2 reduction. It was shown that the Fe-Mabiq outperforms its Co-analogue both in terms of FE and overpotential requirement. A clear difference in the activity between the two compounds was observed even though the first two reductions leading to the formal 'M^0-Mabiq' (M = Fe, Co) are ligand based. The influence of the metal center on the electrochemical properties and activity in CO_2 reduction can also be found in some reports in the literature (*vide supra*). These effects vary from a change in product formation to different overpotential requirements and overall performance differences.[27,149,150] Both Mabiq complexes yielded CO as the only product. Nonetheless, a different mechanism is postulated for the two complexes based on the electrochemical data, as the Co-Mabiq requires the addition of more electrons to initiate catalysis than the Fe-Mabiq complex. This is reflected in the lower overpotential requirement of the Fe-Mabiq. Moreover, the influence of the non-innocent Mabiq ligand to not only act as an electron reservoir—a property that was also observed for redox-active ligands such as porphyrins[72] or polypyridines[18,122]—but also to take up a proton in the process could be shown. While in earlier reports the ability of Co-Mabiq to act as a "hydride-sink" might be considered a disadvantage,[53,143,144] this property proved to be advantageous for CO_2 reduction by Fe-Mabiq. The protonation of the ligand allowed for the formation of a H-bonding network, trapping the proton source in proximity to the active center. Protonation could then occur either directly via an intramolecular pathway or via an intermolecular pathway. Both mechanisms were postulated for other complexes bearing proton relay groups (Figure 9).[26,57,59–61,71,151–153] The isolated intermediate $\mathbf{I_{PhOH}}$—formed upon reaction of the doubly reduced Fe-Mabiq with two equivalents of PhOH—provides a rare example where such a hydrogen-bonding network is evidenced in the crystal structure while other reports have to rely on computational studies.[60,71] Overall, the non-innocent Mabiq ligand is a unique motif that is capable of storing both electrons and protons, thereby providing a ligand-assisted pathway for the selective reduction of CO_2 to CO.

The Mabiq ligand is unique in yet another aspect as it offers a second binding site. This led to the investigation of a heterobimetallic Cu-Xantphos-Fe-Mabiq complex as electrocatalyst for CO_2 reduction. A second metal in proximity to the active center is a common motif in nature, e.g. in [Ni,Fe]-CODH, and was thus used as inspiration by researchers with the aim to enhance catalysis.[19,46,56,63,154–157] Electrochemical studies of the Cu-Xantphos-Fe-Mabiq complex already showed marked differences between the bimetallic complex and its monometallic parent compound. The redox events were shifted to more positive potentials which is in accord with other reports of bimetallic systems.[139,158,159] The presence of the second metal at the outer binding site further led to a different mechanism for CO_2 reduction which does not involve a protonated intermediate. However, even without the beneficial proton relay the bimetallic complex exhibited a better photocatalytic activity than the monometallic Fe-Mabiq complex. It was

even possible to perform CO_2 reduction in the absence of added PS in a self-sensitized manner in good yield. Only a few fully earth-abundant complexes that catalyze the CO_2 reduction reaction without addition of a PS have been reported thus far (*vide supra*).[84,122,131] Among those, Cu-Fe-Mabiq exhibits one of the highest TONs with 92 ± 30.

Further studies are warranted to shed more light on the mechanism of CO_2 reduction by Cu-Xantphos-Fe-Mabiq and the particular role of the outer Cu center. Investigations which properties of the bimetallic complex particularly enable CO_2 reduction in the absence of PS are of great interest. Early studies have already been undertaken by M. Huber to explore the effect of modifications of the Xantphos ligand on the photophysical properties. Moreover, the second binding site could be harnessed to attach a Mabiq complex to a hetereogeneous support. This could either be an electrode to facilitate electrocatalysis or a semiconductor for enhanced photocatalysis. In collaboration with the *Stutzmann* group preliminary studies have already been undertaken investigating the interaction of the Mabiq ligand with various substrates in order to find a semiconductor with matching energy alignment for favorable electron transfer.

Zusammenfassung und Ausblick

Der erste Teil der hierin beschriebenen Studien handelt von der Untersuchung des Co- als auch des Fe-Mabiq Komplexes hinsichtlich ihrer Eignung als Elektrokatalysatoren für die Reduktion von CO_2. Der Fe-Mabiq übertrifft hierbei den Co-Komplex, sowohl bezüglich der FE, als auch des benötigten Überpotentials. Obwohl die ersten zwei Reduktionen, die zur Bildung des formalen M^0-Mabiq' (M = Fe, Co) Komplexes führen, bei beiden Komplexen ligandenbasiert sind, besteht ein deutlicher Unterschied in der Aktivität zwischen den Komplexen. Der Einfluss des Metallzentrums auf die elektrochemischen Eigenschaften und Aktivität im Zuge der elektrokatalytischen Reduktion von CO_2 wurde ebenfalls bereits in anderen Studien beobachtet (siehe oben). Diese Effekte reichen von einer Änderung der Produktselektivität über Unterschiede beim benötigten Überpotential bis zu Unterschieden bei der generellen Performance während der Katalyse.[27,149,150] Beide Mabiq Komplexe liefern CO als das einzige Produkt. Nichtsdestotrotz implizieren die elektrochemischen Daten unterschiedliche Reaktionsmechanismen für die beiden Komplexe, da im Falle des Co-Komplexes mehr Elektronen für die Initiierung der Katalyse als beim Fe-Komplex benötigt werden. Dies spiegelt sich auch in dem geringeren benötigten Überpotential beim Fe-Mabiq wider. Jedoch agiert der nicht-unschuldige Mabiq Ligand nicht nur als Elektronenreservoir – eine Eigenschaft, die unter Anderem auch bei anderen redox-aktiven Liganden wie Porphyrinen[72] oder Polypyridinen[18,122] beobachtet wurde – sondern ist obendrein in der Lage ein Proton aufzunehmen. Während diese Eigenschaft in früheren Studien als Nachteil aufgefasst werden konnte,[53,143,144] zeigt sie sich hier als vorteilhaft für die Reduktion von CO_2 mit Fe-Mabiq als Katalysator. Die Protonierung des Liganden führt zu einer Bildung eines H-Brückennetzwerks, welches in der Lage ist, die Protonenquelle in direkter Nähe zum aktiven Zentrum festzuhalten. Die Protonierung des aktivierten CO_2 kann anschließend entweder direkt über einen intramolekularen Pfad oder indirekt über einen intermolekularen Weg erfolgen. Beide Mechanismen finden sich in der Literatur für andere Komplexe mit sogenannten Proton-Relay-Gruppen (Figure 9).[26,57,59–61,71,151–153] Das Intermediat der Katalyse, $\mathbf{I_{PhOH}}$, welches bei der Reaktion des zweifach reduzierten Fe-Mabiqs mit zwei Äquivalenten der Protonenquelle PhOH gebildet wird, konnte isoliert werden. Dieses stellt ein seltenes Beispiel dar, bei dem ein solches H-Brückennetzwerk in der Kristallstruktur gezeigt werden kann, während andere Studien sich lediglich auf computerchemische Rechnungen beziehen können.[60,71] Zusammenfassend gesagt verfügt der nicht-unschuldige Mabiq Ligand über ein einzigartiges Motiv, welches ihm erlaubt sowohl Elektronen als auch Protonen zu speichern, und damit einen liganden-assistierten Reaktionspfad für die selektive Reduktion von CO_2 zu CO bietet.

Der Mabiq Ligand ist in einer weiteren Hinsicht einzigartig. Er verfügt über eine zweite Bindungsstelle. Diese Tatsache inspirierte die Untersuchung von heterobimetallischen Cu-Xantphos-Fe-Mabiq Komplexen als Elektrokatalysatoren für die CO_2 Reduktion. Ein zweites Metall in der Nähe des aktiven Zentrums ist ein Motiv, welches häufig in der Natur gefunden werden kann, bspw. in [Ni,Fe]-CODH. Es wurde daher von einigen Wissenschaftlern als Inspiration genutzt,

um Katalysatoren weiter zu verbessern.[19,46,56,63,154–157] Bereits in ersten elektrochemischen Studien des Cu-Xantphos-Fe-Mabiq Komplexes zeigen sich deutliche Unterschiede zwischen dem bimetallischen Komplex und seinem monometallischen Mutterkomplex. Die Redoxevents des Komplexes sind alle zu positiveren Potentialen verschoben. Ein Verhalten, welches mit Berichten anderer bimetallischer Komplexe übereinstimmt.[139,158,159] Obendrein führt die Anwesenheit des zweiten Metalls an der äußeren Bindungsstelle zu einem anderen Mechanismus für die CO_2 Reduktion, welcher nun kein protoniertes Intermediat mehr beinhaltet. Obwohl dem Komplex dadurch das vorteilhafte Proton-Relay fehlt, zeigt der bimetallische Komplex eine bessere photokatalytische Aktivität als der monometallische Fe-Mabiq Komplex. Die photokatalytische CO_2 Reduktion kann außerdem in der Abwesenheit des PS, sozusagen in einer selbst-sensibilisierten Reaktion, mit guten Ausbeuten durchgeführt werden. Bisher wurden nur wenige Komplexe ohne seltene Erden publiziert, die in der Lage sind photokatalytisch CO_2 ohne Anwesenheit eines PS zu reduzieren (siehe oben).[84,122,131] Unter diesen zeigt der Cu-Fe-Mabiq eine der höchsten TONs mit 92 ± 30.

Weiterführende Studien sind nötig, um mehr Klarheit über den Mechanimus der CO_2 Reduktion durch Cu-Xantphos-Fe-Mabiq und insbesondere die Rolle des äußeren Cu-Zentrums zu erhalten. Auch Untersuchungen, die aufzeigen können, welche Eigenschaften des bimetallischen Komplexes es ihm erlauben die CO_2 Reduktion in der Abwesenheit eines PS durchzuführen, sind von höchstem Interesse. Erste Studien, die den Einfluss von Modifikationen des Xantphos Liganden auf die photophysikalischen Eigenschaften untersuchen, wurden bereits von M. Huber unternommen. Des Weiteren kann die zweite Bindungsstelle auch dafür genutzt werden, den Mabiq Liganden an einen heterogenen Untergrund zu binden. Dieser kann entweder eine Elektrode sein, um die Elektrokatalyse zu vereinfachen oder ein Halbleiter für verbesserte Photokatalyse. In Kollaboration mit der *Stutzmann* Gruppe wurden bereits erste vorläufige Studien durchgeführt, die die Interaktion des Mabiq Liganden mit verschiedenen Substraten untersucht, um einen passenden Halbleiter für optimalen Elektrontransfer zu finden.

Appendix

Supporting Information: Multifaceted role of the Noninnocent Mabiq Ligand in Promoting Selective Reduction of CO_2 to CO

The Supporting Information including additional data such as CVs, calculation of proton dependence, overpotential requirement determination, headspace analysis in controlled potential electrolysis (CPE) experiments, DFT calculations, crystallographic parameters, UV-Vis, liquid injection field desorption ionization mass spectrometry (LIFDI-MS), and IR spectra is available free of charge at https://pubs.acs.org/doi/10.1021/acscatal.1c4636.

CCDC 2111145–2111146 contains the supplementary crystallographic data for this paper. These data can be obtained free of charge via www.ccdc.ac.uk/data_request/cif, or by emailing data_request@ccdc.cam.ac.uk, or by contacting The Cambridge Crystallographic Data Centre, 12 Union Road, Cambridge CB2 1EZ, U.K.; fax: +44 1223 336033.

The Multi-Faceted Role of the Non-Innocent Mabiq Ligand in Promoting Selective Reduction of CO_2 to CO

*Kerstin Rickmeyer†, Lukas Niederegger†, Martin Keilwerth‡, Corinna R. Hess†**

† Department of Chemistry and Catalysis Research Center (CRC), Technical University of Munich, Lichtenbergstr. 4, 85748 Garching, Germany

‡ Department of Chemistry and Pharmacy, Inorganic Chemistry, Friedrich-Alexander-University Erlangen-Nürnberg (FAU), Egerlandstr. 1, 91058 Erlangen, Germany

Corresponding Author

*corinna.hess@ch.tum.de

Table of Contents

General

All chemicals were purchased from Sigma Aldrich and used without further purification unless noted otherwise. Metal compounds were synthesized in an inert atmosphere glove box (Ar), using anhydrous solvents. Dry solvents were obtained from an MBraun SPS, deoxygenated via freeze-pump-thaw cycles and stored over 3 Å (MeCN) or 4 Å activated molecular sieves. Tetrabutylammonium hexafluorophosphate ($[N(n\text{-}Bu)_4]PF_6$) was recrystallized three times from ethanol,[1] and ferrocene was sublimed prior to use. CD_3CN was purchased from Eurisotope, filtered through activated aluminum oxide (activated, standard grade, neutral, Brokmann I, 58 Å pore size), distilled, deoxygenated by freeze-pump-thaw method, stored over 3 Å molecular sieves and filtered over activated aluminum oxide once more prior to use. Carbon dioxide (5.0 purity, Westfahlen AG, Münster, Germany) was passed through a 3 Å molecular sieve drying column to remove trace water.[2] Carbon monoxide was obtained in a 3.7 purity (Westfahlen AG, Münster, Germany).

Instrumentation

Electronic spectra were measured on a Shimadzu UV-3600 Plus UV-Vis-NIR spectrophotometer or an Agilent Cary 60 UV-Vis spectrophotometer.

Solution state NMR spectra were measured on a Bruker Avance Ultrashield (400 MHz ^{1}H) or a Bruker Avance HD (300 or 400 MHz ^{13}C, respectively) spectrometer with Topspin 2.1 software. The data was analyzed using MestreNova (Mestrelab Research S.L.). Evans' method[3] was used for solution state magnetic susceptibility measurements, using THF-d_8 as the solvent and cyclohexane or toluene as standard.

Electro spray ionization mass spectrometry (ESI-MS) was performed on a LCQ-FLEET (Thermo) equipped with a 3D ion trap. The instrument is combined with preceding high performance liquid chromatography (HPLC) and two ultra-violet (UV) spectrophotometric detectors (i.e. UltiMate 3000 HPLC system, Dionex).

Microanalysis were carried out at the Technische Universität München or by Mikroanalytisches Laboratorium Kolbe.

Liquid Injection Field Desorption Ionization Mass Spectrometry (LIFDI-MS) was measured directly from an inert atmosphere glovebox with a Thermo Fisher Scientific Exactive Plus Orbitrap equipped with an ion source from Linden CMS.[4]

Infrared (IR) spectroscopy was performed in an Ar-filled glove box with a Bruker ALPHA FT-IR spectrometer with Opus/Mentor software equipped with a PLATINUM-ATR unit for analysis of solid samples or a LIQUID CELL A145 for solution samples. A concentration of 6 mM of the respective sample was used for solution state IR measurements, unless stated otherwise.

Zero-field ^{57}Fe Mössbauer spectra were recorded on a WissEl Mössbauer spectrometer (MRG-500) at 77 K in constant acceleration mode. ^{57}Co/Rh was used as radiation source. The MFit program software by E. Bill was used for the quantitative evaluation of the spectral parameters (least-square fitting to Lorentzian peaks). The temperature of the samples was controlled by an MBBC-HE0106 MÖSSBAUER He/N_2 cryostat within an accuracy of ±0.3 K. Isomer shifts were determined relative to a α-iron at 298 K.

Single crystal analysis

Crystallographic data were collected on an X-Ray single crystal diffractometer equipped with a TXS rotating anode with MoK_α radiation ($\lambda = 0.71073$ Å), a CMOS detector (Apex III, $\varkappa$-CMOS) and a Helios optic using the Apex III software package.[5] The measurements were performed on single crystals overlaid with perfluorinated ether. A suitable crystal was transferred to the diffractometer on top of a kapton micro sampler. The measurements were carried out at 100 K using a nitrogen stream. Initial lattice parameters were determined by a matrix scan. Reflections were corrected for Lorentz and polarization effects, scan speed, and background using SAINT.[6] Absorption corrections, including odd and even ordered spherical harmonics were performed using SADABS.[6] Space group assignments were based upon systematic absences, E statistics, and successful refinement of the structures. Structures were solved by SHELXT[7] with the aid of successive difference Fourier maps, and were refined against all data using SHELXL-2018[8] in conjunction with SHELXLE.[9] Hydrogen atoms were assigned to ideal positions and refined using a riding model with an isotropic thermal parameter 1.2 times that of the attached carbon atom (1.5 times for methyl hydrogen atoms). If not mentioned otherwise, non-hydrogen atoms were refined with anisotropic displacement parameters. Full-matrix least squares refinements were carried out by minimizing $\sum w(F_o^2 - F_c^2)^2$ with the SHELXL[8] weighting scheme. Neutral atom scattering factors for all atoms and anomalous dispersion corrections for the non-hydrogen atoms were taken from International Tables for Crystallography.[10] Disordered solvent molecules were treated as a diffuse contribution to the overall scattering without specific atoms positions using the PLATON/SQUEEZE procedure.[11] For **[2]**$^-$, overall 261 electrons corresponding to 3.5 residual ether molecules were determined. Images of the crystal structures were generated using Mercury.[12] CCDC 2111145 and 2111146 contains the supplementary crystallographic data for this paper.

Computational studies

Density Functional Theory (DFT) calculations were performed with the ORCA program package.[13] Geometry optimizations of the complex were performed at the B3LYP level of DFT. The all-electron Gaussian basis sets were those developed by the Ahlrich's group.[14] Triple-ζ quality basis sets (TZV(P)) with one set of polarization functions on the metals and on the atoms directly coordinated to the metal center were used.[14b, 14c] For the carbon and hydrogen atoms, slightly smaller polarized split-valence SV(P) basis sets were used that were of double-ζ quality in the valence region and contained a polarizing set of d functions on the non-hydrogen atoms. Auxiliary basis sets used to expand the electron density in the resolution-of-the-identity (RI) approach were chosen,[15] where applicable, to match the orbital basis. SCF calculations were tightly converged (1×10^{-8} E_h in energy, 1×10^{-7} E_h in the density change, and 5×10^{-7} E_h in maximum element of the DIIS error vector). Geometry optimization was carried out in redundant internal coordinates without imposing symmetry constraints. The geometry was considered converged after the energy change was less than 1×10^{-6} E_h, the gradient norm and maximum gradient element were smaller than 3×10^{-5} and 1×10^{-4} E_h Bor^{-1}, respectively, and the root-mean square and maximum displacements of all atoms were smaller than 6×10^{-4} and 1×10^{-3} Bohr, respectively. Orbital/spin density plots were created with orca_plot[13] and visualized using VMD.[16] The broken-symmetry (BS) approach has been described previously.[17] The label BS(*n*,*m*) denotes *n* spin up electrons and *m* spin down electrons. As both approaches – the unrestricted Kohn-Sham (UKS) and the BS approach – gave similar final single point energies and orbital natures, the molecular orbitals (MOs) obtained from the BS(3,1) DFT calculation were used. To generate the MO diagram the quasi-restricted orbitals (QROs) were used for doubly occupied orbitals whereas corresponding orbitals (UCOs) were used for the depiction of the single occupied molecular orbitals (SOMOs).

The ^{57}Fe Mößbauer isomer shift was obtained from DFT calculation by applying the following equation: $\delta = \alpha(\rho - C) + \beta$ with $\alpha = -0.298$, $\beta = 1.118$ and $C = 11580$ for B3LYP with a TZVP basis.[18]

Synthesis

HMabiq,[19] [Co(Mabiq)(THF)]PF_6 (**[1]**$^+$)[20] as well as the Fe-complexes [Fe(Mabiq)$(MeCN)_2$]PF_6 (**[2]**$^+$)[21] and [Fe(Mabiq)] (**[2]**^{0})[21] were synthesized as previously described.

Na(OEt_2)[Fe(Mabiq)] (**[2]**$^-$) was synthesized by stirring [Fe(Mabiq)] (**[2]**^{0}) (25 mg, 41.8 μmol) with 2 equiv. Na (1.9 mg, 83.6 μmol) in 5 mL dry and deoxygenated THF in an Ar-filled glove box for 17 h. The solution color turned from turquoise to blue during the reaction. The solution was filtered through celite and the solvent was removed under reduced pressure. Single crystals suitable for XRD were obtained by slow evaporation of a concentrated solution of Na(OEt_2)[Fe(Mabiq)] in diethylether yielding 20.3 mg (70%) of dark violet crystals.

LIFDI-MS: [Na[Fe(Mabiq)]]$^+$ (*m*/*z*: 620.2026, calc. 620.2075), [Fe(Mabiq)]$^+$ (*m*/*z*: 597.2162, calc. 597.2178); elemental analysis calcd. (%) for $C_{37}H_{43}N_8FeNaO$: C, 63.98; H, 6.24; N, 16.13 found C, 63.50; H, 6.27; N, 15.98; UV-Vis [λ_{max}, nm (ε, $M^{-1}cm^{-1}$), in THF]: 395 (1.6 x 10^4), 616 (1.5 x 10^4), 697 (6.3 x 10^3), 768 (6.6 x 10^3), 940 (6.0 x 10^3).

Electrochemical studies

Cyclic Voltammetry

Cyclic Voltammetry was carried out with a BioLogic SP200 potentiostat with EC-Lab software, using 3 mm diameter glassy carbon disk electrodes (PalmSens, Houten Netherlands) as working and counter electrodes. Prior to use, electrodes were polished with 0.05 μm alumina suspensions (CH Instruments Inc., USA). $Ag/AgNO_3$ (10 mM $AgNO_3$ and 0.1 M $[N(n\text{-}Bu)_4]PF_6$ in MeCN) was used as the reference electrode, separated via a Vycor 3535 frit (Advanced Glass & Ceramics, Holden, MA). CV measurements were performed in a five-necked glass cell under an Ar atmosphere. For measurements under CO_2 or CO atmosphere, the solution was purged with the respective gas for 5 min and the cell was kept under that atmosphere during the experiment. Unless noted otherwise, a scan rate of 100 mV/s was applied. Potentials are reported with reference to an internal standard of ferrocenium/ferrocene ($Fc^{+/0}$, given by V_{Fc}).

Differential Pulse Voltammetry

Differential Pulse Voltammetry (DPV) was carried out with a BioLogic SP200 potentiostat with EC-Lab software using the same set-up as for CV measurements. A pulse height (P_H) of 25 mV, a pulse width (P_w) of 300 ms, a step height (S_H) of −2 mV, a step (S_T) of 600 ms and a sampling time of 120 ms was used for all experiments.

Bulk electrolysis

Bulk electrolysis was performed in a custom-made H-cell adapted from Elgrishi et al.,[22] where the working and counter compartment are separated from each other via a fine porous glass frit (POR 4). $Ag/AgNO_3$ (10 mM $AgNO_3$ and 0.1 M $[N(n\text{-}Bu)_4]PF_6$ in MeCN) was used as the reference electrode, separated from the solution via a Vycor 3535 frit (Advanced Glass & Ceramics, Holden, MA). A glassy carbon plate (35 mm x 10 mm x 3 mm, HTW Germany) served

as the working electrode and Pt mesh was used as the counter electrode. For all bulk electrolysis experiments, 4 mL of a 500 μM solution of the respective complex with 43 mM PhOH and 0.1 M $[N(n\text{-}Bu)_4]PF_6$ in dry, deoxygenated MeCN were added to the working compartment, and 3 mL of electrolyte solution (0.1 M $[N(n\text{-}Bu)_4]PF_6$ in dry, deoxygenated MeCN) were added to the counter compartment of the cell under inert gas. The solution was purged with CO_2 for 10 min. In experiments using the isotopically labelled $^{13}CO_2$, the time was reduced to 5 minutes and CD_3CN was used instead of MeCN to allow direct analysis of the solution by ^1H and ^{13}C-NMR. Controlled Current Electrolysis (CCE) was performed on a BioLogic SP200 potentiostat with EC-Lab software whereas Controlled Potential Electrolysis (CPE) was carried out using an EmStat 3+ (PalmSens, Houten Netherlands) potentiostat.

For headspace analysis of gaseous products, the cell was sealed with gas-tight septa and a 5 mL headspace sample was removed using a gas-tight syringe. The sample was directly injected into the gas-chromatograph (SRI 8610C Gas Chromatograph), and analyzed using a thermal conductivity (TCD) and a flame ionization detector equipped with a methanizer (FID-M). The detectors were calibrated using standard gas mixtures of CO in N_2 (AirProducts) and dilutions of H_2 or CO with N_2, respectively. In order to quantify the amount of CO produced, the headspace volume of the cell was determined. The amount of CO generated in the reaction (n_{CO}) was calculated as follows:

$$n_{CO} = \frac{x_{CO} \times V_h}{V_M} \quad (1)$$

where x_{CO} is the measured amount of CO in ppm, V_h is the headspace volume of the cell, and $V_M = 24{,}471\ \frac{L}{mol}$ describes the molar volume. All experiments were carried out in at least triplicate. The turn-over number (TON) corresponding to the headspace sample taken at the end

of the bulk electrolysis after 1 h was calculated according to equation (2), where $n_{catalyst}$ represents the amount of catalyst in [mol] used for the experiment and n_{CO} being the CO produced after bulk electrolysis as derived using equation (1):

$$TON = \frac{n_{CO}}{n_{catalyst}} \tag{2}$$

Faradaic efficiencies were calculated according to equation (3) using the Faraday constant = $96485.5332\ \frac{C}{mol}$, the amount of CO produced, n_{CO}, in [mol], and the charge, Q, in [C]; the latter value was determined by integrating the respective chronopotentiogram.

$$FE = \frac{n_{CO} \times 2F}{Q} \times 100 \tag{3}$$

Spectroelectrochemistry (SEC) was carried out by performing a standard bulk electrolysis experiment as described above. A 200 μL aliquot of the of the bulk electrolysis sample was diluted with 1.8 mL THF in an air-tight cuvette, and the spectrum was recorded. Generally, an absorption spectrum was measured prior to bulk electrolysis and after 10 min, 30 min and 1 h, respectively.

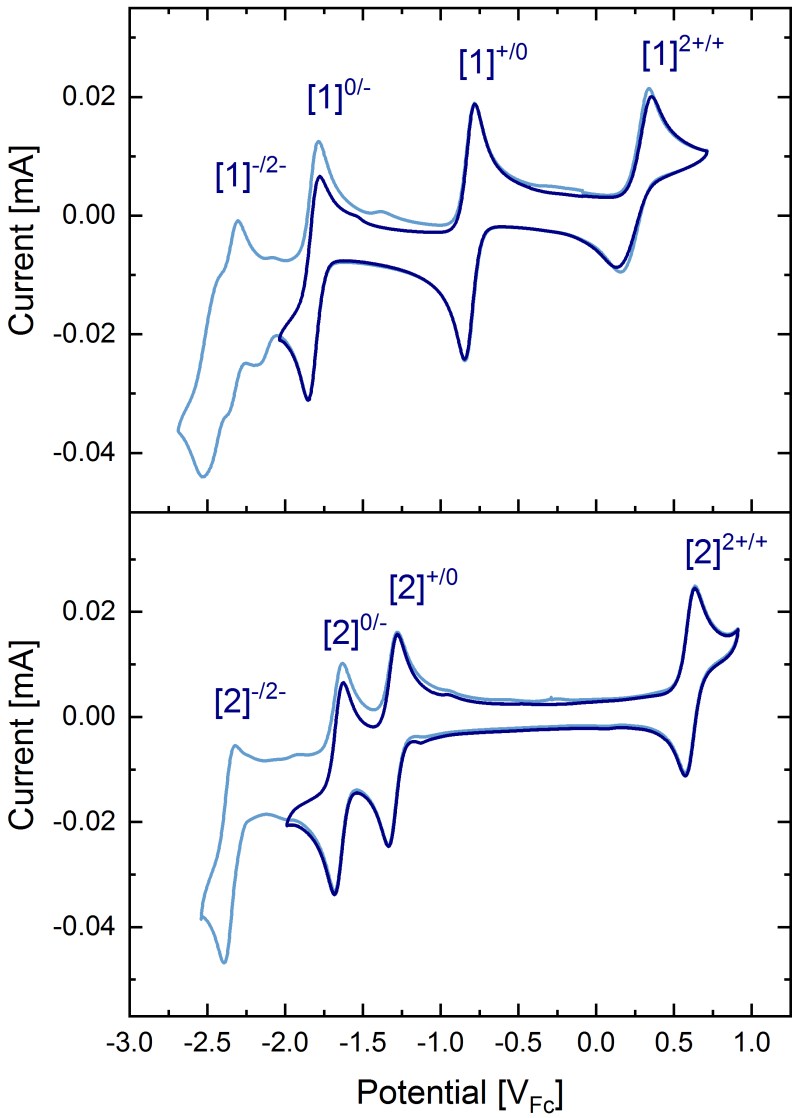

Figure S1. Cyclic Voltammograms of a 1 mM solution of **[1]**$^{+}$ (top) or **[2]**$^{+}$ (bottom) under Ar in MeCN; 0.1 M [N(*n*-Bu)$_4$]PF$_6$; MeCN; 100 mV/s scan rate.

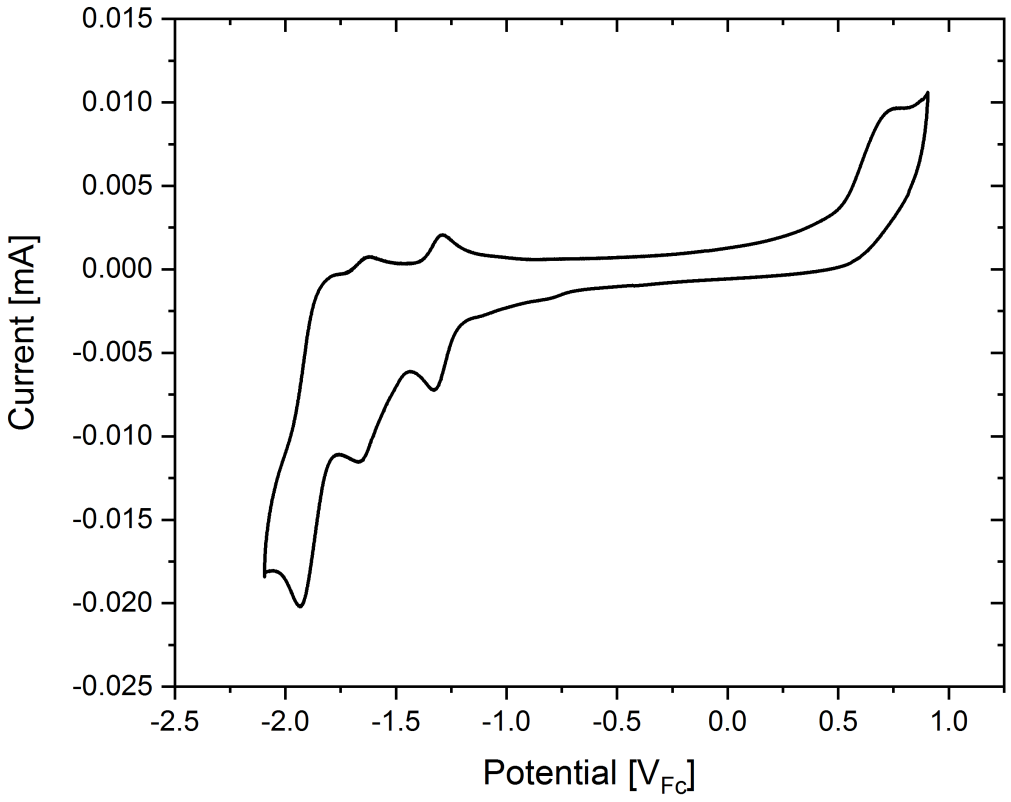

Figure S2. CV of a 1 mM solution of [Zn(Mabiq)(OTf)] under Ar in MeCN; 0.1 M $[N(n\text{-}Bu)_4]PF_6$; MeCN; 100 mV/s scan rate.[23] The $E_{1/2}$ for the first two reductions are as follows: $E_{1/2}([Zn(Mabiq)]^{+/0}) = -1.308\ V_{Fc}$ and $E_{1/2}([Zn(Mabiq)]^{0/-}) = -1.643\ V_{Fc}$.

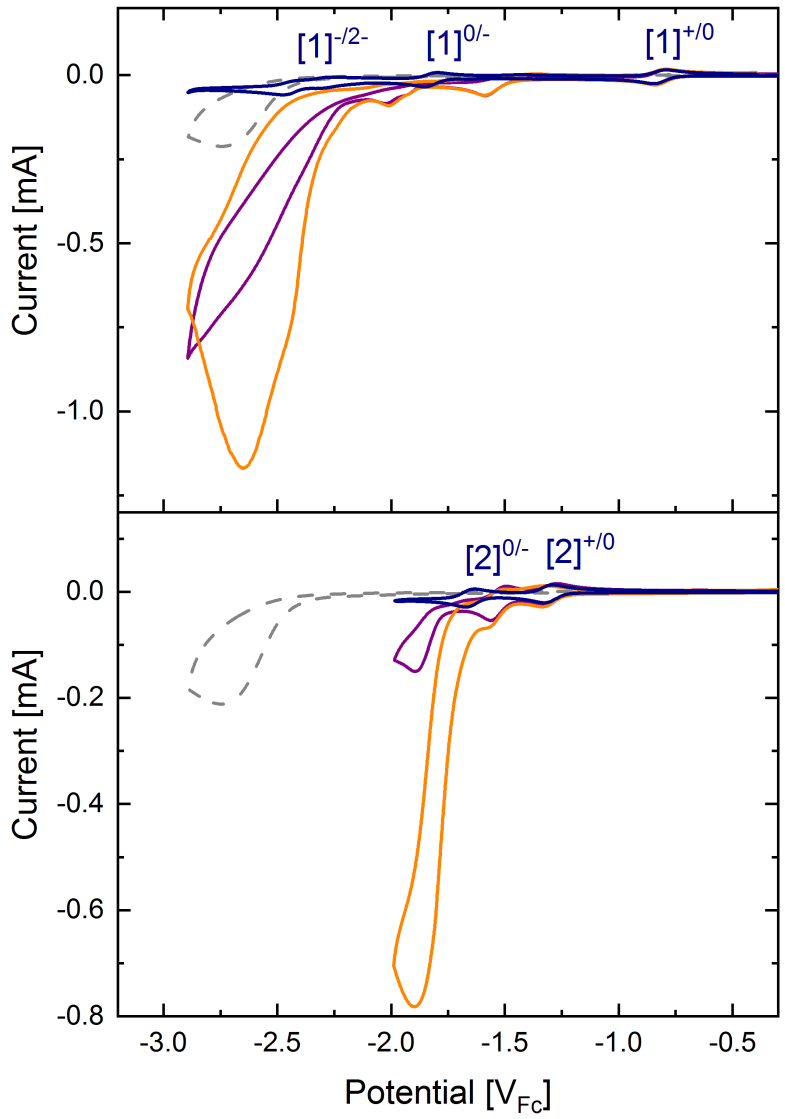

Figure S3. CV of a 1 mM solution of **[1]**$^{+}$ (top) or **[2]**$^{+}$ (bottom) in MeCN (0.1 M [N(*n*-Bu)$_4$]PF$_6$, 100 mV/s scan rate). Dark blue: under Ar; Purple: in the presence of 85 mM PhOH; Orange: with subsequent addition of CO_2. The background CV of PhOH in MeCN is shown by the grey dashed line.

Proton dependence of the redox couples of $[1]^+$ and $[2]^+$

Varying equivalents of PhOH were added to a 1 mM solution of **[1]**$^+$ and **[2]**$^+$, respectively, to assess the proton dependence of the **[X]**$^{0/-}$ couple (X = **1** or **2**). The respective CVs both in the presence and absence of CO_2 are shown below.

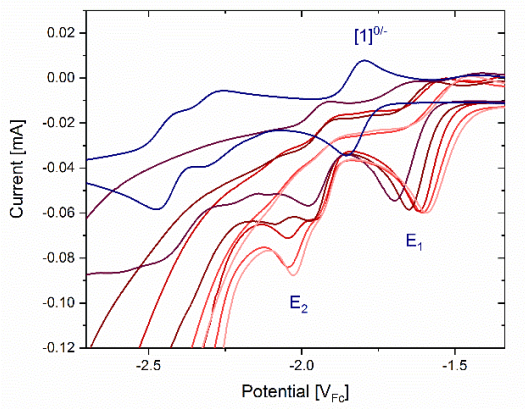

Figure S4. Addition of varying equivalents of PhOH to a 1 mM solution of **[1]**$^+$ in MeCN (0.1 M $[N(n\text{-}Bu)_4]PF_6$, 100 mV/s scan rate). Blue: **[1]**$^+$ only; Dark to light red: consecutive titration with 10, 25, 50, 75 and 85 equiv. of PhOH.

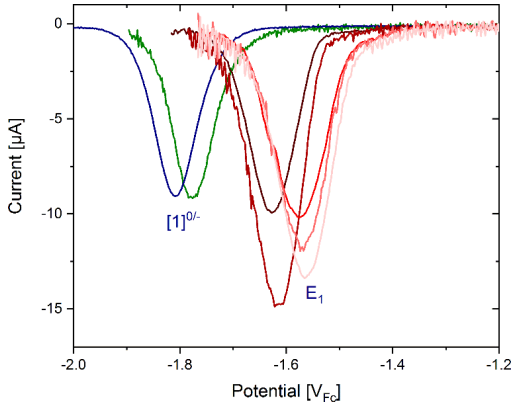

Figure S5. DPV measurements upon addition of varying equivalents of PhOH to a 1 mM solution of **[1]**$^+$ in MeCN (0.1 M $[N(n\text{-}Bu)_4]PF_6$, P_H = 25 mV, P_w = 300 ms, S_H = -2 mV, S_T = 600 ms). Blue: **[1]**$^+$ only under Ar; Green: under CO_2 atmosphere; Dark to light red: consecutive titration of the CO_2 saturated solution of **[1]**$^+$ with 10, 25, 50, 75 and 85 equiv. of PhOH.

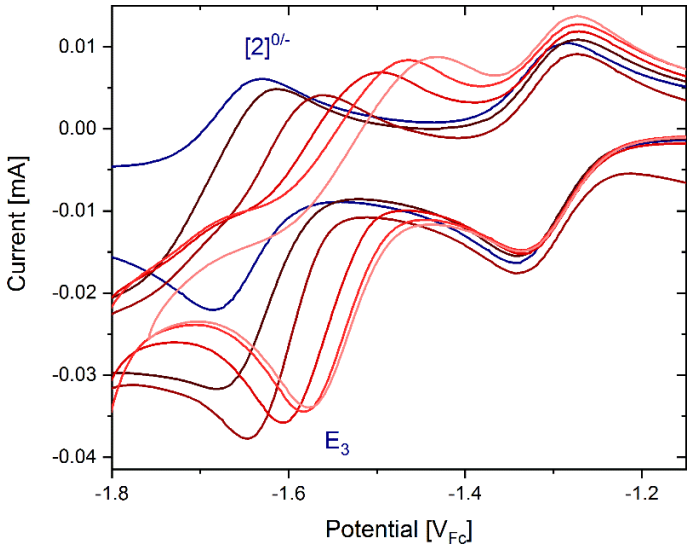

Figure S6. Addition of varying equivalents of PhOH to a 1 mM solution of **[2]**$^{+}$ in MeCN (0.1 M [N(*n*-Bu)$_4$]PF$_6$, 100 mV/s scan rate). Blue: **[2]**$^{+}$ only; Dark to light red: consecutive titration with 10, 25, 50, 75 and 85 equiv. of PhOH.

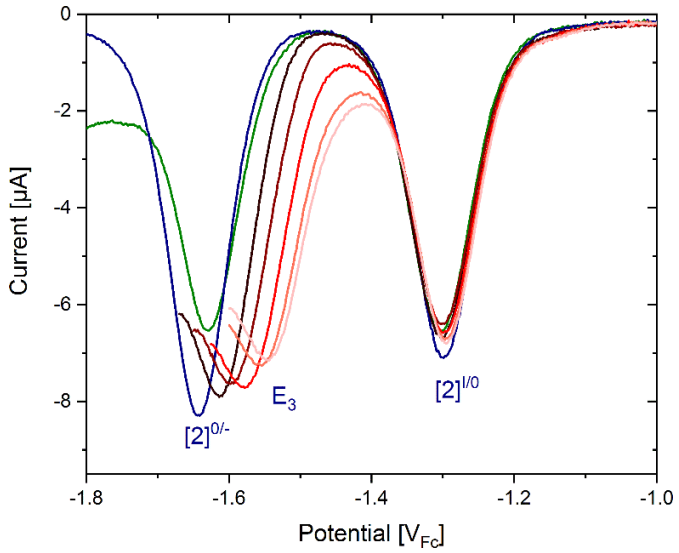

Figure S7. DPV measurements upon addition of varying equivalents of PhOH to a 1 mM solution of **[2]**$^{+}$ in MeCN (0.1 M [N(*n*-Bu)$_4$]PF$_6$, P_H = 25 mV, P_w = 300 ms, S_H = -2 mV, S_T = 600 ms). Blue: **[2]**$^{+}$ only under Ar; Green: under CO_2 atmosphere; Dark to light red: consecutive titration of the CO_2 saturated solution of **[2]**$^{+}$with 10, 25, 50, 75 and 85 equiv. of PhOH.

The phenol dependence of the redox processes were subsequently established using the equations described by Cometto et al.[24]

The apparent redox potential in the presence of PhOH of the $\mathbf{[X]^{0/-}}$ couple is related to $E^0(\mathbf{[X]^{0/-}})$ via the following equation (4) with the gas constant $R = 8.314$ J K^{-1} mol^{-1}, the temperature $T = 298.15$ K, the Faraday constant $F = 96485.33$ C mol^{-1}, the number of PhOH molecules (n) involved and the apparent binding equilibrium constant K.

$$E^0_{app} = E^0\left(\left[X^{0/-}\right]\right) + \frac{RT}{F}\ln(1 + K[PhOH]^n) \tag{4}$$

Rearranging the equation gives:

$$e^{\frac{F}{RT}(E^0_{app} - E^0([X]^{0/-})} = 1 + K[PhOH]^n \tag{5}$$

The fits for the $[PhOH]^n$ dependence (n = 1 or 2) both in the presence and absence of CO_2 of the $\mathbf{[X]^{0/-}}$ couple are shown below. For the CVs in the presence of only PhOH the couples were reversible, such that the $E_{1/2}$ values could be obtained from the CVs. In the presence of CO_2, differential pulse voltammograms (DPVs) were measured instead due to the irreversibility of the redox event.

Table S1. E_{app} used for the $[PhOH]^n$ dependence analysis.

	E_{app} [V_{Fc}]			
[PhOH] [mM]	$\mathbf{[1]^+}$ under Ar	$\mathbf{[1]^+}$ under CO_2	$\mathbf{[2]^+}$ under Ar	$\mathbf{[2]^+}$ under CO_2
10	−1.658	−1.626	−1.647	−1.612
25	−1.607	−1.616	−1.604	−1.600
50	−1.560	−1.580	−1.550	−1.578
75	−1.534	−1.568	−1.525	−1.554
85	−1.523	−1.562	−1.515	−1.546

For complex **[1]**$^{+}$ (Figure S8-9) the proton-dependent shift of the **[1]**$^{0/-}$ couple is in good agreement with the calculated values, assuming a one-electron and two-proton step. The same holds true for the **[2]**$^{0/-}$ couple of complex **[2]**$^{+}$ (Figure S10-11), where a better fit also is obtained for n = 2 molecules of PhOH.

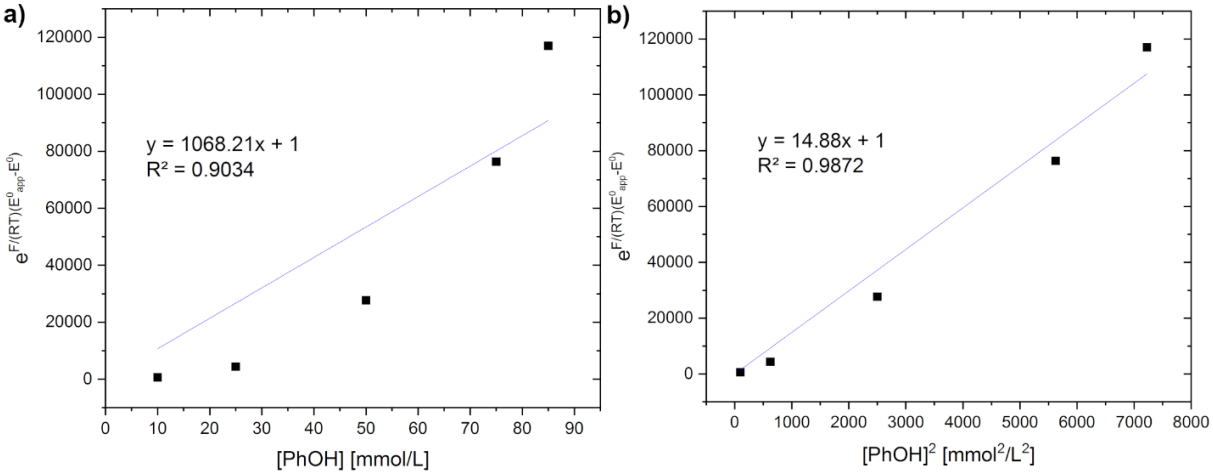

Figure S8. $e^{\frac{F}{RT}(E^0_{app}-E^0([1]^{0/-})}$ as a function of [PhOH] (**a**) and [PhOH]² (**b**) of the titration of **[1]**$^{+}$ with PhOH under an Ar atmosphere.

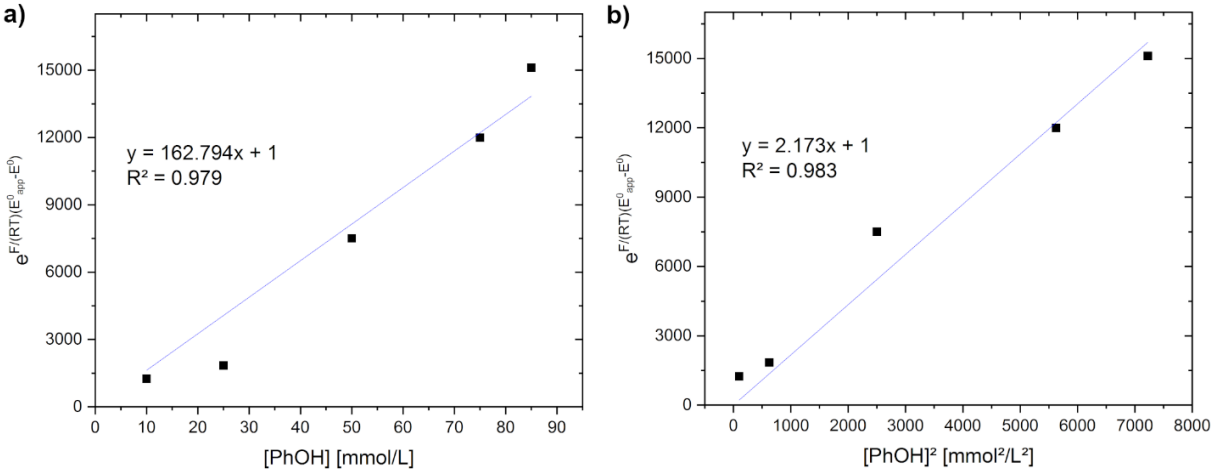

Figure S9. $e^{\frac{F}{RT}(E^0_{app}-E^0([1]^{0/-})}$ as a function of [PhOH] (**a**) and [PhOH]² (**b**) of the titration of **[1]**$^{+}$ in the presence of CO_2.

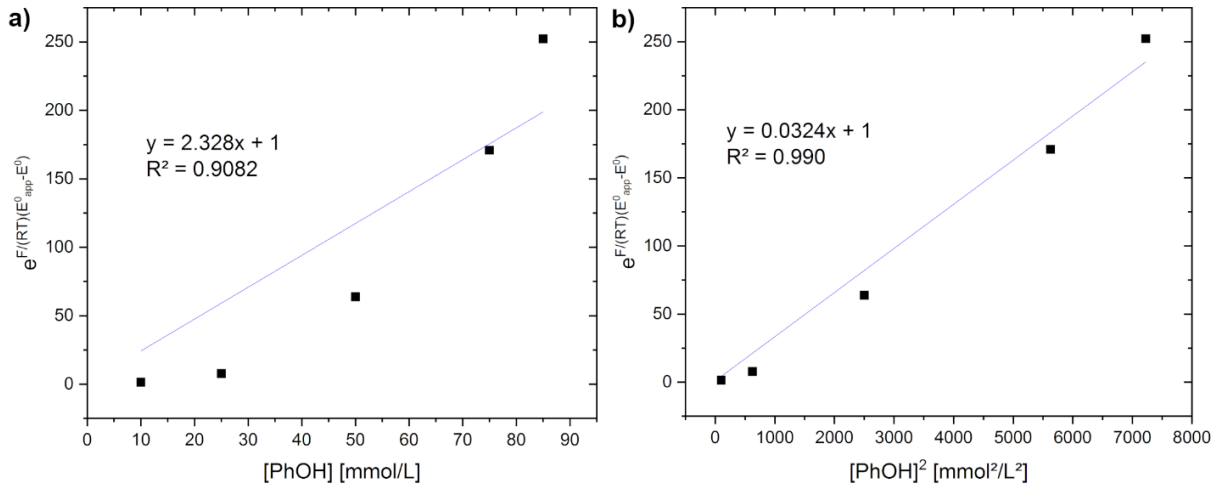

Figure S10. $e^{\frac{F}{RT}(E^0_{app}-E^0([2]^{0/-})}$ as a function of [PhOH] (**a**) and [PhOH]² (**b**) of the titration of **[2]**⁺ with PhOH under an Ar atmosphere.

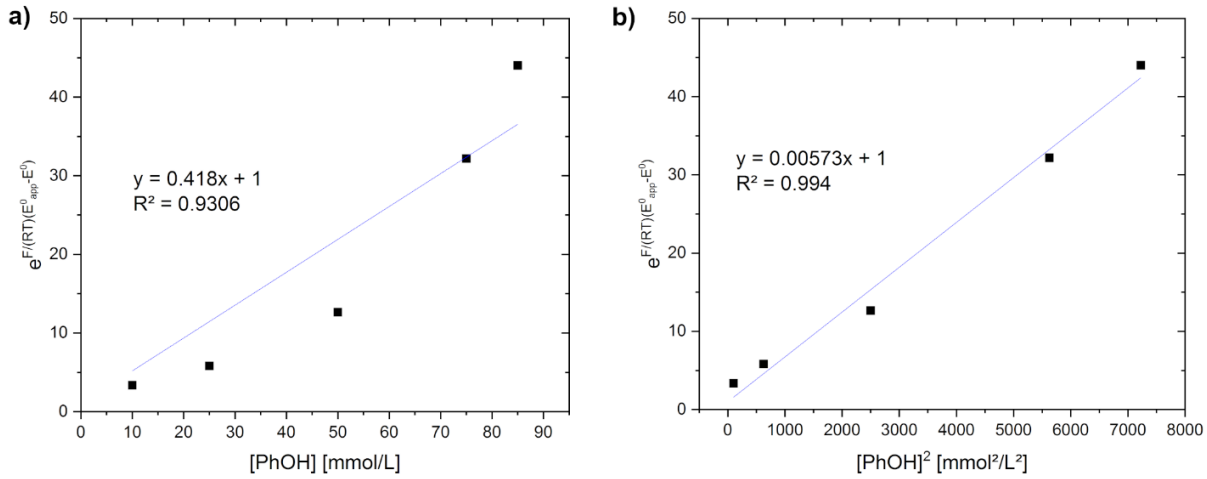

Figure S11. $e^{\frac{F}{RT}(E^0_{app}-E^0([2]^{0/-})}$ as a function of [PhOH] (**a**) and [PhOH]² (**b**) of the titration of **[2]**⁺ with PhOH in the presence of CO_2.

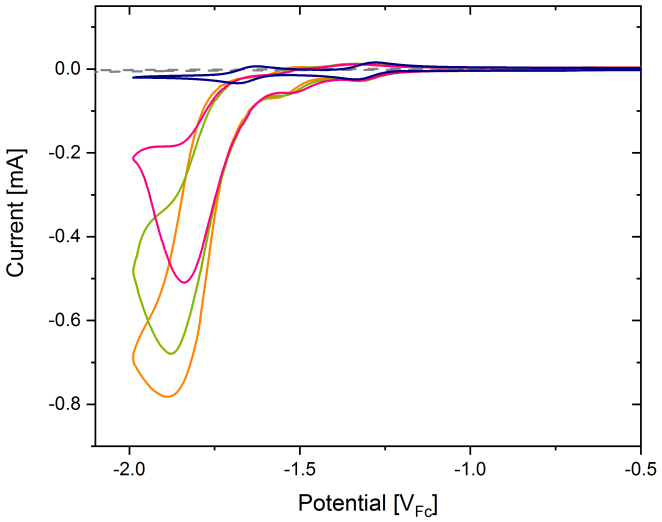

Figure S12. CV of a 1 mM solution of **[2]**$^{+}$ under Ar atmosphere (blue); in the presence of CO_2 and 85 equiv. PhOH (orange); in the presence of CO_2 and 100 equiv. PhOH (green); or in the presence of CO_2 and 172 equiv. PhOH (pink). CVs were carried out in MeCN, 0.1 M [N(*n*-Bu)$_4$]PF_6, 100 mV/s scan rate.

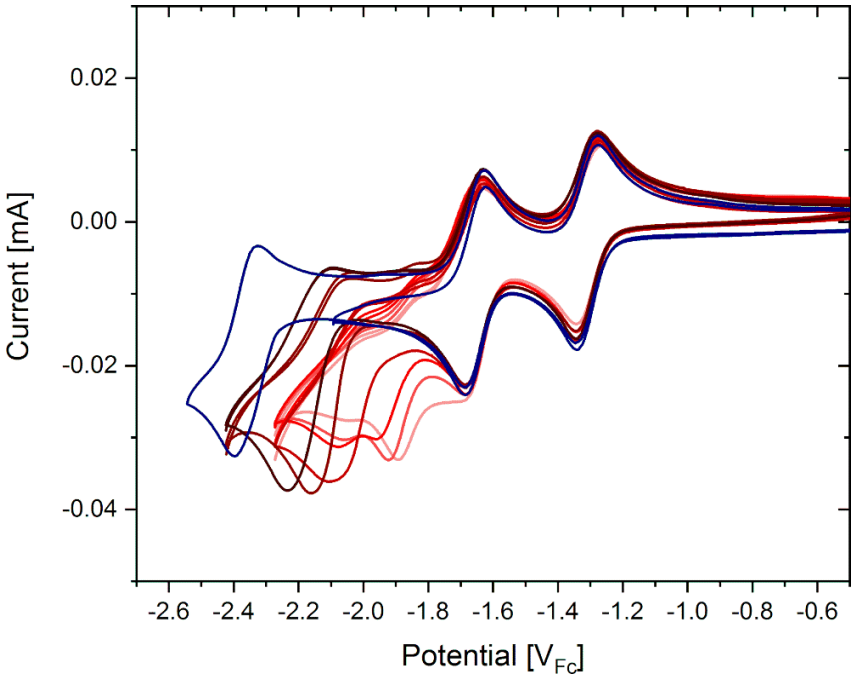

Figure S13. Addition of varying equivalents of trifluoroethanol (TFE) to a 1 mM solution of **[2]**$^{+}$ in MeCN (0.1 M $[N(n\text{-}Bu)_4]PF_6$, 100 mV/s scan rate). Blue: **[2]**$^{+}$ only; Dark to light red: consecutive titration with 10, 25, 50, 75, 100 and 150 equiv. TFE.

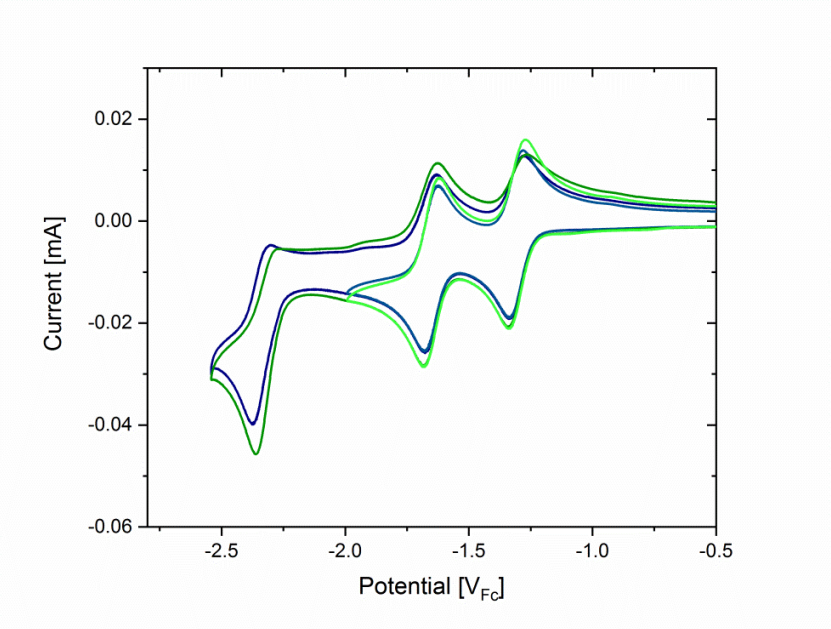

Figure S14. CV of a 1 mM solution of **[2]**$^{+}$ in MeCN (0.1 M [N(*n*-Bu)$_4$]PF$_6$, 100 mV/s scan rate). Blue: **[2]**$^{+}$ only; Lime green: in the presence of 100 mM anisol; Green: in the presence of 100 mM anisol, but upon scanning to lower potential.

CPE experiments

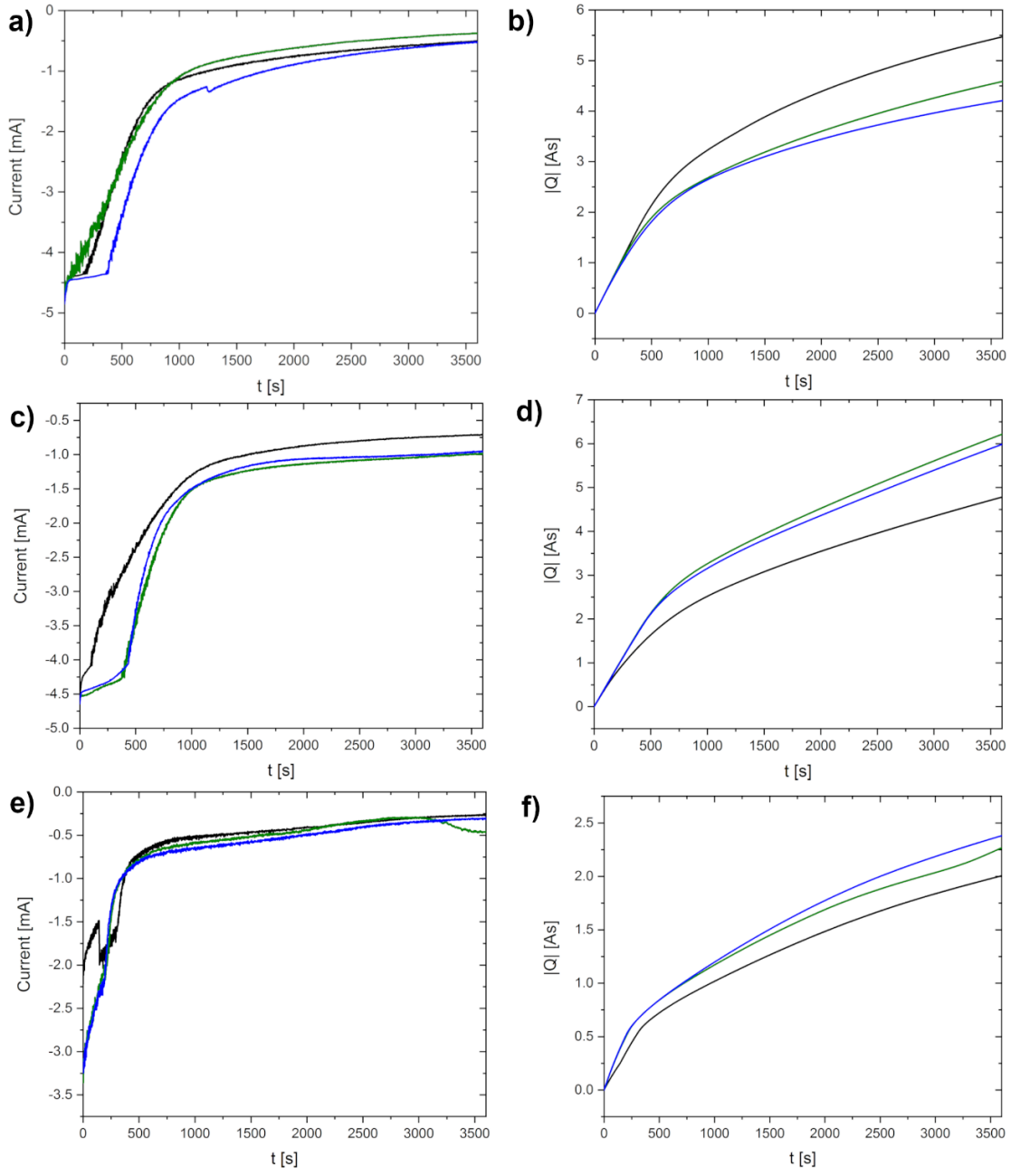

Figure S15. Current (**a,c,e**) and charge (**b,d,f**) over time plots for CPE of **[2]**$^{+}$ at −1.84 V_{Fc} (**a,b**) and −2.1 V_{Fc} (**c,d**) and of **[1]**$^{+}$ at −2.34 V_{Fc} (**e,f**). Triplicate measurements are depicted by the black, blue and green traces. General conditions for CPE experiments: 0.5 mM catalyst, 43 mM PhOH, 0.28 M CO_2 in 0.1 M [N(*n*-Bu)$_4$]PF_6 in dry and deoxygenated MeCN.

Table S2. Headspace analysis results after bulk electrolysis of **[1]**$^+$ or **[2]**$^+$.

Catalyst	E_{CPE} [V_{Fc}]	CO			H_2		
		n [μmol]	TON	FE [a] [%]	n [μmol]	TON	FE [%]
[1]$^+$ [b]	−2.34	6.5 ± 0.8	3.2 ± 0.4	37 ± 2	0.7 ± 0.2	0.36 ± 0.08	4 ± 1
[1]$^+$ [c]	−2.34	3.9 ± 0.2	2 ± 0.1	34 ± 3	*n.d.*	*n.d.*	*n.d.*
[2]$^+$ [c]	−1.84	20 ± 1	10 ± 1	84 ± 6	*n.d.*	*n.d.*	*n.d.*
[2]$^+$ [c]	−2.1	21 ± 2	11 ± 1	84 ± 1	*n.d.*	*n.d.*	*n.d.*
No [d]	−2.34	0.088 ± 0.007	—	1 ± 0.5	0.2 ± 0.3	—	3 ± 4
[1]$^+$ **no CO_2** [e]	−2-34	0.2 ± 0.06	0.1 ± 0.03	0.5 ± 0.1	28 ± 6	14 ± 3	65 ± 14
[2]$^+$ **no CO_2** [e]	−1.84	0.012 ± 0.007	(6 ± 4) × 10^{-3}	0.11 ± 0.07	4.3 ± 0.5	2.2 ± 0.3	40 ± 5

General conditions: 43 mM PhOH in 0.1 M [N(*n*-Bu)$_4$]PF_6 in MeCN.

n.d. = below detection limit of TCD

a) uncorrected FEs are displayed here. The corrected FEs, which take into account the initial electrons to generate the active species as well as the background current, are shown in Table S3

b) 500 μM catalyst, 0.28 M CO_2,[25] electrolysis for 2h;

c) 500 μM, 0.28 M CO_2,[25] electrolysis for 1h;

d) 0.28 M CO_2,[25] electrolysis for 2h;

e) electrolysis for 2h

From the CV it can be concluded that prior to catalysis, either three electrons ($\mathbf{[1]^+}$) or two electrons ($\mathbf{[2]^+}$) must be added to the M^{2+}-Mabiq complex to generate the pre-catalytic species. Since only ten turnovers are achieved by $\mathbf{[2]^+}$ throughout the bulk electrolysis period, and for $\mathbf{[1]^+}$ only three turnovers, the initial electrons required to generate the active species account for at least 10% of the charge passed. Furthermore, subtraction of the background current—which corresponds to the current passed in the presence of CO_2 and phenol but the absence of catalyst, when no catalysis takes place—yields the corrected charge Q_{corr}. Note that the background current for at –2.34 V_{Fc} was determined in the absence of PhOH. Using the corrected charges for the calculations, faradaic efficiencies of 60 ± 6% (47 ± 4% without background correction) for $\mathbf{[1]^+}$ and 96 ± 11% (93 ± 9% without background correction) for $\mathbf{[2]^+}$ are achieved. Since the catalytic wave is broad, CPE was also conducted for $\mathbf{[2]^+}$ at a lower potential (E_{CPE} = –2.1 V_{Fc}). At this potential CO was also the sole product obtained with FE = 84 ± 1% (uncorrected) and FE = 92 ± 7% (with and 90 ± 6% without background correction).

Table S3. Charge passed during CPE experiments and corrected charge, taking into account the initial electrons required for formation of the pre-catalytic species and the background current of the electrode, along with the corresponding Faradaic efficiencies.

Catalyst	E_{CPE} [V_{Fc}]	|Q| [C]	$\|Q_{corr}\|$ [C]	$\|Q_{corr}'\|$ [C]	FE(CO) [%]	FE_{corr}(CO) [%]	FE_{corr}' (CO) [%]
[1]$^+$	−2.34	2.2 ± 0.2	1.6 ± 0.2[a)]	1.3 ± 0.3[c)]	34 ± 3	47 ± 4[a)]	60 ± 6[c)]
[2]$^+$	−1.84	4.8 ± 0.5	4.4 ± 0.5[b)]	4.3 ± 0.5[d)]	84 ± 6	93 ± 9[b)]	96 ± 11[d)]
[2]$^+$	−2.1	5.6 ± 0.6	5.3 ± 0.6[b)]	5.1 ± 0.6[e)]	84 ± 1	90 ± 6[b)]	92 ± 7[e)]

General conditions: 500 μM catalyst, 0.28 M CO_2, 43 mM PhOH in 0.1 M [N(*n*-Bu)$_4$]PF_6 in MeCN, electrolysis for 1h

a) Assuming three electrons are initially required to generate the active species
b) Assuming two electrons are initially required to generate the active species
c) Assuming three electrons are initially required to generate the active species and a background current of 0.4 ± 0.1 C
d) Assuming two electrons are initially required to generate the active species and a background current of 0.12 ± 0.01 C
e) Assuming two electrons are initially required to generate the active species and a background current of 0.15 ± 0.02 C

Determination of $E^0_{CO2/CO,MeCN}$

For the conversion of applied potentials into overpotentials (η) we referred to the method reported by Azcarate et al.[25] Based on this method 1 M solutions of CO_2 and CO under standard conditions were used as standard states. The standard potential $E^0_{CO2/CO,MeCN,HA}$ for the reduction of CO_2 to CO in MeCN (solvent, S) in the presence of the acid HA is given by the following equation:

$$E^0_{CO_2/CO,MeCN,HA} = E_{L,S} + E^0_{CO_2/CO,aq} - \frac{RTln10}{F} pK_{a,HA,S} - \frac{RT}{2F} \times ln\left(\frac{K_{h,CO,S\rightarrow g}}{K_{h,CO_2,S\rightarrow g}}\right) - \frac{\left(2\Delta G^0_{t,H^+,S\rightarrow aq} - \Delta G^0_{t,H_2O,S\rightarrow aq}\right)}{2F} \quad (6)$$

with the various parameters as follows: $E^0_{CO_2/CO,aq}$= –0.106 $V_{SHE,}$[26] $E_{L,S}$= 0.099 V for MeCN as solvent S,[27] $\Delta G^0_{t,H^+,S\rightarrow aq}$= –0.475,[27] $\Delta G^0_{t,H_2O,S\rightarrow aq}$= –0.242,[28] $K_{h,CO_2,S\rightarrow g}$= 3.6[25] and $K_{h,CO,S\rightarrow g}$= 400.[25]

This leads to the following expression for $E^0_{CO_2/CO,MeCN,HA}$:

$$E^0_{CO_2/CO,MeCN,HA} = 0.287 - \frac{RTln10}{F} pK_{a,MeCN} \text{ in } V_{SHE}\ ^{25} \quad (7)$$

Although phenol is the proton source used in the electrocatalytic reaction, as per the approach of Azcarate et al. it is not considered the strongest acid present in solution. In the presence of even small amounts of water—which is also generated in the reaction—CO_2 is considered the strongest acid present in solution ($pK_a(CO_2)$ = 17.03 vs. pK_a(PhOH) = 29.14 in MeCN).[25, 29] Applying the previous equation for $E^0_{CO2/CO}$ described by Azcarate et al., and using the $pK_a(CO_2)$, $E^0_{CO2/CO}$ = –0.72 V_{SHE} = –1.34 V_{Fc} is derived.[25]

Work by the Artero group further presented a parameter which denotes when homoconjugation of an acid needs to be taken into consideration.[30]

$$\kappa = K_c c_{HA} \tag{8}$$

If $\kappa > 1$ (where κ depends on the association constant of the acid K_c and its concentration c_{HA}), the effect of homoconjugation cannot be neglected. Phenol has an association constant of K_c = 104.2,[1] which together with the concentration of c_{HA} = 43 mM gives κ = 681.5. Therefore, homoconjugation should be taken into account.

The equilibrium electrode potential for CO_2 to CO reduction during bulk electrolysis when homoconjugation of the acid is taken into account can be approximated using the method and equations reported by Matsubara,[31] as summarized below.

$$E^{eq} \approx E^0 + \frac{RT}{F}\ln(K_C) + \frac{RT}{2F} ln\left[\frac{8}{r^3}\frac{c_{CO}^{eq}(c_{AH}^*)^2}{(c_X^*)^3}\frac{D_{CO}(D_{AHA^-})^2}{\sqrt{(D_X)^3(D_{AH})^2 D_{CO_2}}}(c_{AH}^*)^2\right] \tag{9}$$

c_i^* is the molar concentration of the species i in the bulk solution, D_i is the diffusion coefficient of species i, c_i^{eq} is the molar concentration of species i in equilibrium with the species in the gas phase at 1 bar, and r is the ratio of the diffusion-convection layer thickness (δ) of substrates to the reaction-diffusion layer thickness (μ) for the electrocatalyst X.

$$\delta = \sqrt{\frac{D_{CO_2}}{D_X}} \cdot r \cdot \mu \tag{10}$$

The reaction-diffusion layer thickness (μ) was given as:

$$\mu = \sqrt{\frac{D_X}{2k_{max}c_{CO_2}^*}} \tag{11}$$

Following the procedure by Matsubara, k_{max} is related to the effective current density (i_{CO}), which is -9×10^{-5} A/cm^2 and -3×10^{-4} A/cm^2 for **[1]**$^+$ and **[2]**$^+$, respectively:

$$\frac{i_{CO}}{F} = \frac{c_X^* \sqrt{2k_{max} c_{CO_2}^* D_X}}{1 + e^{(E_{CPE} - E_{cat/2})\frac{F}{RT}}} \quad (12)$$

E_{CPE} is the potential applied during bulk electrolysis and $E_{cat/2}$ is the potential corresponding to the half of the catalytic peak current (tabulated in section 'TOF determination based on CPE data', page S36). Using the approximation of $\delta = 50\ \mu$m and equations 10-12, r was estimated as 10 and 1.55 for **[1]**$^+$ and **[2]**$^+$, respectively.

The diffusion coefficients of the complexes ($D_1 = 2.08 \times 10^{-5}$ cm^2/s, $D_2 = 2.2 \times 10^{-5}$ cm^2/s) were determined using the Randles-Sevcik equation (*vide infra*, section 'TOF determination based on CPE data', page S33). The concentration of the catalyst (c_X^*) is 0.5 mM, the acid concentration in the bulk solution is $c_{AH}^* = 43$ mM, c_{CO}^{eq} was reported as 9 mM and $E^0 = -1.63$ V_{Fc} in "dry" acetonitrile.[31] The diffusion coefficients for CO_2, CO and phenol in acetonitrile were estimated as reported using the Stokes-Einstein law: $D_{CO_2} = 5.2 \times 10^{-5}$ cm^2/s, $D_{CO} = 5.7 \times 10^{-5}$ cm^2/s, $D_{AH} = 2.6 \times 10^{-5}$ cm^2/s; D_{AHA^-} is smaller than D_{AH} by a factor of $2^{0.6}$.[31] With these values, E^{eq} was determined as -1.36 V_{Fc} and -1.28 V_{Fc} for **[1]**$^+$ and **[2]**$^+$, respectively, according to equation 9, where given the estimates for r, the potential has an error of ± 50 mV. The required overpotentials for **[1]**$^+$ and **[2]**$^+$ taking into account homoconjugation are therefore 0.98 ± 0.05 V_{Fc} and 0.56 ± 0.05 V_{Fc}. The values for $E^0_{CO2/CO}$ and for the overpotential requirement of **[1]**$^+$ and **[2]**$^+$ obtained are thus comparable to the values determined using the aforementioned method of Azcarate et al.

SEC-UV-Vis experiments

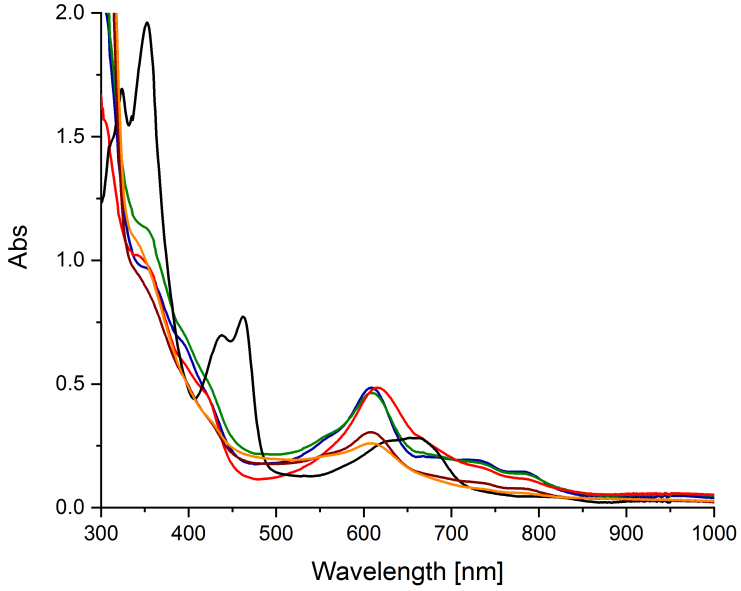

Figure S16. SEC-UV-Vis of **[2]**$^{+}$ with 85 equiv. PhOH in MeCN purged with CO_2 (0.1 M [N(*n*-Bu)$_4$]PF_6, applied potential –1.85 V_{Fc}). Black: 0 min; Red: 10 min; Blue: 30 min; Green: 60 min; Brown: 90 min, Orange: 120 min.

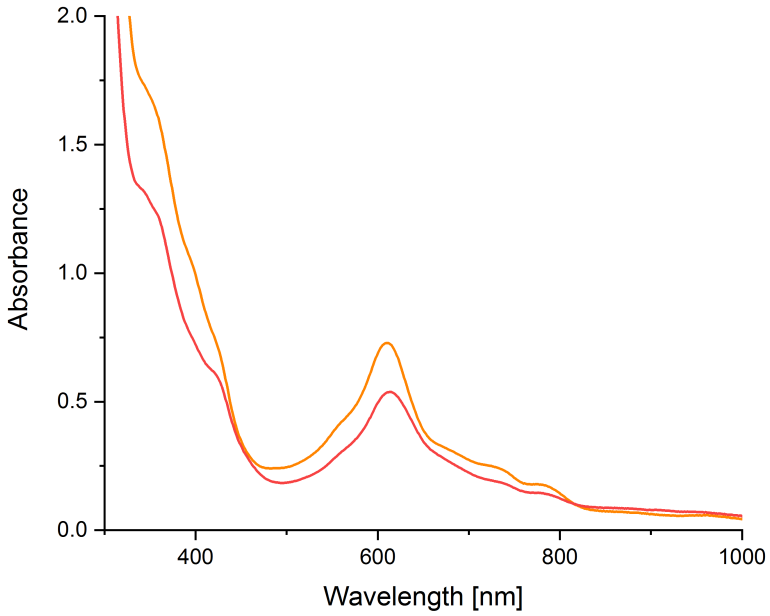

Figure S17. SEC-UV-Vis of **[2]**$^{+}$ with 85 equiv. PhOH in MeCN (0.1 M [N(*n*-Bu)$_4$]PF$_6$) and purged with CO_2. Absorption spectra were recorded after 1 h bulk electrolysis at −1.85 V_{Fc} (orange) and −1.65 V_{Fc} (red), respectively.

Post-bulk assessment

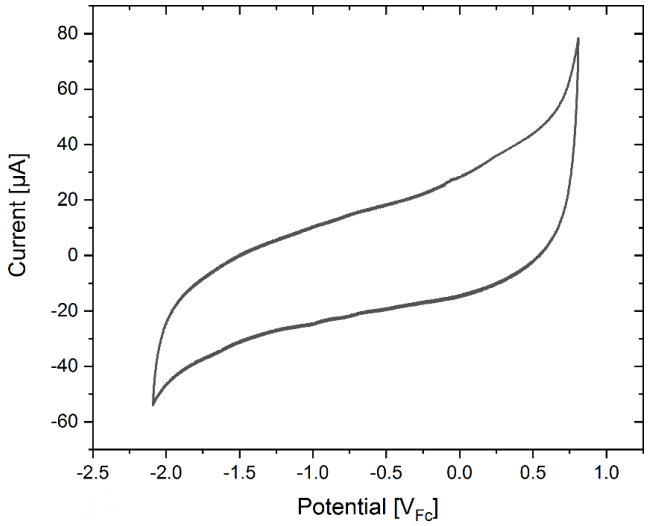

Figure S18. Rinse-test after 1 h CPE of **[2]**$^{+}$ at −1.84 V_{Fc}. Subsequent to bulk electrolysis, the glassy carbon plate was rinsed with MeCN. The electrode was placed in a fresh solution of 0.1 M $[N(n\text{-}Bu)_4]PF_6$ in MeCN, and a CV was measured under Ar with 100 mV/s scan rate; counter electrode: Pt-net.

Table S4. Results of CPE experiments with **[2]**$^{+}$ prior to and after electrode polishing. CPE experiments were run either for 30 or 60 min, after which time the experiment was stopped and the amount of CO produced was measured. The working electrode was then polished, the cell purged once more with CO_2, and CPE was continued for another 30 or 60 min, after which product formation was again determined.

	TON_{CO} (FE_{CO})	
Applied CPE time	Prior to electrode polishing	After electrode polishing
30 min [a)]	4 (93% [a)]/ 97%[b)])	3.6 (94%[c)]/ 99%[d)])
60 min [a)]	8.1 (81%[a)]/ 85%[b)])	2.2 (55%[c)]/ 60%[d)])

General conditions: 500 μM **[2]**$^{+}$, 0.28 M CO_2, 43 mM PhOH in 0.1 M $[N(n\text{-}Bu)_4]PF_6$ in MeCN; CPE at −1.84 V_{Fc}

a) taking two initial electrons into account

b) taking the background current and two initial electrons into account

c) no charge correction was applied

d) only the background correction was applied

TOF calculations based on CPE data

Diffusion coefficients, D_{obs}, for each complex were determined from the redox peaks in the non-catalytic CVs of **[X]**$^+$ (X = 1= Co; X = 2 = Fe) based on the Randles-Sevcik equation.

$$i_{redox} = 0.446n^{3/2}Ac_{cat}\left(\frac{\nu F^3 D_{obs}}{RT}\right)^{1/2} \quad (13)$$

i_{redox} is the reduction peak current of the redox couple of the catalyst in the non-catalytic CV under Ar; n = 1 is the number of electrons transferred in the redox process; c_{cat} = 1×10^{-6} mol/cm^3 is the concentration of the catalyst dissolved in the solution; F = 96485 A·s/mol is Faraday's constant; A = 0.0707 cm^2 is the surface area of the glassy carbon working electrode in the CV measurements; T = 298 K is the temperature; R = 8.314 V·A·s·K^{-1}·mol^{-1} is the ideal gas constant; and ν is the scan rate in V·s^{-1}.

D_{obs} was determined at the **[X]**$^{0/-}$ couple by measuring i_{redox} as a function of scan rate. The representative voltammograms of the complexes at different scan rates and the respective plots of i_{redox} as a function of $\nu^{1/2}$ for both complexes are shown below.

Complex	D_{obs}(**[X]**$^{0/-}$) [10^{-6} cm^2 s^{-1}]
[1]$^+$	19.9 ± 0.7
[2]$^+$	21.5 ± 0.4

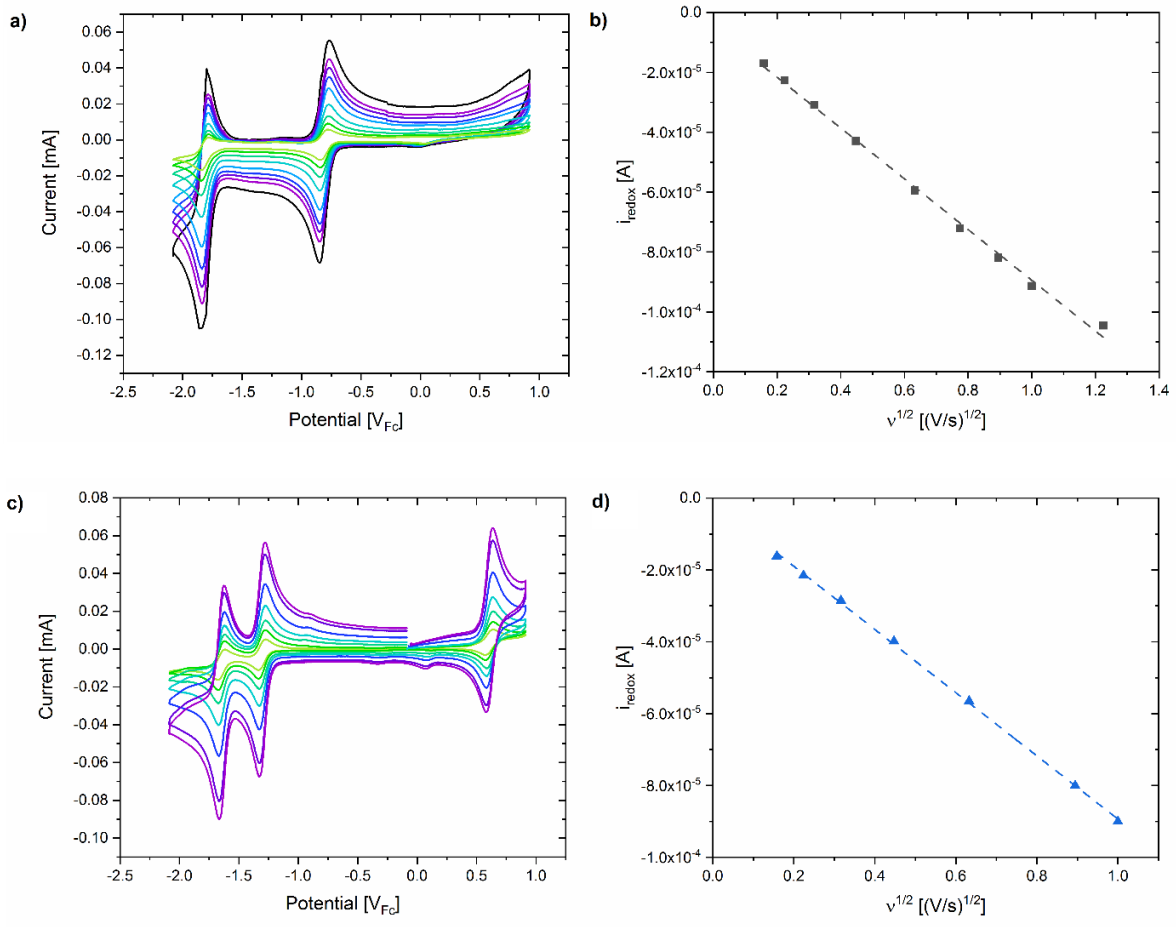

Figure S19. a) Scan rate dependent CVs of **[1]**$^{+}$ (1 mM) in MeCN (0.1 M [N(n-Bu)$_4$]PF$_6$); scan rates: 25 mV/s, 50 mV/s, 100 mV/s, 200 mV/s, 400 mV/s, 600 mV/s, 800 mV/s, 1000 mV/s, 1500 mV/s (green to black); **b)** representative plot of i_{redox} as a function of $\nu^{1/2}$ for the **[1]**$^{0/-}$ couple of 1 mM **[1]**$^{+}$ in MeCN (0.1 M [N(*n*-Bu)$_4$]PF$_6$) under Ar. **c)** Scan rate dependent CVs of **[2]**$^{+}$ (1 mM) in MeCN (0.1 M [N(*n*-Bu)$_4$]PF$_6$) under Ar; scan rates: 25 mV/s, 50 mV/s, 100 mV/s, 200 mV/s, 400 mV/s, 800 mV/s, 1000 mV/s, (green to purple); **d)** representative plot of i_{redox} as a function of $\nu^{1/2}$ for the **[2]**$^{0/-}$ couple of 1 mM **[2]**$^{+}$ in MeCN (0.1 M [N(*n*-Bu)$_4$]PF$_6$) under Ar.

Turnover frequencies for CO production by **[X]**$^{+}$ (X = 1= Co; X = 2 = Fe) are subsequently calculated from CPE data according to the procedure described by the Saveant group.[32] The TOF_{CPE} at a given potential is defined as

$$TOF_{CPE} = \frac{n_{CO}}{n_{cat} \times t} \tag{14}$$

With the number of moles CO produced during the electrolysis given as n_{CO} and n_{cat} as the number of moles of **[X]**$^{+}$ estimated in the reaction-diffusion layer during electrolysis and the time of electrolysis t in s.

For a homogeneous molecular electrocatalyst, n_{cat} is estimated from the space integration of the estimated catalyst amount in the reaction-diffusion layer near the surface of the working electrode as determined by equation 15.[32]

$$n_{cat} = A\sqrt{\frac{D_{obs}}{TOF}}[cat] \tag{15}$$

The active surface of the working electrode was determined as A = 3.94 cm², the electrolysis time is t = 60 min = 3600 s, D_{obs} is the diffusion coefficient for the complexes at the **[X]**$^{0/-}$ couple, [cat] = 0.5 × 10^{-6} mol/cm³ is the concentration of the catalyst, and TOF is the maximum turnover frequency as determined from catalytic CVs at large overpotential. Combining the previous equations leads to the expression for TOF_{CPE} expressed in equation 16.

$$TOF_{CPE} = \frac{n_{CO}}{n_{cat} \times t} = \frac{n_{CO}}{A\sqrt{\frac{D_{obs}}{TOF}}[cat] \times t} \tag{16}$$

If it is assumed that the electron transfer to the catalyst is fast and the redox process is Nernstian, an alternate expression for the potential-dependent TOF_{CPE} can be derived according to equation 17.

$$TOF_{CPE} = \frac{TOF}{1 + \exp\left[\frac{F}{RT}(E_{CPE} - E^0)\right]} \quad (17)$$

Here, F = 96485 A·s/mol is Faraday's constant, R = 8.314 V·A·s·K^{-1}·mol^{-1} is the universal gas constant, T = 298.15 K is the temperature of the solution, E_{CPE} is the applied potential during electrolysis and E^0 is the redox potential of the active species. Due to the presence of a pre-wave in the CV preceding catalysis, E^0 is difficult to determine directly from the CV. Therefore, $E_{cat/2}$, the potential corresponding to the half of the catalytic peak current is used instead of E^0 for the analysis.[33] Combination of equations 16 and 17 yields the following expression for TOF_{CPE}, where all parameters are known constants or measurable values.

$$TOF_{CPE} = \frac{{n_{CO}}^2}{t^2 A^2 D_{obs}[cat]^2}\left(1 + exp\left[\frac{F}{RT}(E_{CPE} - E^0)\right]\right) \quad (18)$$

TOF_{CPE} values for both complexes are listed below.

Complex	E_{CPE} [V_{Fc}]	E^0 [V_{Fc}]	n_{CO} [µmol]	TOF_{CPE}
[1]$^+$	−2.34	−2.42	3.9 ± 0.2	0.36 ± 0.04
[2]$^+$	−1.84	−1.75	20 ± 1	0.39 ± 0.02
[2]$^+$	−2.1	−1.75	21 ± 2	0.65 ± 0.04

Molecular structure of [Na(OEt$_2$)][Fe(Mabiq)] ([2]$^-$)

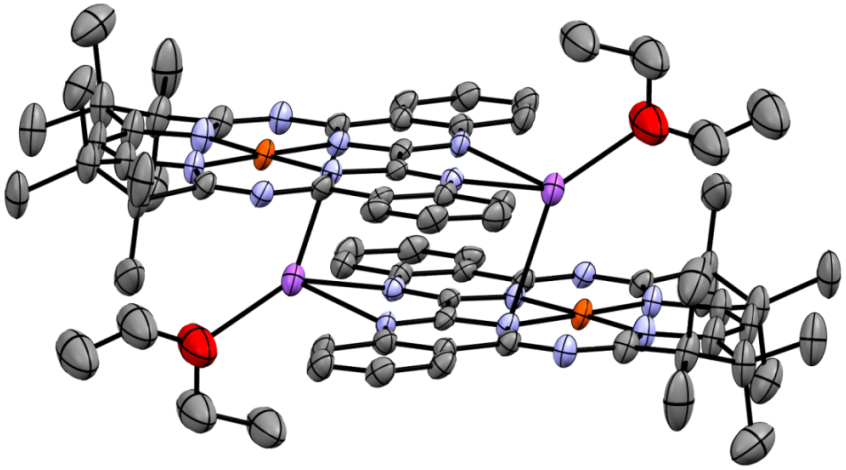

Figure S20. ORTEP style representation of the dimeric unit of **[2]**$^-$ in the solid state. Ellipsoids are shown at the 50% probability level and hydrogen atoms are omitted for clarity.

Scheme S1. Atomic numbering in the molecular structure of **[2]**$^-$.

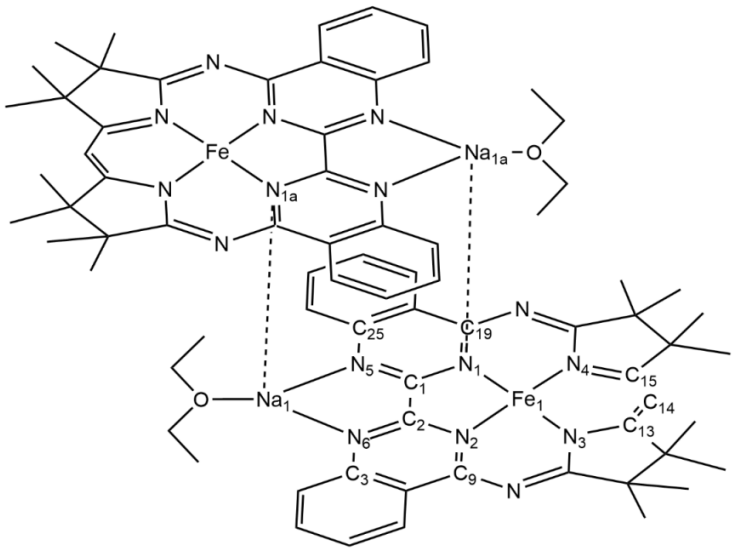

Crystallographic tables

Table S5. Crystallographic refinement data for **[2]**$^{-}$.

Empirical formula	$C_{74}H_{86}Fe_2N_{16}Na_2O_2$
Formula weight	1389.26
Crystal system	Monoclinic
Space group	P 1 2_1/c 1
a (Å)	25.888(9)
b (Å)	16.283(6)
c (Å)	19.033(6)
α (°)	90
β (°)	109.452(8)
γ (°)	90
Volume (Å^3)	7565.(5)
Z	4
ϱcalc (g/cm^3)	1.220
μ (mm^{-1})	0.449
F (000)	2928
Reflns. Collected	72807
Indep. reflns/Rint	13613
Data/restraints/param	13613/56/918
GOF on F^2	1.037
Final R1 indexes [I ≥ 2σ(I)]	0.0788
Final wR2 indexes (all data)	0.2580
Δϱmin/max (eÅ^{-3})	1.314 and −1.268
CCDC number	2111146

Table S6. Select bond lengths for **[2]**$^{-}$; numbering of atoms as indicated in Scheme S1.

Fe1-N1	1.890(4)
Fe1-N2	1.892(4)
Fe1-N3	1.892(4)
Fe1-N4	1.888(5)
N4-C15	1.385(7)
C15-C14	1.389(8)
C14-C13	1.374(8)
N3-C13	1.382(7)
N1-C19	1.370(7)
N1-C1	1.384(7)
C1-C2	1.485(7)
N2-C2	1.369(6)
N2-C9	1.370(6)
N6-C3	1.385(7)
N6-C2	1.300(6)
N5-C1	1.296(6)
N5-C25	1.388(7)
Na1-N5	2.398(5)
Na1-N6	2.436(5)
Na1-N1a	2.867(5)

Table S7. Select bond angles (°) for **[2]**$^{-}$; numbering of atoms as indicated in Scheme S1.

N4-Fe1-N1	91.06(19)
N4-Fe1-N2	175.83(19)
N1-Fe1-N2	84.77(18)
N4-Fe1-N3	92.5(2)
N1-Fe1-N3	176.40(19)
N2-Fe1-N3	91.64(19)
Fe1-N1-Na1a	75.02(14)
N5-Na1-N1a	91.91(15)
N6-Na1-N1a	84.38(15)
N5-Na1-N6	69.37(15)
C13-C14-C15	125.3(5)
Fe1-N4-C15	128.1(4)
Fe1-N3-C13	127.8(4)
Fe1-N1-C1	114.6(3)
Fe1-N2-C2	115.0(3)
N1-C1-C2	112.6(4)
C1-C2-N2	112.8(4)
N5-C1-C2	119.4(5)
C1-C2-N6	119.0(5)
N5-C1-N1	128.0(5)
N6-C2-N2	128.1(5)

Computational Results

Orca Input

```
================================================================================
                                INPUT FILE
================================================================================
!TIGHTOPT
!UKS
!B3LYP def2-SVP
!RIJONX def2/J
!SlowConv
!GRID3 FinalGrid5
!UNO UCO
!LARGEPRINT

%maxcore 2200
%pal
        nprocs 24
end

%scf
        BrokenSym 3,1
        MaxIter 1000
end
%basis
        NewGTO Fe "def2-TZVP" end
        NewGTO N "def2-TZVP" end
        NewGTO O "def2-TZVP" end
        NewGTO Na "def2-TZVP" end
end

* xyz 0 3
Fe      0.000000000      0.000000000      0.000000000
…
…
**                     ****END OF INPUT****
================================================================================
```

Table S8. DFT-optimized (B3LYP, BS(3,1)) geometry (.xyz format) for **[2]**$^{-}$.

	CARTESIAN	COORDINATES	(ANGSTROEM)			
Fe	0.072110	0.12877	0.134590	H	1.201968	-5.392026	-0.908761
Na	5.530405	0.330311	0.896551	H	1.863870	-5.002073	0.683845
O	7.785943	0.242647	1.373330	H	2.963862	-5.449019	-0.650525
N	1.297633	1.478017	0.411415	C	2.161899	-3.394285	-2.389510
N	1.432316	1.099362	0.101378	H	1.218199	-3.804050	-2.780640
N	-1.324363	-1.318275	0.132418	H	2.988902	-3.999297	-2.793278
N	1.469092	1.461803	0.197939	H	2.268975	-2.366703	-2.770760
N	-3.683881	1.675438	0.766354	C	3.625321	-3.067793	1.241165
N	-3.831502	1.127697	-0.421592	H	2.714006	-3.077793	1.858886
N	-0.261689	-3.108993	-0.377307	H	4.337774	-2.370933	1.709556
N	0.078310	3.413095	0.399815	H	4.070221	-4.075342	1.268605
C	-2.580951	0.944120	0.520657	C	4.639488	-2.672663	- 1.011592
C	-2.655313	-0.477138	0.347641	H	4.547865	-2.216330	-2.007241
C	-3.832727	-2.478311	0.236253	H	4.972543	-3.716085	-1.139379
C	-5.050120	-3.206615	0.304435	H	5.445295	-2.143824	-0.477807
H	-5.977312	-2.659480	0.501461	C	3.917940	2.602700	1.910150
C	-5.068122	-4.582546	0.118855	H	3.004442	2.561918	2.523619
H	-6.017370	-5.123759	0.174881	H	4.461632	3.526365	2.164892
C	-3.876624	-5.284561	-0.142896	H	4.550228	1.748193	2.197352
H	-3.896948	-6.367302	-0.288760	C	4.916066	2.638330	-0.383687
C	-2.671722	-4.588739	-0.216841	H	4.791757	2.438212	-1.457206
H	-1.733415	-5.105752	-0.420713	H	5.657093	1.920867	0.003775
C	-2.630999	-3.196149	-0.031119	H	5.354404	3.643682	-0.268571
C	-1.387601	-2.426968	-0.099105	C	2.553875	4.917305	0.754750
C	0.941332	-2.590719	-0.401861	H	1.778416	5.598649	0.376023
C	2.140341	-3.437858	-0.841820	H	3.532762	5.407748	0.621350
C	3.329589	-2.616276	-0.212091	H	2.373225	4.788312	1.830772
C	2.699622	-1.226217	-0.146103	C	2.538288	3.900889	-1.531422
C	3.391582	-0.026814	-0.010315	H	2.542501	2.981303	-2.137454
H	4.481414	-0.083539	-0.014452	H	3.427425	4.493523	-1.798081
C	2.827932	1.235546	0.144934	H	1.646179	4.483959	-1.806148
C	3.597008	2.531326	0.395094	C	-8.248786	-0.286952	2.624578
C	2.505276	3.592665	-0.014172	H	-8.861288	-1.188839	2.447112
C	1.221471	2.794387	0.236450	H	-8.894985	0.467058	3.112794
C	1.114406	-2.803624	0.528553	C	-7.052971	-0.621146	3.496453
C	-2.271740	3.657867	0.797237	H	-7.392690	-1.015597	4.466630
C	-2.166320	5.051621	0.946364	H	-6.441326	0.273355	3.699241
H	-1.178148	5.503324	0.853141	H	-6.416799	-1.392702	3.032670
C	-3.292707	5.829054	1.205675	C	-9.501729	-0.496335	-0.254933
H	-3.199860	6.911843	1.319804	H	-8.766154	-1.096920	-0.813449
C	-4.551984	5.210257	1.319655	H	-10.235720	-0.100191	-0.975167
H	-5.439648	5.816472	1.523551	H	-10.042656	-1.163520	0.434041
C	-4.677999	3.835450	1.174898	C	-8.824939	0.657908	0.471508
H	-5.657454	3.354792	1.262790	H	-8.334652	1.329342	-0.252149
C	-3.543240	3.024134	0.909718	H	-9.562501	1.263384	1.030495
C	2.041279	-4.900682	-0.395665				

Table S9. DFT-derived (B3LYP, BS(3,1)) Löwdin atomic charges and spin populations for **[2]**$^-$.

LOEWDIN ATOMIC CHARGES AND SPIN POPULATIONS					
0 Fe:	-0.061119	1.930825	46 H :	0.029872	-0.000103
1 Na:	-0.063832	0.006171	47 H :	0.023325	0.000098
2 O :	-0.478472	-0.000032	48 H :	0.017791	-0.000178
3 N :	-0.505802	0.002299	49 C :	-0.027166	-0.004345
4 N :	-0.505694	0.001509	50 H :	0.028969	0.000068
5 N :	-0.547276	0.000447	51 H :	0.019642	-0.000268
6 N :	-0.547496	0.000224	52 H :	0.023407	-0.000256
7 N :	-0.615037	0.148696	53 C :	-0.031136	-0.015398
8 N :	-0.615619	0.148660	54 H :	0.024775	0.000053
9 N :	-0.682670	-0.007072	55 H :	0.020930	-0.000297
10 N :	-0.682627	-0.007172	56 H :	0.019109	-0.003206
11 C :	0.515235	0.143310	57 C :	-0.038051	-0.004317
12 C :	0.514716	0.145058	58 H :	0.022339	-0.000473
13 C :	0.266363	-0.036123	59 H :	0.022073	-0.000805
14 C :	-0.032704	0.072990	60 H :	0.020581	-0.000005
15 H :	0.039838	-0.000108	61 C :	-0.031042	-0.015406
16 C :	-0.015846	-0.039243	62 H :	0.024837	0.000056
17 H :	0.022750	0.000077	63 H :	0.019215	-0.003197
18 C :	-0.055497	0.082443	64 H :	0.020780	-0.000304
19 H :	0.021885	-0.000069	65 C :	-0.037818	-0.004267
20 C :	0.007606	-0.030996	66 H :	0.022305	-0.000471
21 H :	0.037226	0.000119	67 H :	0.020502	-0.000008
22 C :	-0.000382	0.059141	68 H :	0.021986	-0.000808
23 C :	0.518973	-0.022976	69 C :	-0.030119	-0.000096
24 C :	0.537185	-0.067873	70 H :	0.029807	-0.000105
25 C :	-0.003729	-0.002839	71 H :	0.017720	-0.000180
26 C :	-0.018194	0.003526	72 H :	0.023425	0.000096
27 C :	0.253984	-0.291608	73 C :	-0.027302	-0.004368
28 C :	-0.055247	0.094612	74 H :	0.023590	-0.000263
29 H :	0.025536	0.000373	75 H :	0.019701	-0.000275
30 C :	0.254031	-0.291283	76 H :	0.028968	0.000063
31 C :	-0.018287	0.003486	77 C :	0.250661	0.000007
32 C :	-0.003837	-0.002879	78 H :	0.027460	0.000003
33 C :	0.537585	-0.067921	79 H :	0.028599	0.000002
34 C :	0.519434	-0.023710	80 C :	-0.014109	0.000078
35 C :	-0.000439	0.059488	81 H :	0.043717	0.000011
36 C :	0.007610	-0.031583	82 H :	0.060171	0.000038
37 H :	0.037269	0.000117	83 H :	0.065100	-0.000010
38 C :	-0.054903	0.082062	84 C :	-0.049336	0.000002
39 H :	0.021961	-0.000072	85 H :	0.041297	0.000001
40 C :	-0.015364	-0.039284	86 H :	0.038127	-0.000001
41 H :	0.023283	0.000079	87 H :	0.028992	0.000000
42 C :	-0.029575	0.072385	88 C :	0.249581	0.000011
43 H :	0.040820	-0.000125	89 H :	0.048724	0.000004
44 C :	0.266036	-0.036209	90 H :	0.028730	0.000002
45 C :	-0.030410	-0.000107			

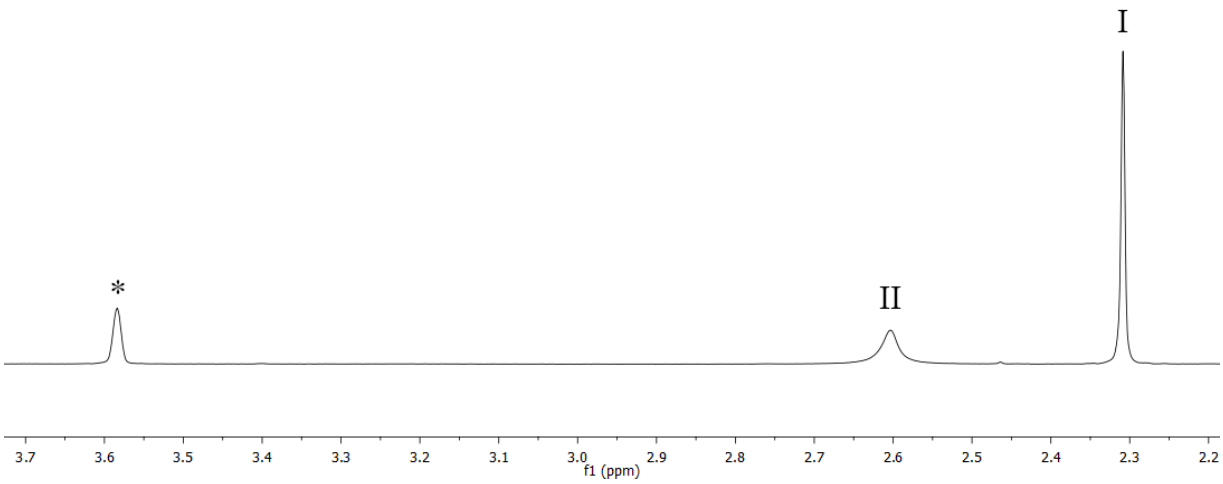

Figure S21. Evans' NMR measurement for **[2]**$^-$ in THF-d_8 with toluene as a standard yielded a μ_{eff} = 2.8 (in a repeat measurement μ_{eff} = 2.7 was obtained). **I** denotes the unaffected and **II** the affected signal of the standard, and the asterisk marks the solvent signal.

Reactivity studies with [2]$^-$

Assay for carbonate detection

4.8 mg of **[2]**$^-$ were dissolved in 500 μL dry and deoxygenated THF in a crimp vial in the glove box. The vial was crimped with a cap containing a septum and the solution was purged with CO_2. The solvent was subsequently removed *in vacuo*. 100 μL of acetic acid were added to the solid *via* the septum and a headspace sample was taken and analyzed by gas chromatography (GC).

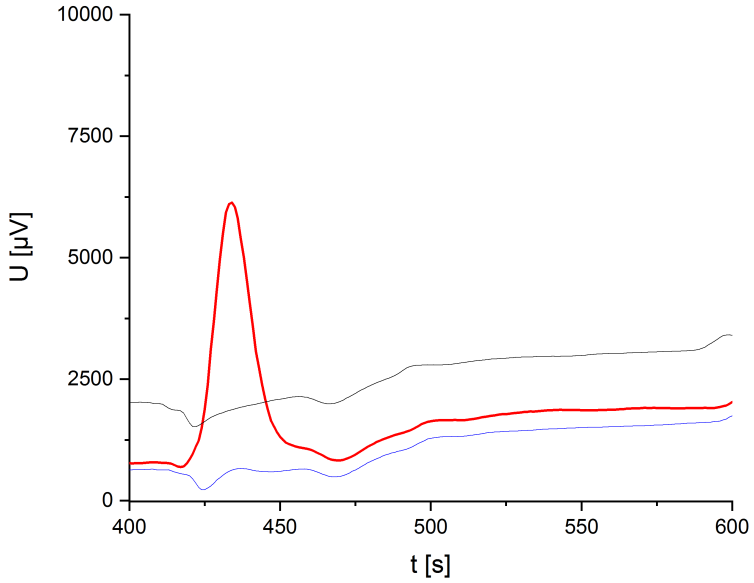

Figure S22. GC traces at the thermal conductivity detector (TCD) measured for a sample of air (blue), a headspace sample from a sealed vial containing 100 μL added acetic acid (black), and the headspace sample after addition of 100 μL acetic acid to the solid **[2]**$^-$/CO_2 product (red).

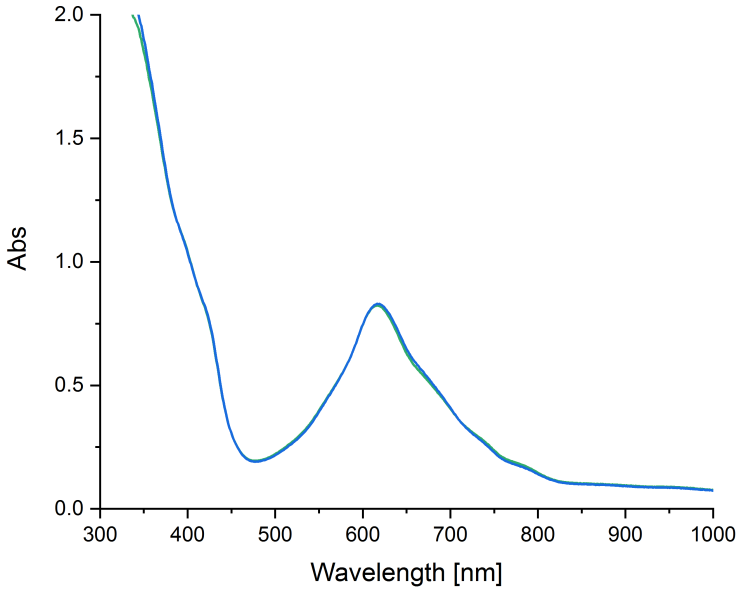

Figure S23. Absorption spectra of an 84 μM solution of **[2]**$^-$ in THF purged with CO_2 (green) and after subsequent addition of 85 equiv. PhOH (blue).

The reactivity of **[2]**^{0} and **[2]**$^{+}$ towards CO was also investigated to confirm our conclusion that the **[2]**$^{-}$/CO_2 product corresponds to **[2-CO]**. The low-spin ferrous containing **[2]**$^{+}$ appears to bind carbon monoxide, as indicated by distinctive changes in the absorption and IR spectra (Figure S24 and S25). However, the product spectra, assigned to **[2-CO]**$^{+}$**,** are markedly different from those observed in the **[2]**$^{-}$/CO_2 reaction. The IR spectrum of a **[2]**^{0}/CO solution (Figure S26) on the other hand, exhibits a stretch at ν = 1954 cm^{-1}, confirming our assignment of **[2-CO]** as the **[2]**$^{-}$/CO_2 reaction product.

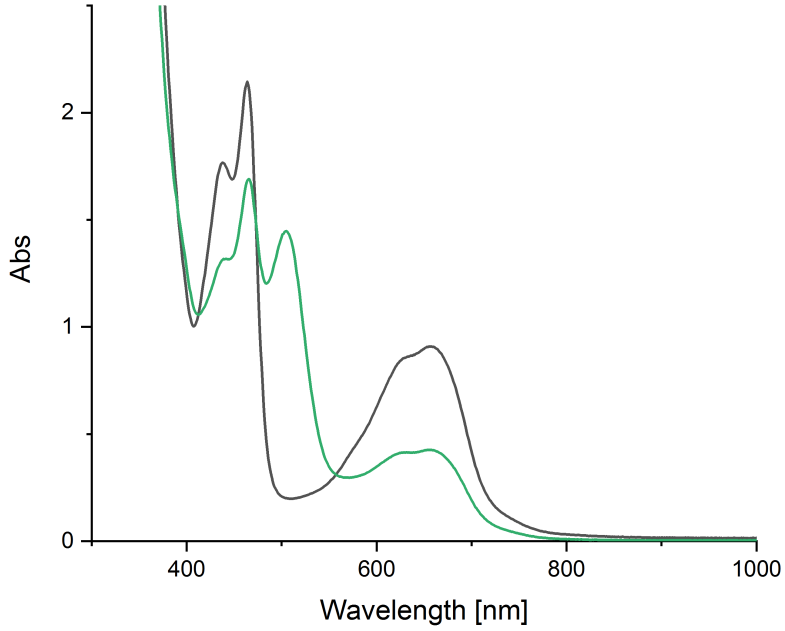

Figure S24. Absorption spectrum of a solution of **[2]**$^{+}$ (136 μM) in 1:1 MeCN/THF before (black) and after addition of CO (green).

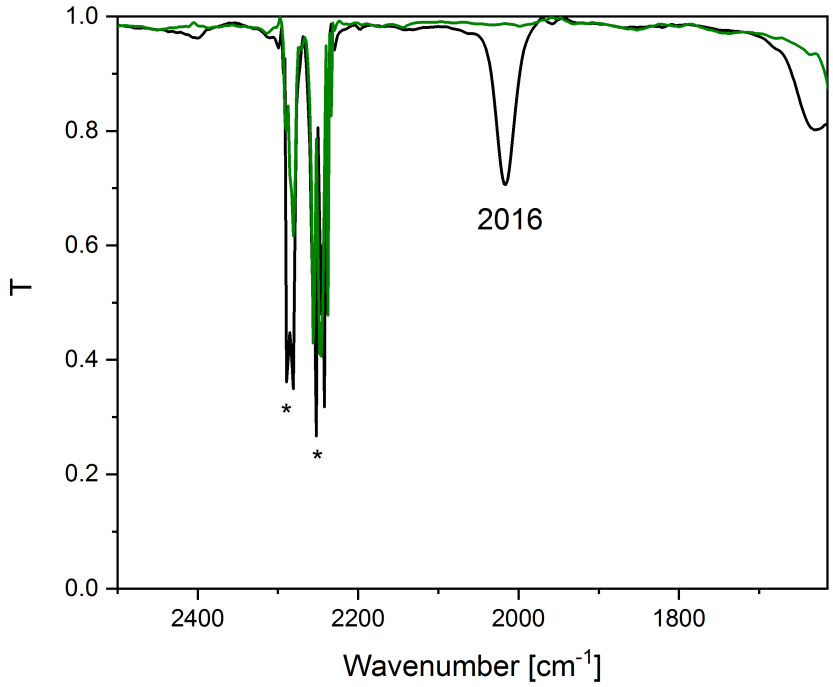

Figure S25. IR spectra of **[2]**$^{+}$ (6 mM) in 1:1 THF/MeCN (green), and of **[2]**$^{+}$ (3 mM) in 1:1 THF/MeCN after addition of CO (black). The stretches assigned with * are residual solvent bands.

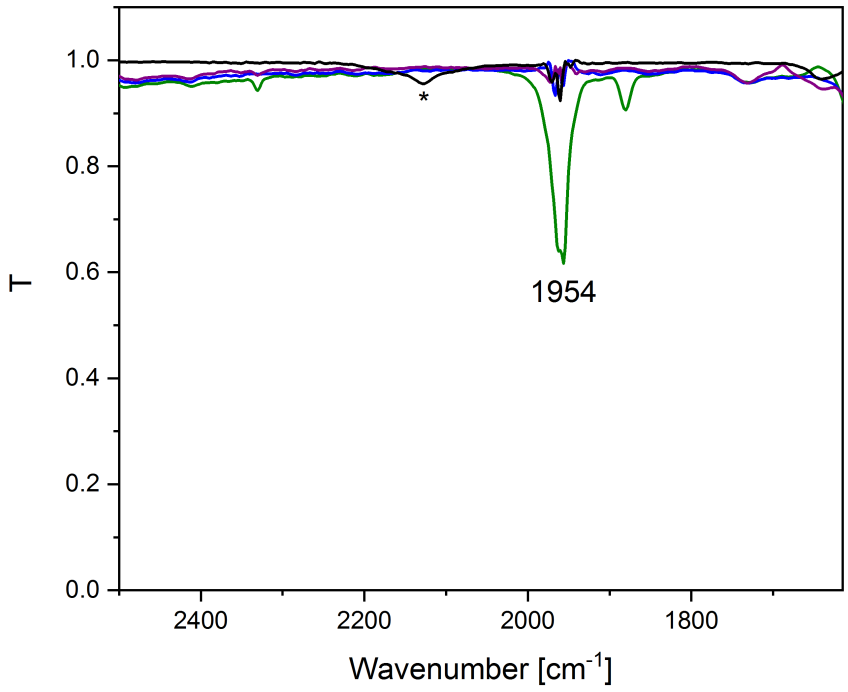

Figure S26. IR spectra of a 6 mM solution of **[2]⁰** in THF. Blue: **[2]⁰** only; Green: after addition of CO; Purple: after subsequent drying and redissolution. The spectrum of free CO in THF is shown as black line and the vibration marked with an asterisk.

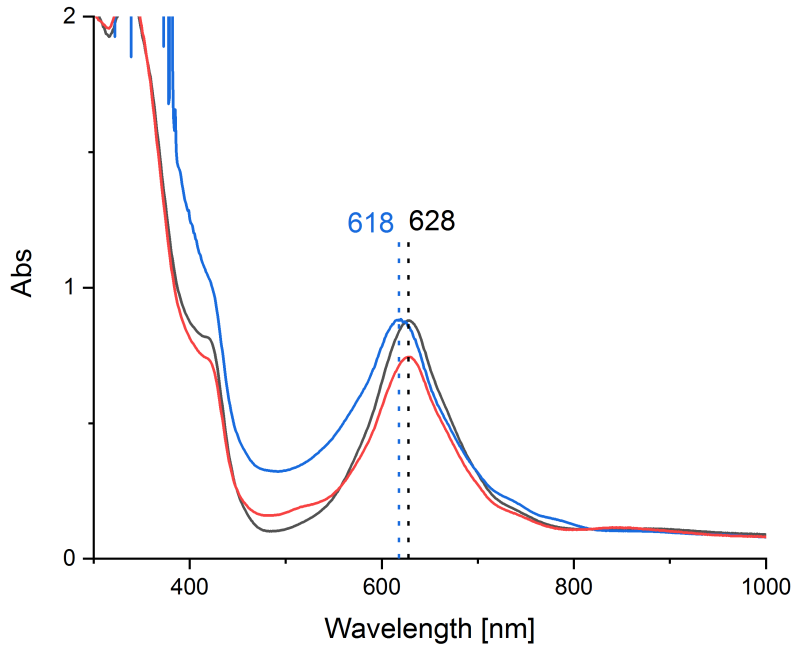

Figure S27. Absorption spectrum of a solution of **[2]**^{0} (80 μM) in THF before (black) and after addition of CO (red), in comparison with the spectrum of a solution of **[2]**$^{-}$ in THF after addition of CO_2 (blue).

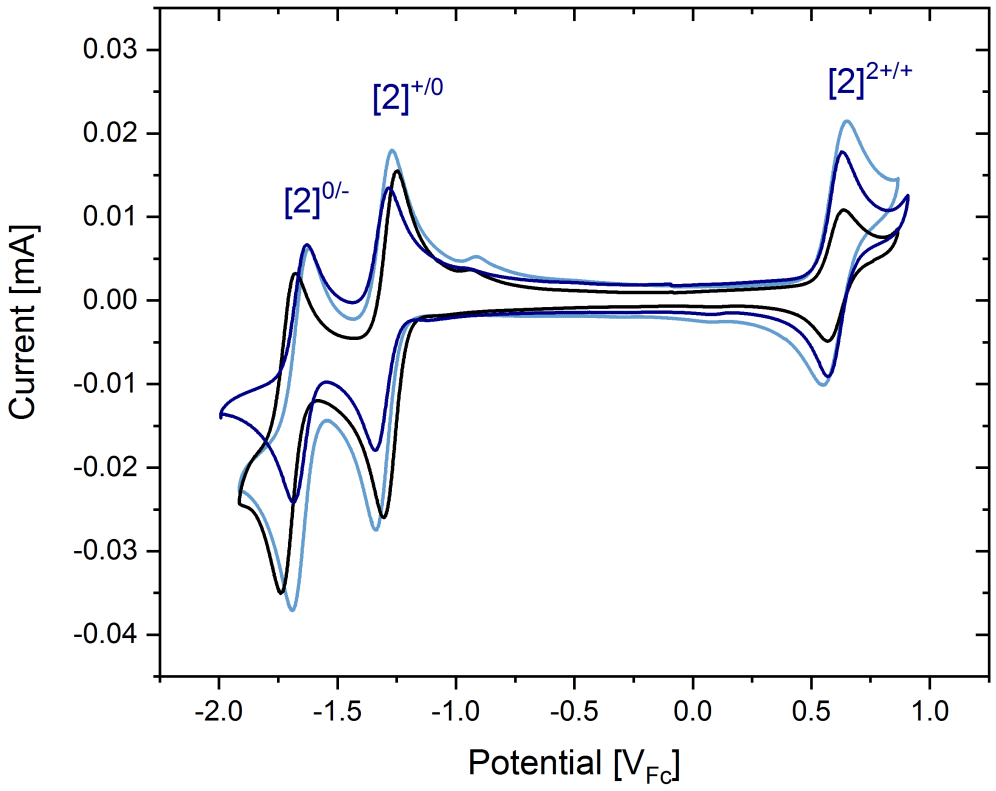

Figure S28. CV of **[2]**$^{+}$ (1 mM; MeCN, 0.1 M [N(*n*-Bu)$_4$]PF$_6$, scan rate 100 mV/s) prior (darkblue) and after addition of CO (black). Purging with Ar yielded the original CV (lightblue).

The data indicates that CO binds weakly to both **[2]**$^{+}$ and **[2]**^{0}.

Table S10. Comparison of peak potentials of the **[2]**$^{+/0}$ and **[2]**$^{0/-}$ couple under Ar and CO.

	[2]$^{+/0}$			**[2]**$^{0/-}$		
	$E_{p,a}$ [V_{Fc}]	$E_{p,c}$ [V_{Fc}]	ΔE [mV]	$E_{p,a}$ [V_{Fc}]	$E_{p,c}$ [V_{Fc}]	ΔE [mV]
Ar	−1.283	−1.339	56	−1.628	−1.691	63
CO	−1.245	−1.305	60	−1.679	−1.743	64

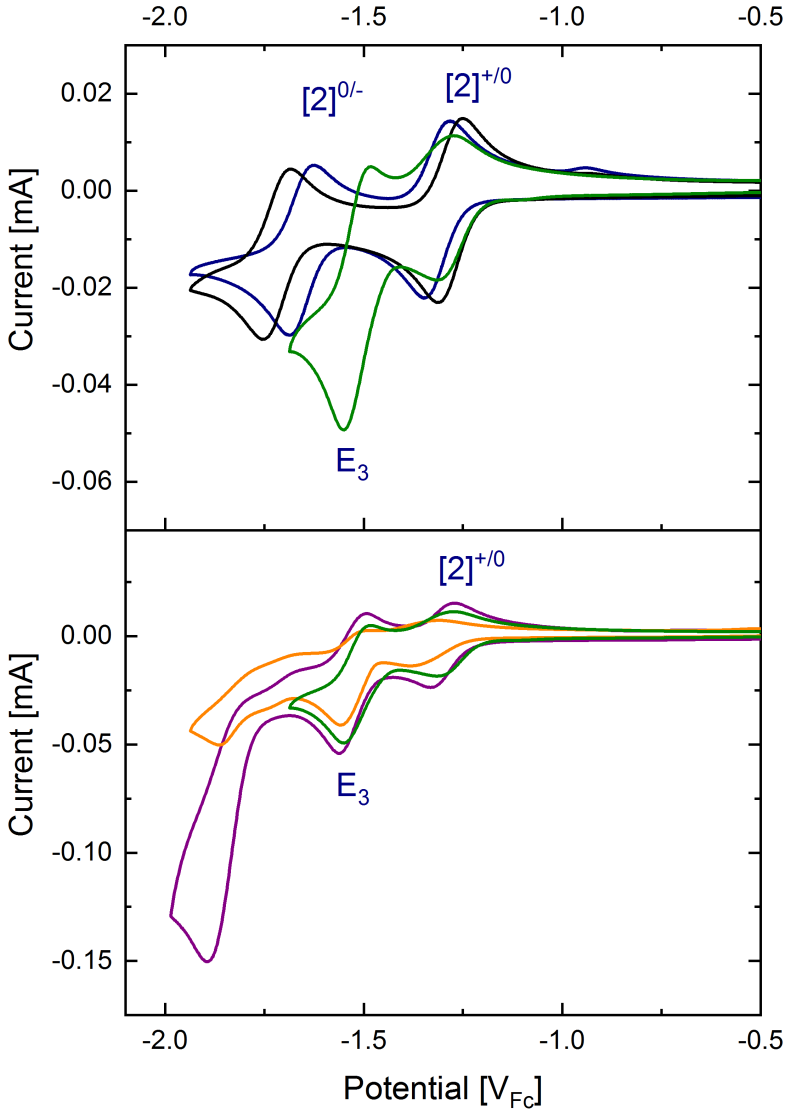

Figure S29. top: CV of **[2]**$^{+}$ (1 mM) in 0.1 M [N(*n*-Bu)$_4$]PF$_6$ in dry and deoxygenated MeCN (blue), in the presence of CO (black) and after subsequent addition of 85 equiv. PhOH (green). Bottom: CV of **[2]**$^{+}$ (1 mM) in 0.1 M [N(*n*-Bu)$_4$]PF$_6$ in dry and deoxygenated MeCN with 85 equiv. PhOH under Ar (purple) and CO atmosphere (orange, green). Applied scan rate: 100 mV/s.

Protonated pre-catalytic intermediate $\mathbf{I_{PhOH}}$

The protonated intermediate $\mathbf{I_{PhOH}}$ was synthesized by stirring $\mathbf{[2]^-}$ (5 mg, 7.2 μmol) with 2 equiv. PhOH (1.4 mg, 14.4 μmol) in toluene for 30 min.

LIFDI-MS: $[Na[Fe(MabiqH)]^+$ (*m/z*: 621.2121, calc. 621.2148).

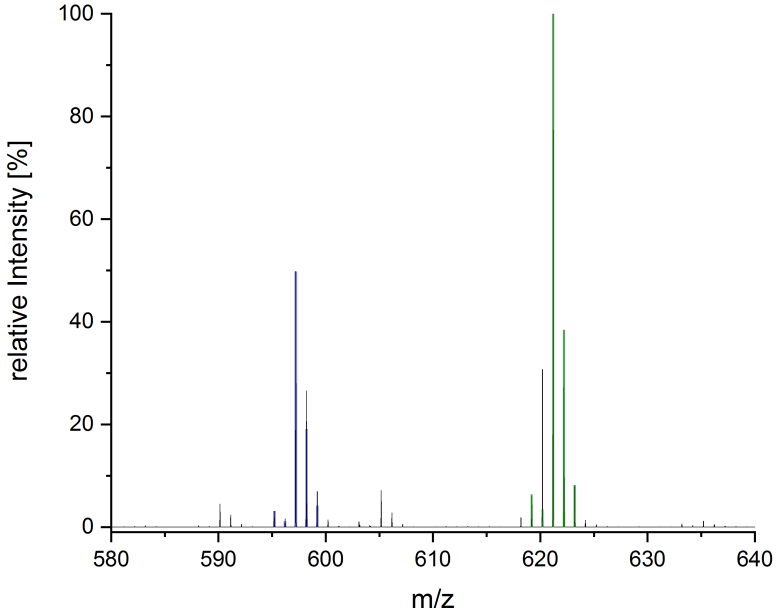

Figure S30. LIFDI-MS of a solution of $\mathbf{[2]^-}$ in THF with 2 equiv. PhOH. *m/z*: 597.21 $[Fe(Mabiq)]^+$; 620.21 $[Fe(Mabiq)Na]^+$; 621.21 $[Fe(MabiqH)Na]^+$. The calculated isotope patterns of $[Fe(Mabiq)]^+$ (blue) and $[Fe(MabiqH)Na]^+$ (green) are shown as an overlay.

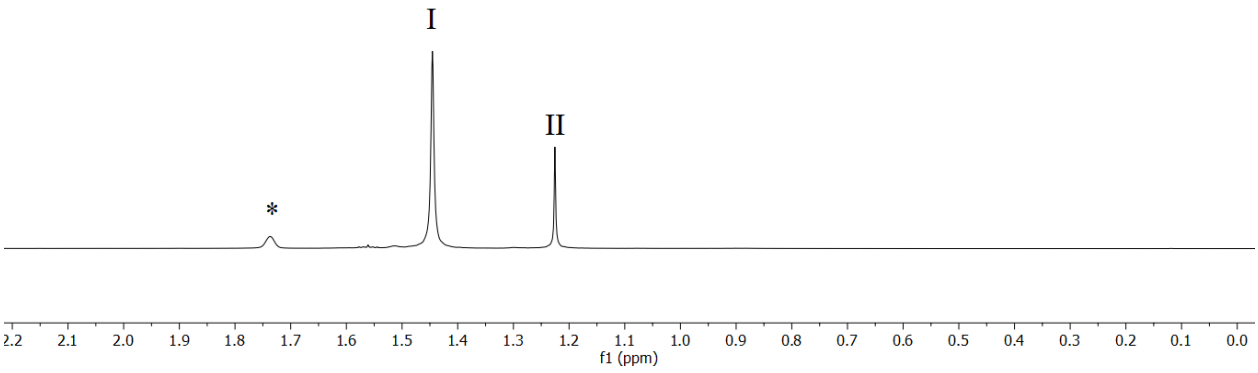

Figure S31. Evans' NMR of $\mathbf{I_{PhOH}}$ in THF-d_8 with cyclohexane as standard. **II** denotes the signal of cyclohexane shifted by the paramagnetic compound and **I** denotes the unaffected signal of cyclohexane ($\mu_{eff} = 2.84\ \mu_B$). The solvent signal is marked with an asterisk.

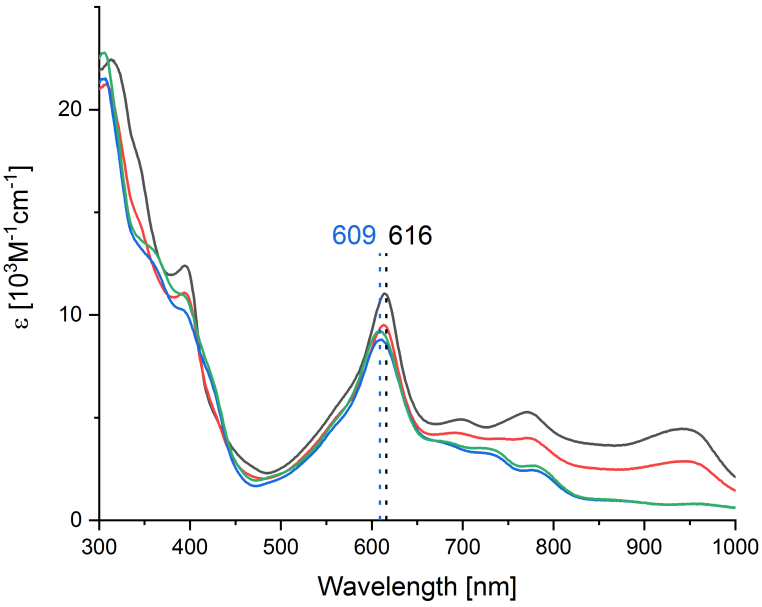

Figure S32. Titration of **[2]**$^-$ with varying amounts of PhOH. To a 10 mM solution of **[2]**$^-$ in THF (black) PhOH was added subsequently; 1 equiv. (red trace), 2 equiv. (blue), 4 equiv. (green). For the measurement a 20 μL sample of each **[2]**$^-$/PhOH solution was diluted with 2 mL dry and deoxygenated THF in an air-tight cuvette.

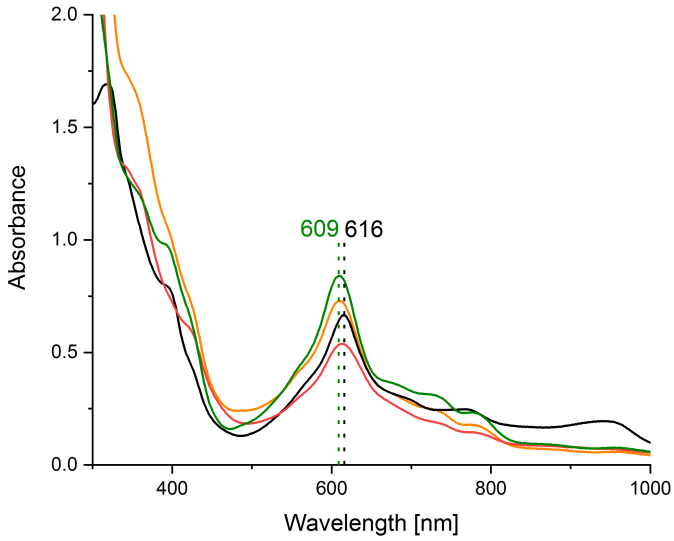

Figure S33. Absorption spectra of a 44 μM solution of **[2]**$^-$ (black) and a 95 μM solution of **[2]**$^-$ with 2 equiv. PhOH (green) in THF. SEC-UV-Vis of **[2]**$^+$ with 85 equiv. PhOH in MeCN (0.1 M [N(*n*-Bu)$_4$]PF$_6$) and purged with CO_2. Absorption spectra were recorded after 1 h bulk electrolysis at −1.85 V_{Fc} (orange) and −1.65 V_{Fc} (red), respectively.

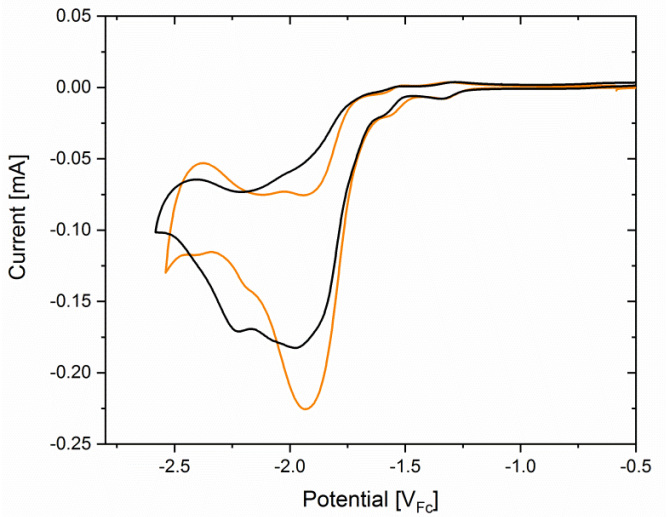

Figure S34. CV of a 0.5 mM solution of $\mathbf{I_{PhOH}}$ (black) and of a 1 mM solution of **[2]**$^+$ (orange, scaled by factor 0.5 for comparison) saturated with CO_2 in the presence of 85 mM PhOH in MeCN (0.1 M [N(*n*-Bu)$_4$]PF$_6$, scan rate 100 mV/s).

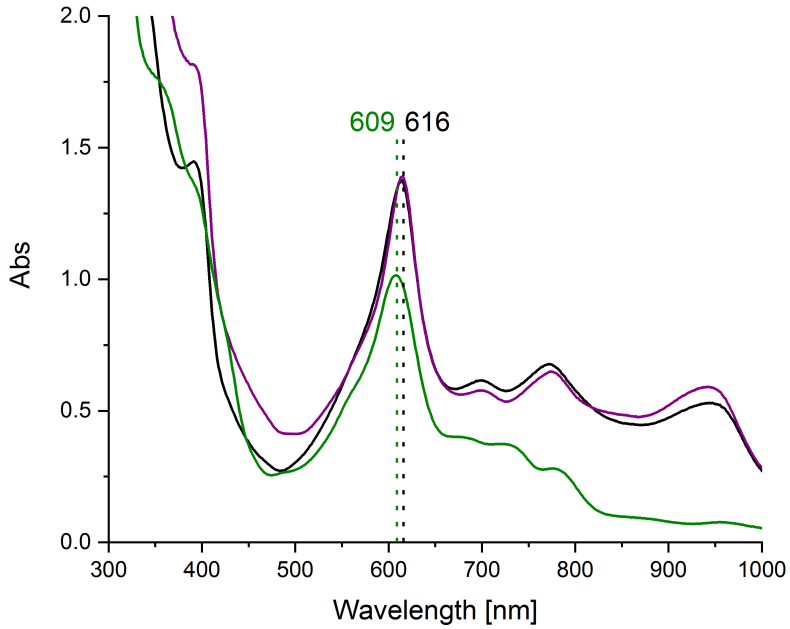

Figure S35. Absorption spectra of **[2]**$^-$ (100 μM) in THF in the absence (black) and presence of 40 equiv. PhOH (green) and after subsequent addition of 200 equiv. of KO^{t}Bu (purple) to the **[2]**$^-$/PhOH solution.

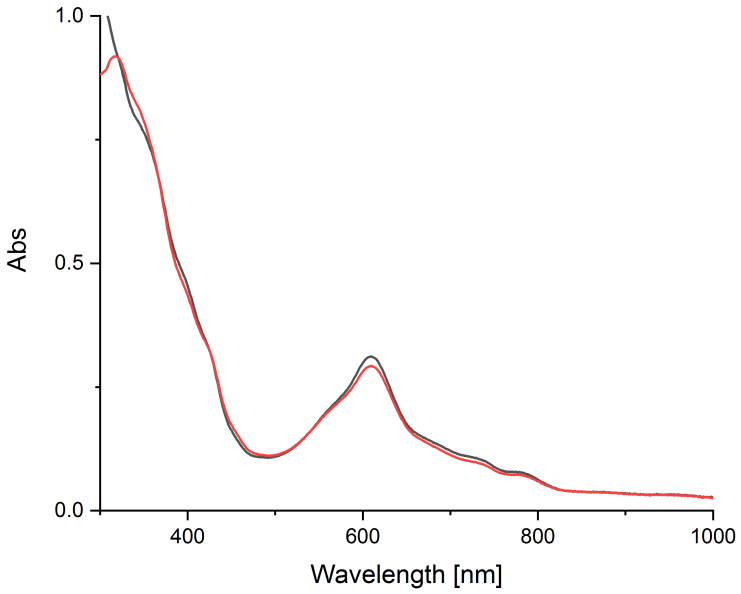

Figure S36. Absorption spectra of a solution of **[2]**$^-$ in the presence of 85 equiv. PhOH in THF (black) and after addition of CO_2 by purging the solution for 10 min (red).

Molecular structure of $\mathbf{I_{PhOH}}$

$\mathbf{I_{PhOH}}$ was generated upon reaction of **[2]**$^-$ with two equivalents of phenol in toluene, and the reaction mixture was stirred for at least 30 minutes and subsequently filtered. Crystals suitable for single crystal X-ray diffraction were obtained by cooling of a concentrated solution of the product in toluene. The compound crystallizes in triclinic space group $P\bar{1}$. In the asymmetric unit, two independent molecules are present, showing the expected molecular structure of the Fe-Mabiq moiety (Figure S37). The Fe ions of the complexes are coordinated by phenolic oxygen atoms in the axial positions. Additionally, three toluene molecules are co-crystallized.

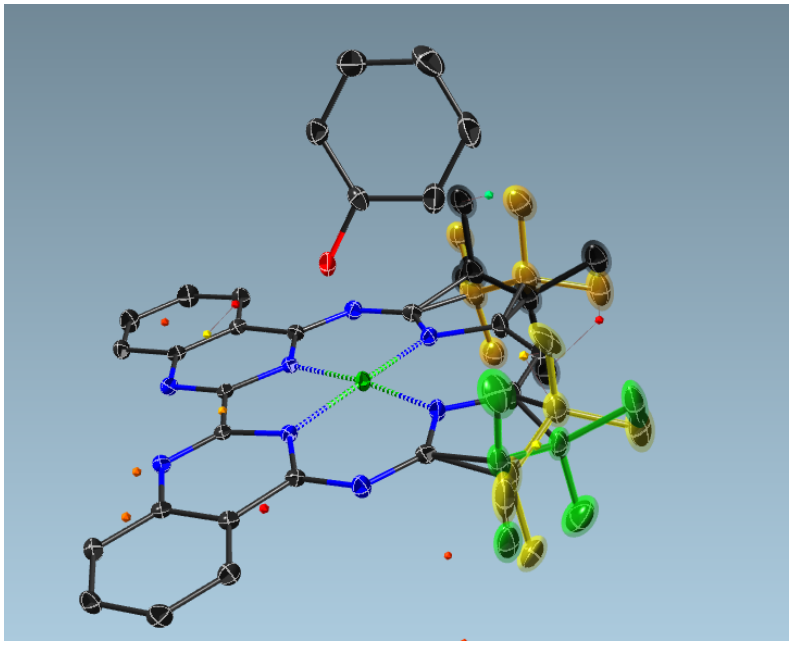

Figure S37. Molecular structure of **$\mathbf{I_{PhOH}}$** in the solid state. One of the independent molecules of Fe-Mabiq is shown; hydrogen atoms as well as co-crystallized solvent molecules (toluene) are omitted for clarity. The Fe ion is axially coordinated by a phenolic oxygen atom. Positional disorder of the Mabiq ligand-backbone as refined by split-layer refinement is depicted in different colors.

Close inspection of the axial ligands reveals indicative peaks of residual electron density at a distance of 0.937 Å (0.942 Å, respectively), which can be attributed to a phenolic OH proton (Figure S38, proton positions marked with white circle). The latter are also involved in intermolecular hydrogen bonding to a neighboring Mabiq ligand, further supporting the protonated state of the hydroxylic group. Additionally, the Fe-O_{Ph} bond distance amounts to 2.421(2)/2.91(2) Å, which is substantially longer than typical Fe-O distances of Fe^{II}- or Fe^{III}-phenolate complexes (Fe-O = 1.86 – 2.05 Å; survey of CSD database (version 5.42) searching unsubstituted phenolate-iron complexes). Consequently, we assign the axial ligands as phenol molecules, rather than deprotonated phenolate ions.

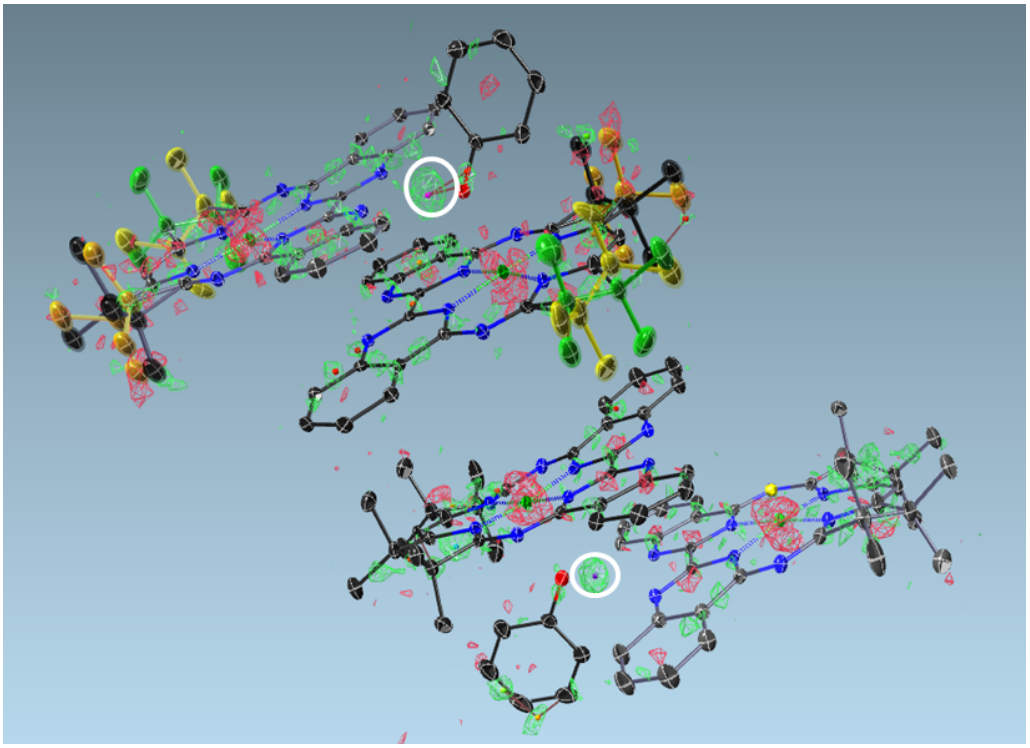

Figure S38. Refined structure of $\mathbf{I_{PhOH}}$ showing the difference electron density map ($F_{observed}$-$F_{calculated}$) including the positive residual electron density maxima corresponding to the phenolic proton (marked with white circle), which also engages in intermolecular H-bonding interactions with the bipyrimidine nitrogen atoms of a neighboring molecule of [Fe(MabiqH)(PhOH)].

The fact that we were able to observe phenolic hydrogen atoms involved in hydrogen bonding renders the axial ligands neutral. Likewise, the co-crystallized toluene molecules do not contribute any charge to the overall crystal structure. Therefore, due to the requirement of charge neutrality, the remaining Mabiq fragments also must be neutral. This contradicts an expected charge of −1 for each Fe(II)-Mabiq unit. Oxidation to Fe(III) offers one possibility to account for the overall charge neutrality, however this can be ruled out based on the experimental evidence: 1) the overall spin state of $\mathbf{I_{PhOH}}$ was determined by Evans' method as $S = 1$, analogous to that of $\mathbf{[2]^-}$ indicating that the electron structure of each Fe-ligand unit remains similar; 2) this is further supported by the absorption spectrum of $\mathbf{I_{PhOH}}$, which exhibits similar features as the spectrum of $\mathbf{[2]^-}$; 3) the Fe-N bond distances of $\mathbf{I_{PhOH}}$ also are similar to those in $\mathbf{[2]^-}$. All of these observations speak against the presence of an Fe(III) ion, thus, we rule out oxidation of the Fe center to account for the added charge.

A more plausible explanation is protonation of the Fe(II)-Mabiq complexes. Several experimental observations again support this hypothesis. Both the spectroscopic and electrochemical data confirm that two equivalents of phenol are required for the formation of $\mathbf{I_{PhOH}}$, and a dependence of the $\mathbf{[2]^{0/-}}$ couple on two PhOH equivalents in the CV of $\mathbf{[2]^+}$ with added PhOH. However, only one equivalent of the phenol coordinates to the Fe center. NaOPh precipitates from the reaction mixture, and was also identified as colorless needles during the crystallization (Figure S40). The second phenol molecule thus acts as a proton donor.

Therefore, we closely investigated the crystal structure towards suspicious residual electron density peaks in the difference Fourier map. Although hydrogen atoms are potentially hard to localize using X-Ray diffraction, the corresponding electron density peaks can usually be observed nowadays, particularly when all other peaks have been successfully attributed. In this case, we

were able to model all positional disorders within the Mabiq backbone as well as that of the co-crystallized toluene molecule. All backbone hydrogen atoms of the Mabiq ligand have been satisfyingly refined using the riding atom model. Consequently, all extrema of the difference electron density map are below 1 e/Å^3, with the majority being located at interatomic bonds, which usually is associated with a model of good quality.

However, investigation of the differential electron map also reveals several residual electron density peaks localized at the diketiminate carbons (C46 and C48, within a distance of 0.934 Å and 0.877 Å) of one Fe-Mabiq unit, as well as its respective counterpart on the other Fe-Mabiq fragment (C13, within a distance of 0.872 Å). This sparked our interest, since in our recent work on related Co-Mabiq complexes, these diketiminate carbon atoms were also predicted to be protonation sites, based on computational studies.[34] Additionally, the anisotropic displacement parameters ADP of the related carbons are slightly axially elongated towards the presumed hydrogen positions, compared to the ADPs of neighboring ligand backbone atoms. Based on this, in combination with the experimentally observed findings described above, we conclude the Fe(II)-Mabiq complex is protonated at the ligand, such that $\mathbf{I_{PhOH}}$ corresponds to [Fe(MabiqH)(PhOH)].

We note that due to the four possible protonation sites indicated by the structure—i.e. the density being distributed among the two diketiminate carbons in each Fe-Mabiq unit within the unit cell—the precise location of the proton among these carbon atoms cannot be determined. Thus, two scenarios would be feasible adding up to a potential more complex disorder of the proton: (1) either both Fe-Mabiq fragments contain one proton and are overall neutral (i.e., two [Fe(MabiqH)(PhOH)] molecules); or (2) one fragment is doubly protonated ([Fe(MabiqH$_2$)(PhOH)]$^+$) while the other molecule in the unit cell acts as a counter ion

([**2(PhOH)**]$^-$). We therefore refrain from an explicit refinement of the H atom position. However, based on our experimental results, the scenario with one proton per fragment seems more likely, as the two Fe-Mabiq fragments exhibit the same bond distances, including near the relevant carbon atoms. Coordination of PhOH to **[2]**$^-$, also is not observed. Figure S39 depicts the differential electron density map with the possible positions of the protons.

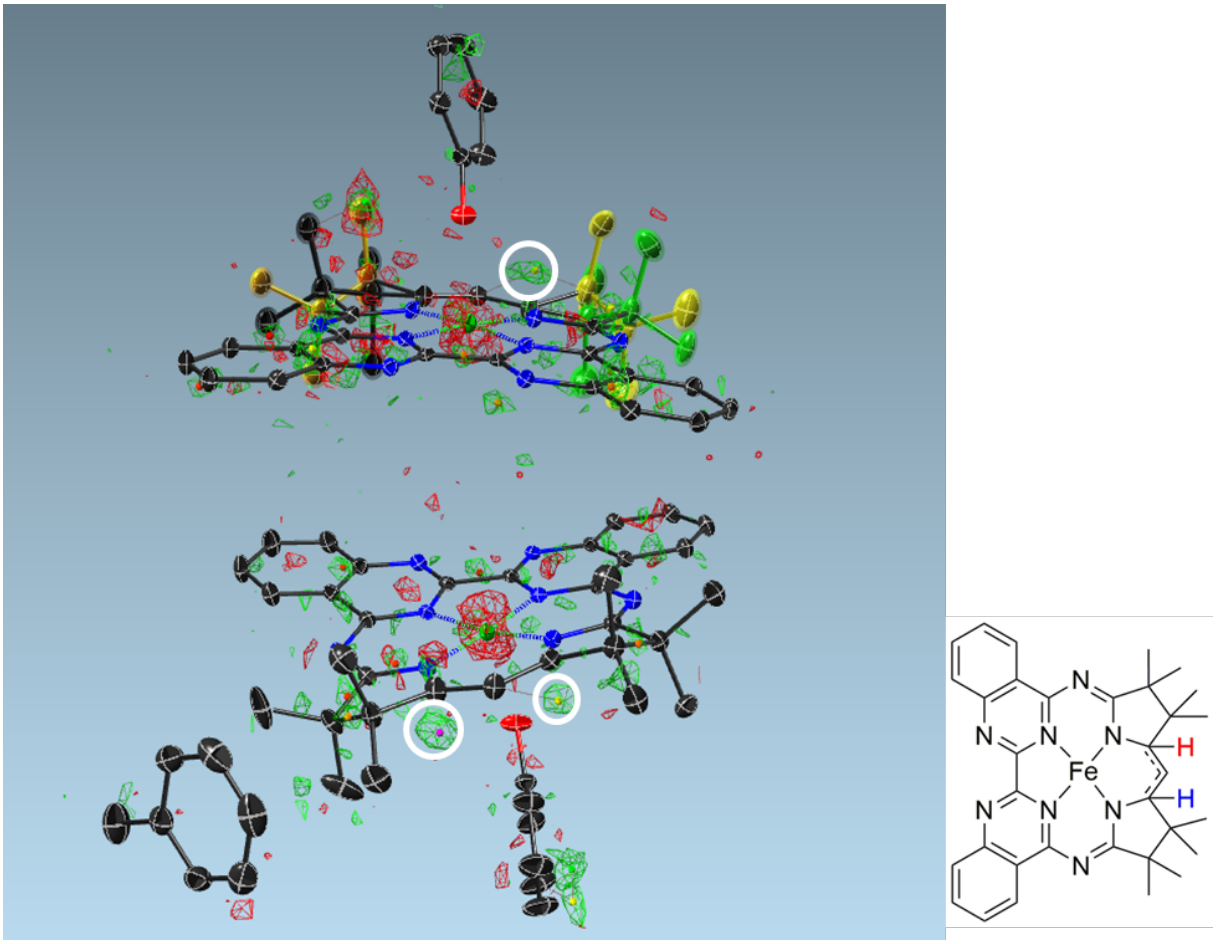

Figure S39. *left:* Refined structure of $\mathbf{I_{PhOH}}$ with the differential electron map. The possible protonation positions are marked in white. *Right*: Suggested alternative locations of the added proton based on the residual electron density.

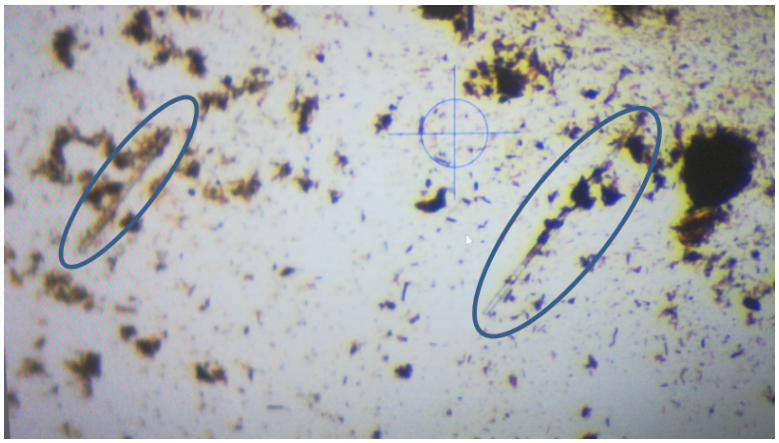

Figure S40. Picture of a sample used for crystal picking. The colorless needles are marked with blue ellipses. (The sample turns brown over longer time periods).

Table S11. Crystallographic refinement data for $\mathbf{I_{PhOH}}$

Empirical formula	$C_{50}H_{50}FeN_8O$
Formula weight	834.83
Crystal system	Triclinic
Space group	$P\bar{1}$
a (Å)	15.0090(19)
b (Å)	17.425(2)
c (Å)	17.6586(18)
α (°)	99.586(5)
β (°)	101.184(5)
γ (°)	107.180(5)
Volume (Å^3)	4203.2(9)
Z	4
ϱcalc (g/cm^3)	1.311
μ (mm^{-1})	0.408
F (000)	1752
Reflns. Collected	113662
Indep. reflns/Rint	15358
Data/restraints/param	15358/763/1349
GOF on F^2	1.029
Final R1 indexes [$I \geq 2\sigma(I)$]	0.0395
Final wR2 indexes (all data)	0.0992
Δϱmin/max (eÅ^{-3})	–0.403 and 0.510
CCDC number	2111145

Scheme S2. Numbering scheme used in this work for $\mathbf{I_{PhOH}}$.

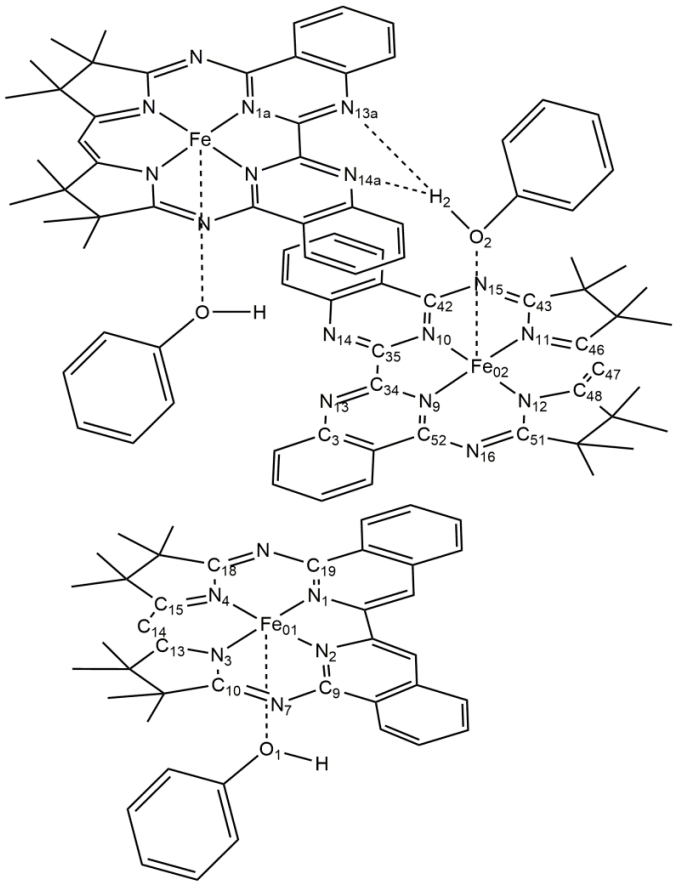

Table S12. Select bond distances for $\mathbf{I_{PhOH}}$.

Fe01-N1	1.913(5)	Fe02-N9	1.911(1)
Fe01-N2	1.918(8)	Fe02-N10	1.909(1)
Fe01-N3	1.903(4)	Fe02-N11	1.901(1)
Fe01-N4	1.906(9)	Fe02-N12	1.902(8)
Fe01-O1	2.420(4)	Fe02-O2	2.391(0)
N1-C1	1.370(3)	N9-C34	1.374(1)
N1-C19	1.361(7)	N9-C52	1.359(6)
N2-C2	1.372(2)	N10-C35	1.376(6)
N2-C9	1.356(9)	N10-C42	1.356(2)
N3-C10	1.360(1)	N11-C43	1.359(1)
N3-C13	1.379(1)	N11-C46	1.378(0)
N4-C15	1.383(3)	N12-C48	1.378(6)
N4-C18	1.357(8)	N12-C51	1.357(6)
N5-C1	1.300(2)	N13-C34	1.297(8)
N5-C25	1.385(2)	N14-C35	1.294(9)
N7-C9	1.344(2)	N15-C42	1.348(1)
N7-C10	1.315(1)	N15-C43	1.312(0)
N8-C18	1.318(4)	N16-C51	1.315(6)
N8-C19	1.344(3)	N16-C52	1.342(7)
C1-C2	1.482(3)	C34-C35	1.483(8)
C13-C14	1.382(3)	C46-C47	1.383(3)
C14-C15	1.379(2)	C47-C48	1.379(6)
		H2-N13a	2.085
		H2-N14a	2.595

References

1. McCarthy, B. D.; Martin, D. J.; Rountree, E. S.; Ullman, A. C.; Dempsey, J. L., Electrochemical reduction of Bronsted acids by glassy carbon in acetonitrile-implications for electrocatalytic hydrogen evolution. *Inorg. Chem.* **2014,** *53* (16), 8350-8361.
2. Sampson, M. D.; Kubiak, C. P., Manganese Electrocatalysts with Bulky Bipyridine Ligands: Utilizing Lewis Acids To Promote Carbon Dioxide Reduction at Low Overpotentials. *J. Am. Chem. Soc.* **2016,** *138* (4), 1386-1393.
3. Evans, D. F., 400. The determination of the paramagnetic susceptibility of substances in solution by nuclear magnetic resonance. *J. Chem. Soc.* **1959**, 2003-2005.
4. Muhr, M.; Heiß, P.; Schütz, M.; Bühler, R.; Gemel, C.; Linden, M. H.; Linden, H. B.; Fischer, R. A., Enabling LIFDI-MS measurements of highly air sensitive organometallic compounds: a combined MS/glovebox technique. *Dalton Trans.* **2021,** *50* (26), 9031-9036.
5. *APEX suite of crystallographic software*, version 2008.4; Bruker AXS Inc.
6. *SAINT, version 7.56a, SADABS, version 2008.1*, Bruker AXS Inc.
7. Sheldrick, G. M., *Acta Crystallogr., Sect. A: Found. Adv.* **2015,** *71*, 3-8.
8. Sheldrick, G. M., *Acta Crystallogr., Sect. C: Struct. Chem.* **2015,** *71*, 3-8.
9. Hubschle, C. B.; Sheldrick, G. M.; Dittrich, B., *J. Appl. Crystallogr.* **2011,** *44*, 1281-1284.
10. Wilson, A. J., *International Tables for Crystallography,*. Kluwer Academic Publishers, Dordrecht, The Netherlands: 1992; Vol. C.
11. Spek, A. L., *Acta Crystallogr., Sect. C: Struct. Chem.* **2015,** *71*, 9-18.
12. Macrae, C. F.; Edigngton, P. R.; McCabe, P.; Pidcock, E.; Shields, G. P.; Taylor, R.; Towler, M.; Streek, J. v. d., *J. Appl. Crystallogr.* **2006,** *39*, 453-457.
13. Neese, F. *ORCA*, Version 3.0.3; Max Plank Institute for Bioinorganic Chemistry, Mühlheim an der Ruhr, Germany, 2012.
14. a) Schäfer, A.; Horn, H.; Ahlrichs, R., Fully optimized contracted Gaussian basis sets for atoms Li to Kr. *J. Chem. Phys.* **1992,** *97* (4), 2571-2577; b) Schäfer, A.; Huber, C.; Ahlrichs, R., Fully optimized contracted Gaussian basis sets of triple zeta valence quality for atoms Li to Kr. *J. Chem. Phys.* **1994,** *100* (8), 5829-5835; c) Weigend, F.; Ahlrichs, R., Balanced basis sets of split valence, triple zeta valence and quadruple zeta valence quality for H to Rn: Design and assessment of accuracy. *Phys. Chem. Chem. Phys.* **2005,** *7* (18), 3297-3305.
15. Eichkorn, K.; Treutler, O.; Öhm, H.; Häser, M.; Ahlrichs, R., Auxiliary basis sets to approximate Coulomb potentials. *Chem. Phys. Lett.* **1995,** *240* (4), 283-290.
16. Humphrey, W.; Dalke, A.; Schulten, K., VMD: Visual molecular dynamics. *J. Mol. Graph.* **1996,** *14* (1), 33-38.
17. a) Noodleman, L.; Davidson, E. R., *Chem. Phys.* **1986,** *109* (1), 131-143; b) Noodleman, L. J., *Chem. Phys.* **1981,** *74*, 5737-5743.
18. Römelt, M.; Ye, S.; Neese, F., Calibration of Modern Density Functional Theory Methods for the Prediction of ^{57}Fe Mössbauer Isomer Shifts: Meta-GGA and Double-Hybrid Functionals. *Inorg. Chem.* **2009,** *48* (3), 784-785.
19. Müller, E.; Bernardinelli, G.; Zelewsky, A. v., A New Macrocyclic Ligand Combining Two Different Coordination Sites: Macrocyclic Biquinazoline (Mabiq'). Synthesis and Structure of the Free Ligand and of a Cobalt(III) Complex. *Inorg. Chem.* **1988,** *27*, 4645-4651.
20. Kaspar, M.; Altmann, P. J.; Pothig, A.; Sproules, S.; Hess, C. R., A macrocyclic 'Co(0)' complex: the relevance of ligand non-innocence to reactivity. *Chem. Commun.* **2017,** *53* (53), 7282-7285.
21. Banerjee, P.; Company, A.; Weyhermüller, T.; Bill, E.; Hess, C. R., Zn and Fe Complexes Containing a Redox Active Macrocyclic Biquinazoline Ligand. *Inorg. Chem.* **2009,** *48* (7), 2944-2955.

22. Elgrishi, N.; Chambers, M. B.; Fontecave, M., Turning it off! Disfavouring hydrogen evolution to enhance selectivity for CO production during homogeneous CO_2 reduction by cobalt-terpyridine complexes. *Chem. Sci.* **2015,** *6* (4), 2522-2531.
23. Lauenstein, R.; Mader, S. L.; Derondeau, H.; Esezobor, O. Z.; Block, M.; Römer, A. J.; Jandl, C.; Riedle, E.; Kaila, V. R. I.; Hauer, J.; Thyrhaug, E.; Hess, C. R., The central role of the metal ion for photoactivity: Zn– vs. Ni–Mabiq. *Chem. Sci.* **2021,** *12* (21), 7521-7532.
24. Cometto, C.; Chen, L.; Lo, P.-K.; Guo, Z.; Lau, K.-C.; Anxolabéhère-Mallart, E.; Fave, C.; Lau, T.-C.; Robert, M., Highly Selective Molecular Catalysts for the CO_2-to-CO Electrochemical Conversion at Very Low Overpotential. Contrasting Fe vs Co Quaterpyridine Complexes upon Mechanistic Studies. *ACS Catal.* **2018,** *8* (4), 3411-3417.
25. Azcarate, I.; Costentin, C.; Robert, M.; Savéant, J.-M., Dissection of Electronic Substituent Effects in Multielectron–Multistep Molecular Catalysis. Electrochemical CO_2-to-CO Conversion Catalyzed by Iron Porphyrins. *J. Phys. Chem. C* **2016,** *120* (51), 28951-28960.
26. Bard, A. J.; Roger, P.; Joseph, J., *Standard potentials in aqueous solution*. International Union of Pure Applied Chemistry ed.; M. Dekker: New York, 1985.
27. Isse, A. A.; Gennaro, A., Absolute Potential of the Standard Hydrogen Electrode and the Problem of Interconversion of Potentials in Different Solvents. *J. Phys. Chem. B* **2010,** *114* (23), 7894-7899.
28. Costentin, C.; Evans, D. H.; Robert, M.; Savéant, J.-M.; Singh, P. S., Electrochemical Approach to Concerted Proton and Electron Transfers. Reduction of the Water–Superoxide Ion Complex. *J. Am. Chem. Soc.* **2005,** *127* (36), 12490-12491.
29. Matsubara, Y., Standard Electrode Potentials for the Reduction of CO_2 to CO in Acetonitrile–Water Mixtures Determined Using a Generalized Method for Proton-Coupled Electron-Transfer Reactions. *ACS Energy Lett.* **2017,** *2* (8), 1886-1891.
30. Fourmond, V.; Jacques, P.-A.; Fontecave, M.; Artero, V., H_2 Evolution and Molecular Electrocatalysts: Determination of Overpotentials and Effect of Homoconjugation. *Inorg. Chem.* **2010,** *49* (22), 10338-10347.
31. Matsubara, Y., Unified Benchmarking of Electrocatalysts in Noninnocent Second Coordination Spheres for CO_2 Reduction. *ACS Energy Lett.* **2019,** *4* (8), 1999-2004.
32. a) Costentin, C.; Robert, M.; Savéant, J.-M., Catalysis of the electrochemical reduction of carbon dioxide. *Chem. Soc. Rev.* **2013,** *42* (6), 2423-2436; b) Costentin, C.; Drouet, S.; Robert, M.; Savéant, J.-M., Turnover Numbers, Turnover Frequencies, and Overpotential in Molecular Catalysis of Electrochemical Reactions. Cyclic Voltammetry and Preparative-Scale Electrolysis. *J. Am. Chem. Soc.* **2012,** *134* (27), 11235-11242.
33. Nie, W.; Tarnopol, D. E.; McCrory, C. C. L., Enhancing a Molecular Electrocatalyst's Activity for CO_2 Reduction by Simultaneously Modulating Three Substituent Effects. *J. Am. Chem. Soc.* **2021,** *143* (10), 3764-3778.
34. Tok, G. C.; Reiter, S.; Freiberg, A. T. S.; Reinschlüssel, L.; Gasteiger, H. A.; de Vivie-Riedle, R.; Hess, C. R., H_2 Evolution from Electrocatalysts with Redox-Active Ligands: Mechanistic Insights from Theory and Experiment vis-à-vis Co-Mabiq. *Inorg. Chem.* **2021,** *60* (18), 13888-13902.

Supporting Information: Influence of a neighbouring Cu centre on electro- and photocatalytic CO_2 reduction by Fe-Mabiq

The Electronic Supplementary Information includes synthesis procedures, NMR, SC-XRD, UV-Vis, GC and CV data. CCDC 2284733 and 2284734 contains the supplementary crystallographic data for this paper. The Electronic Supplementary Information and crystallographic data in CIF or other electronic format is available free of charge at https://doi.org/10.1039/d3cc04777f.

Electronic Supplementary Material (ESI) for Chemical Communications.

Influence of a neighbouring Cu centre on electro- and photocatalytic CO_2 reduction by Fe-Mabiq

*Kerstin Rickmeyer, Matthias Huber, Corinna R. Hess**

Department of Chemistry and Catalysis Research Center (CRC), Technical University of Munich, Lichtenbergstr. 4, 85748 Garching, Germany; Faculty of Chemistry and Pharmacy, University of Regensburg, 93053 Regensburg, Germany

Corresponding Author

*corinna.hess@ch.tum.de

17 April 2024

Note added after first publication: This supplementary information file replaces that originally published on 14 December 2023. Some incorrect values related to product formation were reported in Table S5, S6 and S7. The data in these tables have now been corrected, along with the corresponding y-axis values in Figure S15, S16, S19 and S20.

Table of Contents

General

All chemicals were purchased from Sigma Aldrich and used without further purification unless noted otherwise. Metal compounds were synthesized in an inert atmosphere glove box (Ar), using anhydrous solvents. Dry solvents were obtained from an MBraun SPS, deoxygenated via freeze-pump-thaw cycles and stored over 3 Å (MeCN, Pentane) or 4 Å activated molecular sieves. Tetrabutylammonium hexafluorophosphate ($[N(n\text{-}Bu)_4]PF_6$) was recrystallized three times from ethanol,[1] and ferrocene was sublimed prior to use. Dry CD_3CN was purchased from Sigma Aldrich, deoxygenated by the freeze-pump-thaw method, stored over 3 Å molecular sieves and filtered over activated aluminum oxide prior to use (activated, standard grade, neutral, Brokmann I, 58 Å pore size). Carbon dioxide (5.0 purity, Westfahlen AG, Münster, Germany) was passed through a 3 Å molecular sieve drying column to remove trace water.[2]

Instrumentation

Electronic spectra were measured on an Agilent Cary 60 UV-Vis spectrophotometer.

Solution state NMR spectra were measured on a Bruker Avance Ultrashield (400 MHz ^{1}H, 162 MHz ^{31}P) or a Bruker Avance HD (376 MHz ^{19}F) spectrometer with Topspin 2.1 software. The data was analyzed using MestreNova (Mestrelab Research S.L.). The following abbreviations were used: s = singlet, d = doublet, m = multiplet, dd = doublet of doublets, ddd = doublet of doublet of doublets.

Electrospray Ionisation mass spectrometry (ESI-MS) was performed using a Thermo Scientific Exactive Plus Benchtop LC-MS equipped with a Thermo Scientific Orbitrap Mass Analyzer. THF was used as a solvent, unless noted otherwise.

Elemental analysis was carried out at the Technical University of Munich.

Cyclic Voltammetry was carried out with a BioLogic SP200 potentiostat with EC-Lab software, using 3 mm diameter glassy carbon disk electrodes (PalmSens, Houten Netherlands) as working and counter electrodes. Prior to use, electrodes were polished with 0.05 μm alumina suspensions (CH Instruments Inc., USA). $Ag/AgNO_3$ (10 mM $AgNO_3$ and 0.1 M $[N(n\text{-}Bu)_4]PF_6$ in MeCN) was used as the reference electrode, separated via a Vycor 3535 frit (Advanced Glass & Ceramics, Holden, MA). CV measurements were performed in a five-necked glass cell under an Ar atmosphere. For measurements under CO_2 atmosphere, the solution was purged for 5 min and the cell was kept under that atmosphere during the experiment. Unless noted otherwise, a scan rate of 100 mV/s was applied. Potentials are reported with reference to an internal standard of ferrocenium/ferrocene ($Fc^{+/0}$, given by V_{Fc}).

Photocatalytic experiments were carried out in crimp glass vials with a total volume of 8.5 mL. Dry and deoxygenated MeCN was used as solvent for all experiments except for experiments with $^{13}CO_2$ where CD_3CN was used instead to allow for direct measurement of the liquid phase in the NMR. In a standard experiment 100 mM of BIH as sacrificial electron donor, 200 μM of $[Ru(bpy)_3](PF_6)_2$ as photosensitizer, 2 μM of catalyst and 85 equiv. of PhOH in a total volume of 2 mL were added to the vial in the glove box under red light. The vials were sealed and the solution was purged with CO_2 for 2 min followed by irradiation at 455 nm for 1 h using our previously reported photoreactor.[3, 4] A constant temperature of 20 °C was ensured by cooling with running water. At the end of the irradiation a head space sample was taken using a gastight syringe and analyzed by gas chromatography (GC).

Head space analysis was performed by injecting the gaseous sample directly into the GC (SRI 8610C Gas Chromatograph) and analyzed using a thermal conductivity (TCD) and a flame ionization detector equipped with a methanizer (FID-M). The detectors were calibrated using standard gas mixtures of CO in N_2 (AirProducts) and dilutions of H_2 or CO in N_2, respectively. In order to quantify the amount of gaseous product (H_2 or CO) produced, the headspace volume of the cell was determined. The amount of gaseous product generated in the reaction ($n_{prod,gas}$) was calculated as follows:

$$n_{prod,gas} = \frac{x_{prod,gas} \times V_h}{V_M} \quad (1)$$

where $x_{prod,gas}$ is the measured amount of gaseous product in ppm, $V_h = 6.52\,mL$ is the headspace volume of the cell, and $V_M = 24.471\,\frac{L}{mol}$ describes the molar volume. All experiments were carried out in at least triplicate. To account for gaseous products in solution Henry's law was applied.[5] The partial pressure at the end of the experiment (p_{gas}) was determined according to equation (2), with the ideal gas constant $R = 8.314\,\frac{J}{K*mol}$ and the temperature $T = 298\,K$.

$$p_{gas} = \frac{n_{prod,gas} \times R \times T}{V_h} \quad (2)$$

The amount of gaseous product in solution ($n_{prod,solv}$) can then be determined as follows:

$$n_{prod,solv} = x_{prod,solv} \times n_{MeCN} = \frac{p_{gas} \times \rho_{MeCN} \times V_{MeCN}}{K_{H,gas} \times M_{MeCN}} \quad (3)$$

where $x_{prod,solv}$ is the mole fraction of dissolved gaseous product, n_{MeCN} is the amount of solvent (MeCN) in [mol], $\rho_{MeCN} = 0.786\,\frac{g}{mL}$ is the density of MeCN, $V_{MeCN} = 2\,mL$ is the

reaction volume, $M_{MeCN} = 41.05\ \frac{g}{mol}$ is the molecular weight of MeCN and $K_{H,gas}$ is the Henry constant with $K_{H,CO} = 2507\ \frac{bar*mol_{MeCN}}{mol_{CO}}$ for CO in MeCN and $K_{H,H_2} = 5618\ \frac{bar*mol_{MeCN}}{mol_{H_2}}$ for H_2 in MeCN.[5, 6] The total amount of gaseous product formed ($n_{prod,total}$) is then:

$$n_{prod,total} = n_{prod,gas} + n_{prod,solv} \tag{4}$$

The turn-over number (TON) corresponding to the headspace sample taken at the end of the reaction was calculated according to equation (5), where $n_{catalyst}$ represents the amount of catalyst in [mol] used for the experiment and $n_{prod,total}$ being the total amount of gaseous product produced:

$$TON = \frac{n_{prod,total}}{n_{catalyst}} \tag{5}$$

The TOF in [s^{-1}] was obtained by equation (6) where t is the overall time of the reaction in [s]:

$$TOF = \frac{TON}{t} \tag{6}$$

Mass spectrometry of gaseous samples was performed using a Hiden HPR-20 QIC Benchtop Gas Analysis System equipped with a Secondary Electron Multiplier (SEM) detector.

Quantum yield determination measurements were carried out using our Quantum Yield Determination Set-up (QYDS) as previously described.[3, 4, 7] The components are contained within a black box to protect the sample from any external light sources and the experimenter from the intense stray light. A high-power LED (λ_{exc} = 455 nm) of type LD-CQ7P-1U3U produced by Osram was used as the excitation light source. The current for the LED was

controlled by a power supply of type RND 320-KA3005P from RND lab. The lens system consists of a Thorlabs aspheric condenser lens (f = 32 mm, 50 mm diameter) and a Thorlabs plano-convex lens (f = 100 mm, 50 mm diameter). The light bundle was imaged through an aperture (8 mm × 8 mm square) in front of the cuvette holder and onto the middle of the cuvette. A shutter was placed between the lens system and the aperture to interrupt the incoming light beam during the measurement, as warranted. The 10 mm × 10 mm fused silica sample cuvette was fitted with a ChemGlass valve. The volume of the sample solutions was 2 mL. During the irradiation period the solutions were rigorously stirred. The transmitted light power of the sample solution (P_{sample}) was detected using a Thorlabs power meter of type S175C. To determine the reference power (P_{ref}) a cuvette containing 2 mL of solvent was irradiated using the same input power settings as for the sample before each experiment. The incoming light beam was interrupted via a shutter control box, at which point the timer was also paused. The cuvette was subsequently transferred to the Cary60 UV-Vis instrument and the absorption spectrum was recorded. The cuvette was placed back into the QYDS and the illumination was continued. The quantum yield is given by the amount of product formed divided by the number of absorbed photons.[4, 8] The number of absorbed photons was calculated from the difference of the reference power and the power reaching the photometer.[4] To determine the amount of product formed the absorption at two different wavelengths was monitored.

Infrared (IR) spectroscopy was performed in an Ar-filled glove box with a Bruker ALPHA FT-IR spectrometer with Opus/Mentor software equipped with a PLATINUM-ATR unit for analysis of solid samples. Solution IR was carried out at a concentration of 6 mM in MeCN using a LIQUID CELL A145.

Crystallography

Crystallographic data were collected on an X-Ray single crystal diffractometer equipped with a TXS rotating anode with MoKα radiation (λ = 0.71073 Å), a CMOS detector (Apex IV, κ-CMOS) and a Helios optic using the Apex IV software package.[9] The measurements were performed on single crystals overlaid with perfluorinated ether. A suitable crystal was transferred to the diffractometer on top of a kapton micro sampler. The measurements were carried out at 100 K using a nitrogen stream. Initial lattice parameters were determined by a matrix scan. Reflections were corrected for Lorentz and polarization effects, scan speed, and background using SAINT.[10] Absorption corrections, including odd and even ordered spherical harmonics were performed using SADABS.[10] Space group assignments were based upon systematic absences, E statistics, and successful refinement of the structures. Structures were solved by SHELXT[11] with the aid of successive difference Fourier maps, and were refined against all data using SHELXL-2018[12] in conjunction with SHELXLE.[13] Hydrogen atoms were assigned to ideal positions and refined using a riding model with an isotropic thermal parameter 1.2 times that of the attached carbon atom (1.5 times for methyl hydrogen atoms). If not mentioned otherwise, non-hydrogen atoms were refined with anisotropic displacement parameters. Full-matrix least squares refinements were carried out by minimizing $\sum w({F_o}^2 - {F_c}^2)^2$ with the SHELXL[12] weighting scheme. Neutral atom scattering factors for all atoms and anomalous dispersion corrections for the non-hydrogen atoms were taken from International Tables for Crystallography.[14] Disordered solvent molecules were treated as a diffuse contribution to the overall scattering without specific atoms positions using the PLATON/SQUEEZE procedure.[15] For **1**, overall 156 electrons corresponding to 1.75 residual MeCN molecules and for **2**, overall 183 electrons corresponding to 2 residual diethylether molecules were determined. Images of the

crystal structures were generated using Mercury.[16] CCDC 2284733-2284734 contains the supplementary crystallographic data for this paper.

Synthesis

1,3-dimethyl-2-phenyl-2,3-dihydro-1H-benzo[d]imidazole (BIH) was synthesized according to literature procedures.[17, 18] HMabiq and [Zn(Mabiq)(OTf)] (**4**) were synthesized as previously described.[4, 19]

[Fe(Mabiq)(MeCN)$_2$]OTf (**1**) was synthesized according to a modified literature procedure[20] by adding a solution of Fe(OTf)$_2$ (65.2 mg, 184.3 µmol) in MeCN to a mixture of HMabiq (100 mg, 184.3 µmol) and triethylamine (25.7 µL, 184.3 µmol) in MeCN, leading to an immediate color change to intense green. The mixture was stirred overnight to ensure complete complexation. The solution was filtered through celite, dried and recrystallized from MeCN/Et$_2$O yielding **1** (98.3 mg, 125 µmol, 67.7%).

^{1}H-NMR (400 MHz, CD$_3$CN): δ (ppm) = 9.24 (dd, J = 8.2, 1.5 Hz, 2H), 8.33 (d, J = 8.3 Hz, 2H), 8.11 (ddd, J = 8.3, 6.9, 1.5 Hz, 2H), 7.95 (ddd, J = 8.1, 6.9, 1.2 Hz, 2H), 7.01 (s, 1H), 1.96 (s, 6H), 1.53 (s, 24H). ^{19}F-NMR (376 MHz, THF-d$_8$): δ (ppm) = 77.74. Elemental analysis calcd. (%) for $C_{38}H_{39}F_3FeN_{10}O_3S$: C, 55.08, H, 4.74, N, 16.90, S, 3.87 found C, 54.73, H, 4.51, N, 16.70, S, 3.61. UV-Vis [λ_{max}, nm (ε, 10^3 $M^{-1}cm^{-1}$), in MeCN]: 310 (29.4), 322 (24.4), 351 (44.5), 437 (12.3), 464 (14.8), 630 (5.8), 665 (6.1).

[Cu(Xantphos)Fe(Mabiq)(MeCN)(OTf)]OTf (**2**) was synthesized by adding a solution of **3** (*vide infra*) (19.1 mg, 24.13 µmol) in THF to **1** (20.0 mg, 24.13 µmol) in THF leading to a color

change from green to brown. The solution was stirred for 30 min, filtered through celite, dried and recrystallized from THF/Pentane to give **2** (38.1 mg, 24.13 µmol, 100%). Under these conditions, both NMR and elemental analysis indicate one MeCN coordinated to the Fe center. These samples were used in all catalytic experiments. Single crystals suitable for XRD were obtained from DCM/Et_2O; the corresponding structure shows both triflate anions coordinated to the Fe center instead of MeCN (i.e., [Cu(Xantphos)Fe(Mabiq)$(OTf)_2$]).

^{1}H-NMR (400 MHz, THF-d_8): δ (ppm) = 9.60 (d, *J* = 8.1 Hz, 2H), 8.40 (s, 2H), 7.86 (d, *J* = 7.7 Hz, 2H), 7.38–6.89 (m, 27H), 6.36 (m, 2H), 1.99 (s, 6H), 1.88 (s, 3H), 1.60 (s, 12H), 1.17 (s, 12H). ^{31}P-NMR (162 MHz, THF-d_8): δ (ppm) = 11.05. ^{19}F-NMR (376 MHz, THF-d_8): δ (ppm) = 76.26. Elemental analysis calcd. (%) for $C_{76}H_{68}CuF_6FeN_9O_7P_2S_2$: C, 57.82, H, 4.34, N, 7.98, S, 4.06 found C, 57.64, H, 4.34, N, 7.55, S, 3.91. UV-Vis [λ_{max}, nm (ε, 10^3 $M^{-1}cm^{-1}$), in MeCN]: 310 (34.6), 322 (37.5), 351 (47.65), 437 (13.45), 464 (16.2), 630 (6.15), 665 (6.5).

[Cu(Xantphos)(OTf)] (**3**) was obtained by addition of a solution of [Cu$(MeCN)_4$]OTf (65.1 mg, 172.8 µmol) in THF to 1 equiv. of Xantphos (100 mg, 172.8 µmol). The mixture was stirred for 30 min, filtered through celite and dried, followed by recrystallization from THF/Pentane to give **3** in 100% yield (136.7 mg, 172.8 µmol).

^{1}H-NMR (400 MHz, $CDCl_3$): δ (ppm) = 7.58 (d, *J* = 7.8 Hz, 2H), 7.34 (m, 10H), 7.25 (m, 10H), 7.14 (dd, *J* = 8.8, 6.5 Hz, 2H), 6.65 (m, 2H), 1.68 (s, 6H). ^{31}P-NMR (162 MHz, $CDCl_3$): δ (ppm) = 15.58. ^{19}F-NMR (376 MHz, $CDCl_3$): δ (ppm) = 77.59. ESI-MS: $[Cu(Xantphos)]^+$ (*m*/*z*: 641.1212, calc. 641.1219).

^{1}H-, ^{31}P- and ^{19}F-NMR of 1, 2 and 3

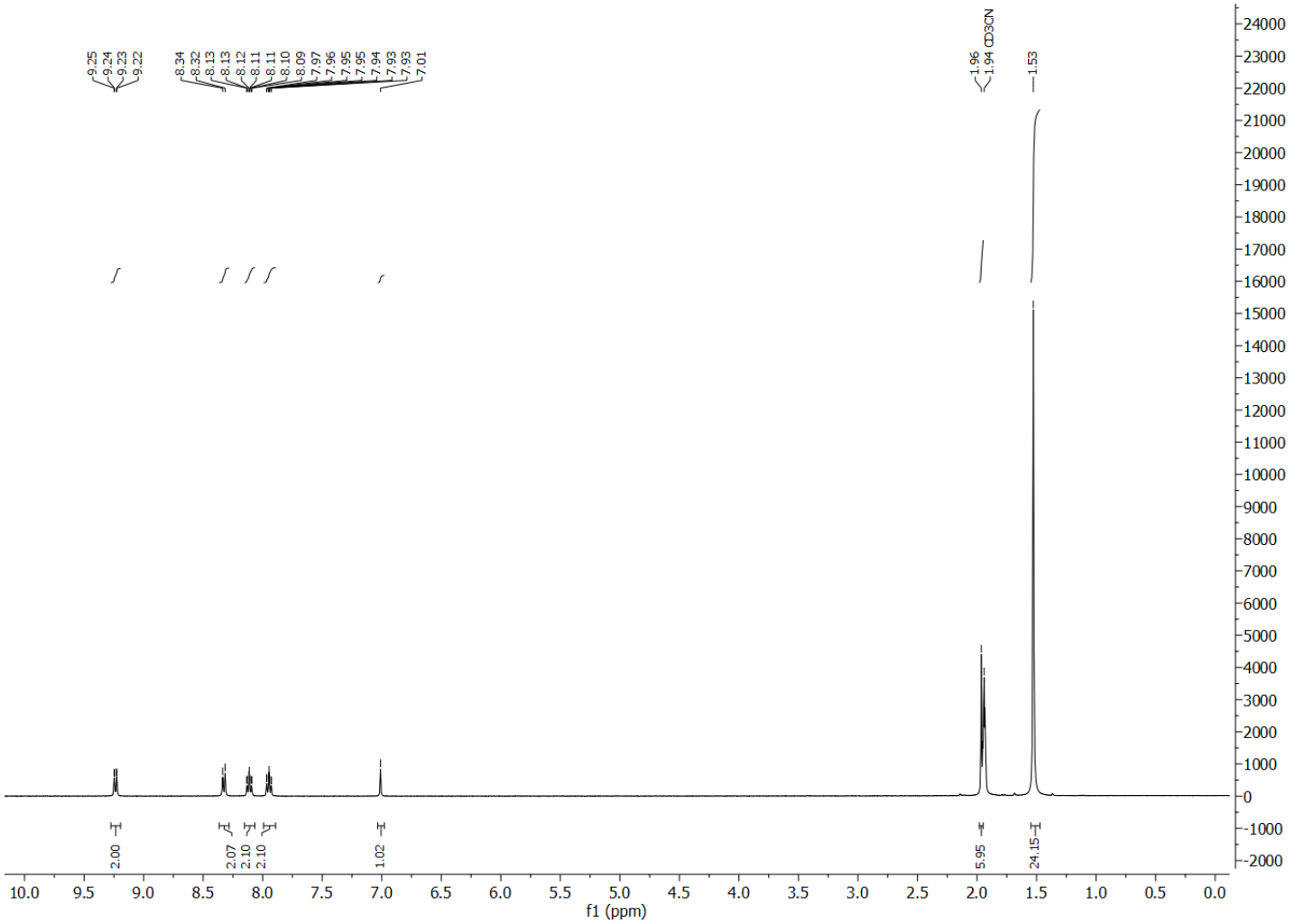

Fig. S1 ^{1}H-NMR of [Fe(Mabiq)(MeCN)$_2$]OTf (**1**) in CD_3CN.

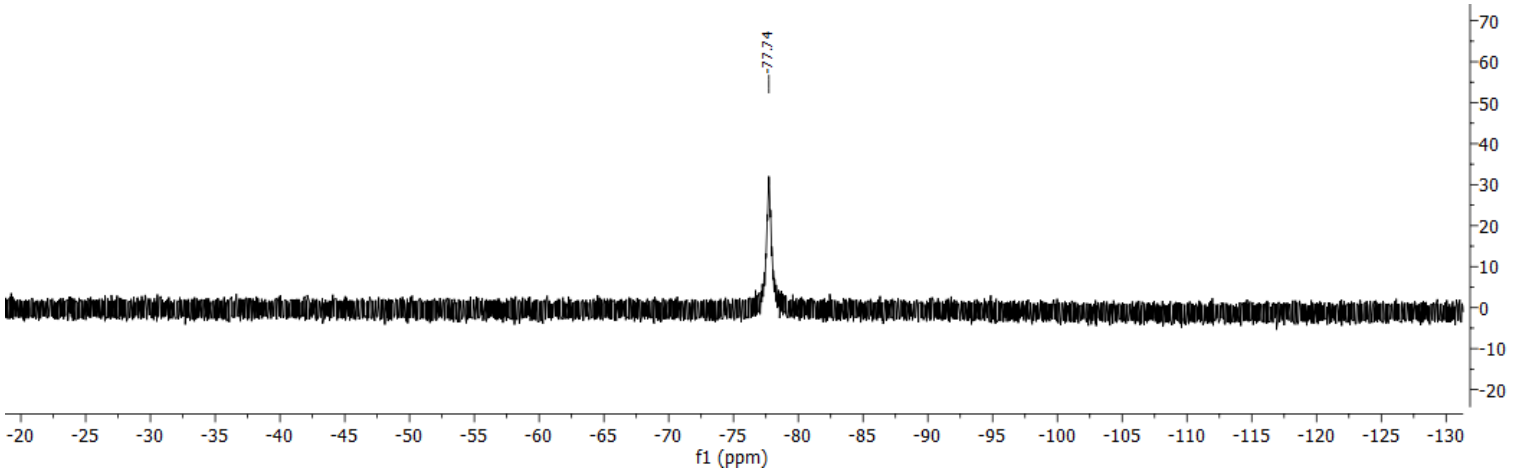

Fig. S2 ^{19}F-NMR of **1** in THF-d_8.

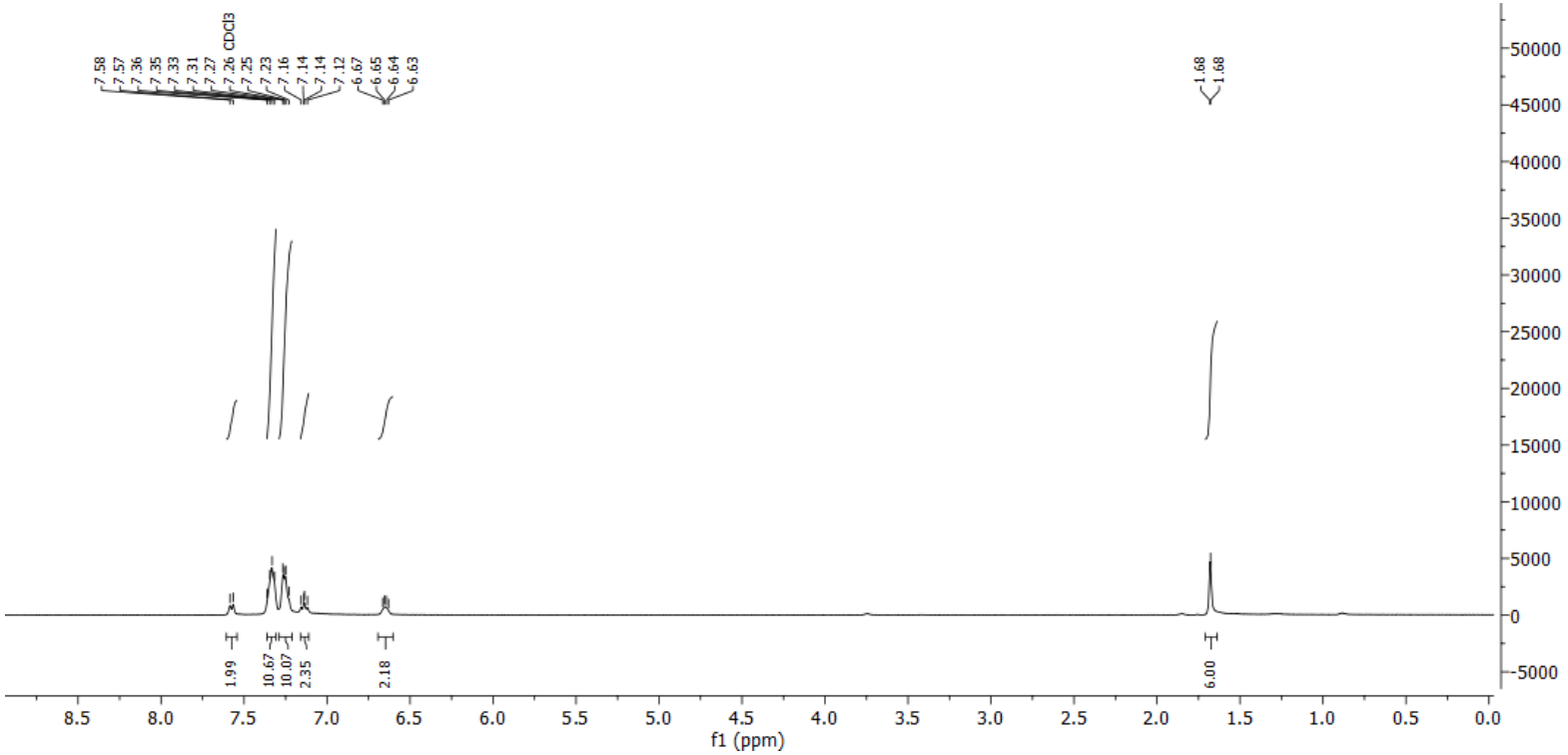

Fig. S3 ^{1}H-NMR of [Cu(Xantphos)]OTf (**3**) in $CDCl_3$.

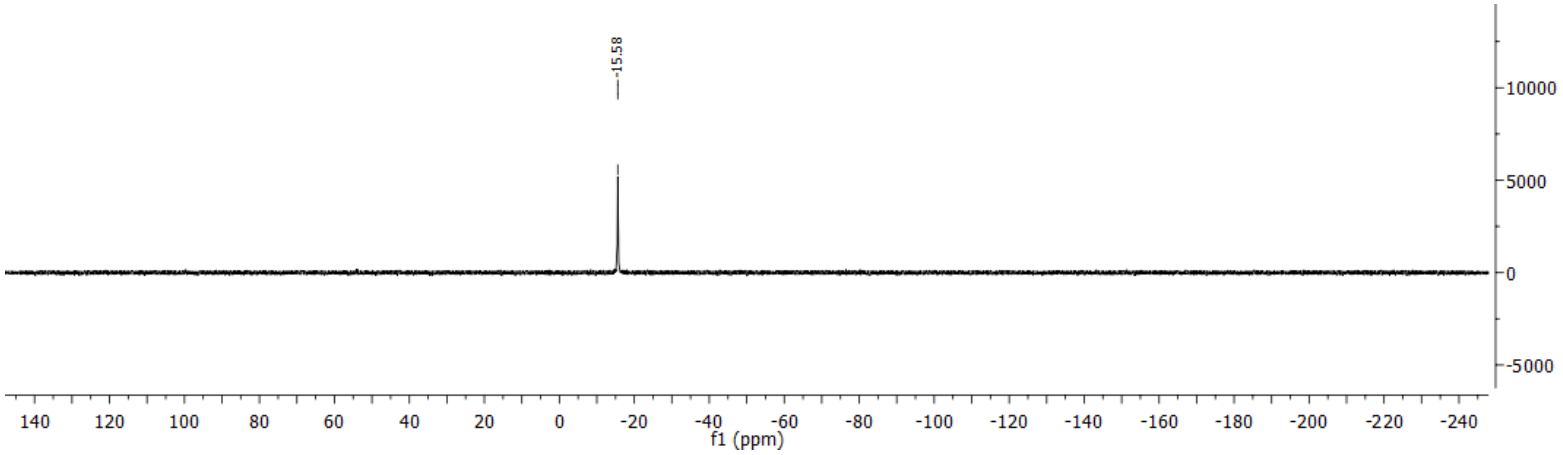

Fig. S4 ^{31}P-NMR of **3** in $CDCl_3$.

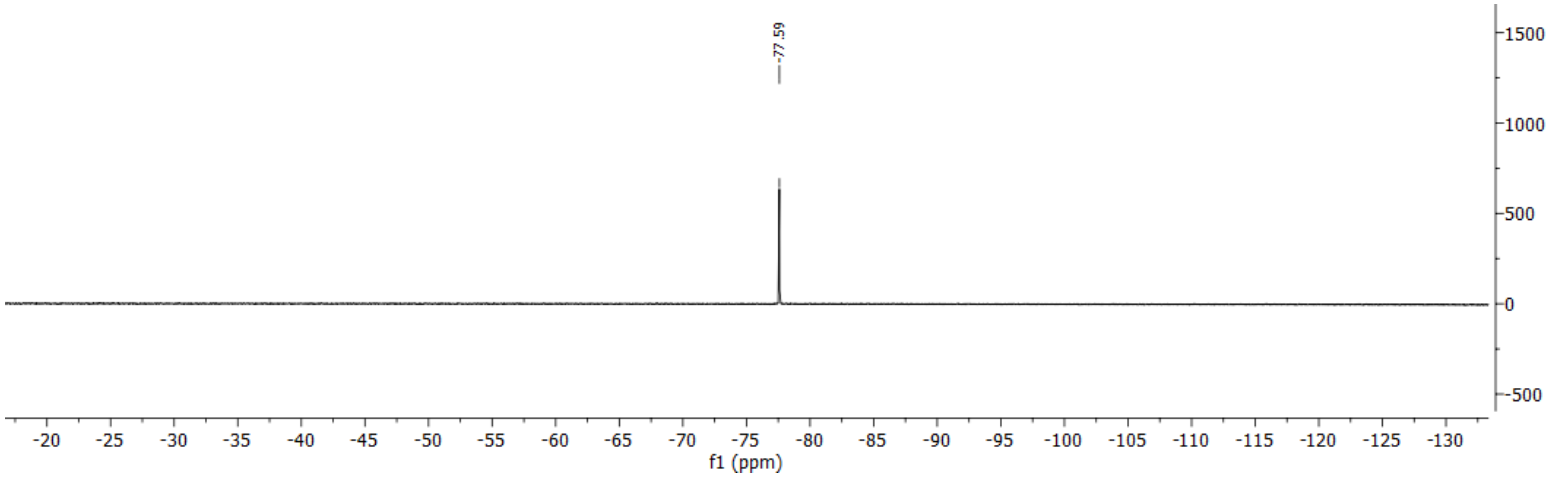

Fig. S5 ^{19}F-NMR of **3** in CD_3CN.

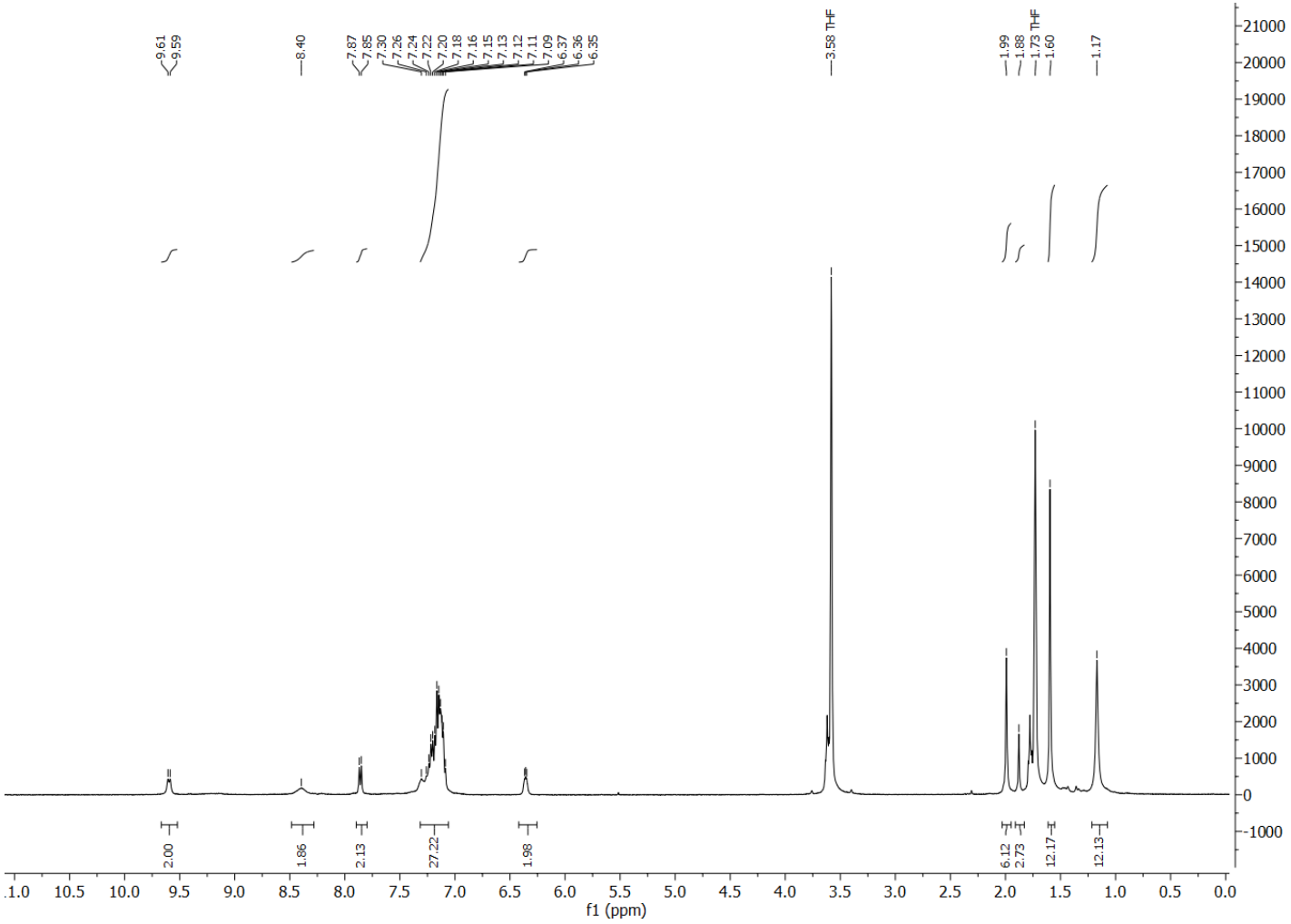

Fig. S6 ^{1}H-NMR of [Cu(Xantphos)Fe(Mabiq)(MeCN)(OTf)]OTf (**2**) in THF-d_8.

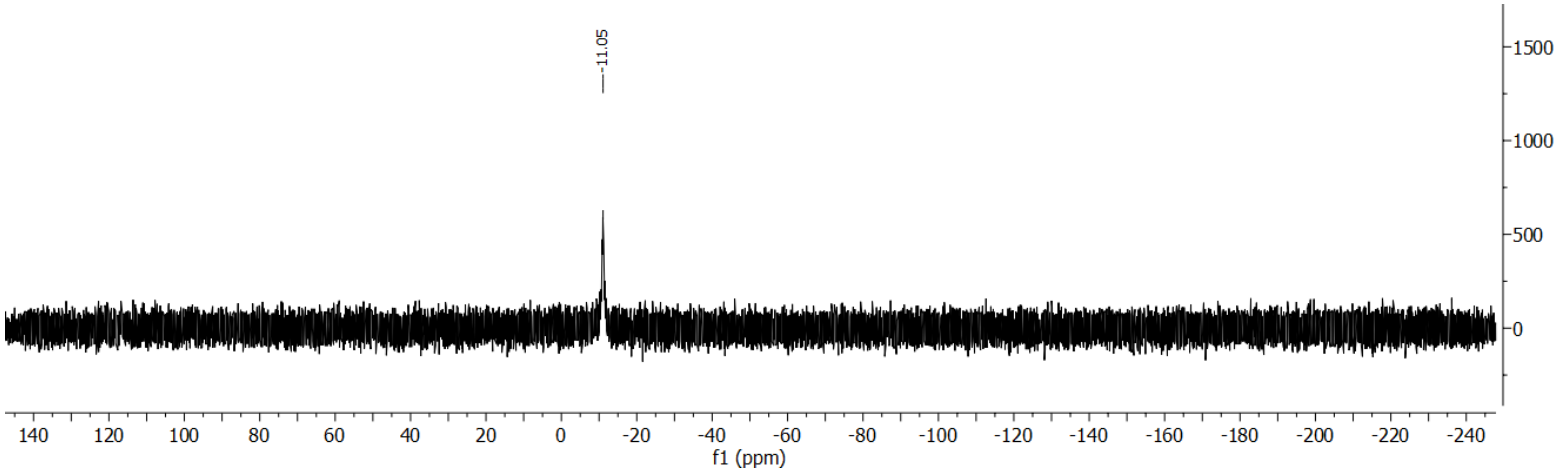

Fig. S7 ^{31}P-NMR of **2** in THF-d_8.

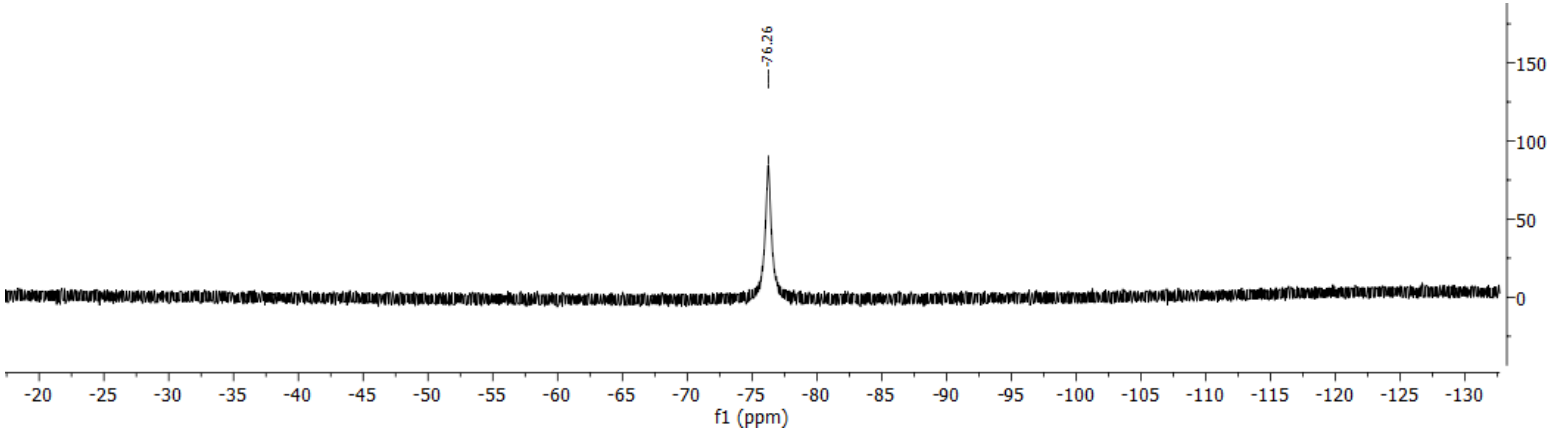

Fig. S8 ^{19}F-NMR of **2** in THF-d_8.

Comparison of ^{1}H-NMR of 1, 2 and 3 in the aromatic region

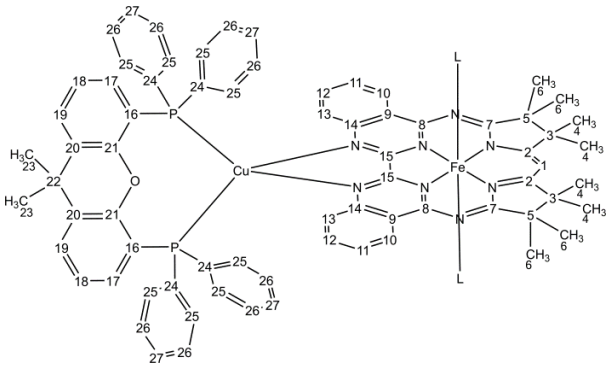

Chart 1 Numbering scheme of **2** used for NMR figures. The same numbering scheme was used for the monometallic complexes for clarity.

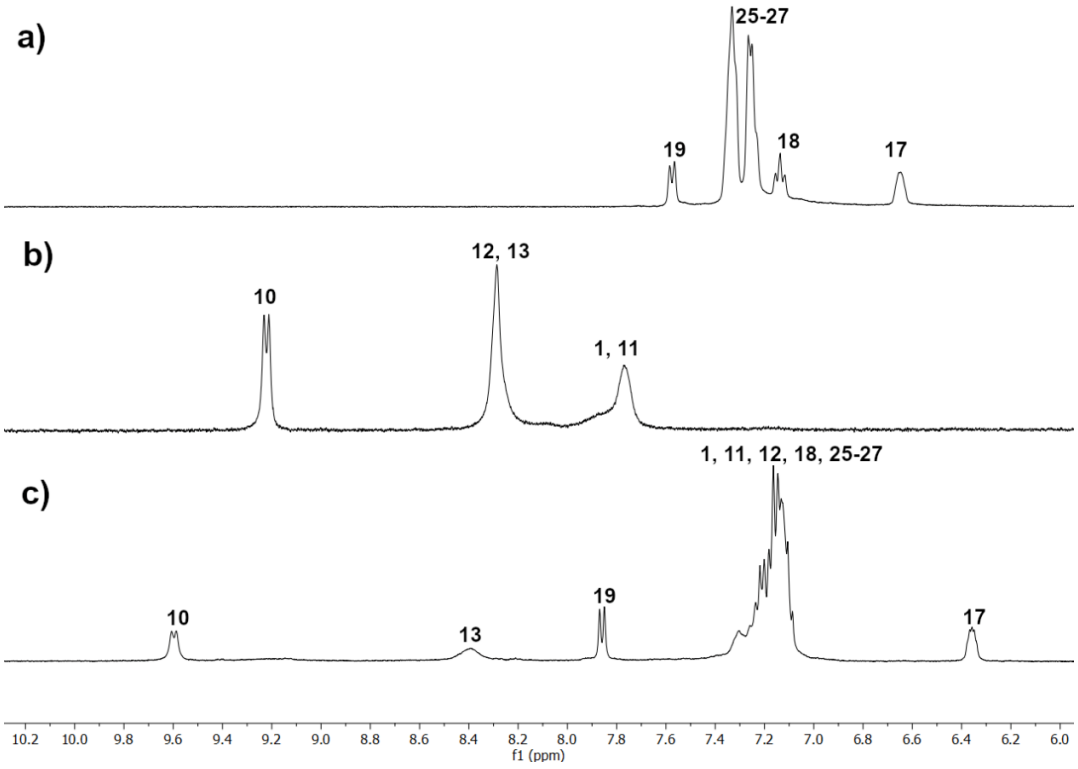

Fig. S9 Aromatic region of ^{1}H-NMR spectra of **3** in $CDCl_3$ (**a**), **1** (**b**) and **2** (**c**) in THF-d_8. The protons are numbered according to the numbering scheme shown in Chart 1.

Molecular structure of 2

For all catalysis experiments **2** was recrystallized from THF/Pentane. Both NMR and elemental analysis indicate one MeCN coordinated to the Fe center (i.e. [Cu(Xantphos)Fe(Mabiq)(MeCN)(OTf)](OTf)). Single crystals suitable for XRD were obtained from DCM/Et_2O; the corresponding structure shows both triflate anions coordinated to the Fe center (i.e. [Cu(Xantphos)Fe(Mabiq)$(OTf)_2$]).

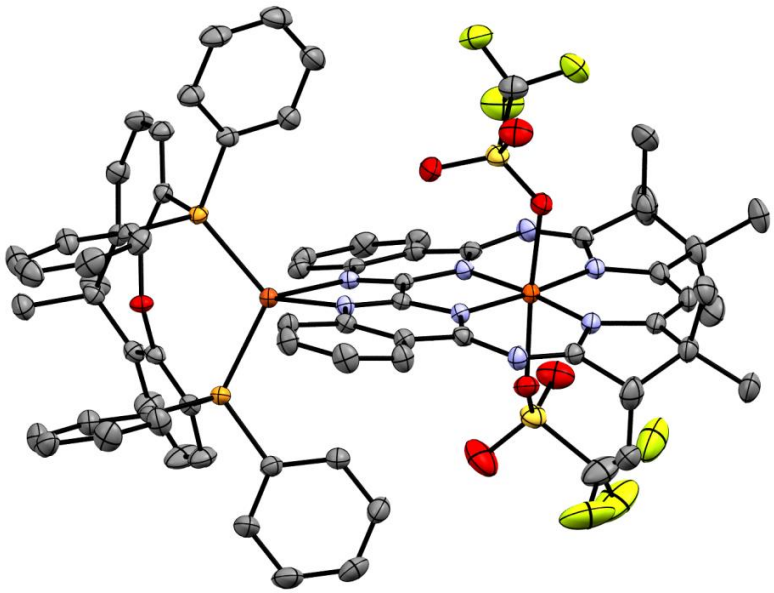

Fig. S10 ORTEP style representation of the asymmetric unit of **2** in the solid state. Ellipsoids are shown at 50% probability level and hydrogen atoms are omitted for clarity.

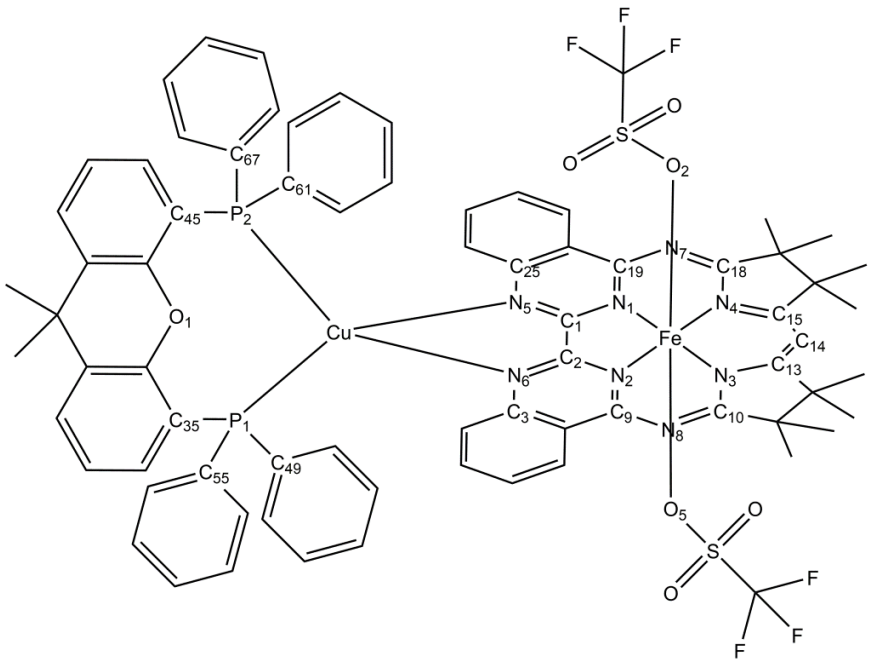

Chart 2 Atomic numbering scheme for **2**.

Table S1 Crystallographic parameters for **2**.

Empirical formula	$C_{74}H_{65}CuF_6FeN_8O_7P_2S_2$
Formula weight	1537.80
Crystal system	Triclinic
Space group	P −1
a (Å)	11.046(2)
b (Å)	18.140(3)
c (Å)	10.185(4)
α (°)	81.621(6)
β (°)	86.362(7)
γ (°)	82.139(7)
Volume (Å³)	3959.9(13)
Z	2
ρcalc (g/cm³)	1.290
μ (mm^{-1})	0.613
F (000)	1584
Reflns. Collected	158292
Indep. reflns/Rint	14430
Data/restraints/param	14430/0/920
GOF on F²	1.062
Final R1 indexes [I ≥ 2σ(I)]	0.0357
Final wR2 indexes (all data)	0.0968
Δρmin/max ($eÅ^{-3}$)	−0.500 and 0.412
CCDC number	2284733

Table S2 Select bond lengths for **2** following the numbering scheme indicated in Chart **2**.

Cu1-P1	2.2924(8)
Cu1-P2	2.2711(6)
Cu1-N5	2.135(2)
Cu1-N6	2.110(2)
Fe1-O2	2.037(2)
Fe1-O5	2.054(2)
Fe1-N1	1.925(2)
Fe1-N2	1.925(2)
Fe1-N3	1.898(2)
Fe1-N4	1.905(2)
P1-C35	1.830(2)
P1-C49	1.828(2)
P1-C55	1.832(2)
P2-C45	1.831(2)
P2-C61	1.823(2)
P2-C67	1.832(2)
N1-C1	1.362(2)
N1-C19	1.346(3)
N2-C2	1.362(2)
N2-C9	1.346(3)
N3-C10	1.368(3)
N3-C13	1.355(3)
N4-C15	1.352(3)
N4-C18	1.368(3)
N5-C1	1.312(3)
N5-C25	1.382(2)
N6-C2	1.305(2)
N6-C3	1.386(3)
C1-C2	1.471(3)
C13-C14	1.388(3)
C14-C15	1.384(3)

Table S3 Select bond angles of **2** following the numbering scheme indicated in Chart **2**.

P1-Cu1-P2	113.48(2)
P1-Cu1-N5	114.16(5)
P1-Cu1-N6	110.79(5)
P2-Cu1-N5	113.75(5)
P2-Cu1-N6	121.14(5)
N5-Cu1-N6	79.30(6)
O2-Fe1-O5	174.08(6)
O2-Fe1-N1	96.20(7)
O2-Fe1-N2	92.08(7)
O2-Fe1-N3	87.46(7)
O2-Fe1-N4	86.66(7)
N1-Fe1-N2	84.29(7)
N1-Fe1-N4	90.84(7)
N2-Fe1-N3	91.05(7)
N3-Fe1-N4	93.92(7)
N5-C1-C2	117.9(2)
C2-N2-C9	117.9(2)
C1-N1-C19	118.4(2)
N6-C2-C1	118.2(2)
C13-C14-C15	125.9(2)

Absorption spectra of 1 and 2

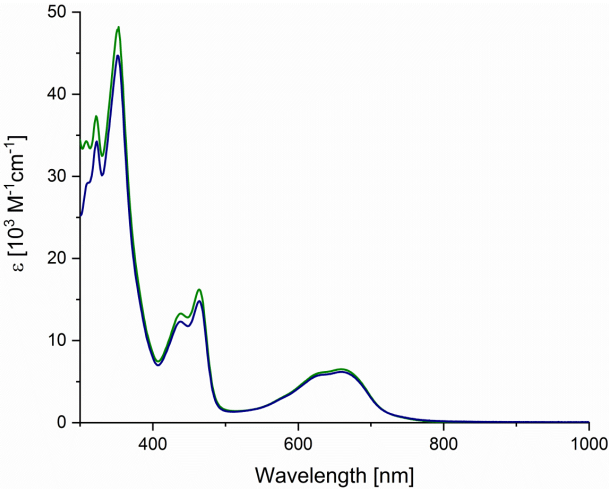

Fig. S11 UV-Vis absorption spectra of **1** (blue) and **2** (green) in MeCN.

IR spectra of 1 and 2

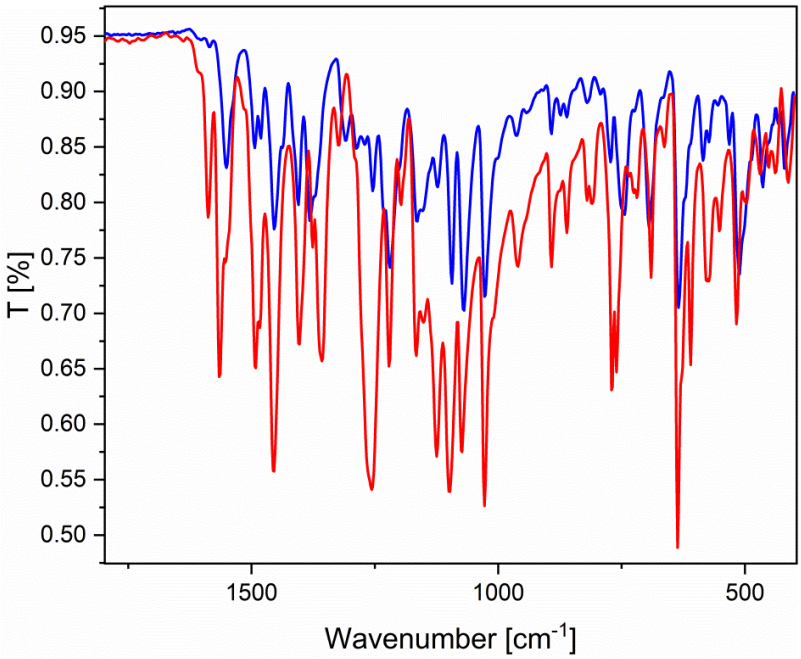

Fig. S12 IR spectra of **1** (red) and **2** (blue) in the solid state.

To assess whether the bimetallic complex dissociates in solution the IR spectrum of **2** in MeCN was compared with a mathematically combined spectrum of **1** and **3** in MeCN. The shifts in the fingerprint region suggest the complex remains stable in solution.

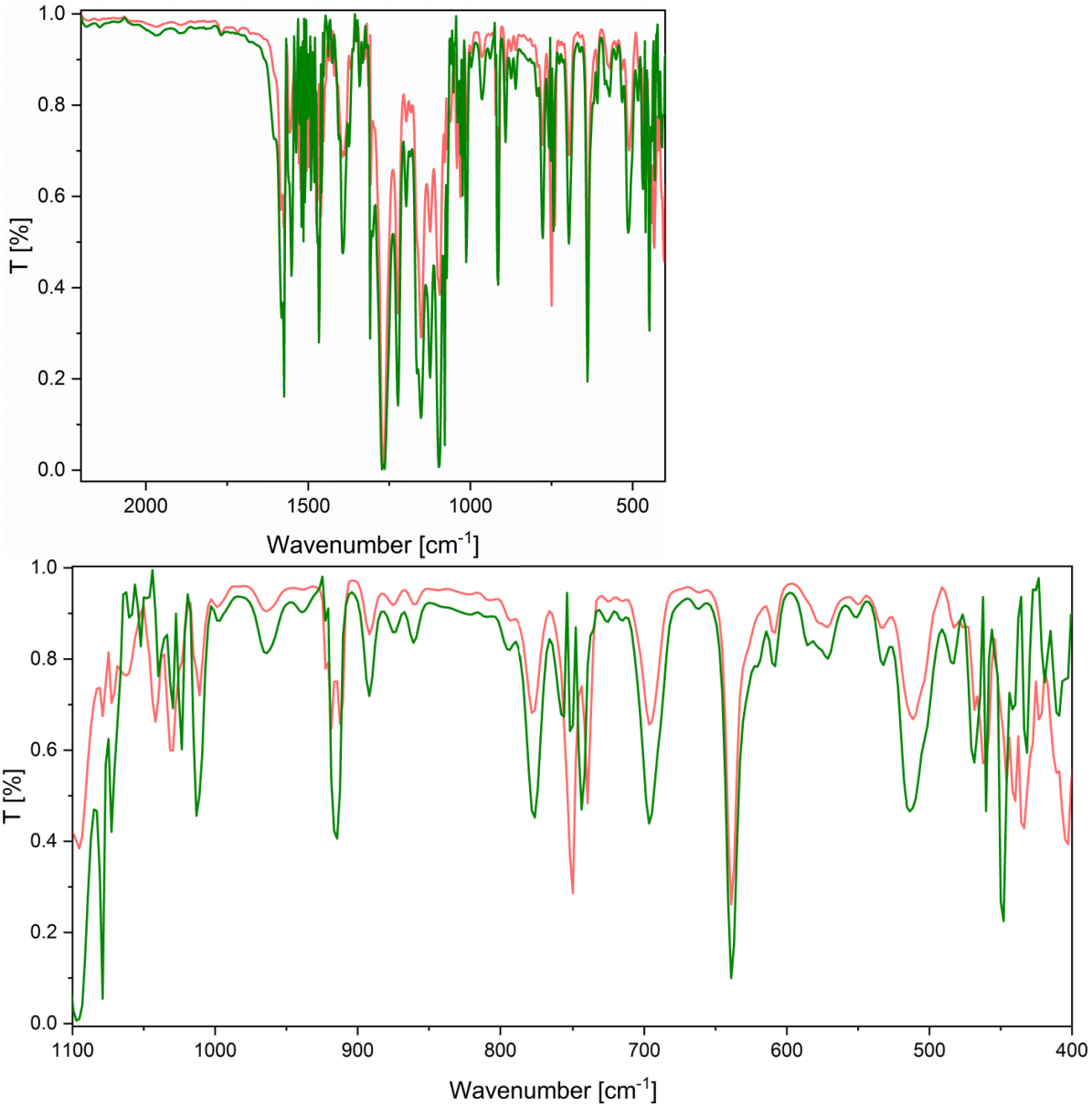

Fig. S13 Top: IR spectrum of a 6 mM solution of **2** in MeCN (green) in comparison to a mathematical combination of solution IR spectra of **1** and **3** (red) Bottom: Zoom-in of the fingerprint region of the upper IR spectra.

CV data for 1 and 2

Table S4 Comparison of redox potentials of **1** and **2** in MeCN.

Complex	$Fe^{III/II}$	Mabiq/$Mabiq^{\bullet-}$	$Mabiq^{\bullet-}/Mabiq^{2-}$	$[Fe(Mabiq)]^{-/2-}$
1	0.60 V_{Fc}	−1.31 V_{Fc}	−1.65 V_{Fc}	−2.35 V_{Fc}
2	0.62 V_{Fc}	−1.17 V_{Fc}	−1.50 V_{Fc}	−1.95 V_{Fc}

[PhOH] dependence of 2

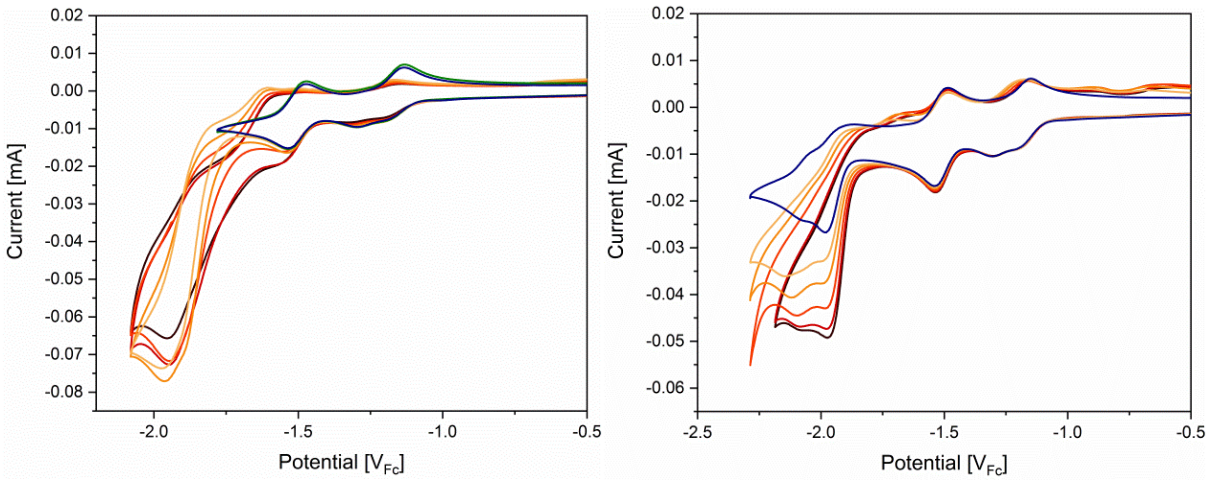

Fig. S14 CV of a 0.5 mM solution of **2** (blue) in MeCN (0.1 M [(*n*-Bu)$_4$N]PF_6) with varying amounts of PhOH (Yellow to black: 10, 25, 50, 75 and 85 equiv.) in the presence (left, green: after purging with CO_2) and absence (right) of CO_2.

Headspace analysis after photocatalysis experiments

Various control experiments were conducted to confirm CO_2 as the product source. In the absence of CO_2 (Ar atmosphere) no significant amounts of CO were detected (Table S5) such that the CO produced under standard conditions does not originate from organic degradation

products. Experiments using isotopically labelled $^{13}CO_2$ further confirmed CO_2 as the product source (Fig. S17). Analysis of the liquid phase of the reaction mixtures by ^{1}H- and ^{13}C-NMR did not reveal any other reaction products.

Table S5 Analysis of photocatalytic CO_2 reduction by **1** and **2**.

entry	complex	deviation from standard conditions	n_{CO} [µmol]	TON_{CO}	TOF_{CO} [s^{-1}]
1	**1**	-	2.65 ± 0.24	663 ± 61	0.18 ± 0.02
2	**2**	-	3.77 ± 0.39	942 ± 98	0.26 ± 0.03
3	**1**	No light	0.0019 ± 0.001	0.4 ± 0.3	$(13 \pm 9)\times10^{-5}$
4	**2**	No light	0.0016 ± 0.001	0.4 ± 0.3	$(11 \pm 7)\times10^{-5}$
5	**1**	No CO_2	0.005 ± 0.006	1 ± 1	$(3.6 \pm 3.9)\times10^{-4}$
6	**2**	No CO_2	0.004 ± 0.003	1 ± 0.6	$(2.7 \pm 2)\times10^{-4}$
7	**1**	No BIH	0.005 ± 0.002	1.3 ± 0.5	$(4 \pm 2)\times10^{-4}$
8	**2**	No BIH	0.006 ± 0.001	1.5 ± 0.3	$(43 \pm 9)\times10^{-5}$
9	**1**	0.05 mL Hg	1.9 ± 0.2	469 ± 59	0.13 ± 0.02
10	**2**	0.05 mL Hg	3.1 ± 0.2	784 ± 55	0.22 ± 0.015
11	**No**	No catalyst	0.07 ± 0.03	-	-
12	**3**	-	0.089 ± 0.007	-*	-*
13	**4**	-	0.013 ± 0.01	-*	-*
14	**1**	No **Ru-PS**	$(50 \pm 5)\times10^{-4}$	1.3 ± 0.12	$(35 \pm 3)\times10^{-5}$
15	**2**	No **Ru-PS**	0.37 ± 0.1	92 ± 30	0.025 ± 0.008
16	**2**	No **Ru-PS**, 0.05 mL Hg	0.94 ± 0.33	236 ± 82	0.065 ± 0.023

Standard conditions: 2 µM complex (**1**, **2** or **3**), 170 µM PhOH, 200 µM **Ru-PS**, 100 mM BIH in a total volume of 2 mL, purged with CO_2 for 2 min, irradiation at 455 nm for 1 h at 20 °C.

* Due to the similar amount of CO produced, it is likely that **Ru-PS** and not **3** or **4** acts as the catalyst in these experiments, therefore no TON and TOF are given for **3** and **4**.

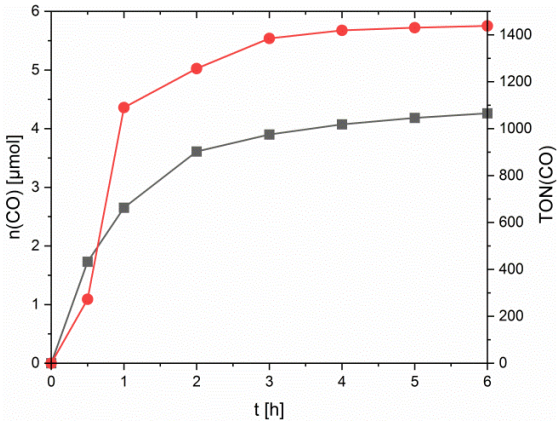

Fig. S15 CO evolution over time by **1** (black) and **2** (red) under standard conditions.

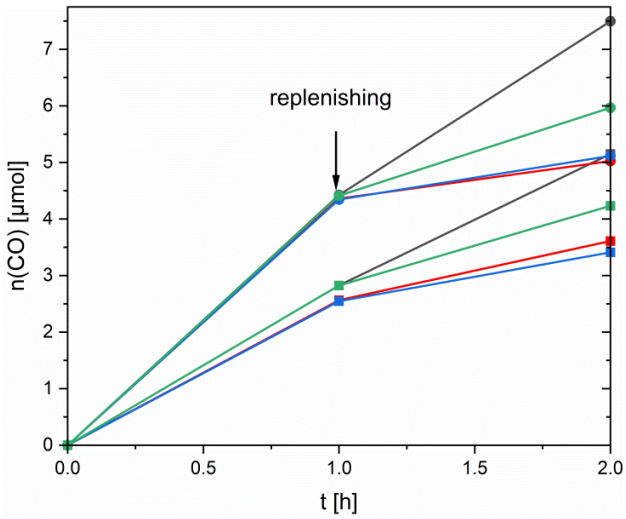

Fig. S16 CO production by **1** (squares) and **2** (dots) with replenishing of CO_2 (red), BIH/**Ru-PS**/CO_2 (blue), catalyst/CO_2 (green) and catalyst/BIH/**Ru-PS**/CO_2 (black) after 1 h. Standard conditions: 2 µM catalyst, 170 µM PhOH, 200 µM **Ru-PS**, 100 mM BIH.

For analysis of the gaseous headspace sample by MS, the headspace sample was taken using a gastight syringe equipped with a valve. The sample was loaded onto the spectrometer by opening the valve of the syringe after which it was slowly drawn into the machine due to the vacuum applied by an internal pump. This is reflected in the shape of the signal. The retention time depended on the time point the valve was opened. The spectrometer was set to monitor a mass of 29 which corresponds to the ^{13}CO.

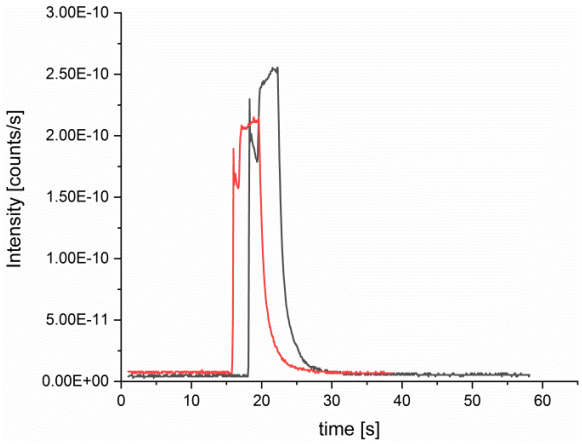

Fig. S17 MS analysis of the headspace after photocatalytic CO_2 reduction by **1** (red) and **2** (black) using $^{13}CO_2$ monitoring a mass of 29.

The precipitation of BI^+ in our experiments—the degradation product of BIH after donating two electrons and one proton—(confirmed by ^{1}H-NMR, see Fig. S18) prevented the use of dynamic light scattering (DLS) to assess nanoparticle formation.

NMR of precipitate after photocatalysis

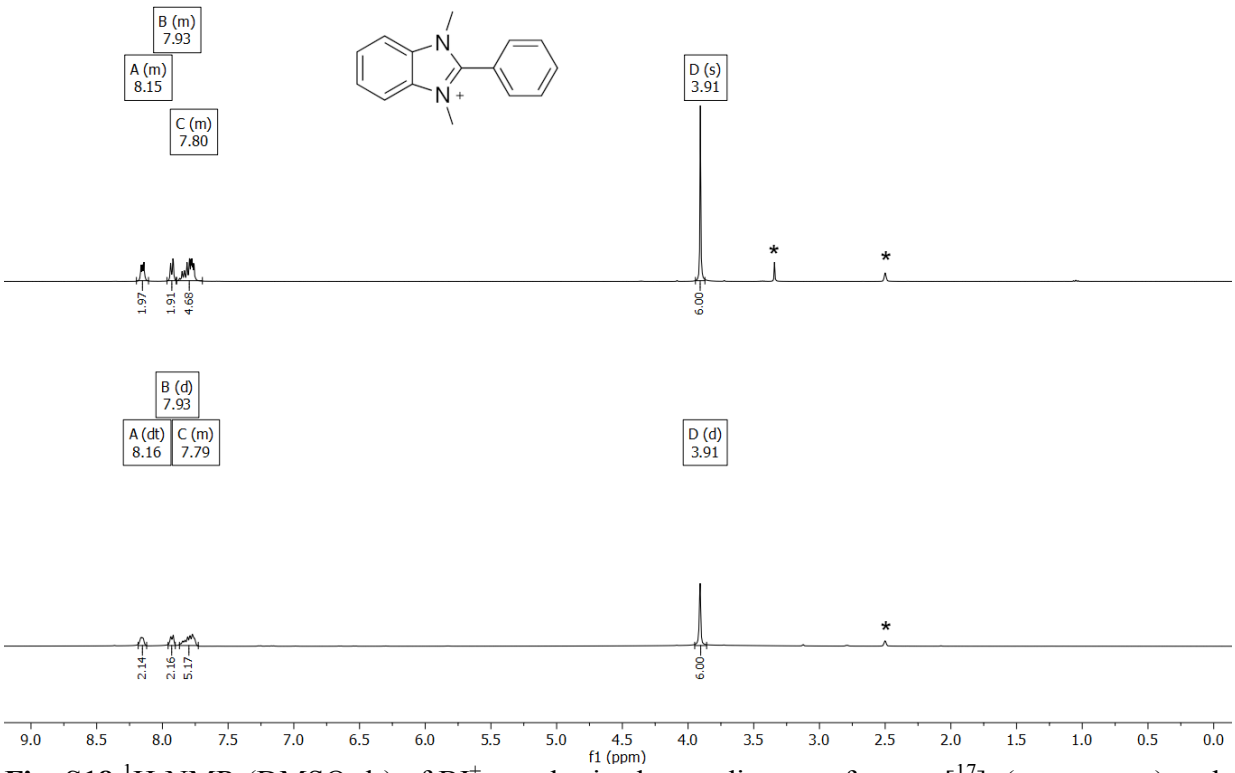

Fig. S18 ^{1}H-NMR (DMSO-d_6) of BI^+, synthesized according to reference [17], (upper trace) and the solid isolated (lower trace) after photocatalytic CO_2 reduction by **1** or **2**, respectively, under standard conditions (2 µM catalyst, 200 µM **Ru-PS**, 170 µM PhOH, 100 mM BIH, purged with CO_2 for 2 min, irradiated at 455 nm for 1 h at 20 °C). Residual solvent signals (DMSO and H_2O in DMSO) are marked with an asterisk.

Concentration dependence for photocatalytic CO_2 reduction

Table S6 Catalyst concentration dependence for photocatalytic CO_2 reduction.

entry	complex	$c_{complex}$ [µM]	n_{CO} [µmol]	TON_{CO}	TOF [s^{-1}]
1	**1**	0.5	0.77 ± 0.09	765 ± 87	0.21 ± 0.02
2	**1**	2	2.65 ± 0.24	663 ± 61	0.18 ± 0.02
3	**1**	50	14 ± 2	139 ± 17	0.039 ± 0.005
4	**2**	0.5	0.1 ± 0.004	114 ± 4	0.03 ± 0.001
5	**2**	2	3.77 ± 0.4	942 ± 98	0.26 ± 0.03
6	**2**	50	17 ± 3	172 ± 32	0.048 ± 0.009

Standard conditions: 85 equiv. PhOH, 200 µM **Ru-PS**, 100 mM BIH in a total volume of 2 mL, purged with CO_2 for 2 min, irradiated at 455 nm for 1 h at 20 °C.

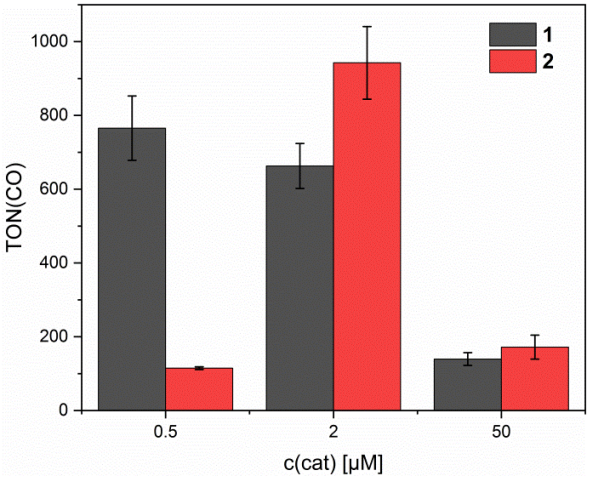

Fig. S19 Photocatalytic CO_2 reduction by **1** (black) and **2** (red) at different catalyst concentrations. Standard conditions: 100 mM BIH, 200 µM **Ru-PS**, 85 equiv. PhOH, CO_2, irradiation at 455 nm for 1 h at 20 °C.

Proton source dependence for photocatalytic CO_2 reduction by 1 and 2

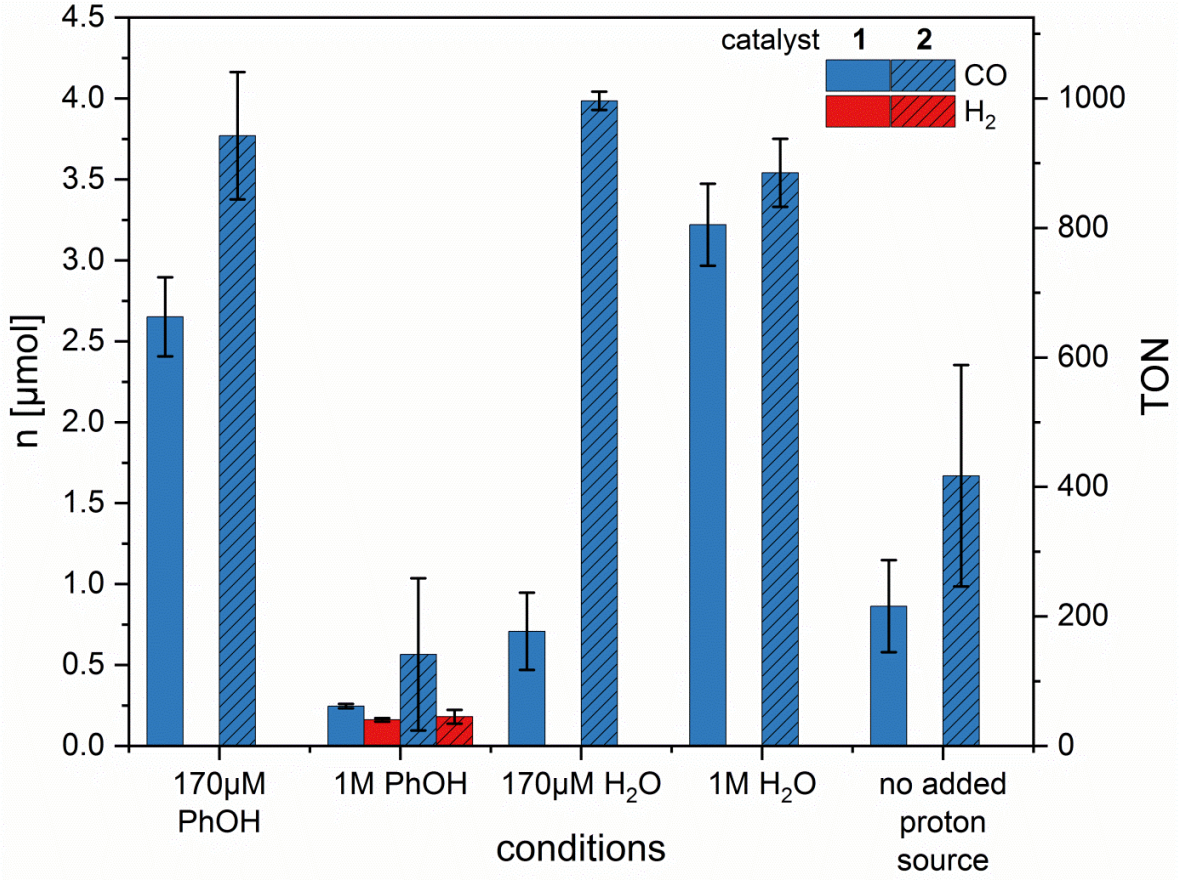

Fig. S20 Results of analysis for photocatalytic CO_2 reduction by **1** (solid columns) and **2** (dashed column) using varying amounts of PhOH or H_2O as proton source. Blue bars depict the amount of CO produced; red bars the amount of H_2 produced. Standard conditions: 2 µM catalyst, 200 µM Ru-PS, 100 mM BIH, proton source and CO_2. The solutions were irradiated for 1 h at 455 nm at 20 °C.

Table S7 Proton source dependence on photocatalytic CO_2 reduction by **1** and **2**.

Entry	Complex	Proton source	n_{CO} [µmol]	TON_{CO}	TOF_{CO} [s^{-1}]	n_{H2} [µmol]	TON_{H2}	TOF_{H2} [s^{-1}]
1	**1**	170 µM PhOH	2.65 ± 0.24	663 ± 61	0.18 ± 0.02			
2	**1**	1 M PhOH	0.25 ± 0.01	62 ± 3	0.0171 ± 0.0009	0.16 ± 0.01	40 ± 3	0.0112 ± 0.0008
3	**1**	170 µM H_2O	0.7 ± 0.2	177 ± 60	0.05 ± 0.02			
4	**1**	1 M H_2O	3.2 ± 0.3	805 ± 63	0.22 ± 0.02			
5	**1**	None	0.86 ± 0.28	216 ± 71	0.06 ± 0.02			
6	**2**	170 µM PhOH	3.77 ± 0.4	942 ± 98	0.26 ± 0.03			
7	**2**	1 M PhOH	0.56 ± 0.47	141 ± 117	0.04 ± 0.03	0.18 ± 0.04	45 ± 11	0.013 ± 0.003
8	**2**	170 µM H_2O	3.99 ± 0.06	996 ± 14	0.277 ± 0.004			
9	**2**	1 M H_2O	3.5 ± 0.2	885 ± 53	0.25 ± 0.01			
10	**2**	None	1.7 ± 0.7	417 ± 171	0.12 ± 0.05			

Standard conditions: 2 µM catalyst, 200 µM **Ru-PS**, 100 mM BIH in a total volume of 2 mL, purged with CO_2 for 2 min, irradiated at 455 nm for 1 h at 20 °C.

CV of 1 and 2 in the presence of H_2O and CO_2

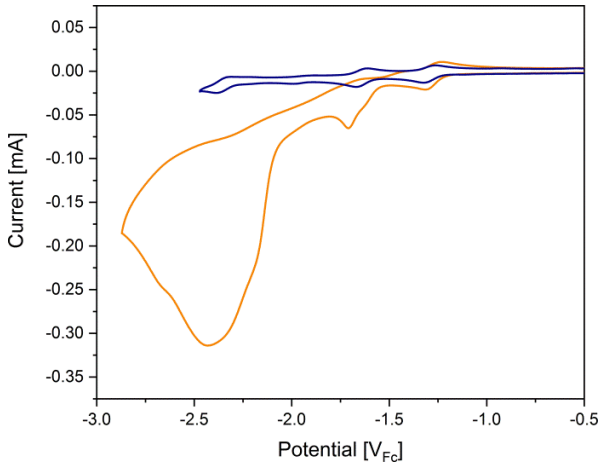

Fig. S21 CV of **1** (0.5 mM) under Ar atmosphere (blue) and Orange: in the presence of CO_2 and 1 M H_2O (0.1 M $[N(n\text{-}Bu)_4]PF_6$ in MeCN, scan rate 100 mV/s).

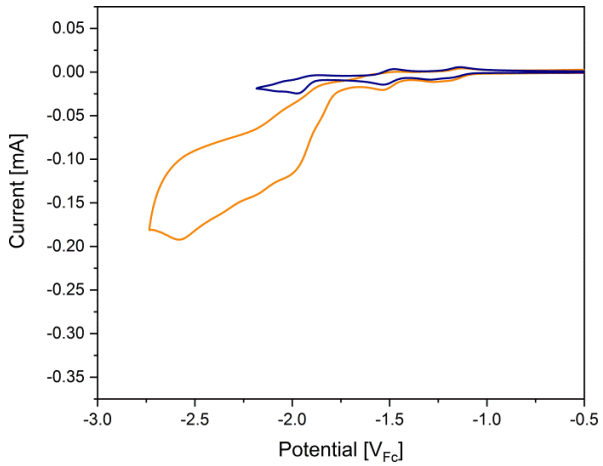

Fig. S22 CV of **2** (0.5 mM) under Ar atmosphere (blue) and Orange: in the presence of CO_2 and 1 M H_2O (0.1 M $[N(n\text{-}Bu)_4]PF_6$ in MeCN, scan rate 100 mV/s).

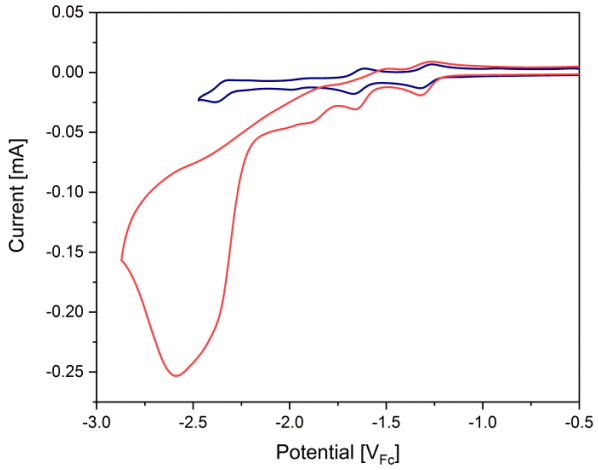

Fig. S23 CV of **1** (0.5 mM) under Ar atmosphere (blue) and Red: in the presence of CO_2 and 100 equiv. H_2O (0.1 M $[N(n\text{-}Bu)_4]PF_6$ in MeCN, scan rate 100 mV/s).

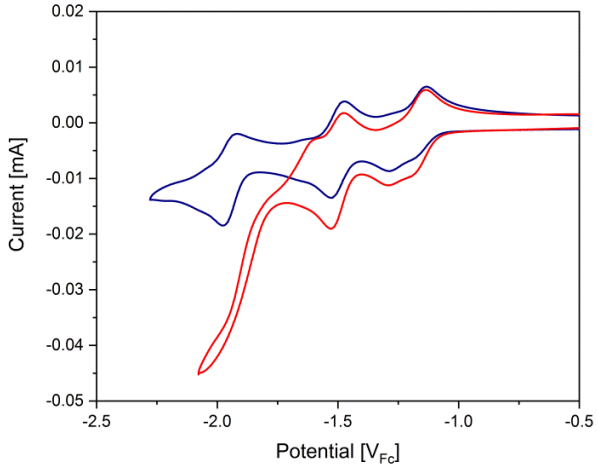

Fig. S24 CV of **2** (0.5 mM) under Ar atmosphere (blue) and Red: in the presence of CO_2 and 100 equiv. H_2O (0.1 M $[N(n\text{-}Bu)_4]PF_6$ in MeCN, scan rate 100 mV/s).

Quantum Yield Determination experiments for the photoreduction of 1 and 2

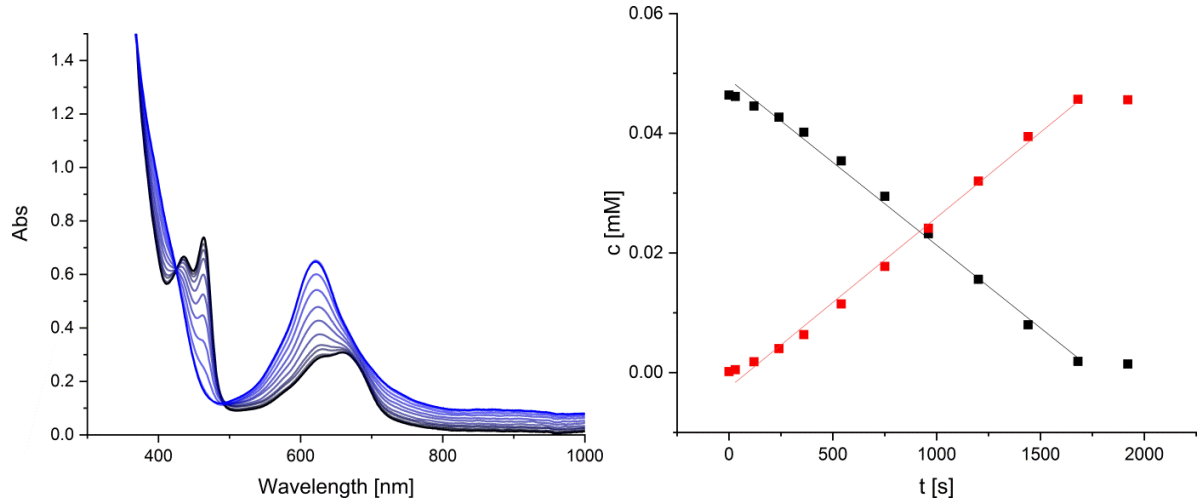

Fig. S25 Photoreduction of **1** (50 µM) in MeCN using 500 equiv. of BIH as SED. Left: UV-Vis spectral evolution from 0 to 2000 s (initial spectrum shown in black). Right: Concentration vs time plot of [Fe(Mabiq)] formation (red) and the consumption of **1** (black) with linear fit for quantum yield determination (QYD). For the QYD the absorption at 464 nm and 622 nm was monitored.

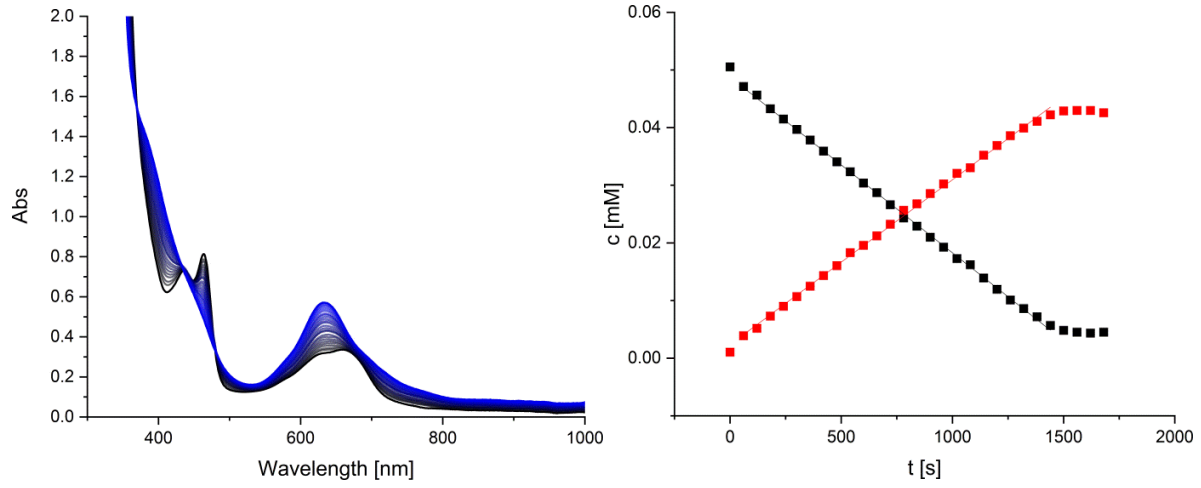

Fig. S26 Photoreduction of **2** (50 µM) in MeCN using 500 equiv. of BIH as SED. Left: UV-Vis spectral evolution from 0 to 1750 s (initial spectrum shown in black). Right: Concentration vs

time plot of [Cu(Xantphos)Fe(Mabiq)]OTf formation (red) and the consumption of **2** (black) with linear fit for QYD. For the QYD the absorption at 464 nm and 622 nm was monitored.

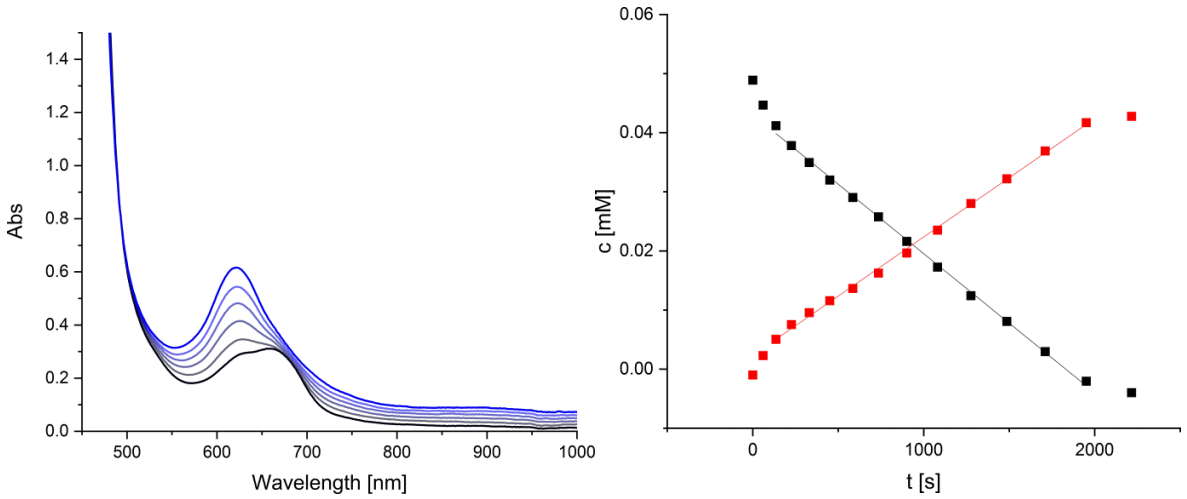

Fig. S27 Photoreduction of **1** (50 µM) in MeCN using 500 equiv. of BIH as SED and 200 µM **Ru-PS**. Left: UV-Vis spectral evolution from 0 to 2250 s (initial spectrum shown in black). Right: Concentration vs time plot of [Fe(Mabiq)] formation (red) and the consumption of **1** (black) with linear fit for QYD. For the QYD the absorption at 622 nm and 660 nm was monitored.

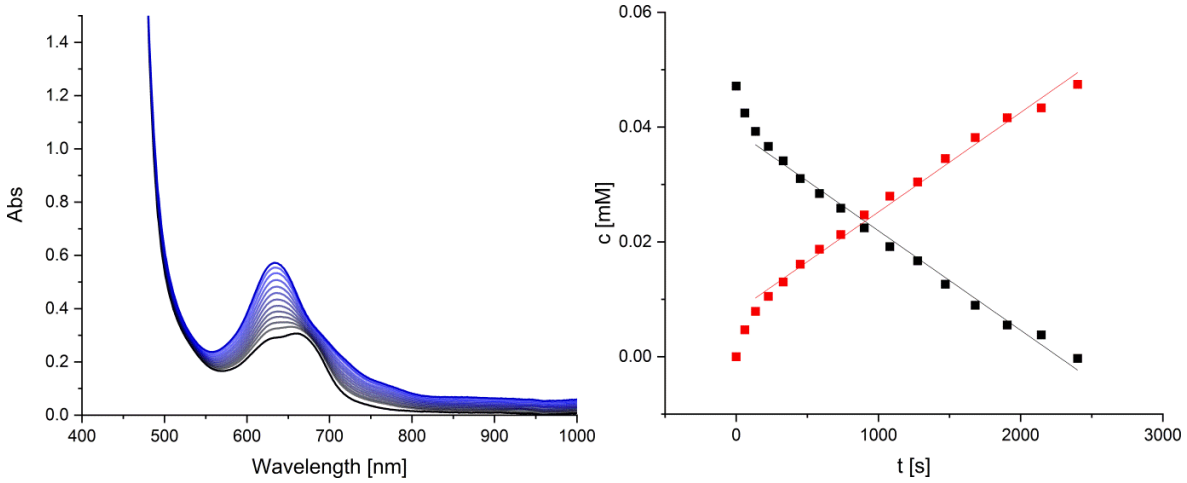

Fig. S28 Photoreduction of **2** (50 µM) in MeCN using 500 equiv. of BIH as SED and 200 µM **Ru-PS**. Left: UV-Vis spectral evolution from 0 to 2500 s (initial spectrum shown in black). Right: Concentration vs time plot of [Cu(Xantphos)Fe(Mabiq)]OTf formation (red) and the consumption of **2** (black) with linear fit for QYD. For the QYD the absorption at 622 nm and 660 nm was monitored.

Table S8 Quantum yields for photoreduction of **1** and **2**

	P_{ref} [mW]	QY	Conversion II⟶I [%]
1 + BIH	302	$8.02\times10^{-5} \pm 4.3\times10^{-6}$	98 ± 2
2 + BIH	304	$5.86\times10^{-5} \pm 8.8\times10^{-6}$	77 ± 5
1 + BIH + **Ru-PS**	19.75	$6.5\times10^{-4} \pm 2.3\times10^{-5}$	87 ± 3
2 + BIH + **Ru-PS**	23.13	$4.07\times10^{-4} \pm 2.8\times10^{-5}$	77 ± 20
1 + NEt_3 [a]	245 [a]	1.8×10^{-4} [a]	100 [a]

a) Solvent: MeCN:THF, 1:1, taken from Ref. [4]

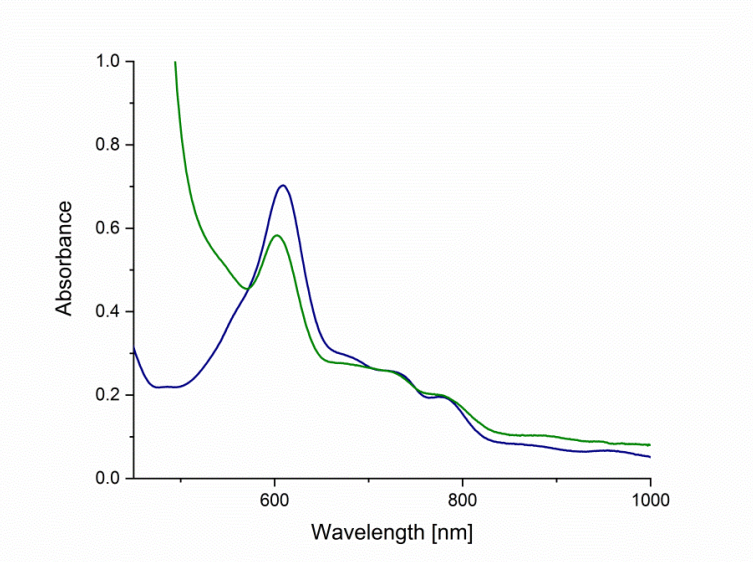

Fig. S29 Green: Absorption spectrum of the intermediate formed upon irradiation of **1** (50 µM) under photocatalytic conditions (200 µM **Ru-PS**, 25 mM BIH, 170 µM PhOH in MeCN). Blue: Absorption spectrum of the isolated intermediate $\mathbf{I_{PhOH}}$ (50 µM in THF).[21]

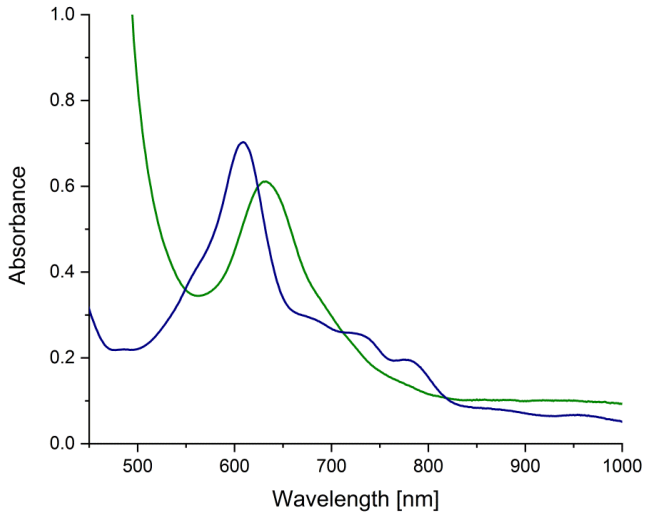

Fig. S30 Green: Absorption spectrum of the intermediate formed upon irradiation of **2** (50 µM) under photocatalytic conditions (200 µM **Ru-PS**, 25 mM BIH, 170 µM PhOH in MeCN). Blue: Absorption spectrum of $\mathbf{I_{PhOH}}$ (50 µM in THF).[21]

Molecular structure of 1

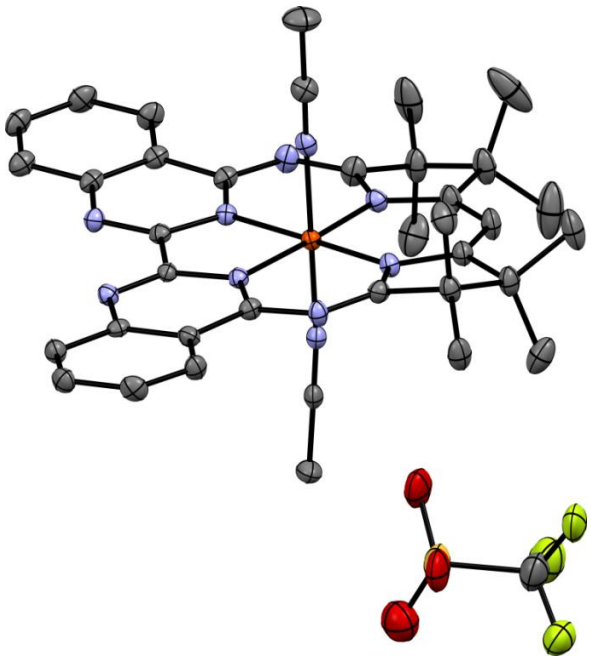

Fig. S31 ORTEP style representation of the asymmetric unit of **1** in the solid state. Ellipsoids are shown at 50% probability level and hydrogen atoms are omitted for clarity. We observed positional disorder of the triflate counter anion and on the diketiminate backbone; for clarity only one component is shown.

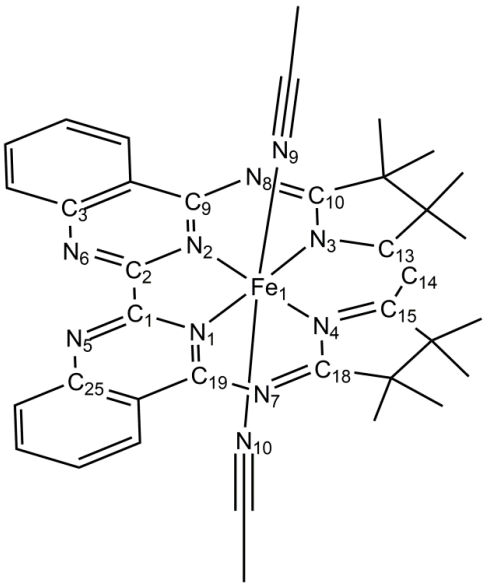

Chart S3 Atomic numbering in the molecular structure of **1**.

Table S9 Crystallographic refinement parameters of **1**.

Empirical formula	$C_{38}H_{39}F_3FeN_{10}O_3S$
Formula weight	828.6972
Crystal system	monoclinic
Space group	P 2_1/c
a (Å)	12.8059(19)
b (Å)	16.387(2)
c (Å)	20.403(3)
α (°)	90
β (°)	105.269(6)
γ (°)	90
Volume (Å³)	4130.35
Z	4
ρcalc (g/cm³)	1.333
μ (mm^{-1})	0.478
F (000)	1720
Reflns. Collected	207033
Indep. reflns/Rint	7259
Data/restraints/param	7259/631/712
GOF on F²	1.123
Final R1 indexes [I ≥ 2σ(I)]	0.0482
Final wR2 indexes (all data)	0.1474
Δρmin/max ($eÅ^{-3}$)	−0606 and 1.007
CCDC number	2284734

Table S10 Select bond lengths for **1**, numbering of atoms as indicated in Chart S3.

Fe1-N1	1.934(1)
Fe1-N2	1.939(8)
Fe1-N3	1.924(0)
Fe1-N4	1.921(2)
Fe1-N9	1.944(4)
Fe1-N10	1.946(5)
C1-C2	1.485(0)
C1-N1	1.375(9)
C1-N5	1.302(9)
C2-N2	1.375(7)
C2-N6	1.307(5)
C3-N6	1.367(9)
N1-C19	1.337(8)
N2-C9	1.335(3)
N3-C10	1.358(6)
N3-C13	1.350(3)
N4-C15	1.358(0)
N4-C18	1.367(9)
N5-C25	1.370(9)
N7-C18	1.299(7)
N7-C19	1.376(6)
N8-C9	1.360(4)
C13-C14	1.392(1)
C14-C15	1.387(4)

Table S11 Select bond angles (°) for **1**, numbering of atoms as indicated in Chart S3.

N1-Fe1-N2	84.05
N1-Fe1-N3	175.03
N1-Fe1-N4	91.42
N2-Fe1-N3	91.04
N2-Fe1-N4	175.12
N3-Fe1-N4	93.50
N9-Fe1-N10	177.71
C2-C1-N1	113.82
C2-C1-N5	118.94
N1-C1-N5	127.22
C1-C2-N2	113.64
C1-C2-N6	119.39
N2-C2-N6	126.94
Fe1-N1-C1	114.22
Fe1-N2-C2	114.17
Fe1-N3-C13	126.51
Fe1-N4-C15	126.17
N3-C13-C14	123.77
C13-C14-C15	125.96
Fe1-N9-C34	177.86
Fe1-N10-C36	172.54

References

1. B. D. McCarthy, D. J. Martin, E. S. Rountree, A. C. Ullman and J. L. Dempsey, *Inorg. Chem.*, 2014, **53**, 8350-8361.
2. M. D. Sampson and C. P. Kubiak, *J. Am. Chem. Soc.*, 2016, **138**, 1386-1393.
3. O. Z. Esezobor, W. Zeng, L. Niederegger, M. Grübel and C. R. Hess, *J. Am. Chem. Soc.*, 2022, **144**, 2994-3004.
4. R. Lauenstein, S. L. Mader, H. Derondeau, O. Z. Esezobor, M. Block, A. J. Römer, C. Jandl, E. Riedle, V. R. I. Kaila, J. Hauer, E. Thyrhaug and C. R. Hess, *Chem. Sci.*, 2021, **12**, 7521-7532.
5. P. M. Stanley, C. Thomas, E. Thyrhaug, A. Urstoeger, M. Schuster, J. Hauer, B. Rieger, J. Warnan and R. A. Fischer, *ACS Catal.*, 2021, **11**, 871-882; E. Portenkirchner, J. Gasiorowski, K. Oppelt, S. Schlager, C. Schwarzinger, H. Neugebauer, G. Knör and N. S. Sariciftci, *ChemCatChem*, 2013, **5**, 1790-1796.
6. Z. K. Lopez-Castillo, S. N. V. K. Aki, M. A. Stadtherr and J. F. Brennecke, *Ind. Eng. Chem. Res.*, 2006, **45**, 5351-5360; E. Brunner, *J. CHem. Eng. Data*, 1985, **30**, 269-273.
7. U. Megerle, R. Lechner, B. König and E. Riedle, *Photochem. Photobiol.Sci.*, 2010, **9**, 1400-1406; H. Volfova, Q. Hu and E. Riedle, *EPA Newsletter*, 2019, 51-69.
8. M. Grübel, I. Bosque, P. J. Altmann, T. Bach and C. R. Hess, *Chem. Sci.*, 2018, **9**, 3313-3317; H. S. Stark, P. J. Altmann, S. Sproules and C. R. Hess, *Inorg. Chem.*, 2018, **57**, 6401-6409.
9. v. APEX suite of crystallographic software.
10. v. a. SAINT, SADBS, version 2008.1.
11. G. M. Sheldrick, *Acta Crystallogr., Sect. A: Found. Adv.*, 2015, **71**, 3-8.
12. G. M. Sheldrick, *Acta Crystallogr., Sect. C: Struct. Chem.*, 2015, **71**, 3-8.
13. C. B. Hubschle, G. M. Sheldrick and B. Dittrich, *J. Appl. Crystallogr.*, 2011, **44**, 1281-1284.
14. A. J. Wilson, *International Tables for Crystallography,*, Kluwer Academic Publishers, Dordrecht, The Netherlands, 1992.
15. A. L. Spek, *Acta Crystallogr., Sect. C: Struct. Chem.*, 2015, **71**, 9-18.
16. C. F. Macrae, P. R. Edigngton, P. McCabe, E. Pidcock, G. P. Shields, R. Taylor, M. Towler and J. v. d. Streek, *J. Appl. Crystallogr.*, 2006, **39**, 453-457.
17. J. C. Craig, N. N. Ekwuribe, C. C. Fu and K. A. M. Walker, *Synthesis*, 1981, 303-305.
18. I.-S. H. Lee, E. H. Jeoung and M. M. Kreevoy, *J. Am. Chem. Soc.*, 1997, **119**, 2722-2728.
19. E. Müller, G. Bernardinelli and A. v. Zelewsky, *Inorg. Chem.*, 1988, **27**, 4645-4651.
20. P. Banerjee, A. Company, T. Weyhermüller, E. Bill and C. R. Hess, *Inorg. Chem.*, 2009, **48**, 2944-2955.
21. K. Rickmeyer, L. Niederegger, M. Keilwerth and C. R. Hess, *ACS Catal.*, 2022, **12**, 3046-3057.

Reprint Permissions

Multifaceted role of the Noninnocent Mabiq Ligand in Promoting Selective Reduction of CO_2 to CO

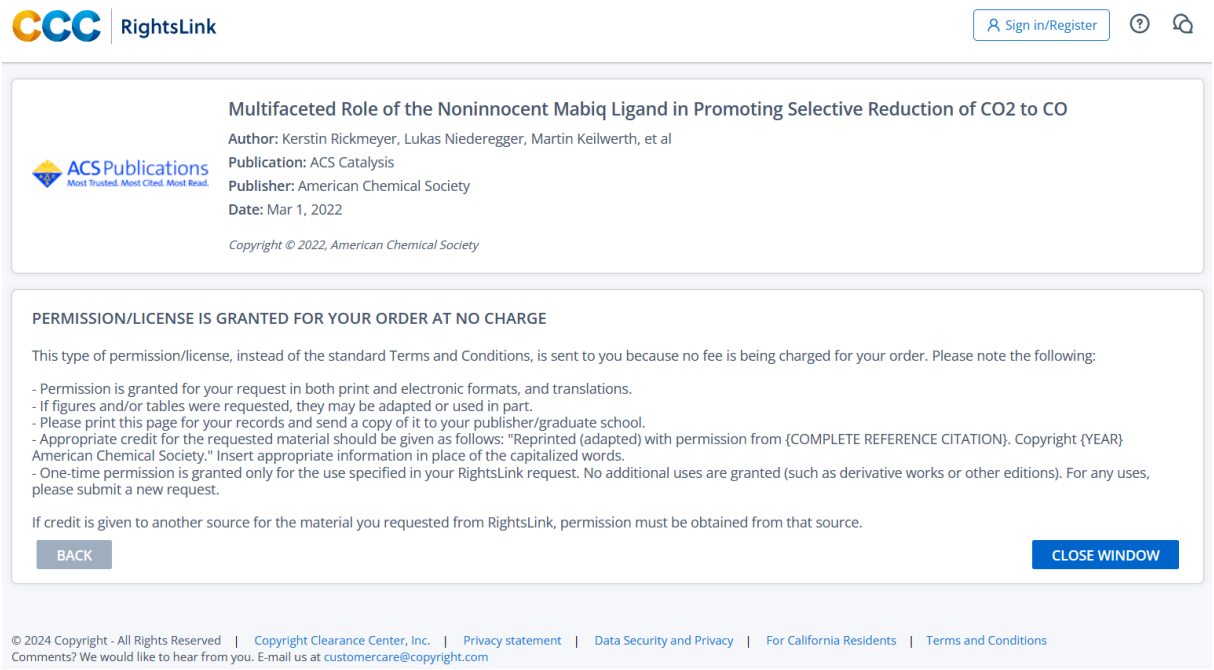

CCC RightsLink

Sign in/Register

ACS Publications
Most Trusted. Most Cited. Most Read.

Multifaceted Role of the Noninnocent Mabiq Ligand in Promoting Selective Reduction of CO2 to CO

Author: Kerstin Rickmeyer, Lukas Niederegger, Martin Keilwerth, et al
Publication: ACS Catalysis
Publisher: American Chemical Society
Date: Mar 1, 2022

Copyright © 2022, American Chemical Society

PERMISSION/LICENSE IS GRANTED FOR YOUR ORDER AT NO CHARGE

This type of permission/license, instead of the standard Terms and Conditions, is sent to you because no fee is being charged for your order. Please note the following:

- Permission is granted for your request in both print and electronic formats, and translations.
- If figures and/or tables were requested, they may be adapted or used in part.
- Please print this page for your records and send a copy of it to your publisher/graduate school.
- Appropriate credit for the requested material should be given as follows: "Reprinted (adapted) with permission from {COMPLETE REFERENCE CITATION}. Copyright {YEAR} American Chemical Society." Insert appropriate information in place of the capitalized words.
- One-time permission is granted only for the use specified in your RightsLink request. No additional uses are granted (such as derivative works or other editions). For any uses, please submit a new request.

If credit is given to another source for the material you requested from RightsLink, permission must be obtained from that source.

BACK

CLOSE WINDOW

Influence of a neighbouring Cu centre on electro- and photocatalytic CO_2 reduction by Fe-Mabiq

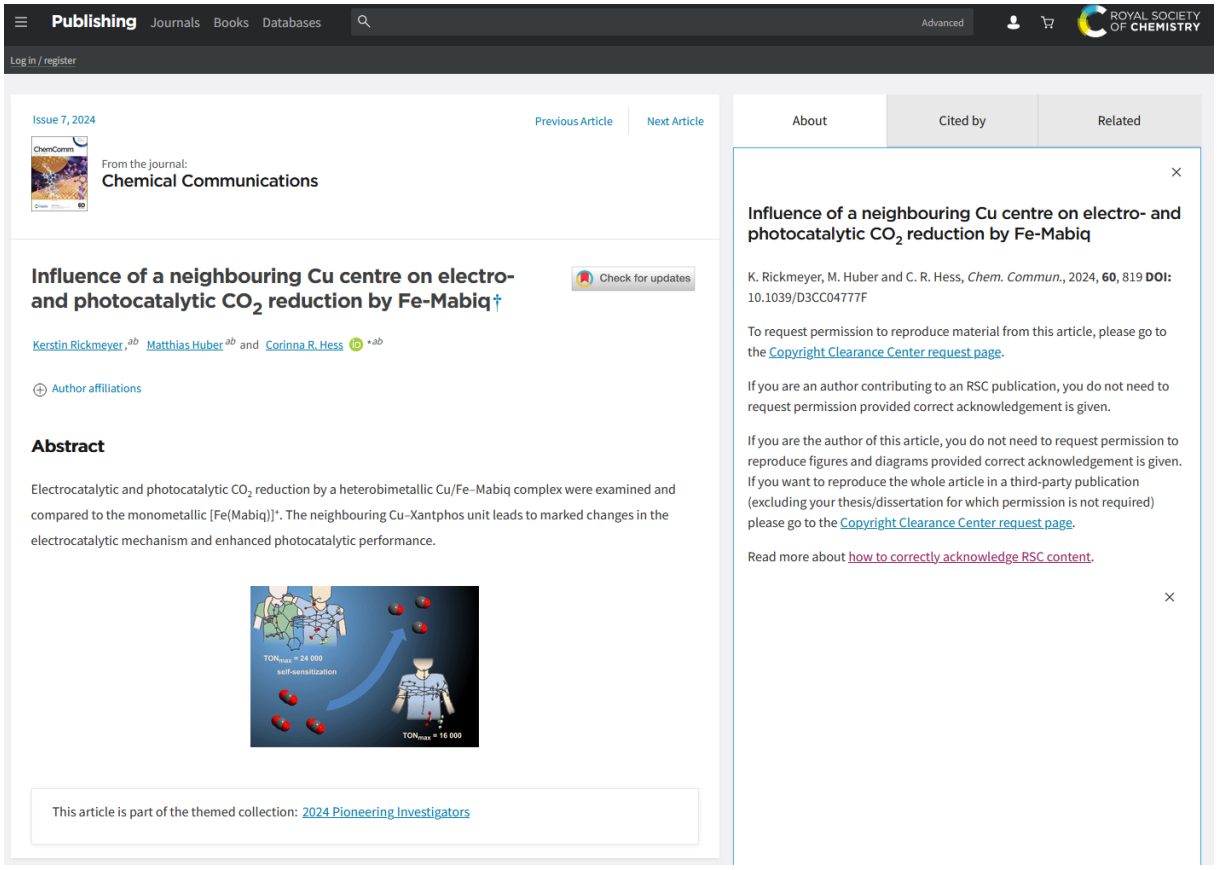

References

(1) Francke, R.; Schille, B.; Roemelt, M. *Chem. Rev.* **2018**, *118*, 4631–4701.

(2) Dalle, K. E.; Warnan, J.; Leung, J. J.; Reuillard, B.; Karmel, I. S.; Reisner, E. *Chem. Rev.* **2019**, *119*, 2752–2875.

(3) Zito, A. M.; Clarke, L. E.; Barlow, J. M.; Bím, D.; Zhang, Z.; Ripley, K. M.; Li, C. J.; Kummeth, A.; Leonard, M. E.; Alexandrova, A. N.; Brushett, F. R.; Yang, J. Y. *Chem. Rev.* **2023**, *123*, 8069–8098.

(4) Elgrishi, N.; Rountree, K. J.; McCarthy, B. D.; Rountree, E. S.; Eisenhart, T. T.; Dempsey, J. L. *J. Chem. Educ.* **2017**, *95*, 197–206.

(5) Modak, A.; Bhanja, P.; Dutta, S.; Chowdhury, B.; Bhaumik, A. *Green Chem.* **2020**, *22*, 4002–4033.

(6) Barlow, J. M.; Yang, J. Y. *ACS Cent. Sci.* **2019**, *5*, 580–588.

(7) Fokin, I.; Denisiuk, A.; Wurtele, C.; Siewert, I. *Inorg. Chem.* **2019**, *58*, 10444–10453.

(8) Boutin, E.; Robert, M. *Trends in Chemistry* **2021**, *3*, 359–372.

(9) Nam, D.-H.; De Luna, P.; Rosas-Hernández, A.; Thevenon, A.; Li, F.; Agapie, T.; Peters, J. C.; Shekhah, O.; Eddaoudi, M.; Sargent, E. H. *Nat. Mater.* **2020**, *19*, 266–276.

(10) Bonetto, R.; Crisanti, F.; Sartorel, A. *ACS Omega* **2020**, *5*, 21309–21319.

(11) Benson, E. E.; Kubiak, C. P.; Sathrum, A. J.; Smieja, J. M. *Chem. Soc. Rev.* **2009**, *38*, 89–99.

(12) Meshitsuka, S.; Ichikawa, M.; Tamaru, K. *J. Chem. Soc., Chem. Commun.* **1974**, 158–159.

(13) Russell, P. G.; Kovac, N.; Srinivasan, S.; Steinberg, M. *J. Electrochem. Soc.* **1977**, *124*, 1329.

(14) Grice, K. A. *Coord. Chem. Rev.* **2017**, *336*, 78–95.

(15) Hawecker, J.; Lehn, J.-M.; Ziessel, R. *J. Chem. Soc., Chem. Commun.* **1985**, 56–58.

(16) White, T. A.; Maji, S.; Ott, S. *Dalton Trans.* **2014**, *43*, 15028–15037.

(17) Dubois, D. L. *Comments Inorg. Chem.* **1997**, *19*, 307–325.

(18) Elgrishi, N.; Chambers, M. B.; Wang, X.; Fontecave, M. *Chem. Soc. Rev.* **2017**, *46*, 761–796.

(19) Bullock, R. M. et al. *Science* **2020**, *369*, eabc3183.

(20) Nuss, P.; Eckelman, M. J. *PLoS ONE* **2014**, *9*, ed. by Janssen, P. J., e101298.

(21) Vesborg, P. C. K.; Jaramillo, T. F. *RSC Adv.* **2012**, *2*, 7933.

(22) Sampson, M. D.; Kubiak, C. P. *J. Am. Chem. Soc.* **2016**, *138*, 1386–1393.

(23) Roy, S. S.; Talukdar, K.; Jurss, J. W. *ChemSusChem* **2021**, *14*, 662–670.

(24) Azcarate, I.; Costentin, C.; Robert, M.; Savéant, J.-M. *J. Am. Chem. Soc.* **2016**, *138*, 16639–16644.

(25) Bonetto, R.; Altieri, R.; Tagliapietra, M.; Barbon, A.; Bonchio, M.; Robert, M.; Sartorel, A. *ChemSusChem* **2020**, *13*, 4111–4120.

(26) Costentin, C.; Drouet, S.; Robert, M.; Saveant, J.-M. *Science* **2012**, *338*, 90–94.

(27) Chen, L.; Guo, Z.; Wei, X. G.; Gallenkamp, C.; Bonin, J.; Anxolabehere-Mallart, E.; Lau, K. C.; Lau, T. C.; Robert, M. *J. Am. Chem. Soc.* **2015**, *137*, 10918–21.

(28) Massie, A. A.; Schremmer, C.; Rüter, I.; Dechert, S.; Siewert, I.; Meyer, F. *ACS Catal.* **2021**, *11*, 3257–3267.

(29) Chapovetsky, A.; Do, T. H.; Haiges, R.; Takase, M. K.; Marinescu, S. C. *J. Am. Chem. Soc.* **2016**, *138*, 5765–8.

(30) Chan, S. L.-F.; Lam, T. L.; Yang, C.; Yan, S.-C.; Cheng, N. M. *Chem. Commun.* **2015**, *51*, 7799–7801.

(31) Elgrishi, N.; Chambers, M. B.; Fontecave, M. *Chem. Sci.* **2015**, *6*, 2522–2531.

(32) Froehlich, J. D.; Kubiak, C. P. *J. Am. Chem. Soc.* **2015**, *137*, 3565–3573.

(33) Burks, D. B.; Davis, S.; Lamb, R. W.; Liu, X.; Rodrigues, R. R.; Liyanage, N. P.; Sun, Y.; Webster, C. E.; Delcamp, J. H.; Papish, E. T. *Chem. Commun.* **2018**, *54*, 3819–3822.

(34) Lilio, A. M.; Grice, K. A.; Kubiak, C. P. *Eur. J. Inorg. Chem.* **2013**, *2013*, 4016–4023.

(35) Haines, R. J.; Wittrig, R. E.; Kubiak, C. P. *Inorg. Chem.* **1994**, *33*, 4723–4728.

(36) Donovan, E. S.; Barry, B. M.; Larsen, C. A.; Wirtz, M. N.; Geiger, W. E.; Kemp, R. A. *Chem. Commun.* **2016**, *52*, 1685–1688.

(37) Costentin, C.; Savéant, J.-M. *ChemElectroChem* **2014**, *1*, 1226–1236.

(38) Matsubara, Y.; Grills, D. C.; Kuwahara, Y. *ACS Catalysis* **2015**, *5*, 6440–6452.

(39) Matsubara, Y. *ACS Energy Lett.* **2017**, *2*, 1886–1891.

(40) Pegis, M. L.; Roberts, J. A. S.; Wasylenko, D. J.; Mader, E. A.; Appel, A. M.; Mayer, J. M. *Inorg. Chem.* **2015**, *54*, 11883–11888.

(41) Matsubara, Y. *ACS Energy Lett.* **2019**, *4*, 1999–2004.

(42) Azcarate, I.; Costentin, C.; Robert, M.; Savéant, J.-M. *J. Phys. Chem. C* **2016**, *120*, 28951–28960.

(43) Fourmond, V.; Jacques, P.-A.; Fontecave, M.; Artero, V. *Inorg. Chem.* **2010**, *49*, 10338–10347.

(44) Rickmeyer, K.; Niederegger, L.; Keilwerth, M.; Hess, C. R. *ACS Catal.* **2022**, *12*, 3046–3057.

(45) Saha, P.; Amanullah, S.; Dey, A. *Acc. Chem. Res.* **2022**, *55*, 134–144.

(46) Jeoung, J.-H.; Dobbek, H. *Science* **2007**, *318*, 1461–1464.

(47) Jiang, C.; Nichols, A. W.; Machan, C. W. *Dalton Trans.* **2019**, *48*, 9454–9468.

(48) Amanullah, S.; Saha, P.; Nayek, A.; Ahmed, M. E.; Dey, A. *Chem. Soc. Rev.* **2021**, *50*, 3755–3823.

(49) Su, X.; McCardle, K. M.; Panetier, J. A.; Jurss, J. W. *Chem. Commun.* **2018**, *54*, 3351–3354.

(50) Derrick, J. S.; Loipersberger, M.; Chatterjee, R.; Iovan, D. A.; Smith, P. T.; Chakarawet, K.; Yano, J.; Long, J. R.; Head-Gordon, M.; Chang, C. J. *J. Am. Chem. Soc.* **2020**, *142*, 20489–20501.

(51) Nie, W.; Tarnopol, D. E.; McCrory, C. C. L. *J. Am. Chem. Soc.* **2021**, *143*, 3764–3778.

(52) Elgrishi, N.; Chambers, M. B.; Artero, V.; Fontecave, M. *Phys. Chem. Chem. Phys.* **2014**, *16*, 13635–44.

(53) Queyriaux, N. *ACS Catal.* **2021**, *11*, 4024–4035.

(54) Lyaskovskyy, V.; de Bruin, B. *ACS Catal.* **2012**, *2*, 270–279.

(55) Barlow, J. M.; Ziller, J. W.; Yang, J. Y. *ACS Catal.* **2021**, *11*, 8155–8164.

(56) Hong, D.; Kawanishi, T.; Tsukakoshi, Y.; Kotani, H.; Ishizuka, T.; Kojima, T. *J. Am. Chem. Soc.* **2019**, *141*, 20309–20317.

(57) Fujita, E.; Creutz, C.; Sutin, N.; Brunschwig, B. S. *Inorg. Chem.* **1993**, *32*, 2657–2662.

(58) Costentin, C.; Passard, G.; Robert, M.; Savéant, J.-M. *Proc. Natl. Acad. Sci. U S A* **2014**, *111*, 14990–14994.

(59) Rosas-Hernández, A.; Junge, H.; Beller, M.; Roemelt, M.; Francke, R. *Catal. Sci. Technol.* **2017**, *7*, 459–465.

(60) Chapovetsky, A.; Welborn, M.; Luna, J. M.; Haiges, R.; Miller T. F., 3.; Marinescu, S. C. *ACS Cent. Sci.* **2018**, *4*, 397–404.

(61) Costentin, C.; Drouet, S.; Passard, G.; Robert, M.; Saveant, J. M. *J. Am. Chem. Soc.* **2013**, *135*, 9023–31.

(62) Bhugun, I.; Lexa, D.; Savéant, J.-M. *J. Phys. Chem.* **1996**, *100*, 19981–19985.

(63) Zhou, J.; Nie, W.; Tarnopol, D. E.; McCrory, C. C. *Chem. Catalysis* **2024**, *4*, 101006.

(64) Malakar, C. C.; Dell'Amico, L.; Zhang, W. *Eur. J. Org. Chem.* **2022**, *26*, e202201114.

(65) Gotico, P.; Del Vecchio, A.; Audisio, D.; Quaranta, A.; Halime, Z.; Leibl, W.; Aukauloo, A. *ChemPhotoChem* **2018**, *2*, 715–719.

(66) Liu, D.; Zhang, M.; Huang, H.-H.; Feng, Q.; Su, C.; Mo, A.; Wang, J.-W.; Qi, Z.; Zhang, X.; Jiang, L.; Chen, Z. *ACS Sustainable Chem. Eng.* **2021**, *9*, 9273–9281.

(67) Gonell, S.; Massey, M. D.; Moseley, I. P.; Schauer, C. K.; Muckerman, J. T.; Miller, A. J. M. *J. Am. Chem. Soc.* **2019**, *141*, 6658–6671.

(68) Gonell, S.; Assaf, E. A.; Duffee, K. D.; Schauer, C. K.; Miller, A. J. M. *J. Am. Chem. Soc.* **2020**, *142*, 8980–8999.

(69) Gonell, S.; Lloret-Fillol, J.; Miller, A. J. M. *ACS Catal.* **2021**, *11*, 615–626.

(70) Amanullah, S.; Saha, P.; Dey, A. *J. Am. Chem. Soc.* **2021**, *143*, 13579–13592.

(71) Costentin, C.; Passard, G.; Robert, M.; Savéant, J.-M. *J. Am. Chem. Soc.* **2014**, *136*, 11821–11829.

(72) Römelt, C.; Song, J.; Tarrago, M.; Rees, J. A.; van Gastel, M.; Weyhermüller, T.; DeBeer, S.; Bill, E.; Neese, F.; Ye, S. *Inorg. Chem.* **2017**, *56*, 4745–4750.

(73) Mondal, B.; Rana, A.; Sen, P.; Dey, A. *J. Am. Chem. Soc.* **2015**, *137*, 11214–11217.

(74) Margarit, C. G.; Asimow, N. G.; Costentin, C.; Nocera, D. G. *ACS Energy Lett.* **2020**, *5*, 72–78.

(75) Berardi, S.; Drouet, S.; Francàs, L.; Gimbert-Suriñach, C.; Guttentag, M.; Richmond, C.; Stoll, T.; Llobet, A. *Chem. Soc. Rev.* **2014**, *43*, 7501–7519.

(76) Pellegrin, Y.; Odobel, F. *C. R. Chimie* **2017**, *20*, 283–295.

(77) Arikawa, Y.; Tabata, I.; Miura, Y.; Tajiri, H.; Seto, Y.; Horiuchi, S.; Sakuda, E.; Umakoshi, K. *Chem. Eur. J.* **2020**, *26*, 5603–5606.

(78) Back, C.; Seo, Y.; Choi, S.; Choe, M. S.; Lee, D.; Baeg, J.-O.; Son, H.-J.; Kang, S. O. *Inorg. Chem.* **2021**, *60*, 14151–14164.

(79) Bassan, E.; Inoue, R.; Fabry, D.; Calogero, F.; Potenti, S.; Gualandi, A.; Cozzi, P. G.; Kamogawa, K.; Ceroni, P.; Tamaki, Y.; Ishitani, O. *Sustainable Energy Fuels* **2023**, *7*, 3454–3463.

(80) Boudreaux, C. M.; Nugegoda, D.; Yao, W.; Le, N.; Frey, N. C.; Li, Q.; Qu, F.; Zeller, M.; Webster, C. E.; Delcamp, J. H.; Papish, E. T. *ACS Catal.* **2022**, *12*, 8718–8728.

(81) Das, S.; Nugegoda, D.; Yao, W.; Qu, F.; Figgins, M. T.; Lamb, R. W.; Webster, C. E.; Delcamp, J. H.; Papish, E. T. *Eur. J. Inorg. Chem.* **2022**, *2022*, e202101016.

(82) Fei, H.; Sampson, M. D.; Lee, Y.; Kubiak, C. P.; Cohen, S. M. *Inorg. Chem.* **2015**, *54*, 6821–6828.

(83) Gracia, L.-L.; Luci, L.; Bruschi, C.; Sambri, L.; Weis, P.; Fuhr, O.; Bizzarri, C. *Chem. Eur. J.* **2020**, *26*, 9929–9937.

(84) Guo, Z.; Cheng, S.; Cometto, C.; Anxolabéhère-Mallart, E.; Ng, S.-M.; Ko, C.-C.; Liu, G.; Chen, L.; Robert, M.; Lau, T.-C. *J. Am. Chem. Soc.* **2016**, *138*, 9413–9416.

(85) Huang, H.-H.; Zhang, J.-H.; Dai, M.; Liu, L.; Ye, Z.; Liu, J.; Zhong, D.-C.; Wang, J.-W.; Zhao, C.; Ke, Z. *Proc. Natl. Acad. Sci.* **2022**, *119*, e2119267119.

(86) Kamogawa, K.; Shimoda, Y.; Miyata, K.; Onda, K.; Yamazaki, Y.; Tamaki, Y.; Ishitani, O. *Chem. Sci.* **2021**, *12*, 9682–9693.

(87) Li, N.-X.; Zhi, Y.; Lu, X.-B.; Xu, Q.-Q.; Mu, W.-H. *Catal. Lett.* **2022**, DOI: 10.1007/s10562-022-03953-0.

(88) Liyanage, N. P.; Yang, W.; Guertin, S.; Sinha Roy, S.; Carpenter, C. A.; Adams, R. E.; Schmehl, R. H.; Delcamp, J. H.; Jurss, J. W. *Chem. Commun.* **2019**, *55*, 993–996.

(89) Manafe, S. Y.; Le, N.; Lambert, E. C.; Curiac, C.; Nugegoda, D.; Das, S.; Hunt, L. A.; Qu, F.; Whitt, L. M.; Fedin, I.; Hammer, N. I.; Webster, C. E.; Delcamp, J. H.; Papish, E. T. *ACS Catal.* **2024**, *14*, 6589–6602.

(90) Rosas-Hernández, A.; Steinlechner, C.; Junge, H.; Beller, M. *Green Chem.* **2017**, *19*, 2356–2360.

(91) Steinlechner, C.; Roesel, A. F.; Oberem, E.; Päpcke, A.; Rockstroh, N.; Gloaguen, F.; Lochbrunner, S.; Ludwig, R.; Spannenberg, A.; Junge, H.; Francke, R.; Beller, M. *ACS Catal.* **2019**, *9*, 2091–2100.

(92) Takeda, H.; Kamiyama, H.; Okamoto, K.; Irimajiri, M.; Mizutani, T.; Koike, K.; Sekine, A.; Ishitani, O. *J. Am. Chem. Soc.* **2018**, *140*, 17241–17254.

(93) Tamaki, Y.; Koike, K.; Ishitani, O. *Chem. Sci.* **2015**, *6*, 7213–7221.

(94) Thomas, C.; Wittig, M.; Rieger, B. *ChemCatChem* **2022**, *14*, e202200841.

(95) Wang, J.-W. et al. *J. Am. Chem. Soc.* **2023**, *145*, 676–688.

(96) Yamazaki, Y.; Onoda, T.; Ishikawa, J.; Furukawa, S.; Tanaka, C.; Utsugi, T.; Tsubomura, T. *Front. Chem.* **2019**, *7*, 288.

(97) Ishida, H.; Terada, T.; Tanaka, K.; Tanaka, T. *Inorg. Chem.* **1990**, *29*, 905–911.

(98) Sampaio, R. N.; Grills, D. C.; Polyansky, D. E.; Szalda, D. J.; Fujita, E. *J. Am. Chem. Soc.* **2020**, *142*, 2413–2428.

(99) Zhao, J.; Wu, W.; Sun, J.; Guo, S. *Chem. Soc. Rev.* **2013**, *42*, 5323.

(100) Lazorski, M. S.; Castellano, F. N. *Polyhedron* **2014**, *82*, 57–70.

(101) Grübel, M. Photoredoxchemistry with Nickel-based Catalysts, Ph.D. Thesis, Technical University of Munich, 2019.

(102) Sasikumar, D.; John, A. T.; Sunny, J.; Hariharan, M. *Chem. Soc. Rev.* **2020**, *49*, 6122–6140.

(103) Marian, C. M. *Annu. Rev. Phys. Chem.* **2021**, *72*, 617–640.

(104) Leung, C.-F.; Lau, T.-C. *Energy Fuels* **2021**, *35*, 18888–18899.

(105) Kim, D.; Dang, V. Q.; Teets, T. S. *Chem. Sci.* **2024**, *15*, 77–94.

(106) Shon, J.-H.; Teets, T. S. *ACS Energy Lett.* **2019**, *4*, 558–566.

(107) McCusker, J. K. *Science* **2019**, *363*, 484–488.

(108) Ma, F.; Luo, Z.-M.; Wang, J.-W.; Aramburu-Trošelj, B. M.; Ouyang, G. *Coord. Chem. Rev.* **2024**, *500*, 215529.

(109) Takeda, H.; Cometto, C.; Ishitani, O.; Robert, M. *ACS Catal.* **2017**, *7*, 70–88.

(110) Beaudelot, J.; Oger, S.; Peruško, S.; Phan, T.-A.; Teunens, T.; Moucheron, C.; Evano, G. *Chem. Rev.* **2022**, *122*, 16365–16609.

(111) Zhang, Y.; Schulz, M.; Wächtler, M.; Karnahl, M.; Dietzek, B. *Coord. Chem. Rev.* **2018**, *356*, 127–146.

(112) Takeda, H.; Ohashi, K.; Sekine, A.; Ishitani, O. *J. Am. Chem. Soc.* **2016**, *138*, 4354–4357.

(113) Luo, S.-P.; Mejía, E.; Friedrich, A.; Pazidis, A.; Junge, H.; Surkus, A.-E.; Jackstell, R.; Denurra, S.; Gladiali, S.; Lochbrunner, S.; Beller, M. *Angew. Chem. Int. Ed.* **2012**, *52*, 419–423.

(114) Bizzarri, C.; Arndt, A. P.; Kohaut, S.; Fink, K.; Nieger, M. *J. Organomet. Chem.* **2018**, *871*, 140–149.

(115) Gracia, L.-L.; Barani, E.; Braun, J.; Carter, A. B.; Fuhr, O.; Powell, A. K.; Fink, K.; Bizzarri, C. *ChemCatChem* **2022**, *14*, e202201163.

(116) Kübler, J. A.; Pfund, B.; Wenger, O. S. *JACS Au* **2022**, *2*, 2367–2380.

(117) Zhang, J.-X.; Hu, C.-Y.; Wang, W.; Wang, H.; Bian, Z.-Y. *Appl. Catal., A* **2016**, *522*, 145–151.

(118) Rao, H.; Lim, C.-H.; Bonin, J.; Miyake, G. M.; Robert, M. *J. Am. Chem. Soc.* **2018**, *140*, 17830–17834.

(119) Wang, Y.; Gao, X.-W.; Li, J.; Chao, D. *Chem. Commun.* **2020**, *56*, 12170–12173.

(120) Wang, Y.; Liu, T.; Chen, L.; Chao, D. *Inorg. Chem.* **2021**, *60*, 5590–5597.

(121) Kientz, M.; Lowe, G.; McCarthy, B. G.; Miyake, G. M.; Bonin, J.; Robert, M. *ChemPhotoChem* **2022**, *6*, e202200009.

(122) De La Torre, P.; Derrick, J. S.; Snider, A.; Smith, P. T.; Loipersberger, M.; Head-Gordon, M.; Chang, C. J. *ACS Catal.* **2022**, *12*, 8484–8493.

(123) Zhang, Y.; Heberle, M.; Wächtler, M.; Karnahl, M.; Dietzek, B. *RSC Adv.* **2016**, *6*, 105801–105805.

(124) Sartor, S. M.; Lattke, Y. M.; McCarthy, B. G.; Miyake, G. M.; Damrauer, N. H. *J. Phys. Chem. A* **2019**, *123*, 4727–4736.

(125) Vlcek, A. A.; Dodsworth, E. S.; Pietro, W. J.; Lever, A. B. P. *Inorg. Chem.* **1995**, *34*, 1906–1913.

(126) Gholamkhass, B.; Mametsuka, H.; Koike, K.; Tanabe, T.; Furue, M.; Ishitani, O. *Inorg. Chem.* **2005**, *44*, 2326–2336.

(127) Tamaki, Y.; Morimoto, T.; Koike, K.; Ishitani, O. *Proc. Natl. Acad. Sci. U S A* **2012**, *109*, 15673–15678.

(128) Tamaki, Y.; Ishitani, O. *ACS Catal.* **2017**, *7*, 3394–3409.

(129) Yamazaki, Y.; Takeda, H.; Ishitani, O. *J. Photochem. Photobiol., C* **2015**, *25*, 106–137.

(130) Das, S.; Rodrigues, R. R.; Lamb, R. W.; Qu, F.; Reinheimer, E.; Boudreaux, C. M.; Webster, C. E.; Delcamp, J. H.; Papish, E. T. *Inorg. Chem.* **2019**, *58*, 8012–8020.

(131) Rao, H.; Bonin, J.; Robert, M. *Chem. Commun.* **2017**, *53*, 2830–2833.

(132) Bonchio, M.; Bonin, J.; Ishitani, O.; Lu, T.-B.; Morikawa, T.; Morris, A. J.; Reisner, E.; Sarkar, D.; Toma, F. M.; Robert, M. *Nat. Catal.* **2023**, *6*, 657–665.

(133) Murov, S. L., *Handbook of photochemistry*, 2. ed., rev. and expanded; Carmichael, I., Hug, G. L., Eds., Literaturverz. S. 351 - 376; Dekker: New York [u.a.], 1993; 420 pp.

(134) Kuhn, H. J.; Braslavsky, S. E.; Schmidt, R. *Pure Appl. Chem.* **2004**, *76*, 2105–2146.

(135) Boutin, E.; Merakeb, L.; Ma, B.; Boudy, B.; Wang, M.; Bonin, J.; Anxolabéhère-Mallart, E.; Robert, M. *Chem. Soc. Rev.* **2020**, *49*, 5772–5809.

(136) Banerjee, P.; Company, A.; Weyhermüller, T.; Bill, E.; Hess, C. R. *Inorg. Chem.* **2009**, *48*, 2944–2955.

(137) Puttock, E. V.; Banerjee, P.; Kaspar, M.; Drennen, L.; Yufit, D. S.; Bill, E.; Sproules, S.; Hess, C. R. *Inorg. Chem.* **2015**, *54*, 5864–5873.

(138) Grübel, M.; Bosque, I.; Altmann, P. J.; Bach, T.; Hess, C. R. *Chem. Sci.* **2018**, *9*, 3313–3317.

(139) Stark, H. S.; Altmann, P. J.; Sproules, S.; Hess, C. R. *Inorg. Chem.* **2018**, *57*, 6401–6409.

(140) Lauenstein, R.; Mader, S. L.; Derondeau, H.; Esezobor, O. Z.; Block, M.; Römer, A. J.; Jandl, C.; Riedle, E.; Kaila, V. R. I.; Hauer, J.; Thyrhaug, E.; Hess, C. R. *Chem. Sci.* **2021**, *12*, 7521–7532.

(141) Rickmeyer, K.; Huber, M.; Hess, C. R. *Chem. Commun.* **2024**, *60*, 819–822.

(142) Esezobor, O. Z.; Zeng, W.; Niederegger, L.; Grübel, M.; Hess, C. R. *J. Am. Chem. Soc.* **2022**, *144*, 2994–3004.

(143) Tok, G. C.; Freiberg, A. T. S.; Gasteiger, H. A.; Hess, C. R. *ChemCatChem* **2019**, *11*, 3973–3981.

(144) Tok, G. C.; Reiter, S.; Freiberg, A. T. S.; Reinschlüssel, L.; Gasteiger, H. A.; de Vivie-Riedle, R.; Hess, C. R. *Inorg. Chem.* **2021**, *60*, 13888–13902.

(145) Boyce, S. A. J.; Moutet, J.; Niederegger, L.; Simler, T.; Nocton, G.; Hess, C. R. *Inorg. Chem.* **2021**, *60*, 403–411.

(146) Grau, S.; Schilling, M.; Moonshiram, D.; Benet-Buchholz, J.; Luber, S.; Llobet, A.; Gimbert-Suriñach, C. *ChemSusChem* **2020**, *13*, 2745–2752.

(147) Fernández, S.; Franco, F.; Casadevall, C.; Martin-Diaconescu, V.; Luis, J. M.; Lloret-Fillol, J. *J. Am. Chem. Soc.* **2020**, *142*, 120–133.

(148) Kaspar, M.; Altmann, P. J.; Pöthig, A.; Sproules, S.; Hess, C. R. *Chem. Commun.* **2017**, *53*, 7282–7285.

(149) Cometto, C.; Chen, L.; Lo, P.-K.; Guo, Z.; Lau, K.-C.; Anxolabéhère-Mallart, E.; Fave, C.; Lau, T.-C.; Robert, M. *ACS Catal.* **2018**, *8*, 3411–3417.

(150) Behar, D.; Dhanasekaran, T.; Neta, P.; Hosten, C. M.; Ejeh, D.; Hambright, P.; Fujita, E. *J. Phys. Chem. A* **1998**, *102*, 2870–2877.

(151) Liu, J. J.; Chapovetsky, A.; Haiges, R.; Marinescu, S. C. *Inorg. Chem.* **2021**, *60*, 17517–17528.

(152) Rosas-Hernández, A.; Alsabeh, P. G.; Barsch, E.; Junge, H.; Ludwig, R.; Beller, M. *Chem. Commun.* **2016**, *52*, 8393–8396.

(153) Chabolla, S. A.; Yang, J. Y. *ACS Cent. Sci.* **2018**, *4*, 315–317.

(154) Chen, H.; Chen, L.; Chen, G.; Robert, M.; Lau, T.-C. *ChemPhysChem* **2021**, *22*, 1835–1843.

(155) Cheng, M.; Yu, Y.; Zhou, X.; Luo, Y.; Wang, M. *ACS Catal.* **2019**, *9*, 768–774.

(156) Léonard, N. G.; Dhaoui, R.; Chantarojsiri, T.; Yang, J. Y. *ACS Catal.* **2021**, *11*, 10923–10932.

(157) Ouyang, T.; Huang, H.-H.; Wang, J.-W.; Zhong, D.-C.; Lu, T.-B. *Angew. Chem. Int. Ed.* **2017**, *56*, 738–743.

(158) Reath, A. H.; Ziller, J. W.; Tsay, C.; Ryan, A. J.; Yang, J. Y. *Inorg. Chem.* **2017**, *56*, 3713–3718.

(159) Golwankar, R. R.; Kumar, A.; Day, V. W.; Blakemore, J. D. *Chem. Eur. J.* **2022**, *28*, e202200344.